AD-A111 719   OHIO UNIV ATHENS AVIONICS ENGINEERING CENTER   F/G 20/14
                  INVESTIGATION AND DEVELOPMENT OF VHF GROUND-AIR PROPAGATION COM--ETC(U)
                  MAR 81   K A CHAMBERLIN   DOT-FA78WA-4189
UNCLASSIFIED   OU/AEC/EER-81-1   NL

1.0

1.1

1.25

2.8
3.2
3.6
4.0

2.5

2.2

2.0

1.4

1.8

1.6

MICROCOPY RESOLUTION TEST CHART

NATIONAL BUREAU OF STANDARDS 1963-A

INVESTIGATION AND DEVELOPMENT OF VHF GROUND-AIR PROPAGATION

COMPUTER MODELING INCLUDING THE ATTENUATING EFFECTS

OF FORESTED AREAS FOR WITHIN-LINE-OF-SIGHT

PROPAGATION PATHS

By

Kent A. Chamberlin

Avionics Engineering Center
Department of Electrical Engineering
Ohio University
Athens, Ohio 45701

MARCH 1981

FINAL REPORT

PREPARED FOR

DTIC
ELECT
MAR 0 5 1982

NOTICE

This document is disseminated under the sponsorship of the
Department of Transportation in the interest of information
exchange. The United States Government assumes no liability
for the contents or use thereof.

1. Report No.	2. Government Accession No.	3. Recipient's Catalog No.

4. Title and Subtitle	5. Report Date
Investigation and Development of VHF Ground-Air Propagation Computer Modeling Including the Attenuating Effects of Forested Areas for Within-Line-of-Sight Propagation Paths	March 1981
	6. Performing Organization Code

7. Author(s)	8. Performing Organization Report No.
Kent A. Chamberlin	OU/AEC/EER 51-1

9. Performing Organization Name and Address	10. Work Unit No.
Avionics Engineering Center Department of Electrical Engineering Ohio University Athens, Ohio 45701	
	11. Contract or Grant No.
	DOT-FA78WA-4189
	13. Type of Report and Period Covered

12. Sponsoring Agency Name and Address	13. Type of Report and Period Covered
U.S. Department of Transportation Federal Aviation Administration, Airway Facilities Service Washington, D.C. 20590	Final Report
	14. Sponsoring Agency Code

15. Supplementary Notes

16. Abstract

An investigation into short-distance (5-100 nm), air-ground, VHF propagation computer models is presented. An evaluation of existing propagation models is afforded by measured signal strength data, collected for this study, obtained for a variety of propagation paths; this evaluation shows existing models to be deficient due to their incapability to calculate attenuation caused by trees for within-line-of-sight propagation paths. The theory behind, and the development of, a computer model that does successfully account for tree attenuation is discussed and documented. A complete description of signal strength data collection is given detailing measurement equipment, site conditions, and data reduction.

17. Key Words VHF air-ground propagation, line of sight, tree attenuation, vertical polarization, propagation modeling, GTD, moment methods, physical optics, coverage area, vertical lobing, antenna pattern distortion, RCAG modeling, reflection coefficient, signal strength measurements	18. Distribution Statement This document is available to the U.S. public through the National Technical Information Service, Springfield, Virginia 22161

19. Security Classif. (of this report)	20. Security Classif. (of this page)	21. No. of Pages	22. Price
Unclassified	Unclassified	172	

Form DOT F 1700.7 (8-69)

i

METRIC CONVERSION FACTORS

Approximate Conversions to Metric Measures

Symbol	When You Know	Multiply by	To Find	Symbol
		LENGTH		
in	inches	*2.5	centimeters	cm
ft	feet	30	centimeters	cm
yd	yards	0.9	meters	m
mi	miles	1.6	kilometers	km
		AREA		
in²	square inches	6.5	square centimeters	cm²
ft²	square feet	0.09	square meters	m²
yd²	square yards	0.8	square meters	m²
mi²	square miles	2.6	square kilometers	km²
	acres	0.4	hectares	ha
		MASS (weight)		
oz	ounces	28	grams	g
lb	pounds	0.45	kilograms	kg
	short tons (2000 lb)	0.9	tonnes	t
		VOLUME		
tsp	teaspoons	5	milliliters	ml
tbsp	tablespoons	15	milliliters	ml
fl oz	fluid ounces	30	milliliters	ml
c	cups	0.24	liters	l
pt	pints	0.47	liters	l
qt	quarts	0.95	liters	l
gal	gallons	3.8	liters	l
ft³	cubic feet	0.03	cubic meters	m³
yd³	cubic yards	0.76	cubic meters	m³
		TEMPERATURE (exact)		
°F	Fahrenheit temperature	5/9 (after subtracting 32)	Celsius temperature	°C

*1 in = 2.54 cm (exactly). For other exact conversions and more detailed tables, see NBS Misc. Publ. 286, Units of Weights and Measures, Price $2.25, SD Catalog No. C13.10.286.

Approximate Conversions from Metric Measures

Symbol	When You Know	Multiply by	To Find	Symbol
		LENGTH		
mm	millimeters	0.04	inches	in
cm	centimeters	0.4	inches	in
m	meters	3.3	feet	ft
m	meters	1.1	yards	yd
km	kilometers	0.6	miles	mi
		AREA		
cm²	square centimeters	0.16	square inches	in²
m²	square meters	1.2	square yards	yd²
km²	square kilometers	0.4	square miles	mi²
ha	hectares (10,000 m²)	2.5	acres	
		MASS (weight)		
g	grams	0.035	ounces	oz
kg	kilograms	2.2	pounds	lb
t	tonnes (1000 kg)	1.1	short tons	
		VOLUME		
ml	milliliters	0.03	fluid ounces	fl oz
l	liters	2.1	pints	pt
l	liters	1.06	quarts	qt
l	liters	0.26	gallons	gal
m³	cubic meters	35	cubic feet	ft³
m³	cubic meters	1.3	cubic yards	yd³
		TEMPERATURE (exact)		
°C	Celsius temperature	9/5 (then add 32)	Fahrenheit temperature	°F
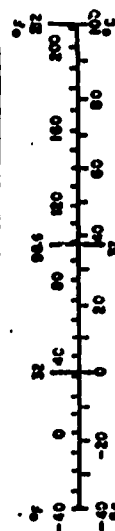
TABLE OF CONTENTS

I. INTRODUCTION AND SUMMARY

A. Summary. The objective of this work is to investigate and develop the capability to model coverage area for VHF communications sites. As a first step towards realizing this objective, measured signal strength data were collected systematically to provide insight into the major factors that influence propagation for the frequency range and conditions of interest. These measurements were collected using a variety of aircraft equipped with standard VHF communications antennas. Prior to these measurements, airborne antenna lobing considerations caused concern that non-standard airborne equipment might be necessary to obtain accurate and repeatable measurements. However, the measured data presented here do not reveal any noticeable degree of lobing effects or variation in observed signal strength with different aircraft. Thus, the capability to collect accurate and repeatable airborne signal strength data using standard equipment is in itself a significiant finding. Further, the measured data enable propagation models to be evaluated.

Experiments designed to determine the effect of signal scattering from a standard RCAG antenna platform caused by the supporting tower, nearby towers, lightning rods, and other antennas on the platform, show that no measurable scattering exists. The radiation pattern for an antenna mounted on a standard RCAG tower is essentially isotropic. However, these same experiments did show appreciable antenna pattern distortion resulting from terrain variations within the reflecting zone as well as from tree cover, even though the aircraft was within clear line of sight. The effect of trees on signal strength, which has been observed to cause up to 15 dB attenuation within line of sight, is not included in existing propagation models. The contribution of the work presented here includes introduction of tree attenuation effects into an existing GTD terrain scattering model. This effort has resulted in a propagation model that has a demonstrated accuracy greater than any other known model for the conditions of interest here.

The theory that explains tree attenuation effects, which is consistent with classical electromagnetic theory, states that signal reduction within line of sight is caused by an out-of-phase reflection from tree tops. This theory is only valid for near-grazing incidence, which corresponds to aircraft positions near the horizon; because coverage area typically extends to near the horizon, the theory is appropriate for this application.

Input data necessary to implement the newly-developed model can be obtained from readily-available topographical maps in addition to aerial photographs. These maps and photographs are used to specify general terrain contours and tree cover locations. At most, two man days of data reduction time are sufficient to generate input data for the modeling process.

Other propagation and scattering models investigated were physical optics, moment methods, and the Institute for Telecommunication

Sciences (ITS) Longley-Rice model. Both the moment methods model and the ITS model were implemented at Ohio University. The moment methods model, which calculates parasitic scattering from conducting structures, is not considered applicable here because parasitic scattering was measured to be insignificant for standard site configurations. However, if a site is encountered where parasitic scattering is considered to be a factor, indications are that the moment methods implementation would provide meaningful results. The ITS model, which operates on a statistical best-estimate of signal strength based upon previously-collected data from other sites, is not intended for the typically low-power, short propagation path application addressed here. However, for high-power communications sites, where coverage distance is expected to extend to greater than 100 nmi., the ITS model should be capable of providing a good estimate of received signal strength.

The work reported here has focused on the factors affecting VHF ground-to-air propagation for short propagation paths. As a result of this work, the capability to model such propagation paths has been enhanced substantially. Based upon comparisons of modeled data with measured data, it now appears feasible to estimate system performance using the model introduced here.

B. <u>Background</u>. The purpose of this analytical and experimental effort is to demonstrate the use of mathematical methods to predict the expected ground-to-air coverage area from any standard remote, communications, air/ground (RCAG) facility. The benefit of such analysis is primarily wise selection of future RCAG sites, permitting time and cost savings in the planning and construction process. The research presented in this report was funded by the Federal Aviation Administration (FAA) under Contract FA79WA-4189.

Until recently, stringent siting requirements were not considered essential due to the limited number of facilities in operation in addition to relatively wide frequency separation between channels. In 1976 [1], however, as a result of increasing communication demands and the non-availability of additional frequency spectrum, the channel separation was reduced from 50 KHz to 25 KHz. This decrease, in addition to the increasing number of transmitter sites, operating at lower radiated powers, placed greater emphasis on the necessity for proper spacing and siting of new facilities in order to prevent co-channel and adjacent-channel interference, while continuing to provide adequate coverage.

The FAA has used several modeling techniques, including smooth-earth and line-of-sight, to predict communication coverage areas in the past. The smooth-earth model determines the vertical antenna pattern for all sites as a function of transmitter antenna height and receiver elevation angle assuming constant terrain elevation in the reflecting zone. The smooth-earth model determines antenna gain for a given aircraft position from which received power can be calculated. Such a prediction technique has obvious shortcomings when terrain

variations in the reflecting zone are in the mie region or the region of spectral reflection, a real probability at VHF. The line-of-sight model (implemented for the FAA by the Electromagnetic Compatibility Analysis Center (ECAC)) works under the assumption that if no physical blockage exists between the receiving and transmitting antennas, communication will be adequate; for sufficient transmitter power, this will be the case. However, with lower transmitter powers necessary to prevent co-channel and adjacent-channel interference, line of-sight does not always guarantee reception. Conversely, because of knife-edge diffraction, being beyond line-of-sight does not necessarily dictate that an inadequate signal will exist. Because of these demonstrated deficiencies, Ohio University was contracted to investigate and evaluate more sophisticated models and determine their applicability with regards to FAA requirements. Accordingly, a literature search was performed to identify all existing scattering or propagation modeling techniques within the frequency range of interest. Candidate techniques or models that were discovered in this search were the Longley-Rice Statistical Model, developed at the Institute for Telecommunication Sciences (ITS), moment-methods scattering technique, physical-optics terrain model, and geometrical theory of diffraction (GTD) terrain model. The application and performance of each of these models or techniques is presented in Section II.

Of the existing models analyzed, the ITS model appeared most suitable for longer-range predictions, while the GTD model appeared more appropriate for close-range predictions for reasons discussed in Section II. However, all models, including GTD have a common deficiency due to their insensitivity to the effects of trees or forests on propagation, a factor which has been found during this study to have profound effects. Consequently, after an additional literature search, a novel modeling technique for dealing with forests proposed by Tamir was included in a GTD model. The analysis of tree effects in propagation modeling, supported by measured data, is a major innovative technical contribution of this work.

To provide insight into factors affecting propagation and to allow for a meaningful evaluation of any prospective model, a series of airborne signal strength measurements was made by both the FAA National Aviation Facilities Experimental Center (NAFEC), Atlantic City, New Jersey, and Ohio University. (Note: NAFEC has been recently renamed FAA Technical Center.) Such measurements have been performed routinely by the FAA for facility certification; however, data from past measurements have not been documented nor reduced in a manner that would allow subsequent analysis to correlate signal strength with aircraft position. Consequently, a major facet of the research reported here is the design and execution of well-documented, repeatable signal strength experiments. Subsequent to the measurements, signal strength data are reduced from analog strip chart recordings and placed in computer files, thus providing a convenient and accurate means for analysis, comparison, and presentation. Section IV discusses the data collection effort, giving specifics on measurement equipment, data reduction, site documentation, as well as an analysis of the measured data.

C. Statement of the Problem. As stated, the objective of this research is to establish a computer model capable of predicting the ground-to-air coverage area for a standard RCAG site. Clearly, the first step towards this objective is to determine the radiated signal parameters associated with a standard RCAG site. Many of these parameters are dictated by FAA specifications [2] and are as follows:

1. Polarization is vertical.

2. Operating frequencies are between 117.975 to 136.000 MHz.

3. Effective radiated power is typically 5 watts; however, power of up to 100 watts may be necessary in some circumstances.

4. Ground-to-air coverage area is defined to extend to the point at which the signal incident to the antenna drops below -87 dBm.

5. A General Instruments Corporation TACO VHF antenna (Model D-2276) is used for transmitting.

6. Configurations of antennas and lightning rods on this supporting lower core standard, i.e., the proximity of the transmitting antenna with respect to other elements, and supporting structures is the same for all RCAG sites.

7. Antenna heights may vary from 40 to 70 feet depending upon local terrain configuration.

It should be noted that these statements will apply particularly to all future sites although some existing sites are not consistent with these specifications.

Given the above conditions for which signal coverage is sought, the next step towards achieving the stated objective is to investigate known factors affecting propagation as they relate to standard RCAG facilities.

II. EXISTING METHODS FOR COMMUNICATIONS COVERAGE PREDICTION

A. <u>Introduction.</u> Factors known to affect VHF wave propagation, and hence signal strength, are readily identified in the literature [3, 4]; these factors are listed below:

    1.   Distance between transmitter and receiver.

    2.   Vertical lobing and ground constants (conductivity and permittivity).

    3.   Conducting obstructions and structures.

    4.   Tropospheric effects.

    5.   Terrain (including diffraction).

    6.   Vegetation.

It should be noted that there are no priorities associated with the above factors, since any may dominate depending upon the particular site being evaluated.

The task of predicting signal strength becomes one of determining the impact of each of the above factors on propagation. Computer models or modeling schemes are presently available that use the above factors in making signal strength predictions. The purpose of this section is to present these existing models and to discuss their performance either with respect to measured data or by using a theoretical analysis. The discussions of existing models will be brief and heuristic in nature since these are thoroughly covered in the literature indicated.

Vertical lobing will occur as a result of a changing path length, and thus a changing phase relationship, between the direct and reflected wave as the receiver changes in elevation angle with respect to the transmitter. A commonly-used method for determining vertical lobing patterns is to work under the assumption that the area in the reflecting zone of the transmitting antenna is essentially flat. Using this flat-earth model, analyses can also be made on the effects of changing ground constants by calculating the attenuation and phase shift imposed upon the reflected wave which is represented by the complex reflection coefficient. The fundamental drawback to the flat-earth model is that very few sites are flat enough for the assumption of flat earth to be valid at VHF.

Induced currents will appear on any conducting object in the presence of a time-varying electromagnetic field. For this reason, a conducting structure or obstruction in the presence of a transmitting antenna will to some degree change the radiation pattern. For a standard RCAG site, near-by conducting structures are the supporting tower, other antennas on the tower, lightning rods, and other towers

at the site. To investigate the effects of these structures, a moment methods, scattering model was implemented on the Ohio University computer. The results of this simulation showed variations of approximately 2.5 dB in a 360° orbit for a standard RCAG site. Subsequent signal strength measurements, which are presented in Section V, show that the variation due to conducting structures are so small as to be immeasurable in an actual standard facility. Consequently, further work on modeling of conducting structures was deemed unnecessary. A brief description of moment methods techniques is presented in Section IIC to document one phase of the total research effort.

A computer model that has proven successful for predicting ground-to-air communications capability at VHF has been developed by the Institute for Telecommunications Sciences (ITS). This model is based upon the statistics derived from a large body of measured signal strength data collected over a wide variety of conditions. Computer algorithms are employed to relate parameters describing the condition under which measurements were taken to measure signal strength. Although the ITS model was designed for ground-to-ground coverage prediction, accurate predictions have been obtained for ground-to-air coverage [5] for relatively long distances (100-160 nm) and high transmitter powers (100W -10KW). Comparisons of ITS model predictions with measured data from several RCAG sites taken at shorter distances (10-40 nm) and lower transmitter powers (5-10W) show less agreement than for the longer distances and higher powers. The lack of agreement between measured and predicted data for short propagation paths is not surprising considering the theory of operation for the ITS model, which is discussed in greater detail in Section IID. The ITS model was acquired from the Institute for Telecommunication Sciences for use in this study and made operational on the Ohio University Computer. It is capable of predicting coverage area for any given site with considerably less effort than would be required for any other model investigated. Because the ITS model can be readily implemented, and because of its proven ground-to-air prediction capability for certain applications, the ITS model is considered to be a valuable tool for RCAG site modeling.

Some recent work by other researchers has been devoted to determining the phase and amplitude of signals radiated in the presence of irregular terrain for the purpose of predicting the performance characteristics of Instrument Landing Systems (ILS). Two modeling techniques that have provided accurate results in ILS modeling fall under the categories of Physical Optics (PO) and the Geometrical Theory of Diffraction (GTD). Computer models implementing PO or GTD require input data on transmitting and receiving antenna locations as well as data on the terrain between the antennas. As will be expanded upon in Sections IIE and F, both modeling schemes calculate the scattered fields by an analysis of wave interaction with the ground; the total received field is the complex sum of the direct field with the scattered field. Signal strength values predicted by PO or GTD are by far more sensitive to terrain variations than any other modeling techniques investigated. Consequently, closer agreement between predicted

and measured signal strength can be realized by PO and GTD than for other known models for short (10-40 nm) propagation paths. Despite their relatively good performance in signal strength prediction accuracy, neither modeling technique had been capable of accounting for the effects of vegetation prior to the research reported here. Section III discusses the theory of VHF propagation through vegetation and how it is how accounted for by a GTD computer model.

B. Flat-Earth Model. To determine the vertical lobing pattern for a given antenna height, image theory is used along with the assumption that the terrain in the reflecting zone of the antenna is essentially flat. The reason for determining the vertical lobing pattern is to insure that a null in the pattern does not occur at a location where communication coverage is needed.

There are very few sites where the reflecting zone is flat enough to enable accurate prediction of signal strength using the flat-earth model; however, the concepts involved are important to an understanding of signal strength prediction techniques in general. These concepts, which form the basis for image theory, address the geometry, mathematics, and boundary conditions for a vertically polarized wave propagating above a ground plane. Detailed descriptions of image theory are provided by many texts on electromagnetics [6,7]; the abbreviated discussion presented here is to establish notation and to expose deficiencies with respect to the application under study.

Figure 2-1 shows a vertically polarized antenna radiating at a height h above a ground plane. The observation point is at an angle o with respect to the reference coordinate system, and is in the far field of the antenna array. As shown in Figure 2-1a, there are two possible paths by which signal energy will reach the observation point, a direct and reflected path. The energy propagating along the direct path will decrease inversely with distance and incur a phase variation of $e^{-j\beta R_d}$, where R_d is the path distance and β is the phase constant. The reflected path signal will also vary inversely with path distance, R_r, and in addition may incur losses due to an incomplete reflection at the air/ground-plane boundary. The phase of the signal arriving at the observation point from the reflected path will be $e^{-j\beta R_r}$ plus an additional phase shift occurring at the boundary. The phase shift and loss imposed upon the reflected signal is represented by the reflection coefficient, Γ , which is a complex variable dependent upon the incidence angle, Ψ , and the electrical constants of the ground plane. Given the above information about the phase shift and losses incurred by both the direct and reflected signals, the composite received signal at the observation point can be calculated:

$$E_r = E_0 \left(\frac{e^{-j\beta R_d}}{R_d} + \Gamma \frac{e^{-j\beta R_r}}{R_r} \right) \qquad (2-1)$$

-7-
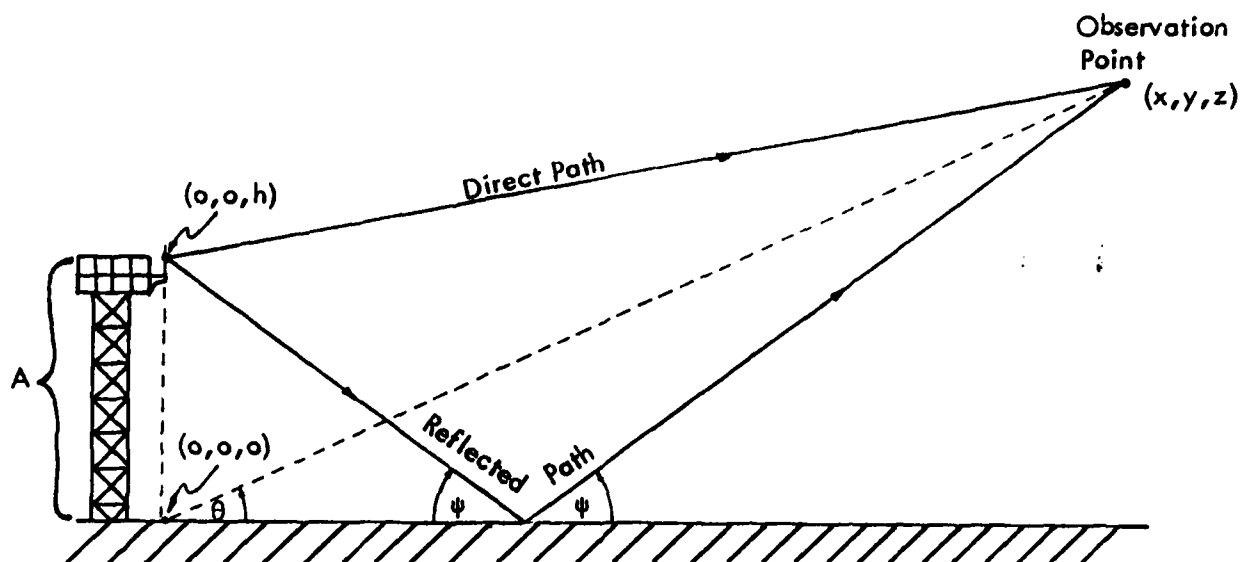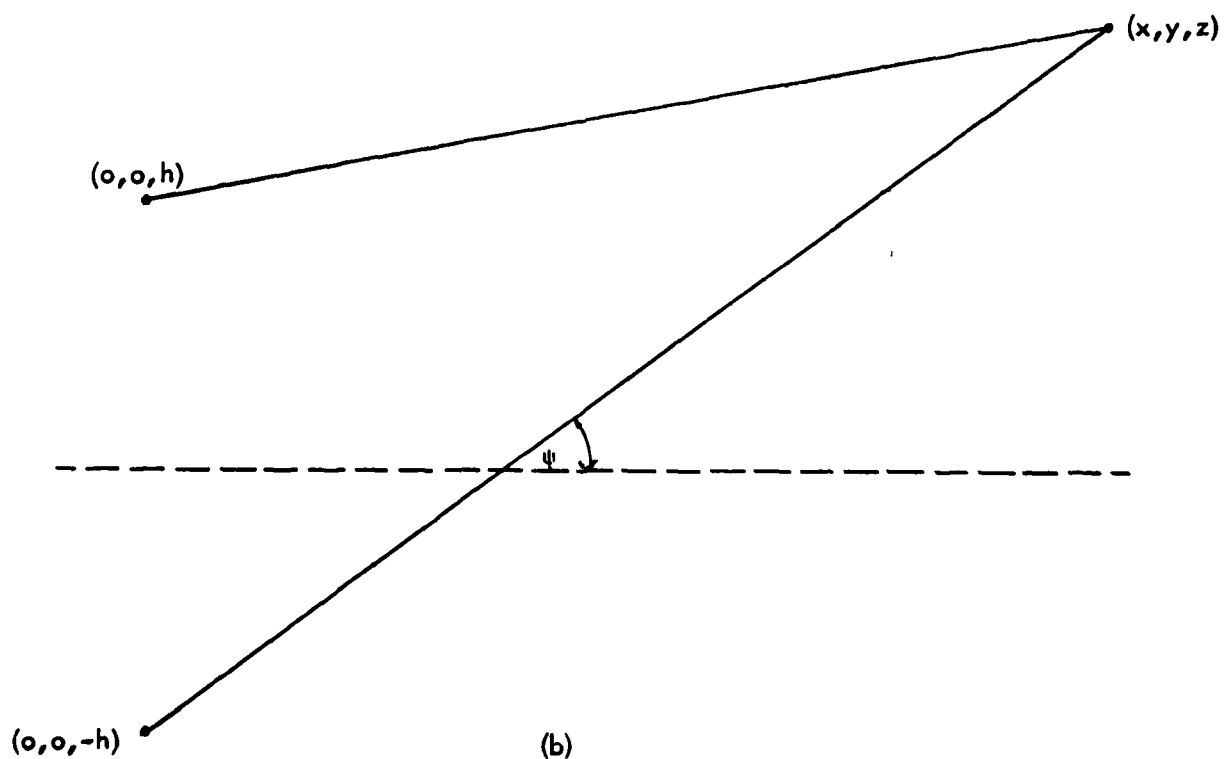
Figure 2-1. Geometry of Antenna Radiating Above a Conducting Ground
Plane Plus Equivalent Representation Using Image Theory.

Where E_r is the received field, and E_0 is a constant representing the field intensity at some arbitrary distance $(R > 0)$.

In order to use Equation 2-i, the distances R_r and R_d must be determined. Clearly, the direct path distance is equal to:

$$R_d = \sqrt{x^2 + y^2 + (z-h)^2}$$

Determination of the reflected path distance is aided using image theory which states that an equivalent representation of ground plane effects for the configuration of Figure 1-1a can be realized by removing the ground plane and adding an in-phase source as shown in Figure 1-1b (this added, or image, source would be out of phase for horizontal polarization). The image source is multiplied by the reflection coefficient to account for losses and phase shift incurred at the reflection boundary. The statement of equivalency for the configurations of Figures 1-1a and 1b for the sector $0° \leq 0 \leq 180°$ is true because the electromagnetic fields within that sector for both configurations are equal. Using the geometry of the imaged configuration shown in Figure 1-1b, the reflected path distance is readily calculated:

$$R_r = \sqrt{x^2 + y^2 + (z+h)^2}$$

Thus, the composite received field can be determined once reflection coefficient values are known.

The behavior of the vertical-polarization reflection coefficient is illustrated in Figures 2-2 and 2-3 where the magnitude and phase of the reflection coefficient are plotted against incidence angle for commonly-encountered ground planes. The equation used to generate these curves is given in Appendix A, and the ground constants describing the electrical properties of the ground planes are given on the figures. It is clear from Figure 2-2, that the greater the ground-plane electrical constants differ from those of free space, the closer the reflection coefficient magnitude approaches unity, resulting in a greater percentage of signal reflecting from the ground plane to the observation point.

Referring to Figure 2-2, it is seen that as the incidence angle approaches grazing (i.e., a 90° incidence angle), the magnitude of the reflection coefficient approaches unity for all values of ground-plane electrical parameters. The phase angle of the reflection coefficient, as seen in Figure 2-3, approaches -180° as the incidence angle goes to grazing (an exception to this would be reflection from a perfectly-conducting ground-plane, where the phase angle would remain at a constant 0° for all incidence angles). Thus, a reflection coefficient of -1 will occur approaching grazing incidence for all realizable ground planes.

The effect of the reflection coefficient on the observed field intensity is shown in Figure 2-4 which shows plots of relative
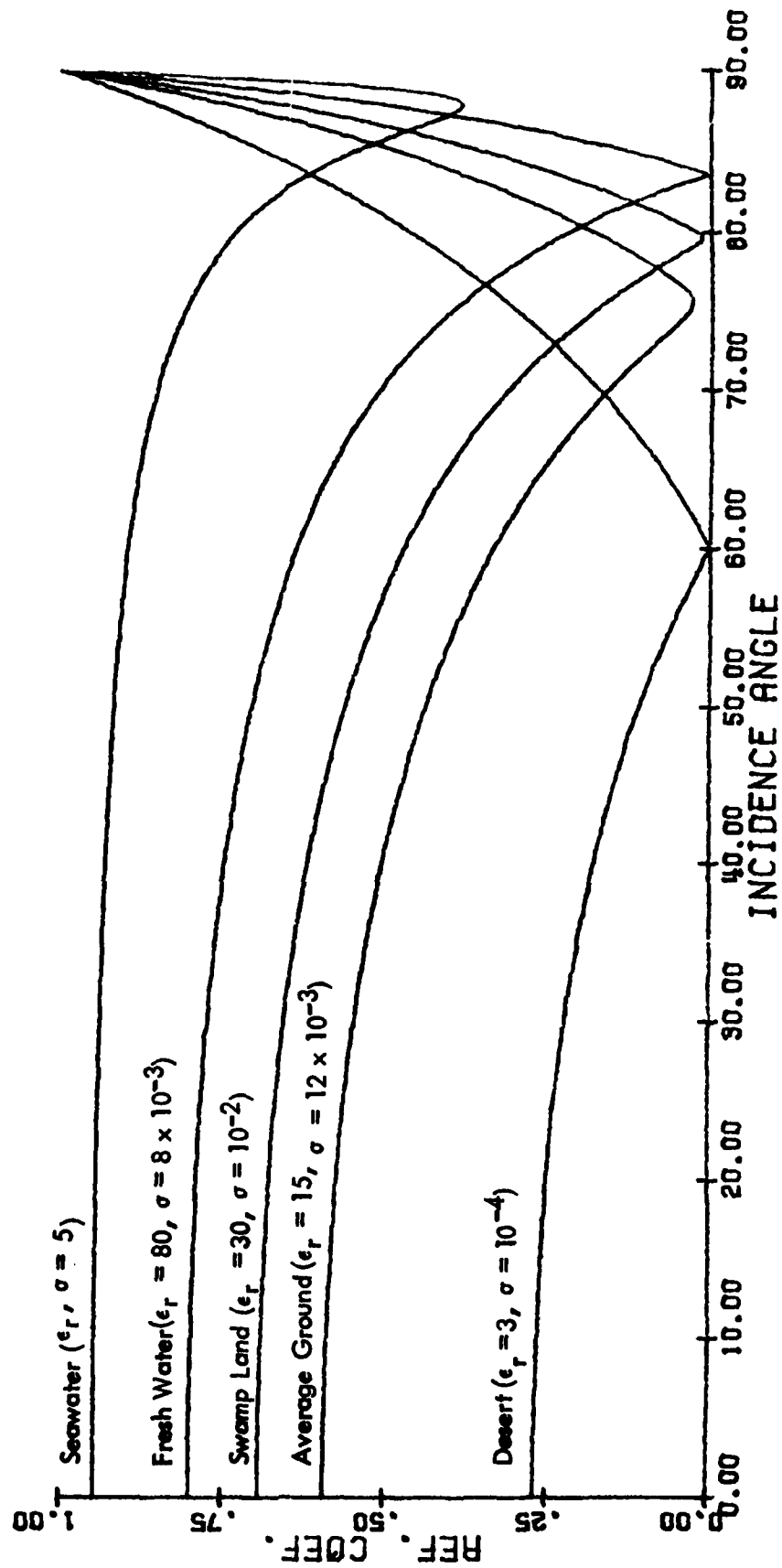
Figure 2-2. Magnitude of Voltage Reflection Coefficient as a Function of Incidence Angle for Vertical Polarization at 125 MHZ for Typical Ground Planes.
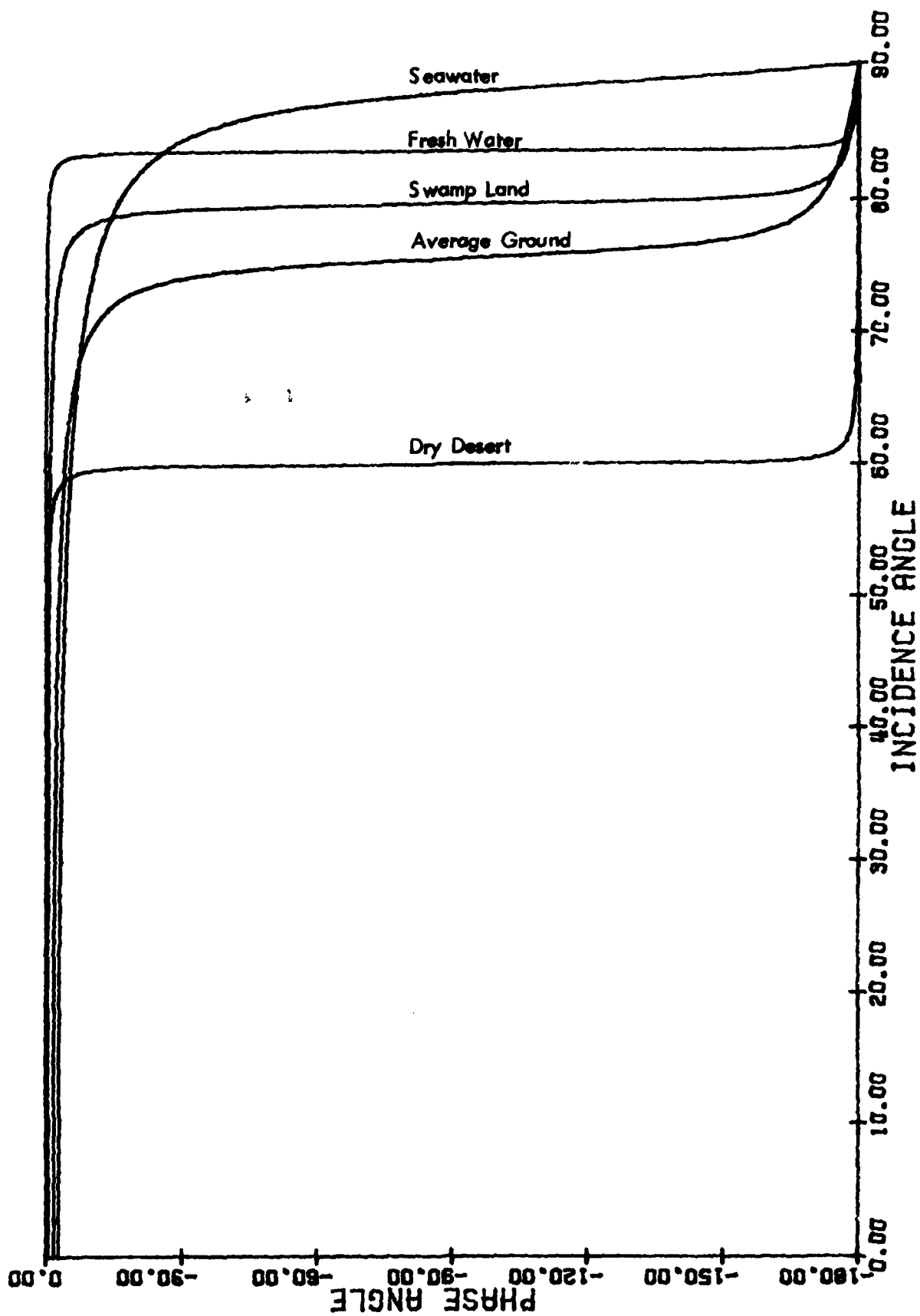
Figure 2-3. Phase of Reflection Coefficient as a Function of Incidence Angle for Vertical Polarization at 125 MHZ for Typical Ground Planes.

-11-
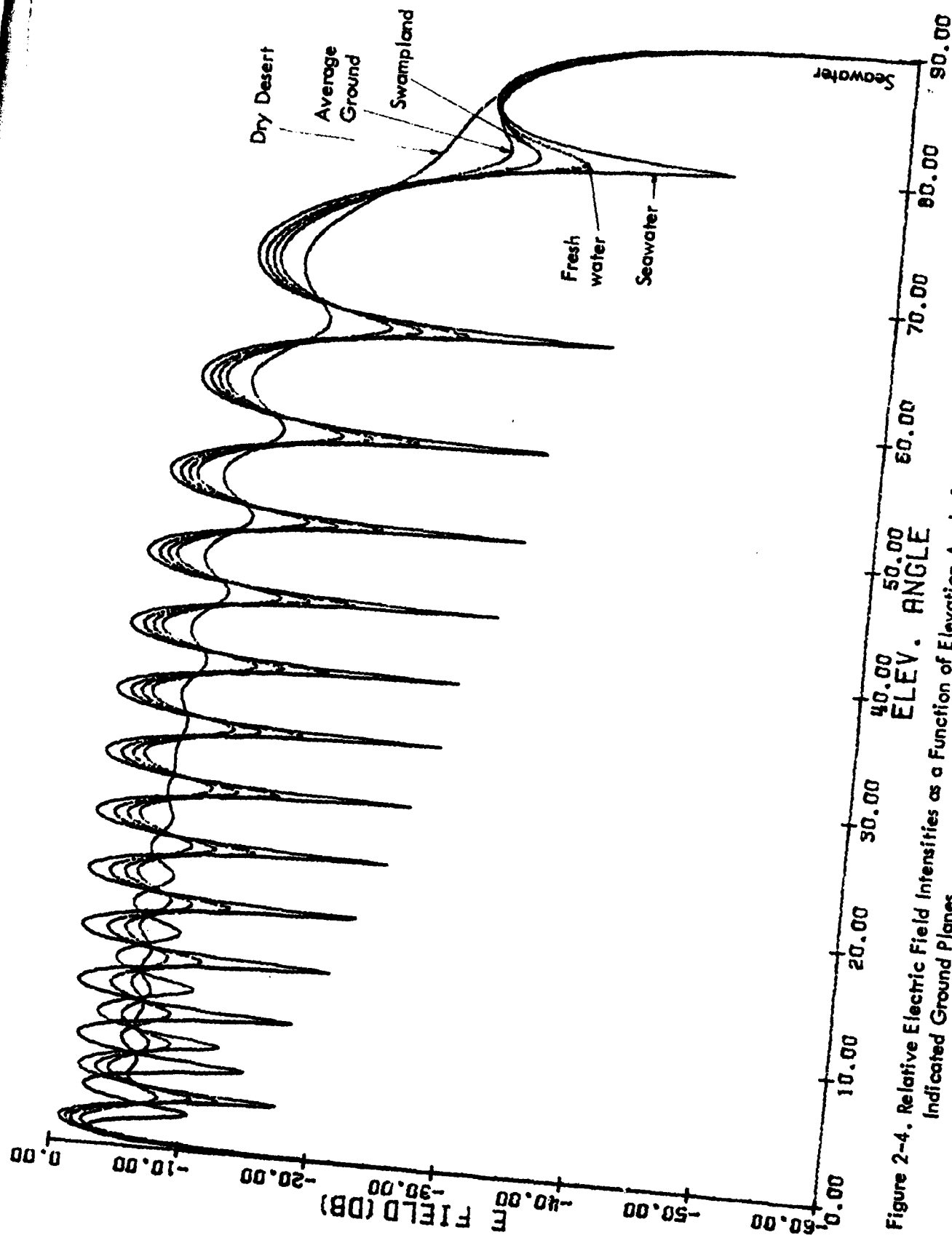
Figure 2-4. Relative Electric Field Intensities as a Function of Elevation Angle for a Vertical Dipole Located 54' Above the Indicated Ground Planes.

electric field as a function of elevation angle for the five ground-
plane types discussed earlier (note that elevation angle, θ , and
incidence angle, ψ , are approximately complementary for observation
points in the far field). Referring to Figure 2-4, a sharp decrease
in electric field is observed at high elevation angles ($\theta \to 90°$) for all
ground planes which is caused by the cos θ antenna pattern. With
decreasing elevation angle, periodic nulls occur corresponding to an
out-of-phase relationship between the direct and reflected signals.
From Equation (2-1) it is seen that this out-of-phase relationship
will exist whenever $\beta(R_r - R_d)$ plus the phase shift of the reflection
coefficient is equal to 180°. The number of nulls within an elevation
angle sector is determined by the antenna height, and the depth of
those nulls is determined by the magnitude of the reflection coef-
ficient. For small values of reflection coefficient magnitude, such
as those associated with low incidence angles over dry desert, can-
cellation and reinforcement from the reflected signal will cause rela-
tively small peak-to-peak variations as a function of elevation angle,
as seen in Figure 2-4. However, for reflection coefficients of
greater magnitude, as with a sea water ground plane, peak-to-peak ver-
tical lobing on the order of 30 decibels may result.

The vertical lobing evident in Figure 2-4 is undesirable in a
communication system. Fortunately, much of the lobing shown in Figure
2-4 will not occur in practical applications due to non-specular, or
diffused, reflection resulting from ground-plane roughness [8].
Ground-plane roughness tends to scatter the reflected signal in a non-
coherent manner which will significantly lower the contribution of the
reflected signal at the observation point, and hence will reduce the
effective reflection coefficient. In fact, measured signal strength
data presented in Section IV for propagation over average ground with
vegatative ground cover show no evidence of vertical lobing below
grazing incidence. However, significant vertical lobing may occur
when the reflecting ground plane is a body of water, which is
inherently flat and generally smooth with respect to the VHF wave-
length of over 7 feet. To minimize such vertical lobing, a
transmitter site should be positioned such that a body of water does
not act as the reflecting ground plane. This can generally be
accomplished by locating the site at least 4000' from the nearest
body of water. The 4000' value is suggested as a rule of thumb because
any surface beyond 4000' will be illuminated by signals incident at an
angle in excess of 89° from normal. Referring to Figures 2-2 and 2-3,
it is seen that there is little difference in the reflection coef-
ficient between different ground planes for incidence angles within
one degree of grazing. Additionally, scattering of the reflected
signal due to surface roughness ceases for near-grazing incidence
angles [9]. Thus, the effective reflection coefficient for near-
grazing incidence will approach -1 independent of terrain roughness
and ground-plane type, and hence the ground plane beyond 4000' is of
little interest when considering relatively-flat terrain.

Again, referring to Figure 2-4, a sharp drop in electric field is
seen approaching 0° elevation angle for all ground planes. The cause

of this decrease is an out-of-phase condition between the direct and reflected signals resulting from the reflection coefficient value of -1 at grazing incidence. Thus, a severe signal null can be expected approaching grazing incidence, which usually will be near the horizon, for all sites. The depth and angular position of this near-horizon null for a particular site will depend upon the antenna height and reflecting ground plane.

The conclusion is clear, viz, it is seen that Signal strength at higher elevation angles will be relatively invarient to elevation angle due to scattering of the reflected signal. Near the horizon, however, a sharp drop in received signal can be expected due to a cancellation of the direct and reflected signals. The coverage area for a particular site is usually sought for minimum enroute altitudes and above. Such altitudes, and for typical propagation distances, correspond to quite low elevation angles, usually near the horizon. Therefore, in order to predict coverage area, an analysis of signal behavior near grazing incidence must be performed. Because local terrain variations can greatly affect received signal strength, the flat-earth model may prove deficient for other than flat-site conditions. Models capable of compensating for terrain variations are available and are discussed in Sections IIE and IIF.

C. Moment Methods. Moment methods provide a means of calculating the fields scattered from a conducting structure immersed in a known electromagnetic field. This very involved task is accomplished by making some simplifying assumptions to represent electromagnetic interactions with that simplified structure. Despite the many approximations used in moment-methods analysis, quite accurate results have been obtained for a wide variety of applications.

The moment method model chosen for the work presented here was written by Richmond [10] although another similar model is available [11]; both models operate under the same basic theoretical concepts and will provide nearly the same results [12]. Richmond's model, known as the "thin-wire" model, operates under the assumption that the structure to be analyzed is made from infinitesmally-thin wires. This approximation is not unrealistic for RCAG site modeling since the scatterers to be modeled (viz, tower components, lightning rods, and antennas) are quite thin compared to the wave-length of around 8 feet. The largest structural component on an RCAG tower is about 1/2 inch in diameter, or .005λ. Using the thin-wire assumption, only currents along the longitudinal axis of any wire comprising a structure need to be considered. Other currents will be present on the actual structure; however, these currents tend to be comparatively small with respect to their contribution to the total scattered field.

The phase and amplitude of the currents along any of the wire segments comprising the structure being modeled is determined by Kirchoff's current law as well as the phase, amplitude and orientation of the source field. The location and orientation of the modeled source field is defined by the user and is modeled as being isotropic.

For a standard RCAG site, the source field generated by the transmitting antenna is also known to be isotropic [13]. The computational and theoretical details for determining the current distribution on a wire structure produced by a known source field are given in a text on the subject written by Harrington [14]. Once the current distribution has been determined, the field generated by those currents, which is the scattered field, can be calculated by a straightforward integration; this integration is performed numerically in the thin-wire model.

To illustrate data requirements for thin-wire model implementation, consider the configuration presented in Figure 2-5 which shows a half-wave dipole radiating over a truncated ground plane in the presence of a lightning rod and parasitic antenna. To simulate the configuration of Figure 2-5, the model requires the 3-dimensional coordinates of the node locations, which are represented by small circles in Figure 2-5, as well as information on which nodes are connected. One constraint on connected nodes is that they be separated by no greater than one-quarter wavelength. For this reason, the lightning rod in Figure 2-5 contains more than just 2 nodes. The source location is assigned by specifying which node pair should receive excitation (the Ohio University version of the thin-wire model has been expanded to accept multiple sources); the source frequency and reference phase are also specified by the user.

Model outputs for the Ohio University version of the thin-wire model include horizontal and vertical radiation patterns, radiation efficiency, standing wave ratio and antenna impedance, and current distribution on the scatterer.

The present limit of 300 nodes has not imposed any difficulty in the modeling of typical RCAG site scatterers. But, as stated, the modeling of RCAG towers, platforms, and antenna-lightning rod configurations, supported by measured data, indicated that further work in this area was unnecessary for a standard facility. However, the thin-wire model should be considered as a candidate model at a site where conducting-structure scattering is suspected of causing deficient coverage.

D. ITS Longley-Rice Model. As stated in the introduction to this section, there are a number of factors known to affect wave propagation. However, the relationship between any of these factors and signal strength is not at all clearly defined due to a strong interaction between those stated factors in conjunction with a changing relationship with changing conditions. Thus, the problem of signal strength characterization lends itself quite readily to a statistical, rather than analytical, analysis. Analytical analyses are possible for signal strength predictions, as will be discussed in the next two sections; however, such analyses require orders of magnitude greater resolution in defining a site than is required for the statistical analysis described in this section.
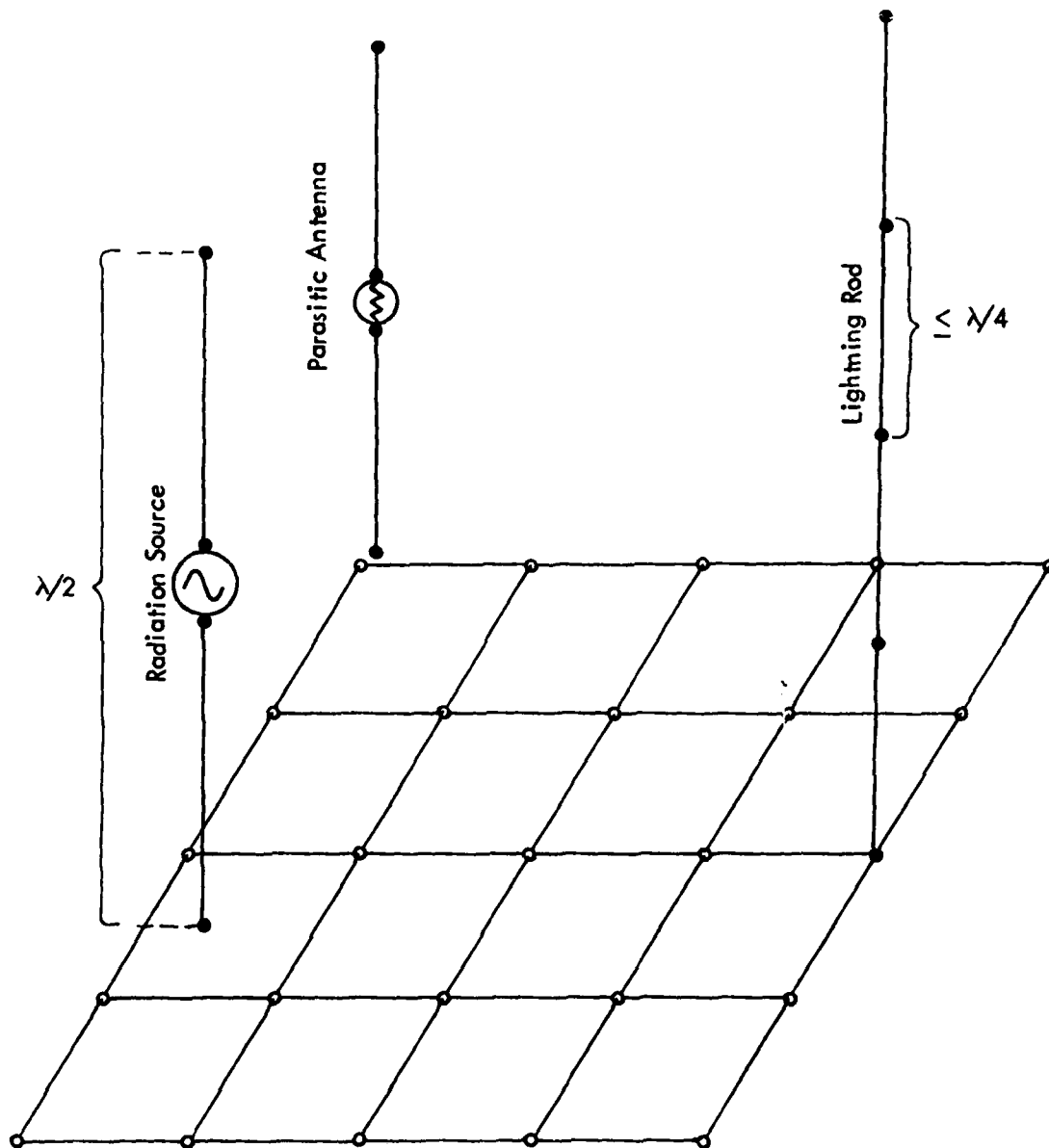
Figure 2-5. Illustration of Data Requirements for the Simulation of a
Half-Wave Dipole Radiating Over a Truncated Ground
Plane in the Presence of a Lightning Rod and a Parasitic
Antenna.

In order to predict the path loss between the transmitter and receiver, the ITS model requires data describing that path. Such data, pertinent to RCAG site coverage prediction, are listed below [15, 16]:

1. Receiver antenna elevation

2. Transmitter antenna elevation

3. Frequency

4. Antenna polarization

5. Elevation angle of and distance to horizon

6. Minimum mean surface refractivity

7. Terrain roughness factor

8. Ground permittivity and conductivity

9. Path distance

10. Climate (continental all year, equatorial, continental subtropical, maritime subtropical, desert, continental temperate, maritime temperate overland, and maritime temperate overseas)

The above data have been collected for a large number of propagation paths; these data, in addition to the measured propagation path loss for each data set, provide the empirical base for the development of computer algorithms relating the propagation path to path loss.

To provide further insight into ITS model operation, consider Figure 2-6 which shows the three general reception regions considered by the ITS model: (1) line of sight, (2) diffraction, and (3) scatter. As shown in the plot of signal strength versus distance presented in Figure 2-6, path loss as a function of distance from the transmitter tends to be characterized by the region in which the receiver is located. Within each region, the functional relationship between path loss and distance can be correlated to terrain roughness, frequency, antenna polarization, ground conductivity and permittivity, and climate. Accordingly, the ITS model first determines the region for which a prediction is sought, and then selects the appropriate algorithm relating signal strength to the pertinent parameters for that region.

One factor that must be considered in determining the reception region is ray bending which will occur as the refractive index of the atmosphere changes as a function of altitude. For typical atmospheric conditions, the refractive index will vary in an exponentially decreasing manner from the earth's surface to free space. The refractive index is the relative atmospheric permittivity minus one expressed
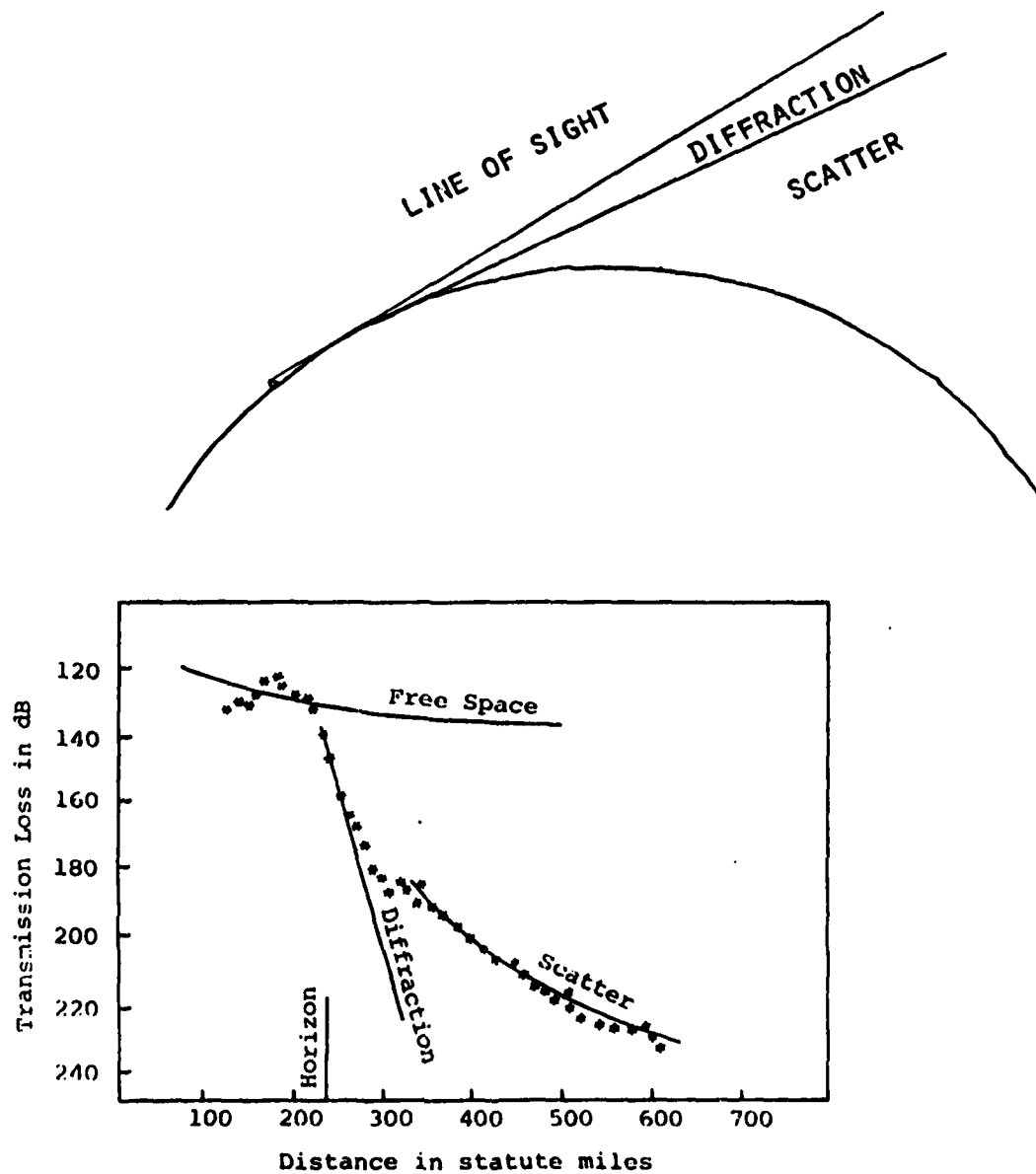
Figure 2-6. Transmission Loss as a Function of Distance for
an Aircraft at 30,000 Feet.

in parts per million. Typical values of such surface refractive index are around 300; the refractive index of free space is zero. The following differential equation relates ray-path bending to changes in the refractive index as a function of height above the earth's surface [17]:

$$\frac{d^2z}{dx^2} = \frac{\partial N}{\partial z} + \gamma_e \qquad (2-2)$$

where x is the distance along a straight-line extension of the earth's surface, N is the refractive index, and γ_e is the earth's curvature. An analysis of Equation (2-2) will show that rays emanating from the transmitting antenna will tend to bend downwards toward the earth's surface. A convenient and equivalent method for modeling ray bending is to assume non-bending rays propagating over an enlarged earth. For typical values of surface refractive index, that exponentially decrease from the surface to free space, the earth radius would appear to be approximately 4/3 times its actual radius if assuming non-bending rays; this earth radius value is used by some less-sophisticated propagation models. The ITS model uses the input value of surface refractivity, assumes an exponential decrease in the refractive index from the surface to free space, and computes an effective earth curvature.

Although not considered by the ITS model, a phenomenon that should be included in any discussion of VHF wave propagation is that of atmospheric anomalies [18]. These anomalies occur when the refractive index changes abruptly with altitude, causing rays, and thus radiated energy, to be diverted from their straight-line direction. This phenomenon occurs when stable and well-defined vertical air layers form, as during an air inversion. Such occurrences may not be common except at sea/mountain or plains/mountain interfaces. The National Weather Service can provide information on the likelihood of such occurrences, and this information should be used as part of siting considerations. Examples of the effects of atmospheric anomalies are shown in Figures 2-7 and 2-8. The ray tracings presented in Figures 2-7 and 2-8 were generated using Equation (2-2) and the functional relationship between refractive index and height which plotted along the right side of these figures. Figure 2-7 depicts radio ducting, where signals are trapped between superrefractive layers and the earth's surface. For this case, aircraft above the superrefractive layers would experience decreased reception, while aircraft below the superrefractive layers would experience fading due to standing waves within the duct. An additional difficulty caused by ducting is that the radiated signal will propagate over a considerably greater distance at low altitudes, thus increasing the potential for co-channel interference. Figure 2-8 shows the creation of a radio hole, where atmospheric conditions cause a signal-deficient region due to
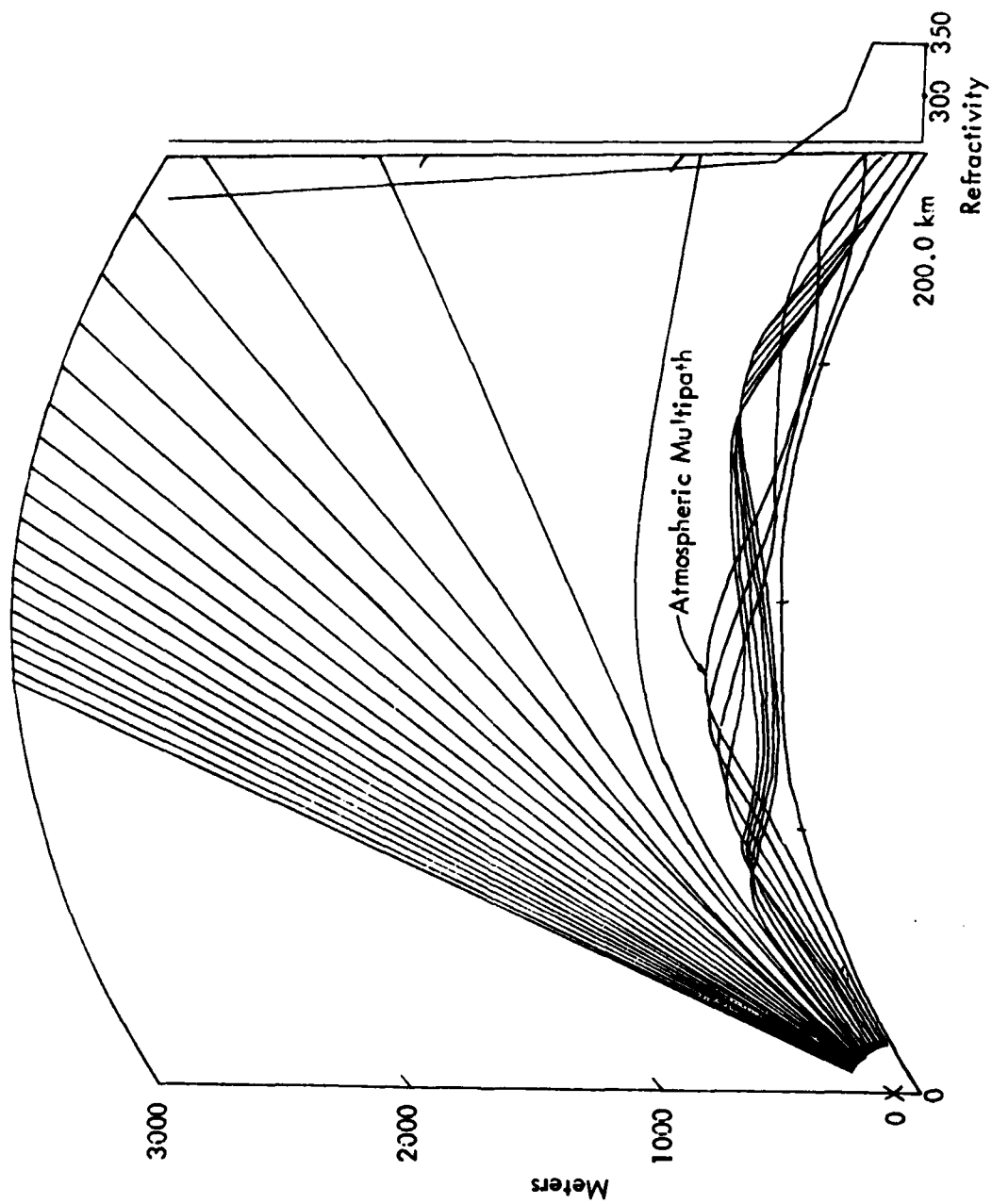
Figure 2-7. Depiction of Radio Ducting Using Ray Tracing. Take-off angles are shown from -5 mrad to +30 mrad in 1-mrad steps.
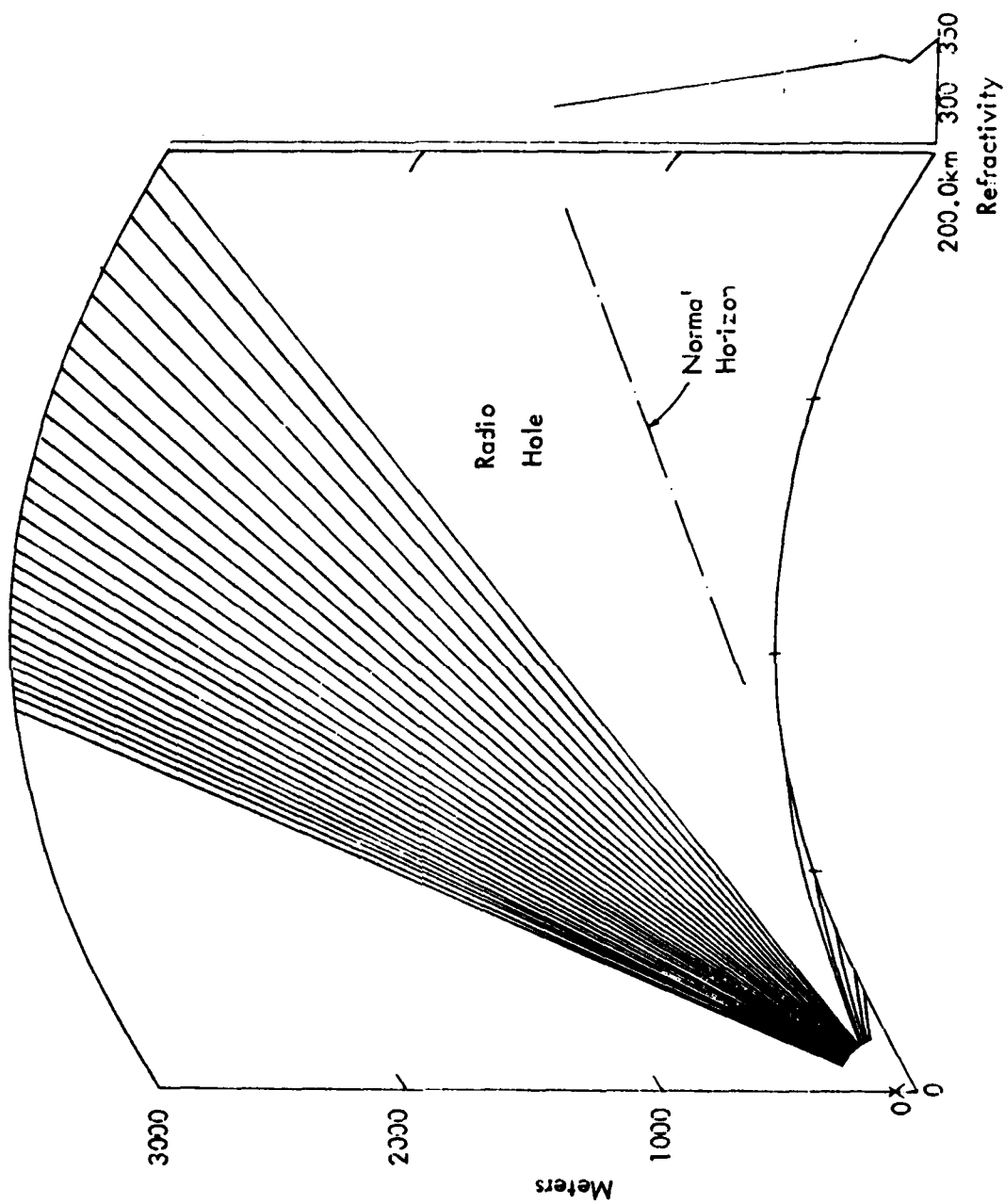
Figure 2-8.   Depiction of a Radio Hole Using Ray Tracing.   Take-off angles are shown from -5 to +30mrad in 1 mrad steps.

-21-

rays being diverted to either side of that region. The signal
strength decrease for aircraft either in a radio hole or above a duct
can be extreme for some tropospheric conditions, even to the point of
totally obscuring the received signal. It should be noted that
Equation (2-2) could be used to characterize the propagation anomalies
described if the functional relationship between refractive index and
height above the earth's surface were known.

In order to make a signal strength coverage prediction for a
transmitter site using the ITS model, all of the parameters listed in
the beginning of this section must be specified for that site. With
the exception of terrain-related parameters, all necessary input
variables will not change with azimuth angle or distance from the
site. Thus, only one value each is required for climate, ground per-
mittivity and conductivity, surface refractivity, antenna polarization,
effective radiated power, frequency, and transmitter and receiver
antenna heights in order to make a prediction for any site at a par-
ticular altitude. However, terrain-related parameters, which are
terrain roughness and elevation angle and distance to the horizon, can
change with azimuth angle and distance from the site. In order to
expedite the calculation of these terrain-related parameters, the ITS
model makes use of the Continental United States (CONUS) data base,
which enables terrain elevation values (in feet MSL) to be called from
computer storage for any specified latitude/longitude pair within
CONUS. Elevation values are quantized to 20-foot increments and are
available for every 30 seconds of arc (approximately 1/2 mile),
although the program used to retrieve the data will linearly extrapo-
late elevation values for any longitude/latitude pair.

The block diagram for the Ohio University version of the ITS
model is given in Figure 2-9. As shown in Figure 2-9, the only input
data to be supplied by the user are the non-terrain-related parameters
plus the site coordinates. Because of the minimal input data required
from the user, the Ohio University version of the ITS model can be
readily implemented. Continuing with the flow diagram of Figure 2-9,
it is seen that signal strength values are predicted beginning with
the 0° azimuth angle for increasing path distances, starting at 20 nm
(this range value was arbitrarily selected--the assumption here is
that the coverage range for any azimuth angle will never be less than
20 nm). The program then successively increments the path distance in
0.5 nm steps, recomputes terrain-related parameters, and predicts
received signal strength until the predicted signal strength falls
below the predetermined threshold value of -87 dBm, whereupon the
azimuth angle and the range at which the predicted signal strength
falls below threshold are recorded. The azimuth angle is then incre-
mented by 5° and the process of determining the predicted coverage
range for this new azimuth angle is performed as described above.
This procedure continues until all azimuth angles from 0° to 355°, in
5° increments, have been considered. The coverage area map is pro-
duced by making a polar plot of coverage range versus azimuth angle;
scaling is adjusted so that the polar plot range is equal to map
range.
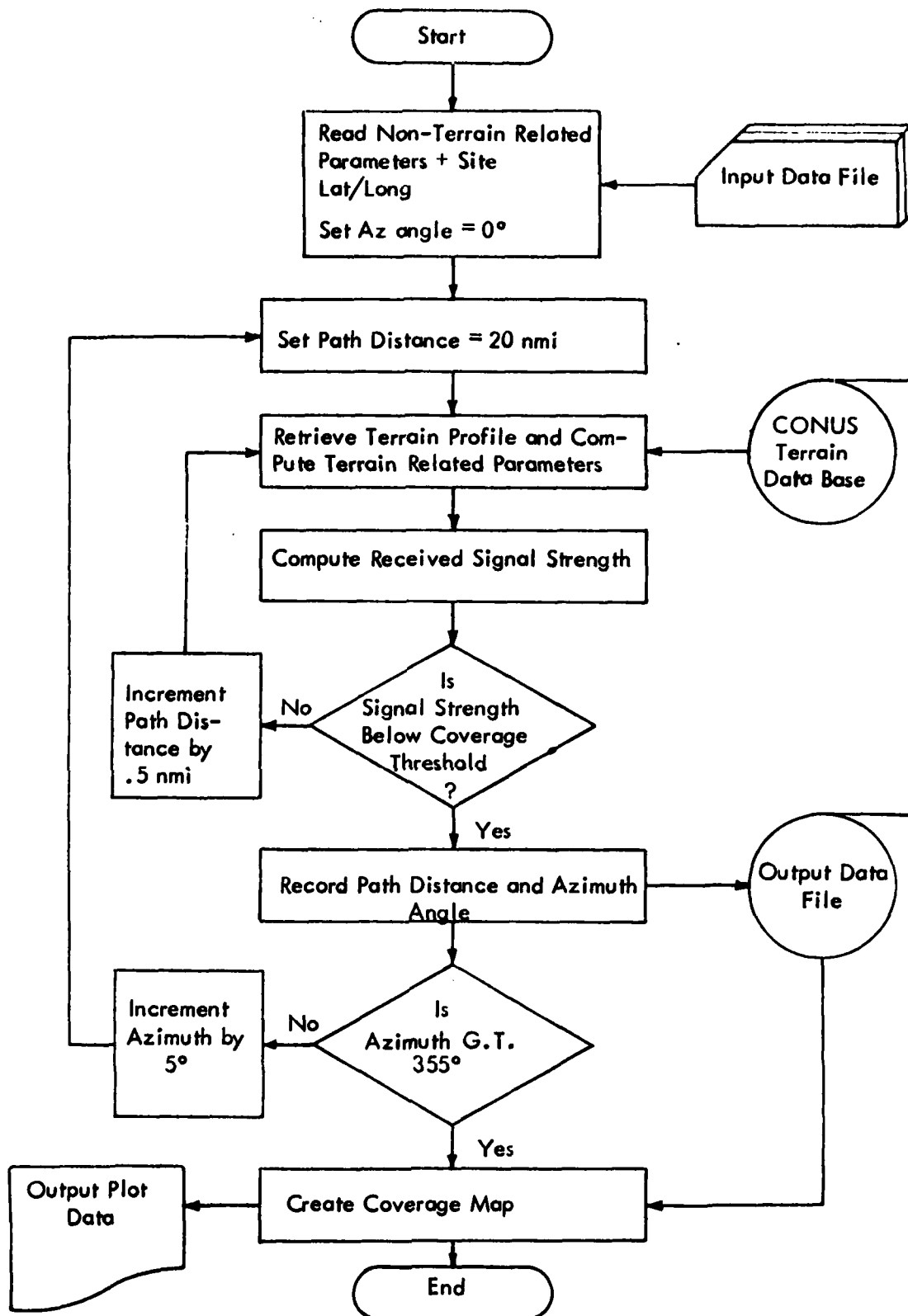
Figure 2-9. Flow Diagram for the Ohio University Version of the ITS Model.

The quantization and relatively-low resolution in the terrain data used by the ITS model prevent accurate predictions for rece locations near the site. Prediction accuracy increases within increasing distance from the site because more data become available to define the terrain between the transmitter and receiver. At some distance, the data defining the terrain will become statistically significant and will enable an accurate prediction to be made. Thus, the ITS model has a known deficiency for short-path predictions. The minimum propagation path at which significant errors will not be incurred will change from site to site; however, good prediction results were reported consistently for propagation paths in excess of 100 nm in reference [19] (predictions for less than 100 nm were not given). Additionally, as is shown in Section VB, general signal strength trends were predicted by the ITS model for a 40 nm propagation path. Therefore, it appears that accurate predictions can be expected from the ITS model for distances greater than some distance between 40 and 100 nm. Additional data-taking would be required to better characterize that distance.

Because of its insensitivity in making short-range predictions, the ITS model is not recommended for other than long-range propagation paths. Thus, the ITS model cannot be used to predict close-in coverage deficient areas caused by nulls in the vertical lobe structure. However, for determining the coverage area for typical low-power (5 watts) RCAG facilities, which usually extend to beyond 50 nm, indications are that overall site performance can be predicted by the ITS model. Prediction accuracy will increase with transmitter power because, as pointed out above, ITS model performance improves with propagation distance. The ITS model will also prove useful in determining the intensity of interfering signals from distant sites.

E. **Physical Optics**. Physical Optics (PO) [20, 21] is a technique used to determine the scattering from large (with respect to a wavelength) conducting objects. PO does not consider ray tracing, as described earlier, but rather determines the induced current distribution on a scatterer produced by a radiation source; the scattered field is then calculated from those induced currents. Thus, on a conceptual basis, there are strong similarities between moment methods and PO. Computationally, however, considerable differences exist because moment methods is concerned with thin-wire structures defined by nodes that are separated by less than a wavelength, and PO is concerned with large surfaces, or plates, with dimensions much greater than a wavelength.

To illustrate how PO is used to determine scattering from irregular terrain, consider the terrain profile and its piecewise linear approximation as is shown in Figure 2-10. The piecewise linear approximation to the actual terrain is used to define the conducting plates on which currents are induced by the radiation source. Computationally, these plates are treated as though they extended to infinity in the ± x directions as shown in Figure 2-10. Thus, a 2-dimensional terrain is considered by PO. Induced currents on the
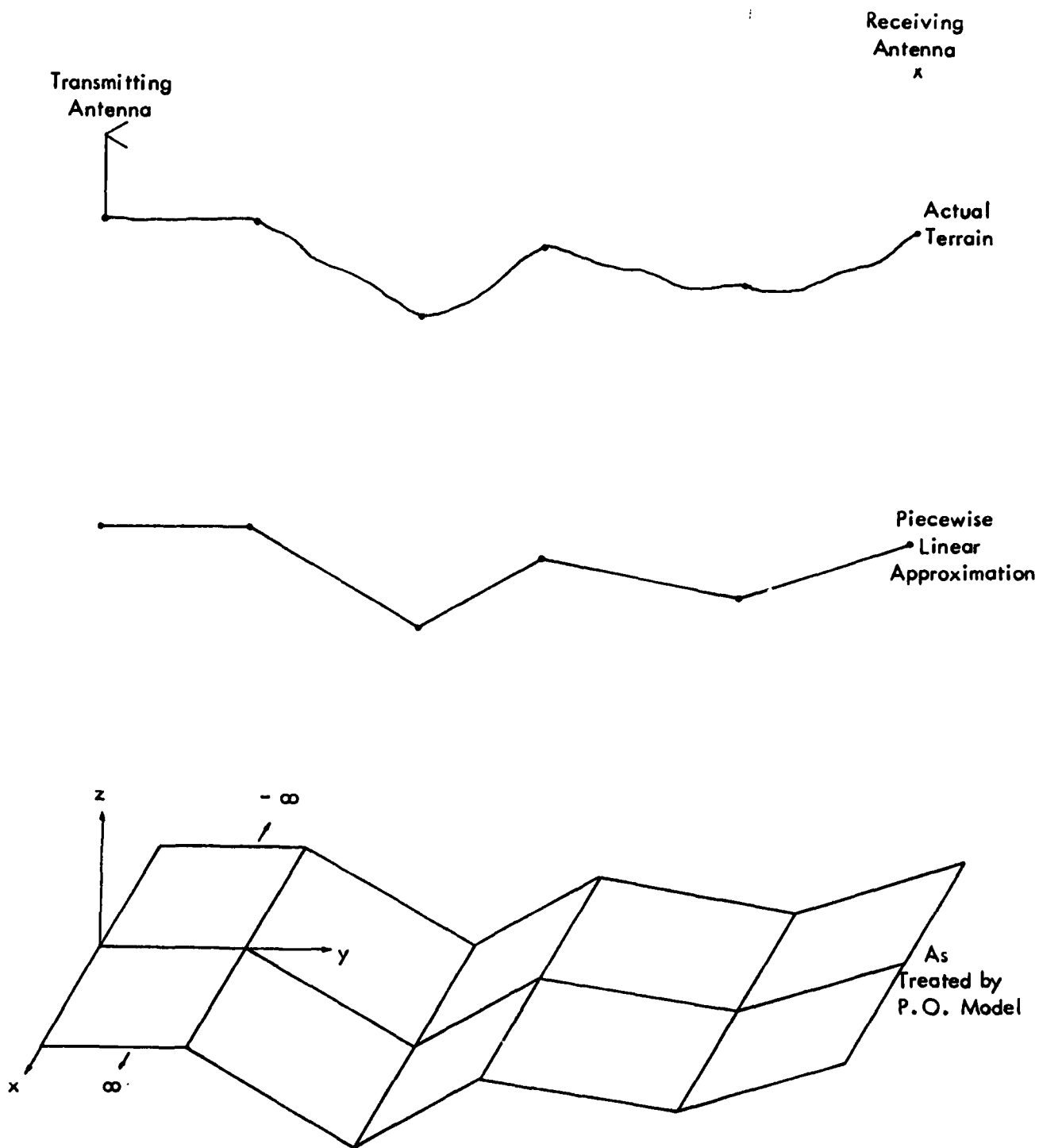
Figure 2-10. Linearization of Terrain Profile Data for Input to P.O. or GTD Computer Model.

plates are computed from the incident magnetic field for all illumi-
nated surfaces; the incident magnetic field and thus the induced
currents are assumed to be zero when the incident field is blocked.
The assumed current at any point on the model terrain is
determined from the orientation, intensity, and phase of the incident
magnetic field at that point. The resultant scattered field is calcu-
lated by integrating these complex current quantities along with an
appropriate weighing function (Green's Function) over all the surfaces
between the transmitter and receiver.

A deficiency of PO modeling results from its not considering
interactions between conducting plates. This factor can cause signi-
ficant errors for certain terrain configurations. Another drawback to
using PO for this application is that ground points of reflection or
diffraction are not explicitly identified, which prevents altering the
phase and amplitude of these signals corresponding to the distance
which they travel through vegetation. Because of the above problems
associated with PO implementation, it was not chosen to characterize
ground scattering for RCAG site coverage, although it should be noted
that PO has provided successful ground-scattering predictions for some
ILS glide-slope modeling applications [22].

Previous work with PO modeling at communication frequencies [23]
with the objective of characterizing large, conducting structures has
shown positive results. Accordingly, PO should be considered for
future applications to model conducting structures that are too large
to be modeled by moment methods, such as a building in close proximity
to a transmitting antenna.

F. Geometrical and Uniform Theories of Diffraction. Thus far,
two types of rays or ray paths, the direct and reflected, have been
discussed in this report. A third and final ray of interest for the
work presented here is the diffracted ray, depicted in Figure 2-11.
The diffracted ray accounts for the electromagnetic energy re-radiated
from a corner or wedge. The initial work mathematically describing
diffraction was published in 1896 by Sommerfield [24] and was con-
cerned with diffraction from a perfectly-conducting half-plane. An
extension of this work, called the Geometrical Theory of Diffraction
and performed by Keller [25], addressed scattering from other than
half-plane geometries and developed series expansions necessary to
calculate diffraction from these more complex geometries. However,
because Keller's series expressions describing diffraction are
expanded about the reflection and shadow boundaries, unrealistic
discontinuities are predicted at and near those boundaries.
Consequently, Kouyoumjian and Pathak [26] developed smoothing func-
tions to eliminate these discontinuities thus enabling predictions
near shadow and reflection boundaries to be more realistic; this non-
rigorous, heuristic solution to the discontinuity problem is termed
the Uniform Theory of Diffraction (UTD). Because of its more
realistic predictions near shadow and reflection boundaries, UTD,
rather than GTD, is generally used for modeling purposes. However,
UTD is commonly referred to as GTD, and it is generally assumed that a
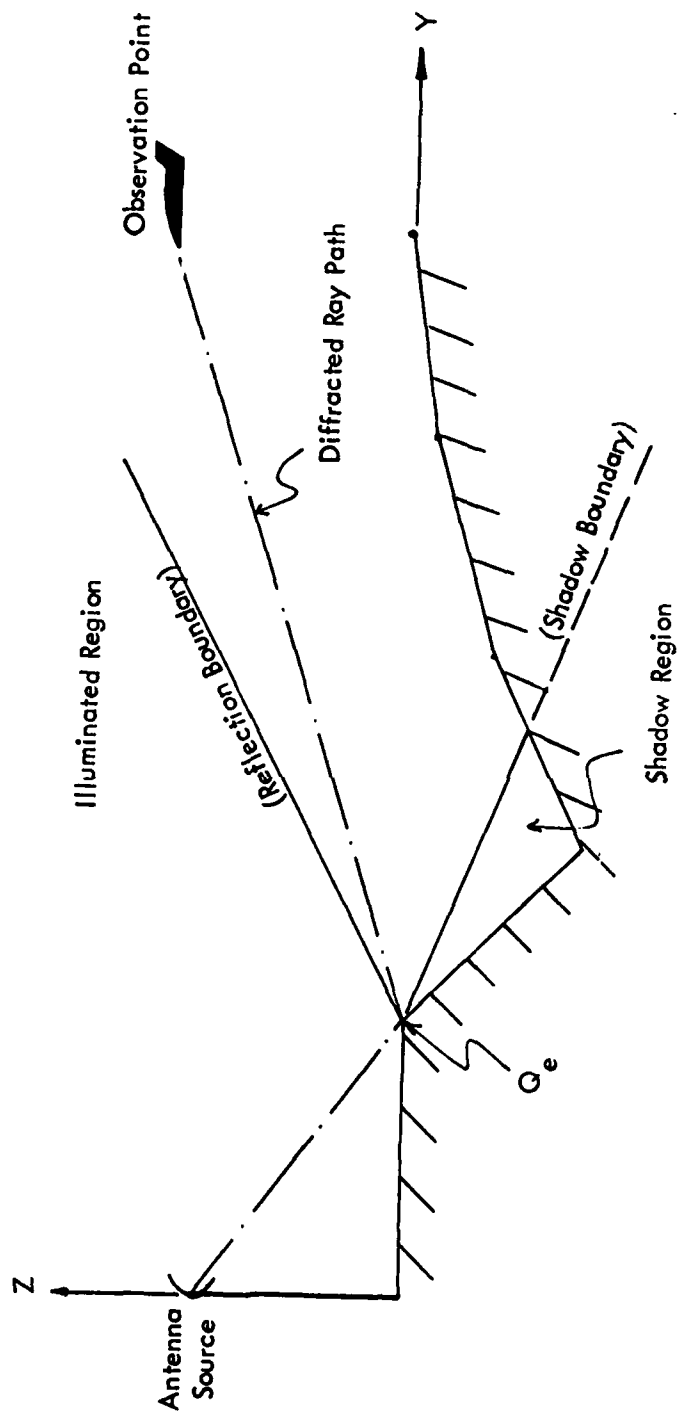
Figure 2-11. Diffracted Ray Geometry.

-27-

GTD model employs UTD concepts. Consistent with this common usage, future reference to GTD in this report is made with the understanding that UTD is implied.

GTD computer models used to predict received signal phase and amplitude in the presence of irregular terrain do so by vectorially summing the contributions of the direct, reflected, and diffracted rays; for some modeling schemes, combinations of these rays are considered. These models generally assume the same piecewise-linear approximation to the terrain as is used by PO and shown in Figure 2-10. This terrain information is used to determine whether certain rays or ray combinations exist, as well as to calculate their phase and amplitude should they be found to exist. The direct ray will exist if there is no physical blockage between the transmitter and receiver; the diffracted ray will exist if there is no blockage between both the transmitter and the diffraction point (denoted Q_e in Figure 2-11), and the diffraction point and the receiver; a reflected ray will exist if there is a point on the terrain profile where the angle of incidence is equal to the angle of reflection, and there is no physical blockage (there may be more than one reflected ray). These existence tests also apply to ray combinations. An example of a ray combination is shown in Figure 2-12 for a diffracted-reflected ray. It should be noted that a GTD model will produce the same results as will image theory for predictions above a perfectly-flat ground plane since there is no diffraction from a smooth surface, leaving only the direct and reflected ray to be calculated.

The GTD computer model chosen for the application addressed in this report was developed at Ohio University [24] and was selected because of its proven success with glide-slope modeling in addition to a programming flexibility afforded by its modular program structure. The Ohio University GTD model considers 12 rays and ray combinations in predicting a received signal:

1. Direct

2. Reflected

3. Diffracted

4. Doubly-reflected

5. Reflected-diffracted

6. Doubly-diffracted

7. Diffracted-reflected

8. Reflected-diffracted-reflected

9. Reflected-reflected-diffracted
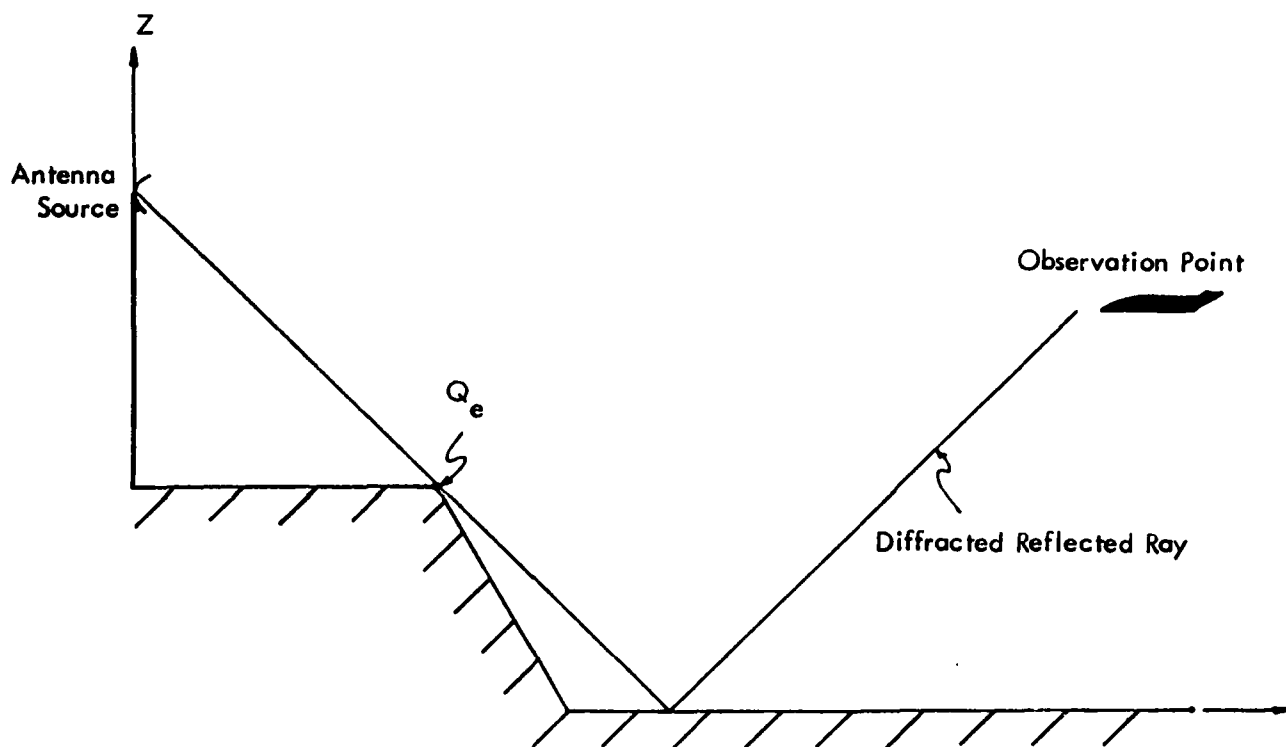
Figure 2-12.   The Diffracted-Reflected Ray (DR) Geometry.

10. Diffracted-reflected-reflected

11. Diffracted-diffracted-reflected

12. Diffracted-reflected-diffracted

Ray combinations other than those listed above can exist for some transmitter-receiver-terrain configurations; however, the contributions from these other ray combinations are considered insignificant for most practical situations.

One important benefit provided by the Ohio University GTD model is a determination of the coordinates of all points where rays intersect the terrain. Since the location of forested areas can also be input to the model, a calculation of the distance that a particular ray travels within a forested area can be made. As is discussed further in Section III, this capability enables the effects of forests to be considered by the model, thus increasing its prediction accuracy.

GTD modeling makes signal strength predictions based solely upon terrain scattering. Thus, GTD modeling can be used to predict signal deficient areas caused by terrain scattering for areas where terrain scattering is the dominant factor affecting propagation. Comparisons of measured and GTD-predicted, ILS glide-path data indicate that ground scattering will be the dominant factor affecting signal strength for at least 30 nm distance from the site at a 3° elevation angle for typical sites. However, because few measured and GTD-predicted data are available for greater ranges or other elevation angles, it is difficult to determine the range or elevation angle at which factors other than terrain scattering begin to dominate. A consideration in determining the range and elevation angle limitation of GTD modeling is the size and location of the first Fresnel Zone corresponding to various receiver positions. Although the Fresnel Zone size and location is site-dependent, a general statement that can be made is that the Fresnel Zone size will increase as the receiver moves away from the site, and will decrease as the elevation angle of the receiver with respect to the site increases; the location of the Fresnel Zone will move away from the site as the receiver increases in distance, and will move nearer the site as the elevation angle increases. For close-in predictions, where the first Fresnel Zone area is small compared to terrain variations, the GTD model will produce accurate results. As the receiver distance increases, however, the area of the first Fresnel Zone will also increase, possibly to the point where multiple diffractive edges and/or reflecting surfaces will be contained within the first Fresnel Zone. If this does happen, the 12 rays and ray combinations discussed earlier may no longer be sufficient to characterize ground scattering, resulting in inaccurate predictions.

The ITS model, discussed in Section IID is deficient for close-range predictions while the GTD model is deficient for long-range pre-

dictions. The appropriate selection of either model for a particular
site will be determined by local terrain and the degree of sensitivity
desired in the prediction. As stated, the GTD model is considerably
more sensitive to signal strength variations caused by terrain than is
the ITS model for close ranges. Thus, if terrain is suspected of
causing vertical lobing resulting in signal deficient areas, the GTD
model might be selected. However, an important consideration in
implementing the GTD model is that it requires high resolution,
accurate terrain data to make meaningful predictions. As shown in
Appendix D, obtaining this data can become a quite involved task.
Further considerations pertinent to GTD model usage will be addressed
in Section III.

III. THEORY, MODELING METHODS, AND MODEL IMPLEMENTATION FOR VHF WAVE
PROPAGATION IN AND NEAR FORESTED MEDIA

A. Introduction. It has long been recognized that trees have
an attenuating effect on radio propagation. Consequently, antennas
are positioned above and away from trees whenever possible. A
general assumption is that if a transmitting antenna is so posi-
tioned, and the receiving antenna is within line of sight, there will
be no attenuation resulting from the trees. However, measured data
collected for the research presented here clearly shows that tree
attenuation will be a significant factor affecting received signal
strength within line of sight near the horizon for typical RCAG
installations. The purpose of this section is to explain the theory
of tree attenuation within line of sight and describe how this pheno-
menon is accounted for in a modified GTD computer model.

Previous work with tree attenuation has been directed towards
transmission and reception from within trees for ground-to-ground
communications. Substantial emphasis was placed on predicting tree
loss for ground-to-ground communication during the Viet Nam war era
[28] which made available data on tree conductivity and permittivity
in addition to some theory on wave interaction with trees. Attempts
to apply that existing theory to ground-to-air communications did not
provide results consistent with measured data except in cases where
propagation was through the trees, where the theory did appear to
provide accurate results.

A theory explaining tree attenuation within line of sight has
been developed and is described in this section. Simply stated, this
theory attributes tree-related losses to an out-of-phase, specular
reflection from tree tops resulting in cancellation of the received
signal. Numerical results obtained using this theory are in close
agreement with measured data. To develop the theory stated above,
some assumptions about the electrical properties of trees at VHF have
to be made. Accordingly, the first step towards explaining the
theory will be to discuss the electrical properties of trees and to
justify a simplification necessary to model forested areas in an
efficient manner. Following that will be a rigorous proof showing
that the plane-wave reflection coefficient, as described in Section
IIB, is sufficient to characterize completely the reflected field. A
discussion is then given describing the volume in which signal energy
is propagated. This discussion, which includes a definition of the
Fresnel Ellipse and Fresnel Zones, is included to afford an analysis
of cases where forested areas are not infinite in extent. Finally, a
method for implementing the theory in a GTD computer model is offered.

B. Electromagnetic Modeling of Tree Effects at VHF. Several
techniques for determining the electrical properties of trees have
been suggested; however, the method seen as being most applicable for
the following analyses is measurement of the phase shift and atte-
nuation seen by signals propagating through actual forested areas.
This phase shift and attenuation can be represented by the complex

-32-

propagation constant, γ , which can then be related to the electrical properties of the forested medium:

$$L_r \sim \frac{L_0 e^{-\gamma R}}{R}$$ (3-1)

where R is the propagation distance through the trees, and $\gamma = \alpha + j\beta$. Thus, it is seen that α relates to losses incurred along the propagation path, and β describes phase shift along the path. The electrical properties of the forested medium, namely conductivity, σ , and permittivity, ϵ , are related to the complex propagation constant by [29]:

$$\alpha = \frac{\omega\sqrt{\mu\epsilon}}{\sqrt{2}} \left[\sqrt{1 + \left(\frac{\epsilon''}{\epsilon'}\right)^2} - 1\right]^{1/2} \quad \text{Nepers/Meter}$$ (3-2)

$$\beta = \frac{\omega\sqrt{\mu\epsilon}}{\sqrt{2}} \left[\sqrt{1 + \left(\frac{\epsilon''}{\epsilon'}\right)^2} + 1\right]^{1/2} \quad \text{Radians/Meter}$$ (3-3)

where ω is the angular frequency, and ϵ' and ϵ'' are the real and imaginary components of the complex permittivities, respectively:

$$\epsilon' = \epsilon_r , \quad \epsilon'' = \sigma/\omega$$ (3-4)

A computer-implemented SUBROUTINE used to generate the complex propagation constant from input electrical constants is listed in Appendix B.

Previous researchers [30,31] have obtained data over forested propagation paths and, using the relationships described above, have calculated the electrical properties of forested media. An additional result observed by these researchers [32] is that for transmission within the range 2-200 MHz, trees electrically appear to be essentially homogeneous. This observation, which is of paramount importance to the development presented here, indicates that trees can be treated as a homogeneous volume of lossy dielectric material of known electrical properties. To illustrate how this homogeneity can help to facilitate tree effect modeling, consider Figure 3-1 which shows a typical mixed forest near a transmitting antenna and a homogeneous, lossy dielectric slab representation of that forest. As seen in Figure 3-1, the forest is represented by a dielectric slab of fixed
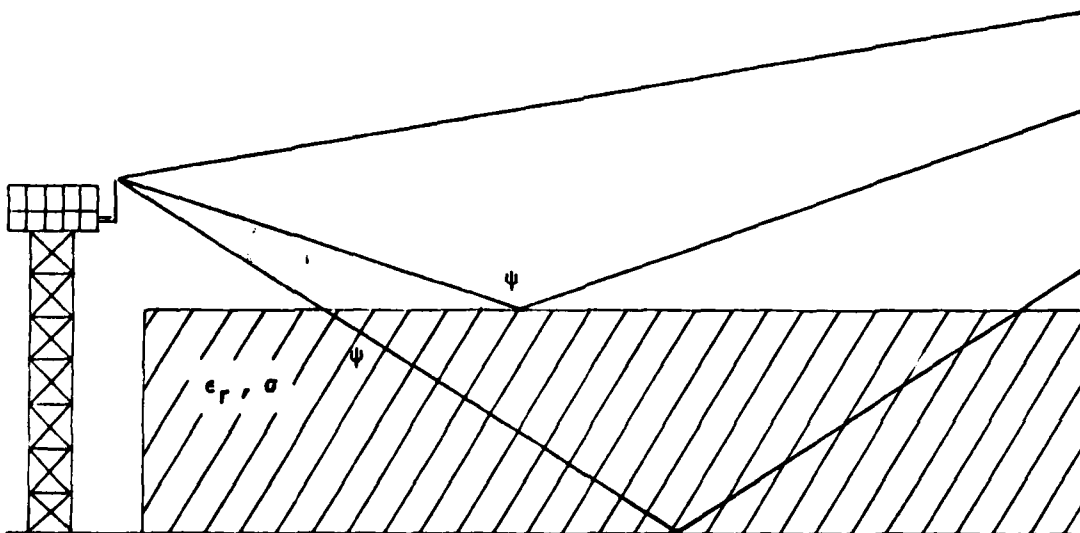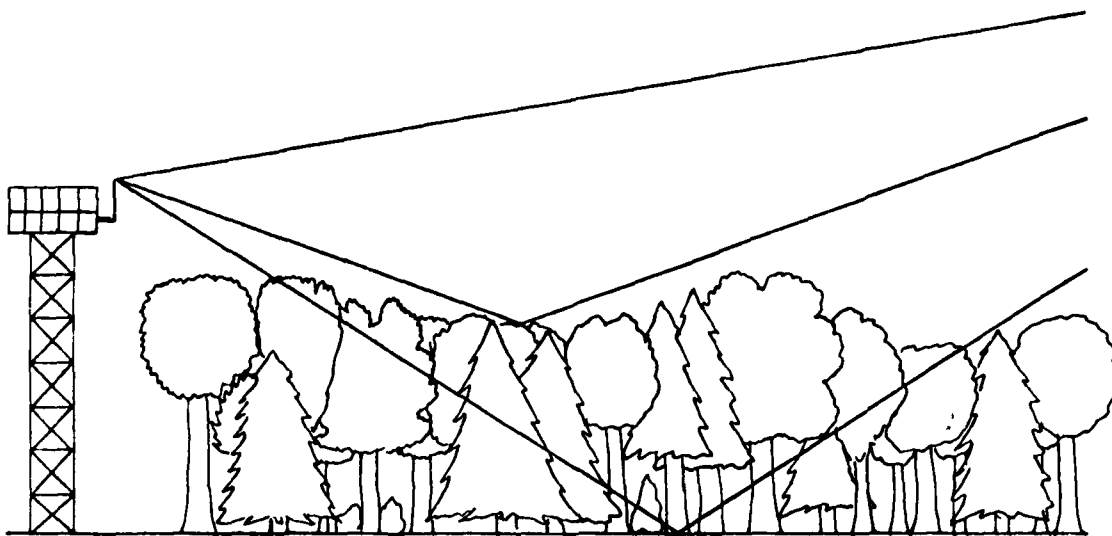
Figure 3-1. Illustration of Modeling Approximation of Forested Regions.

height equal to the mean height of the trees; the justification for using a slab of non-varying height is given below. It should be commented here that tree variability in type, density, and height can exist within a relatively small region, viz., a 4000' radius around the transmitting antenna, and thus a change in electrical properties and height of the slab representation might appear appropriate in modeling tree effects. However, the effect on received signal strength resulting from changes in the properties of the slab representation are typically quite small, especially when compared to the large noise component inherent with measured signal strength data. Thus, a slab with fixed properties is used to model forested areas unless extreme variations within a forest are known to exist.

Figure 3-2 shows a plane wave incident at an angle ψ on an air-forest boundary. Rayleigh [33] suggests that the roughness for such a boundary can be calculated in terms of path difference between a shortest and longest path, represented by 1 and 2 in Figure 3-2, with respect to a wavelength. Using the geometry of Figure 3-2, it is seen that the difference in distance between paths 1 and 2 is:

$$\Delta r = 2h\cos\psi \qquad (3-5)$$

and hence the phase difference at the observation point, assumed to be in the far field, for signals arriving along paths 1 and 2 is:

$$\Delta\phi = \frac{4\pi h}{\lambda} \cos\psi \qquad (3-6)$$

A surface is said to be smooth (i.e., will reflect specularly) if this phase difference falls below some specified threshold, generally between $\pi/4$ and $\pi/8$. Referring to Equation (3-6), it is seen that this condition will be met as either h becomes small or as ψ approaches 90°. Recalling from Section IIB that the solutions sought are for near-grazing incidence, the latter criterion is met, and hence specular reflection can be assumed. Accordingly, a flat, fixed-height slab representation is reasonable for modeling purposes.

The magnitude and phase of the reflection coefficient for average electrical properties of trees are plotted in Figures 3-3 and 3-4, respectively. Comparison of the values plotted in these figures to the reflection coefficient values for typical ground planes as shown in Figures 2-2 and 2-3 shows a considerably lower reflection magnitude for lower incidence angles in addition to a lower incidence angle corresponding to the 180° phase shift in the phase of the reflection coefficient. Thus, it is seen that the effects of trees, due to reflection, will be minimal for incidence angles much less that 90°. As reflections from trees do become significant, which will occur near the horizon, any contribution from the reflection at the observation
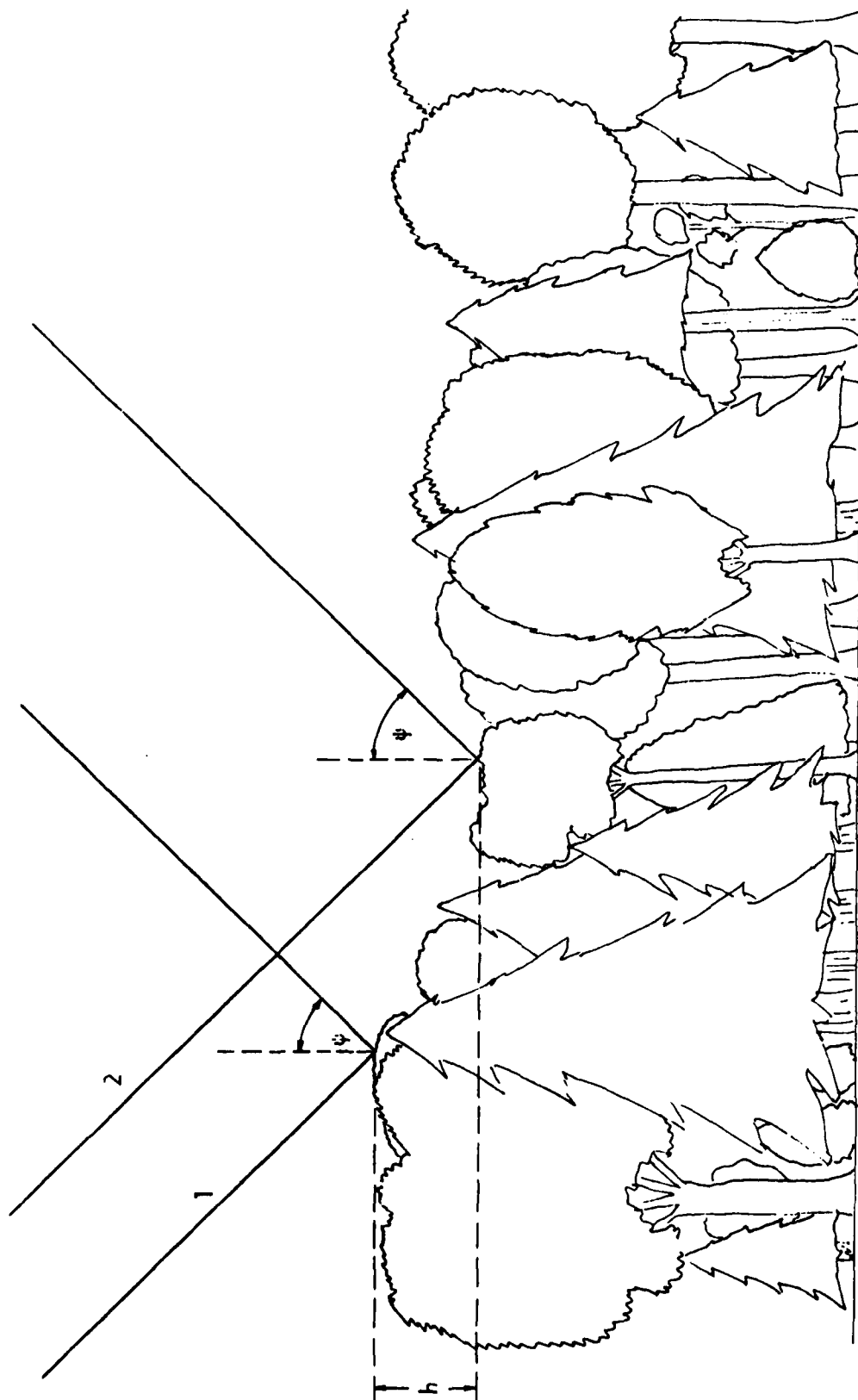
Figure 3-2. Illustration of How Forested Areas are Considered in Simulating Their Effect on Electro-Magnetic Wave Propagation.
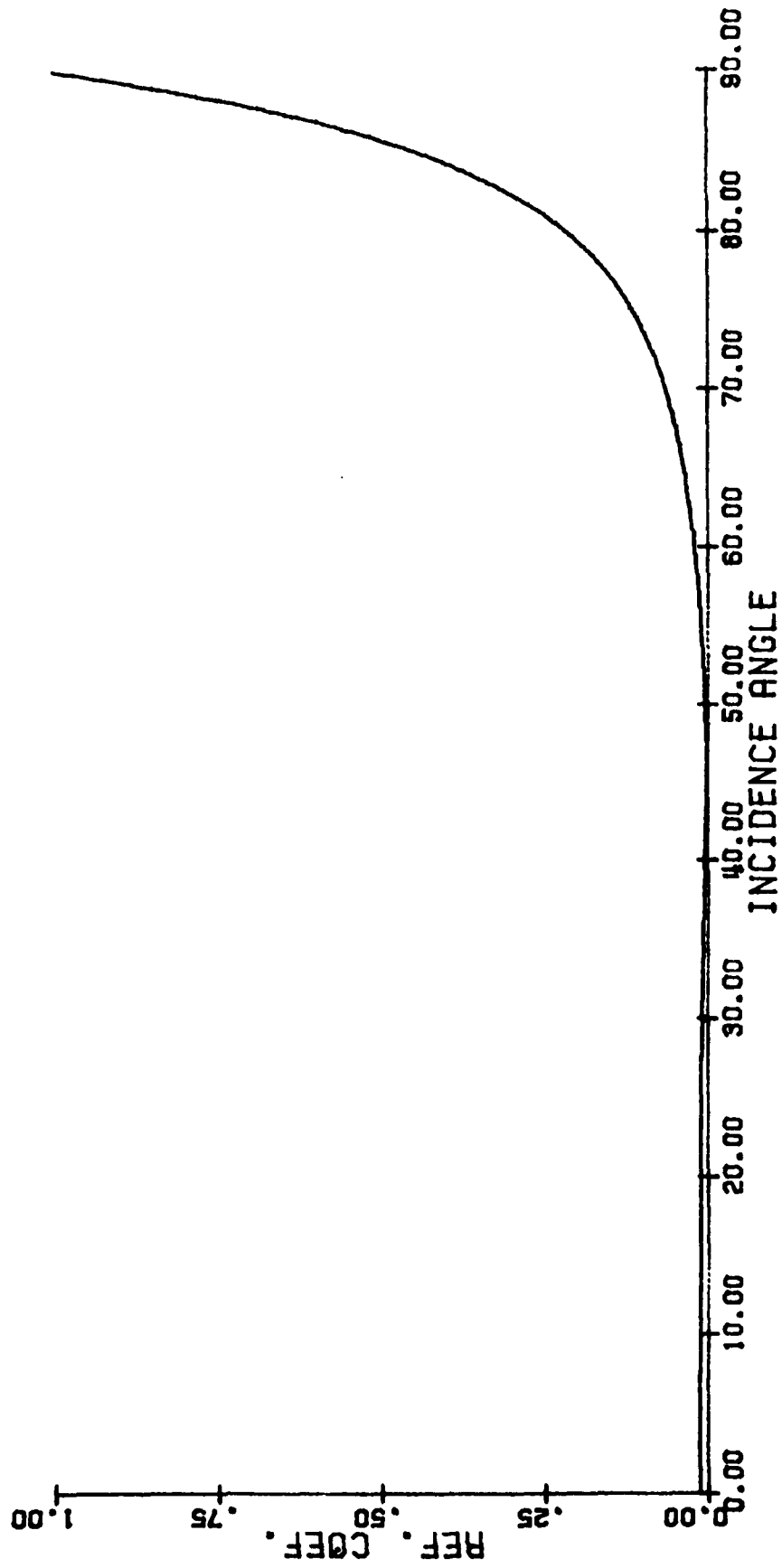
Figure 3-3. Magnitude of Reflection Coefficient as a Function of Incidence Angle for Nominal Electrical Parameters of Trees ($\epsilon_r = 1.05$, $\sigma = 3 \times 10^{-5}$).
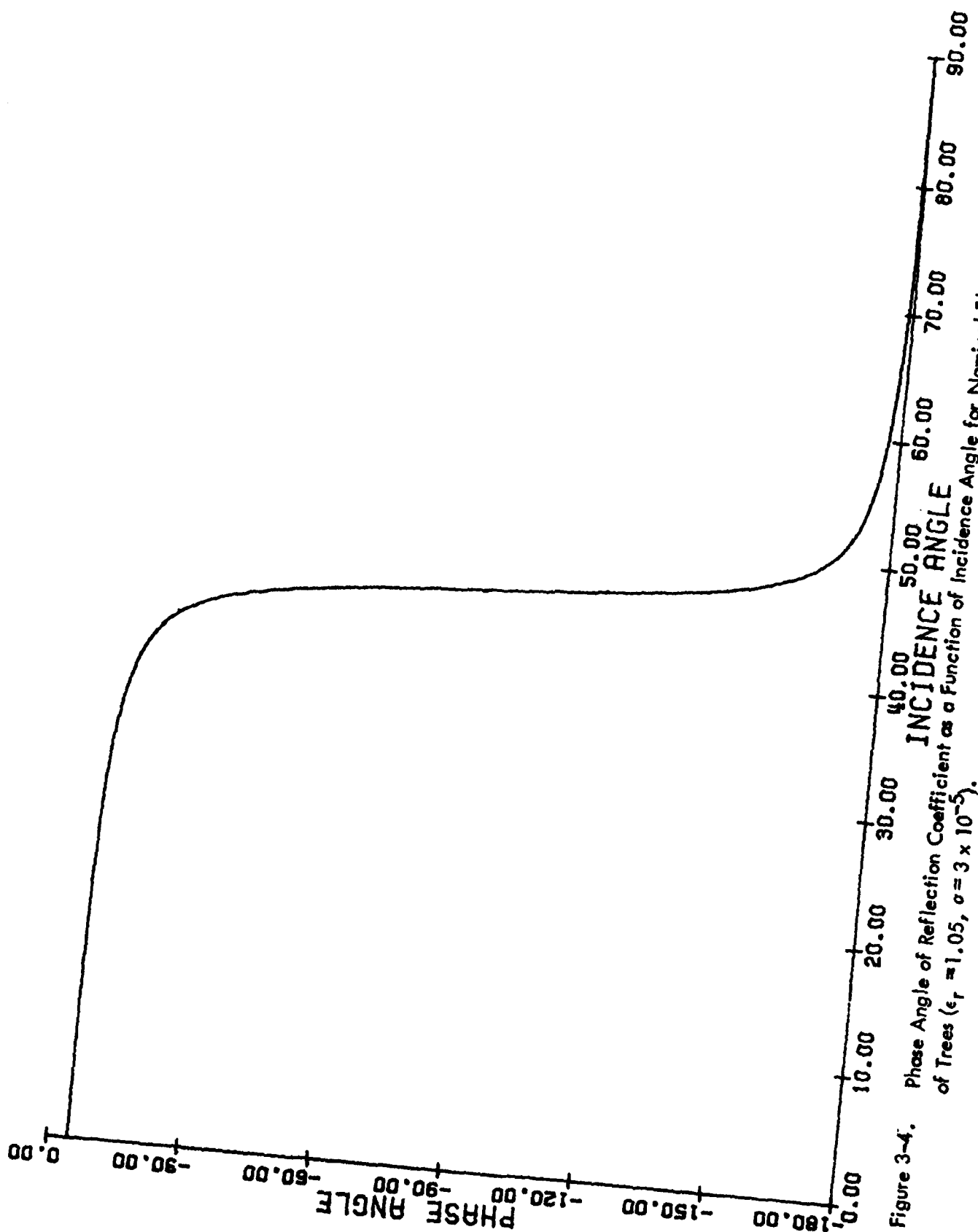
Figure 3-4. Phase Angle of Reflection Coefficient as a Function of Incidence Angle for Nominal Electrical Parameters of Trees ($\epsilon_r = 1.05$, $\sigma = 3 \times 10^{-5}$).

-38-

point will cause cancellation due to the phase of the reflected signal.

To calculate the received signal in the presence of trees, again consider Figure 3-1 which shows the various paths by which signals can reach a far-field, low-angle observation point. As seen in Figure 3-1, signal energy can reach the observation point either directly, by reflecting from the air/forest boundary, or by reflection from the forest/ground boundary. It should be noted that for distant observation points, both of the aforementioned reflected paths will be essentially parallel; they are separated in Figure 3-1 for illustrative purposes. In order to demonstrate typical contributions from each of the three possible propagation paths, consider a case where the observation point is at a distance of 20 nm at 3000' altitude, the transmitting antenna is 50' above the ground, and the trees are average (ε_r = 1.05, σ = 3 x 10^{-5}) and 30' high. For this geometry, the incidence angle on the air/forest boundary is 88.6°. The reflection coefficient on an air/forest boundary with a known incidence angle can be obtained from Figure 3-3, which is, in this case, 0.85. Thus, 85% of the incident signal will be reflected from the boundary towards the observation point, and 15% will be transmitted into the forest medium (note: an 85% reduction in electric field represents a 16.5 dB drop in signal power). Due to refraction, the transmitted angle, ψ_t, in Figure 3-1, will differ from the incidence angle, and can be calculated by Snell's Law [34]:

$$\frac{\sin\psi_t}{\sin\psi} = \frac{1}{\sqrt{\varepsilon_r}} \qquad (3-7)$$

For the conditions stated, ψ_t is calculated to be 77.3°. This refracted signal will reach the forest/ground boundary after traveling a total of 136' through the conductive forest medium. Losses due to passage through the forest medium are approximately 1.5 dB/100', or a total of 2 dB for the refracted signal. The percentage of the refracted signal reflected from the forest/ground boundary is approximately given by the air/ground reflection coefficient; the air/ground and forest/ground reflection are nearly identical due to the relative similarity of the air and forest media when compared to the electrical properties of the ground. Referring to Figure 2-2, for a 77.3° incidence angle, the reflection coefficient is 0.1. Hence, only 10% of the refracted signal, which is over 18 dB below the incident signal at the forest/ground boundary before reflection, is reflected back towards the observation point. After reflection from the ground, total losses are in excess of 40 dB. Without continuing further, it is clear that the contribution from a signal reflected from the ground is insignificant when compared to the direct signal or the signal reflected from the air/forest boundary. Consequently, only the direct and forest-reflected signals are considered in determining received

-39-

signal strength in the presence of tree cover. Accordingly, imaging is performed with respect to the air/forest, as opposed to the forest/ground, boundary.

To provide insight into the variability that can be expected for an extreme in forest parameters, consider Figure 3-5 which presents the vertical lobing pattern for a range of forest types [35]. These plots were made assuming a 70' antenna for all three cases. The forest types plotted in Figure 3-5 range from a sparse alpine-type tree cover (thin), to a dense tropical jungle environment (dense). An immediate conclusion that can be seen from Figure 3-5 is that a denser, more conductive forest will introduce greater attenuation at low elevation angles than will a less dense forest.

With the information presented above, it is possible to calculate expected field strength due to the presence or absence of trees. The validity of those calculations can be verified by measured data from sites where both forested and cleared sectors are present. Plots of calculated signal strength for a 54' high antenna radiating over both average ground and average 38' high trees are shown in Figure 3-6. From this figure it is seen that below 3° elevation, the signal in the absence of trees is greater than with trees. Above 3° elevation, the signal in the absence of trees is seen to dip markedly, resulting from the first null in the array pattern of the radiating antenna and its image. It is likely that such a large dip would not be seen at an actual site unless an extremely flat ground plane existed. This observation is based upon the Rayleigh Criterion discussed earlier. Further, experience suggests that the no-forest trace in Figure 3-6 will asymptote towards the forest trace at around 3° due to scattering of the reflected signal by irregular terrain or obstructions. Measured data are available for forested and non-forested ground planes for a 1.4° elevation angle as will be presented in Section V. Calculated and measured data are in close agreement at that angle.

C. <u>Spherical Wave Reflection from a Plane Boundary</u>. Sections IIB and IIIB of this report involve reflection at boundaries of media with dissimilar electrical properties. In these discussions, the signal incident on the boundary is assumed to be a plane wave. The assumption of plane wave incidence is made to facilitate solution of boundary conditions on the reflecting surface, which is itself planar, since both the incident wave and reflecting plane geometries will be consistent (i.e., both are defined in a rectilinear coordinate system). For cases where the reflecting surface is far from the radiating source, plane wave incidence, rather than the more realistic spherical wave incidence, can provide a first-order approximation to wave interaction with the surface as is shown later in this section. Tamir [36] has shown that effects of spherical wave incidence can account for appreciable signal contributions at low elevation angles above forested areas that are not accounted for when assuming plane-wave incidence. Because the work presented here is concerned with low-elevation signal strength, an analysis must be performed to determine the signal contributions introduced by spherical-wave incidence on a reflection boundary.

-40-

	Thin	Average	Dense
Tree Height	15'	30'	60'
Permittivity	1.03	1.1	1.3
Conductivity	3×10^{-5}	1×10^{-4}	3×10^{-4}
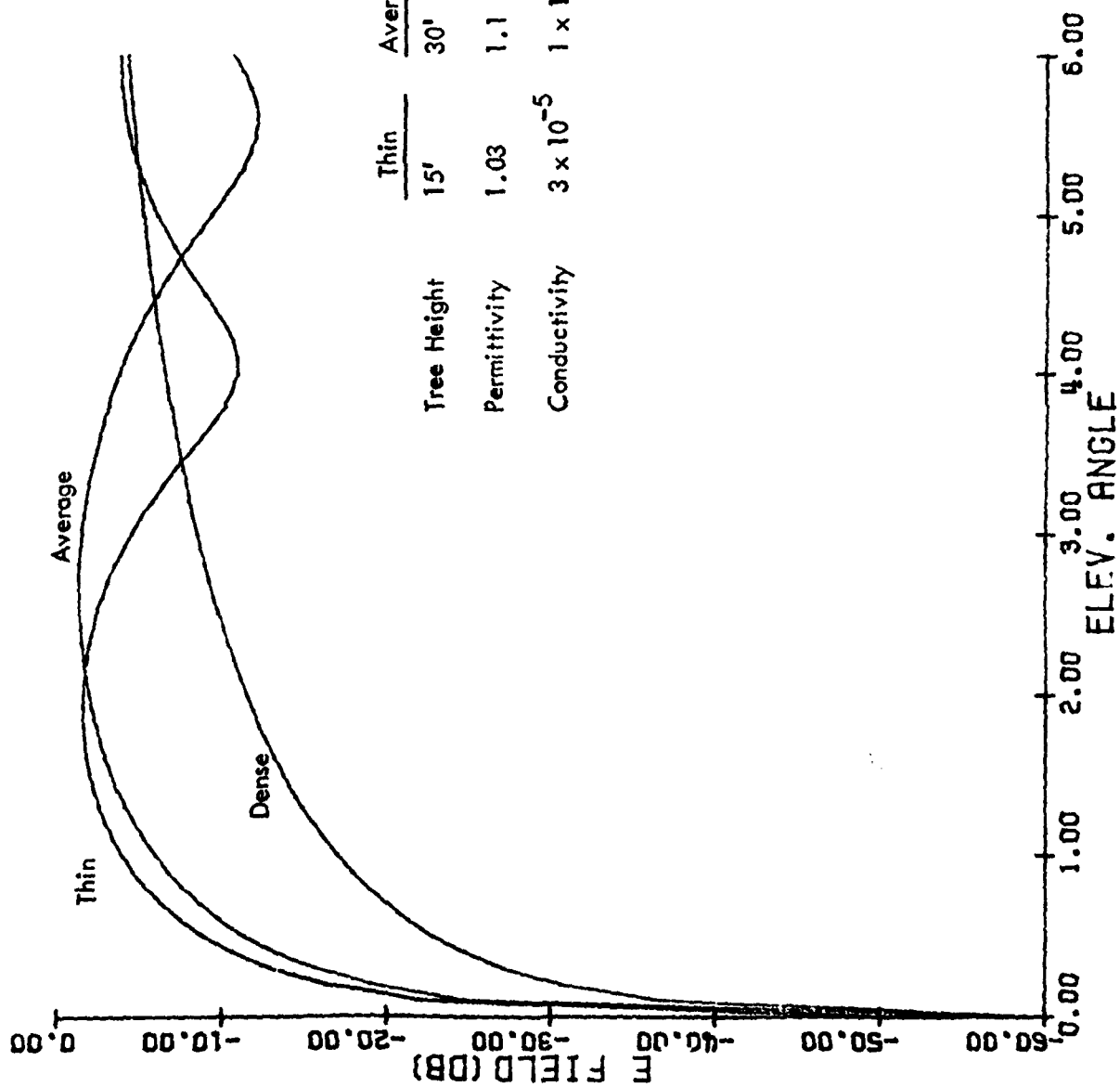
Figure 3-5 Calculated Vertical Lobing Pattern For a 70' Antenna Operating Over Extremes of Forest Parameters.

-41-
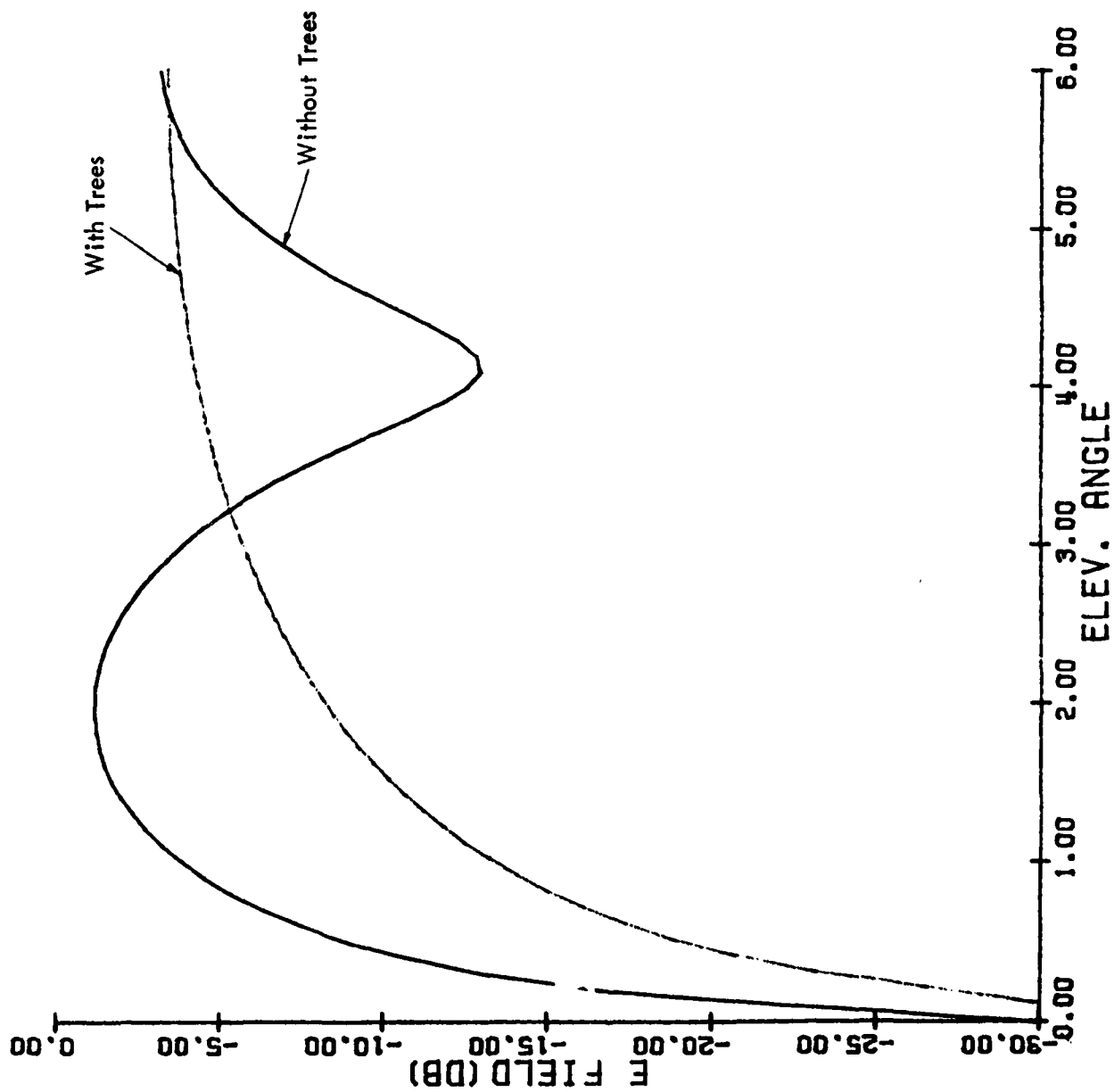
Figure 3-6. Calculated Received Signal Strength at 20 nm Using a 54' Transmitting Antenna Above Flat Ground and Flat Ground with 38' Trees. Electrical parameters: ground – $\epsilon_r = 15$, $= 12 \times 10^{-3}$; Trees – $\epsilon_r = 1.05$, $\sigma = 3 \times 10^{-5}$.

Brekhovskikh [37] suggests that spherical-wave incidence on a planar reflecting surface can be analyzed by representing the spherical wave as an infinite series of plane waves. Because the reflection coefficients for plane waves are known, the contribution of a reflected spherical wave can be computed by summing the contributions of each of the plane wave's components of the spherical wave. The following analysis was given by Brekhovskikh for the general case of spherical wave (acoustic or electromagnetic) reflection from a plane boundary; pertinent aspects of that analysis are presented here, in notation consistent with earlier sections of this report, to explicitly show how his findings relate to VHF communications.

Decomposition of the spherical wave into an infinite sum of plane waves is developed assuming a 2-dimensional x-y coordinate system; continuation to a 3-dimensional space is performed later. For a source located at (0,0), the spherical wave radiated by that source is:

$$\frac{e^{j\gamma r}}{r}$$

where r is the distance to an observation point at (x,y) and is equal to $\sqrt{x^2 + y^2}$. At that same point, a plane wave is defined by:

$$\frac{e^{j(\gamma_x x \; \gamma_y y)}}{r}$$

with $\gamma^2 = \gamma_x^2 + \gamma_y^2$. Clearly, the direction of propagation for such a plane wave is defined by the values of γ_x and γ_y.

Expanding the field described above in terms of a double Fourier integral in terms of x and y yields:

$$\frac{e^{j\gamma r}}{r} = \int\int_{-\infty}^{\infty} A(\gamma_x, \gamma_y) e^{j(\gamma_x x + \gamma_y y)} d\gamma_x d\gamma_y \qquad (3-8)$$

Determination of the weighting function $A(\gamma_x, \gamma_y)$ can be accomplished using an inverse Fourier transform:

$$A(\gamma_x, \gamma_y) = \frac{1}{(2\pi)^2} \int\int_{-\infty}^{\infty} \left(\frac{je^{j\gamma r}}{r} \right) e^{-j(\gamma_x x + \gamma_y y)} d\gamma_x d\gamma_y \qquad (3\text{-}9)$$

Transformation to polar coordinates is accomplished using the following identities:

$$\gamma_x = q\cos\psi , \quad \gamma_y = q\sin\psi , \quad q = \sqrt{\gamma_x^2 + \gamma_y^2}$$
$$x = r\cos\phi, \quad y = r\sin\phi , \quad d_x d_y = r dr d\phi \qquad (3\text{-}10)$$

And thus:

$$A(\gamma_x, \gamma_y) = \frac{1}{(2\pi)^2} \int_0^{2\pi} d\phi \int_0^{\infty} e^{jr[\gamma - q\cos(\psi - \phi)]} dr \qquad (3\text{-}11)$$

If some finite absorption is assumed in the medium, γ will have a positive imaginary component resulting in a zero-valued argument for the upper limit of r, resulting in the following simplification:

$$A(\gamma_x, \gamma_y) = \frac{j}{(2\pi)^2 \gamma} \int_0^{2\pi} \frac{d\delta}{1 - (q/\gamma)\cos\delta} \qquad (3\text{-}12)$$

Integration tables show this to be equal to:

$$A(\gamma_x, \gamma_y) = \frac{j}{2\pi(\gamma^2 - \gamma_x^2 - \gamma_y^2)^{1/2}} \qquad (3\text{-}13)$$

Thus:

$$\frac{e^{j\gamma r}}{r} = \frac{j}{2\pi} \int\int_{-\infty}^{\infty} \frac{e^{j(\gamma_x x + \gamma_y y)}}{(\gamma^2 - \gamma_x^2 - \gamma_y^2)^{1/2}} d\gamma_x d\gamma_y \qquad (3\text{-}14)$$

-44-

Continuation of the above expression to 3-dimensional space can be performed by adding $\pm\ j\gamma z$ to the exponent, and by using the identity:

$$\gamma^2 = \sqrt{\gamma^2 - \gamma_x^2 - \gamma_y^2}$$

elsewhere. A plus sign on the added factor is used for the analysis under consideration here because it is the field in the upper medium; $z > 0$, that is of interest. Thus:

$$\frac{e^{j\gamma r}}{R} = \frac{j}{2\pi} \iint\limits_{-\infty}^{\infty} e^{j(\gamma_x x + \gamma_y y + \gamma_z z)} \frac{d\gamma_x d\gamma_y}{\gamma_z} \tag{3-15}$$

The above expression shows that a spherical wave can be expanded in terms of plane waves. The direction of the plane wave within the integral is defined by γ_x, γ_y, γ_z as shown in Figure 3-7. To facilitate solution of Equation (3-15), a change of variables is introduced:

$$\gamma_x = \gamma\sin\theta\cos\phi, \quad \gamma_y = \gamma\sin\theta\sin\phi, \quad \gamma_z = \gamma\cos\theta \tag{3-16}$$

Consistent with the limits of integration of Equation (3-15), ϕ is varied over 0 to 2π. However, θ cannot be restricted to real values of the variable if agreement with Equation (3-15) is to be realized. For $\gamma_x = \gamma_y = 0$, $\gamma_z = \gamma$; $\gamma_z \to j\infty$ as γ_x or γ_y approach $+\infty$. Also, because $\cos\theta = \gamma_z/\gamma$, from Equation (3-16), θ will vary from 0 to $2\pi-j\infty$. The path of integration is in the form of the contour shown in Figure 3-8.

Applying another transformation of variables:

$$d\gamma_x d\gamma_y d\gamma_z = \gamma\sin\theta d\theta d\phi \tag{3-17}$$

Equation (3-15) can be rewritten:

$$\frac{e^{j\gamma R}}{R} = \frac{j\gamma}{2\pi} \int\limits_0^{\pi/2-j\infty} \int\limits_0^{2\pi} e^{j(\gamma_x x + \gamma_y y + \gamma_z z)} \sin\theta d\theta d\phi \tag{3-18}$$
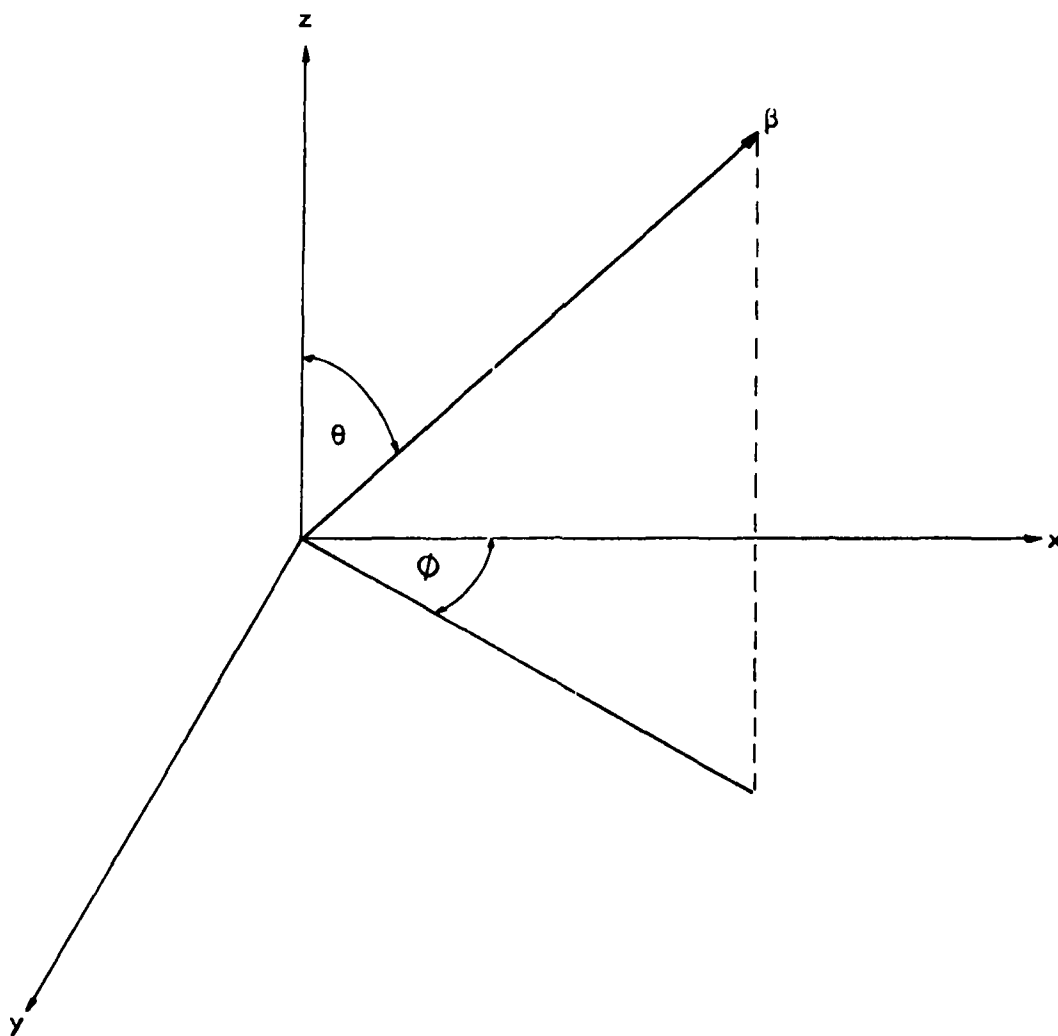
Figure 3-7. Position of Wave Vector, β, with Respect to Polar Coordinate System.
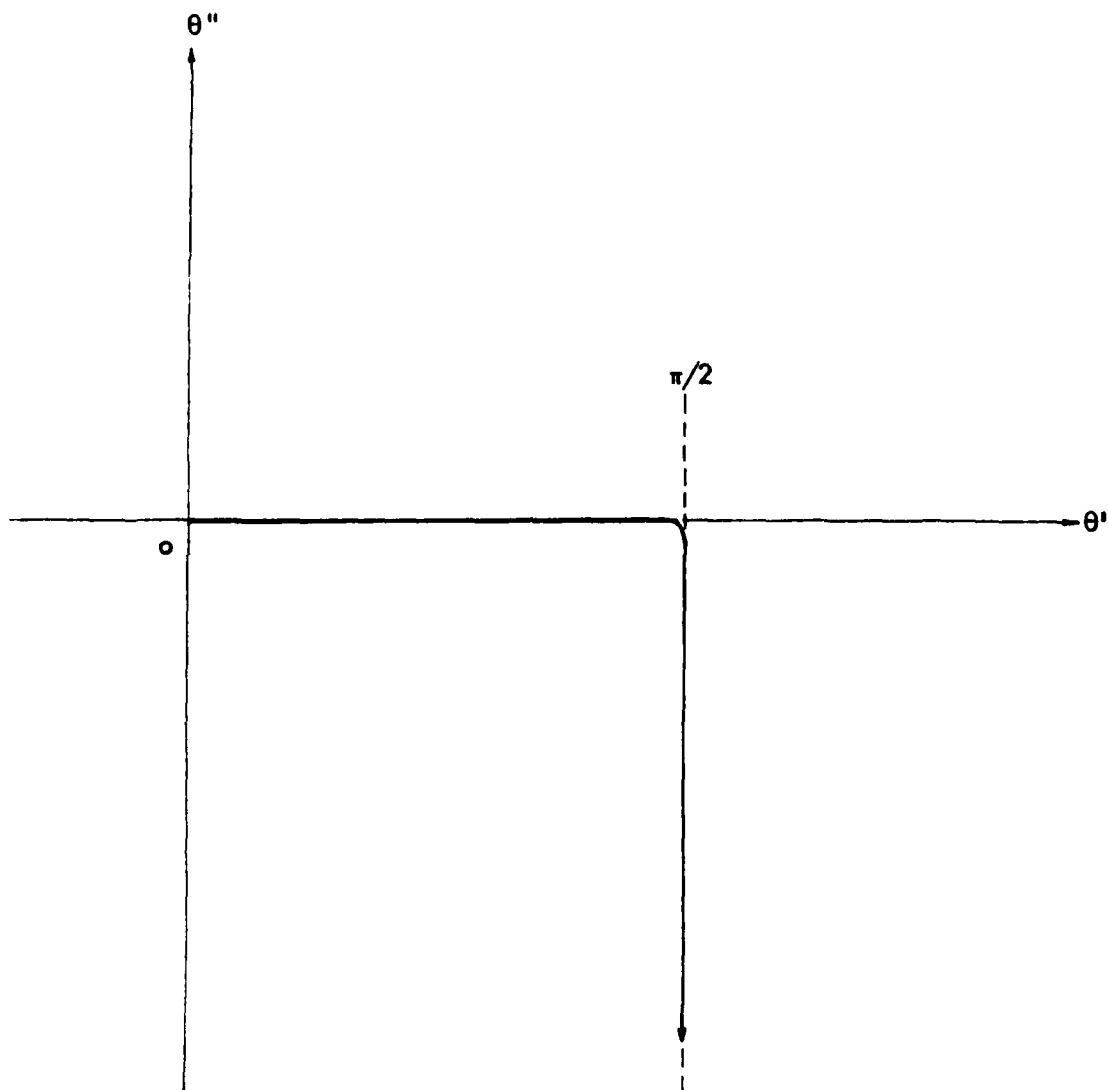
Figure 3-8. Integration Contour in the Complex Plane for the Variable θ.
Note that $\theta = \theta' + i\theta''$.

It should be noted here that the plane wave representation within the integral is not an ordinary plane wave over the specified limits of integration; if it were an ordinary plane wave, the singularity of the spherical wave only at r=0 could not be realized. For non-zero imaginary components of γ, the ordinary plane wave becomes an inhomogeneous plane wave [38], which will attentuate in the direction of the imaginary component of γ. Clearly, for x=y=z=0, there is no attenuation and the infinite sum of unattenuated plane waves gives the required singularity at R=0. For R > 0, the inhomogeneous plane waves become attenuated, resulting in a finite value over the infinite sum.

Equation (3-18) shows that a spherical wave can be decomposed into an infinite number of plane waves. Because the reflection coefficient for a plane wave on a plane boundary is known, the reflected field for a spherical wave on a plane boundary can be determined using the relationship of Equation (3-18) to reconstruct the reflected spherical wave from the individual reflected plane waves. To show how this is accomplished, consider the Figure 3-8, which shows a source radiating above a reflecting plane. Note that the geometry of Figure 3-9 shows the source at $(0, 0, z_0)$ rather than at the origin as was assumed for the discussion of spherical wave decomposition. Thus, z should be replaced by $z + z_0$ in Equation (3-18) to be consistent with this new geometry.

By superposition, the reflected spherical wave can be represented by summing all of the plane waves comprising the spherical wave multiplied by their reflection coefficients. Accordingly, the plane wave components of the reflected spherical wave will be of the form:

$$\Gamma(\theta)e^{j(\gamma_x x + \gamma_y y + \gamma_z(z + z_0))} \tag{3-19}$$

Integrating these reflected plane waves, as in Equation (3-18), will yield the reflected spherical wave; define:

$$\tau = x\sin\theta\cos\phi + y\sin\theta\sin\phi + (z + z_0)\cos\theta,$$

then:

$$\psi_{refl} = (\frac{j\gamma}{2\pi}) \int_0^{\pi/2-j\infty} \int_0^{2\pi} e^{j\gamma\tau} \Gamma(\theta)\sin\theta d\theta d\phi \tag{3-20}$$

Some simplification in Equation (3-20) can be realized taking into account that integration over ϕ reduces to the zero-order Bessel Function. Setting $x = r\cos\phi_1$, $y = \sin\phi_1$, yields:
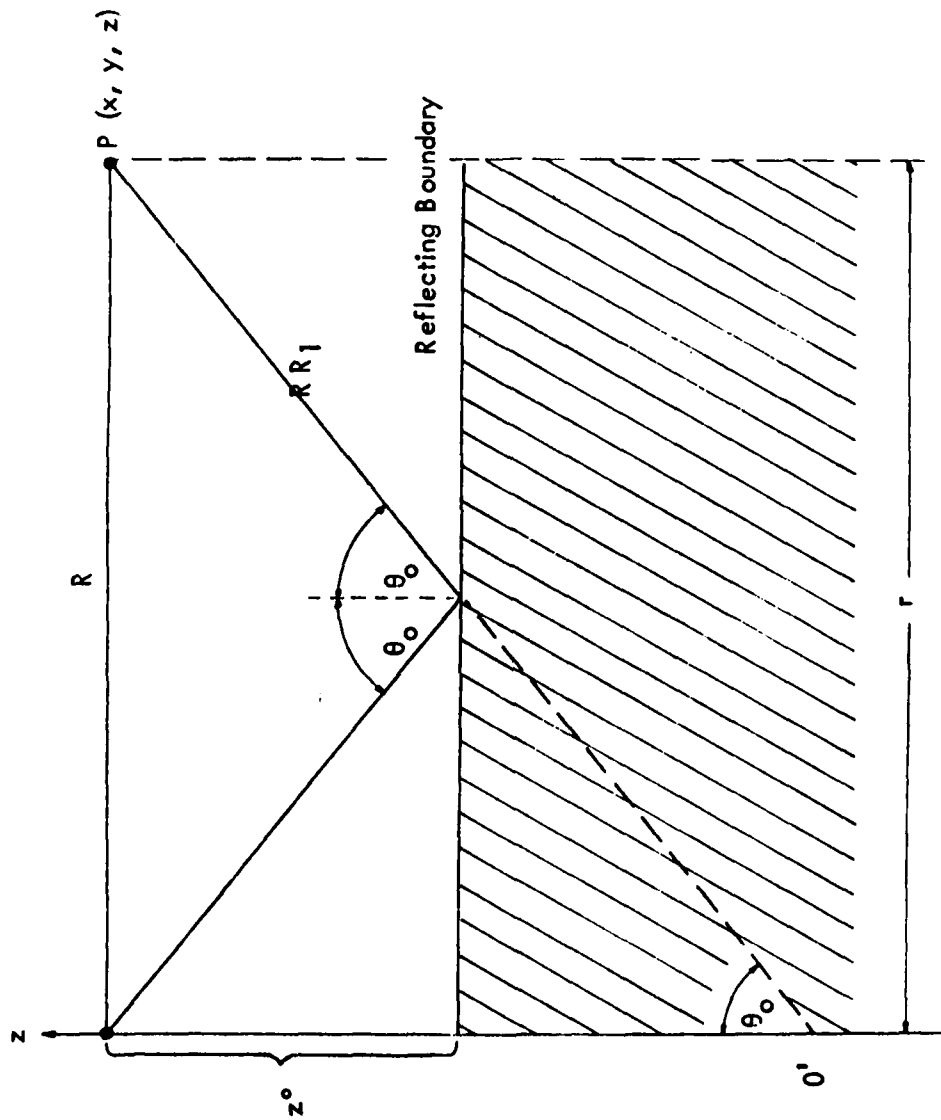
Figure 3-9. Geometry for Analysis of Spherical Wave Reflection from a Plane Boundary.

$$\int_0^{2\pi} e^{j\gamma r\sin\theta\cos(\phi-r_1)}d\phi = 2\pi J_0(\mu) \qquad (3\text{-}21)$$

where $\mu = \gamma r \sin\theta$. Thus, Equation (3-20) becomes:

$$\psi_{refl} = j\beta \int_0^{2\pi-\gamma\infty} J_0(\mu)e^{j\gamma(z + z_0)\cos\theta}\Gamma(\theta)\sin\theta d\theta \qquad (3\text{-}22)$$

A more expeditious solution to Equation (3-22) can be realized by transformation of the Bessel Function into Hankel Functions:

$$J_0(\mu) = \tfrac{1}{2}[H_0^{(1)}(\mu) + H_0^{(2)}(\mu)] \qquad (3\text{-}23)$$

where $H_0^{(1)}(\mu)$ and $H_0^{(2)}(\mu)$ are Hankel Functions of the first and second kind. Using this relationship, the single integral of Equation (3-22) is divided into two separate integrals. Replacing θ by $-\theta$ in the integral in which $H_0^{(2)}$ appears, and using the relationships $H_0^{(2)}(e^{j\pi}\mu) = H_0^{(1)}(\mu)$ and $\Gamma(-\theta) = \Gamma(\theta)$ results in two integrals with the same integrands. The limits of integration differ, one being from 0 to $\pi/2-j\infty$, and the other from $-\pi/2+j\infty$ to 0. The two integrals can be combined into a single integral with limits of integration ranging from $-\pi/2+j\infty$ to $\pi/2-j\infty$:

$$\psi_{refl.} = \left(\frac{j\gamma}{2}\right) \int_{-\pi/2+j\infty}^{\pi/2-j\infty} H_0^{(1)}(\mu)e^{j\gamma(z + z_0)\cos\theta}\Gamma(\theta)\sin\theta d\theta \qquad (3\text{-}24)$$

Solution of Equation (3-24) will yield the exact reflected field resulting from reflection at a plane boundary. Wave polarization effects are characterized by the reflection coefficient. The path of integration for Equation (3-24) is shown in Figure 3-10.

The asymptotic expansion for the Hankel Function is:

$$H_0^{(1)}(\mu) \approx \left(\frac{2}{\pi\mu}\right)^{1/2} e^{j(\mu-\pi/4)}(1 + 1/8j\mu + \ldots) \qquad (3\text{-}25)$$
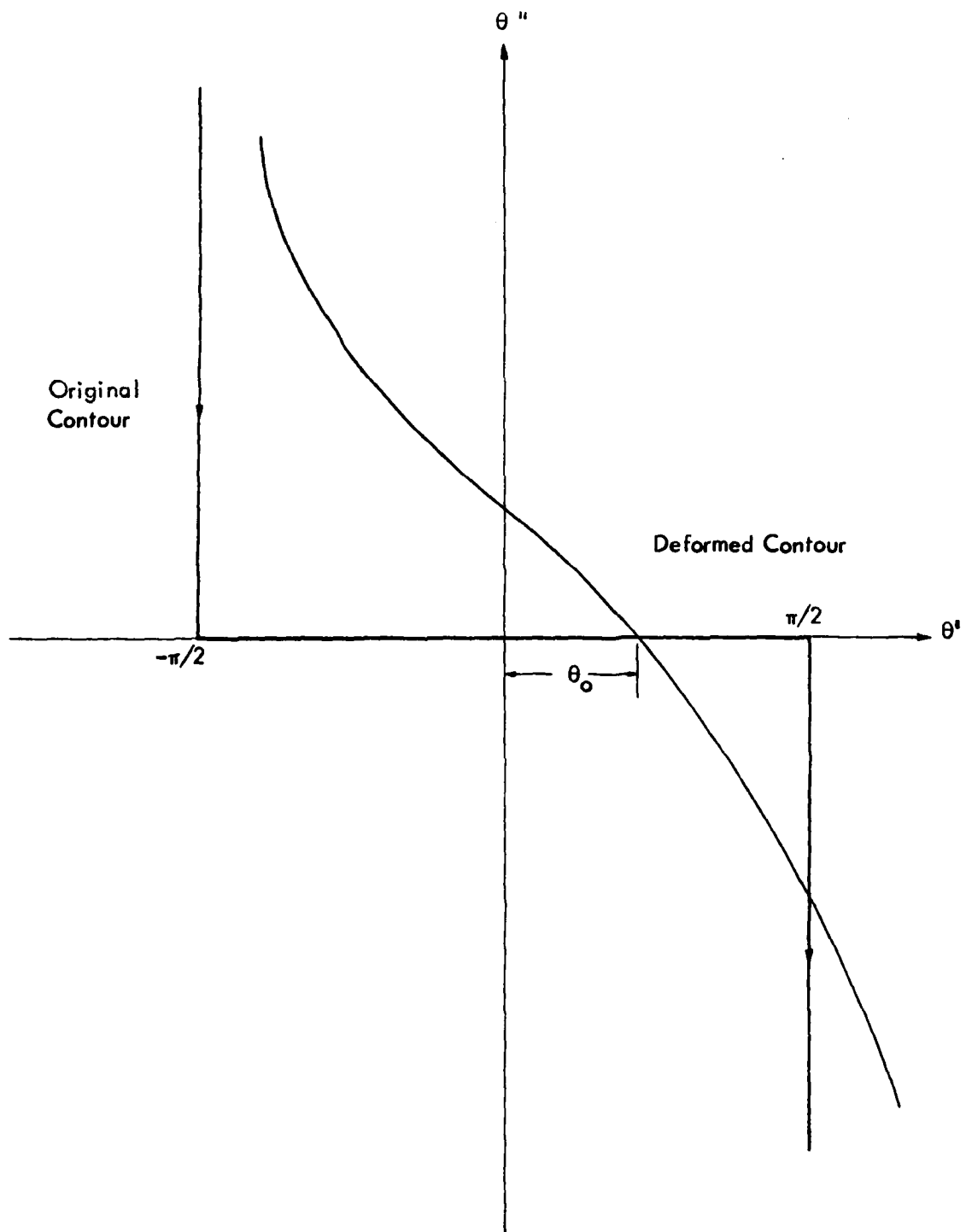
Figure 3-10. Original and Deformed Integration Contour Used in Method of
Steepest Descent Solution.

Because only large values of μ are considered here (recalling that $\mu = \beta r \sin\theta$), only the first term in the expansion need be retained in the integration:

$$\psi_{refl} \approx \left(\frac{\gamma}{2\pi r} \right)^{1/2} e^{j\pi/4} \int_{-\pi/2+j\infty}^{\pi/2-j\infty} e^{j\gamma R_1 \cos(\theta-r_0)}$$

$$x \ (1 + 1/8 j\gamma r \sin\theta)\Gamma(\theta)\sqrt{\sin\theta} \ d\theta$$

(3-26)

noting that $z + z_0 = R_1\cos\theta$; $r + R_1\sin\theta_0$.

Because the value βR_1 in Equation (3-26) is assumed to be large, solution of the integral can be facilitated by the method of steepest descents. Detailed descriptions of this approximation technique are available in the literature [39, 40], and thus only a very brief description will be presented here to establish notation.

The method of steepest descents can be applied to integrals of the the form:

$$I = \int_C e^{\rho f(\xi)} F(\xi)d\xi$$

(3-27)

for large values of the parameter ρ ; $F(\xi)$ and $f(\xi)$ are arbitrary, analytic functions of the complex variable ξ . The value of the integral, I, will be essentially unchanged for certain deformations in the path of integration in the complex plane. Using this fact, a path of integration is chosen such that integration along a short, isolated part of that path will result in a reasonable estimate of the integral. Further, the integrand can be replaced by a simpler function that is equal to the initial integrand within the isolated part of the integration path, without concern for the new functions behavior elsewhere.

The parameter ξ can be assumed to be real and positive without loss of generality. The function $f(\xi)$ may be complex, allowing it to be separated into real and complex components:

$$f(\xi) = f_1(\xi) + jf_2(\xi)$$

Using this, the exponent in Equation (3-27) can be written as:

$$e^{j\rho f_2 + \rho f_1} \qquad\qquad (3\text{-}28)$$

Clearly, for sufficiently large ρ, the integrand will be dominated at the point where f_1 takes on its maximum value. Further, because the function $f(\xi)$ is analytic, the path of steepest descent of f_1 is the path of constant f_2. In the method of steepest descents, the deformed path of integration is selected so as to coincide with the path of steepest descent of f_1 in the neighborhood of the point where f_1 has its maximum value, known as the saddle point. This saddle point exists at the point at which:

$$\frac{df}{d\xi} = 0 \qquad\qquad (3\text{-}29)$$

A change of variables from ξ to s is performed so that integration with respect to s (a real variable) will coincide with the path of steepest descent of f_1 and constant f_2, letting $\xi = \xi$ be the saddle point, the desired path is defined by:

$$f(\xi) = f(\xi_0) - s^2 \qquad\qquad (3\text{-}30)$$

where $-\infty < s < \infty$. The integration path defined by Equation (3-30) is along the real s axis as seen in Figure 3-11.

As described above, a transformation of variables from ξ to s is performed to obtain the desired integration contour. Next, the function $F(\xi)$ is transformed into a function of s:

$$F(\xi)\,\frac{d\xi}{ds} \equiv \Phi(s) \qquad\qquad (3\text{-}31)$$

Taking the above into account, the integral can be rewritten:

$$I \equiv e^{-\rho f(\xi_0)} \int_{-\infty}^{\infty} e^{-\rho s^2} \Phi(s)\,ds \qquad\qquad (3\text{-}32)$$

Because ρ is assumed to be large, only small values of s are of importance; hence it is convenient to represent $\Phi(s)$ in a power series expanded about $s = 0$:

$$\Phi(s) = \Phi(0) + \Phi'(0)s + \tfrac{1}{2}\Phi''(0)s^2 + \ldots \qquad\qquad (3\text{-}33)$$

-53-
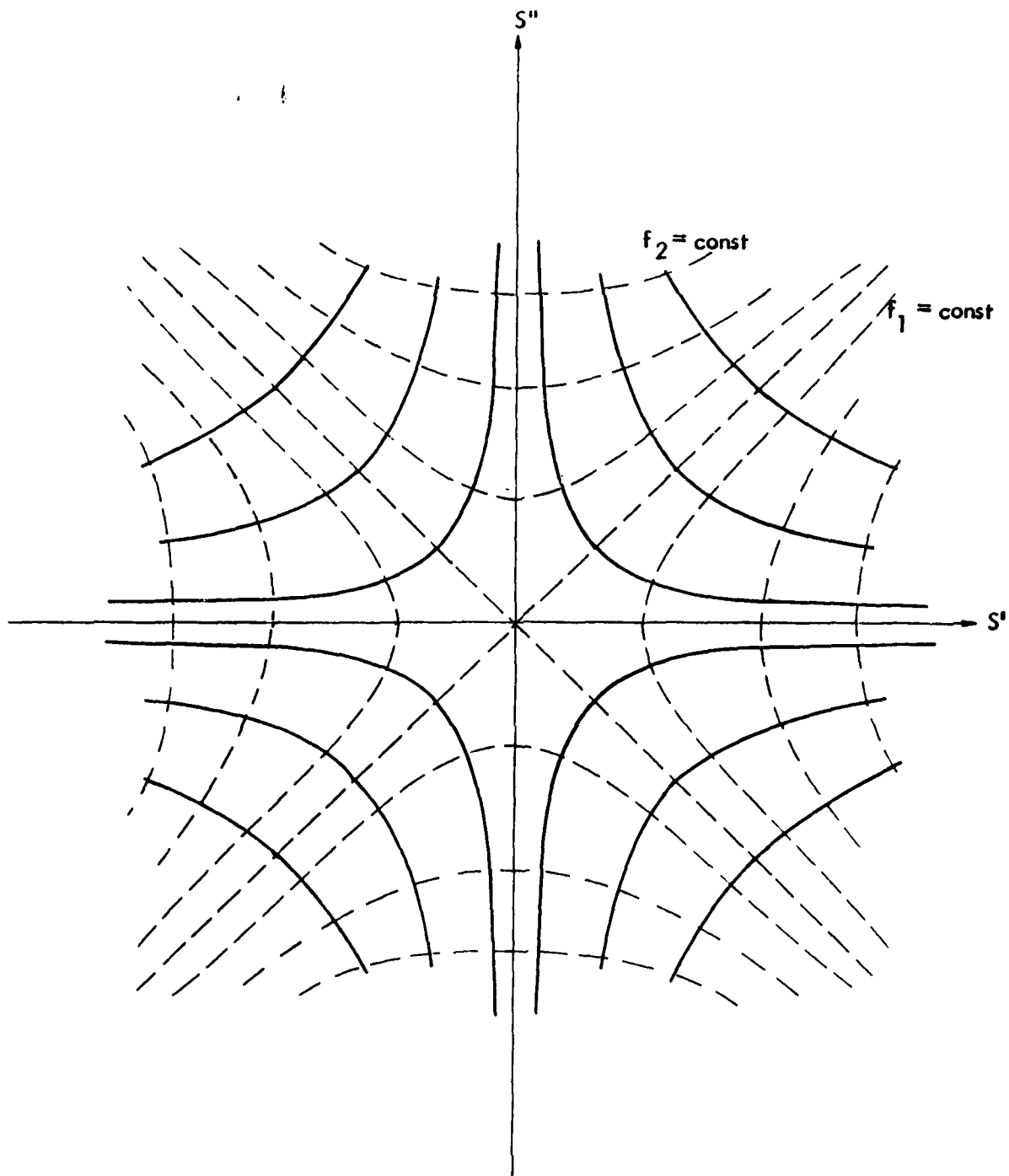
Figure 3-11. The Neighborhood of a Saddle Point.

Substituting the first two terms of this series into the integral yields:

$$\int_{-\infty}^{\infty} e^{-\rho s^2} \, ds = \left(\frac{\pi}{\rho} \right)^{1/2} \quad ,$$

$$\int_{-\infty}^{\infty} e^{-\rho s^2} \, s \, ds = \frac{1}{2} \left(\frac{\pi}{\rho^3} \right)^{1/2} \tag{3-34}$$

providing the following final result:

$$I \equiv e^{\rho f(\xi_0)} \left(\frac{\pi}{\rho} \right)^{1/2} [\phi(0) + (1/4\rho)\phi''(0) + \ldots]$$

An obvious constraint on the accuracy of the above approximation is that $\phi(s)$ be slow varying with respect to the exponential. As a consequence of this constraint, care must be taken to insure that poles of the function $\phi(s)$ are not crossed along the path of integration.

The saddle-point method described above is now applied to Equation (3-26) to calculate the reflected field. Equating Equations (3-26) and (3-27) yields the following identities:

$$\rho = \gamma R_1 \quad f(\theta) = \gamma \cos(\theta - \theta_0)$$

$$F(\theta) = e^{j\pi/4} \left(\frac{\gamma}{2\pi r} \right)^{1/2} (1 + 1/8\gamma r \sin\theta) \, \Gamma(\theta)\sqrt{\sin\theta} \tag{3-35}$$

The saddle point, defined by $df/d\theta = 0$, is at $\theta = \theta_0$. Transformation to the variable s is accomplished by:

$$\cos(\theta - \theta_0) = 1 + js^2 \tag{3-36}$$

with the desired integration path along real values of s. To determine the functional relationship between θ and s, the following identities must be used (recalling that θ is complex):

$$\sin\theta = \sin\theta' \cosh\theta'' + j \cos\theta' \sinh\theta''$$

$$\cos\theta = \cos\theta' \cosh\theta'' - j \sin\theta' \sinh\theta'' \qquad (3\text{-}37)$$

Equating real parts of Equation (3-36) shows the desired integration path:

$$\cos(\theta' - \theta_0) \cosh\theta'' = 1$$

This integration path is shown in Figure 3-10. Before continuing with the integration using the saddle point method, it is necessary to state that the poles of $F(\theta)$, which are seen to correspond to the poles of $\Gamma(\theta)$, are not crossed by the integration contour of Figure 3-10. The branch point at $\theta = 0$ due to the $\sqrt{\sin\theta}$ term is not crossed by the deformed contour, and is therefore not of any consequence in the analysis. For cases where the relative dielectric permittivity of the reflecting boundary, is greater than unity, it can be shown that singularities along the deformed contour of integration do not exist.

Applying the method of steepest descents as described above, the reflected field for a spherical wave on a plane boundary is shown to be:

$$\psi_{refl} = \left(\frac{e^{j\gamma R_1}}{R_1} \right) \left[\Gamma(\theta) - \frac{jN}{\beta R_1} \right] \qquad (3\text{-}38)$$

where N is a second order term accounting for non-plane wave incidence:

$$N = \tfrac{1}{2} \left[\Gamma''(\theta_0) + \Gamma'(\theta_0) \cot\theta_0 \right] \qquad (3\text{-}39)$$

where $\Gamma'(\theta_0)$ and $\Gamma''(\theta_0)$ are derivatives of the reflection coefficient with respect to θ evaluated at $\theta = \theta_0$. Taking the specified derivatives of $\Gamma(\theta)$, and letting $\gamma_0 = \cos\theta_0$, yields:

$$N = \frac{\varepsilon_r(1 - \varepsilon_r)}{q_0^3(\varepsilon_r\gamma_0 + q_0)^3}$$

$$x \quad [\, 2\varepsilon_r(\varepsilon_r - 1) + 3\varepsilon_r \gamma_0^2 + q_0\gamma_0(2\varepsilon_r + 1 - \gamma_0^2) - \varepsilon_r\gamma_0^4 \,]$$

<div align="right">(3-40)</div>

where:

$$q_0 = \sqrt{\varepsilon_r - \sin^2\theta_0} \qquad (3\text{-}41)$$

Thus, all necessary information to calculate a second-order approximation to spherical-wave reflection from a plane boundary is available in Equation (3-41). As seen from Equation (3-38), the first-order approximation is merely the incident wave multiplied by the plane-wave reflection coefficient. The second-order term, N, is referred to as a correction term which describes the lateral wave [40]. Also seen in Equation (3-38) is the inverse-square relationship between distance and the lateral wave intensity. This dependence causes the second-order contribution to attenuate relatively quickly compared to the plane-wave reflected field. As referenced, Tamir's work has shown that the lateral wave may become significant when the direct and plane-wave reflected fields cancel each other. A plot of the second-order term of Equation (3-40) is shown in Figure 3-12 as a function of elevation angle. The zero-decibel points of Figures 3-6 and 3-12 are referenced to the same value. A comparison of the composite direct and plane-wave reflected signal strength of Figure 3-6 with the second-order contribution of Figure 3-12 shows the second-order signal to be relatively small except for angles closely approaching grazing incidence. For aircraft positioned over 1000' above ground level, the second-order term generally will be insignificant with respect to the first-order term. Thus, for minimum enroute altitudes and above signal contributions resulting from lateral-wave propagation need not be considered.

D. Signal Energy Distribution Between Transmitter and Receiver. The GTD model discussed in Section IIF operates under the assumption that signals propagate over infinitesimally thin paths from the transmitter to receiver. For circumstances where the size of scatterers (terrain variations in the case of ILS modeling) are very large with respect to a wavelength, such an assumption has enabled accurate modeling to be performed. However, when including the effects of forested areas, more abrupt variations in reflecting plane height are encountered than are typically encountered when modeling only terrain effects. For example, at a forest boundary, the height of the reflecting plane is seen to instantaneously change by the height of the trees. In practical situations where the presence or absence of trees is not continuous within a reflecting region, accurate modeling may not be realized assuming only a single point of specular reflection (as is assumed by GTD models). This deficiency could be compensated for if diffractive effects at the edge of a forested region could be accurately computed. However, adding a second set of diffraction coefficients to an existing GTD computer model, in addition to implementing new requirements for blockage criteria (trees
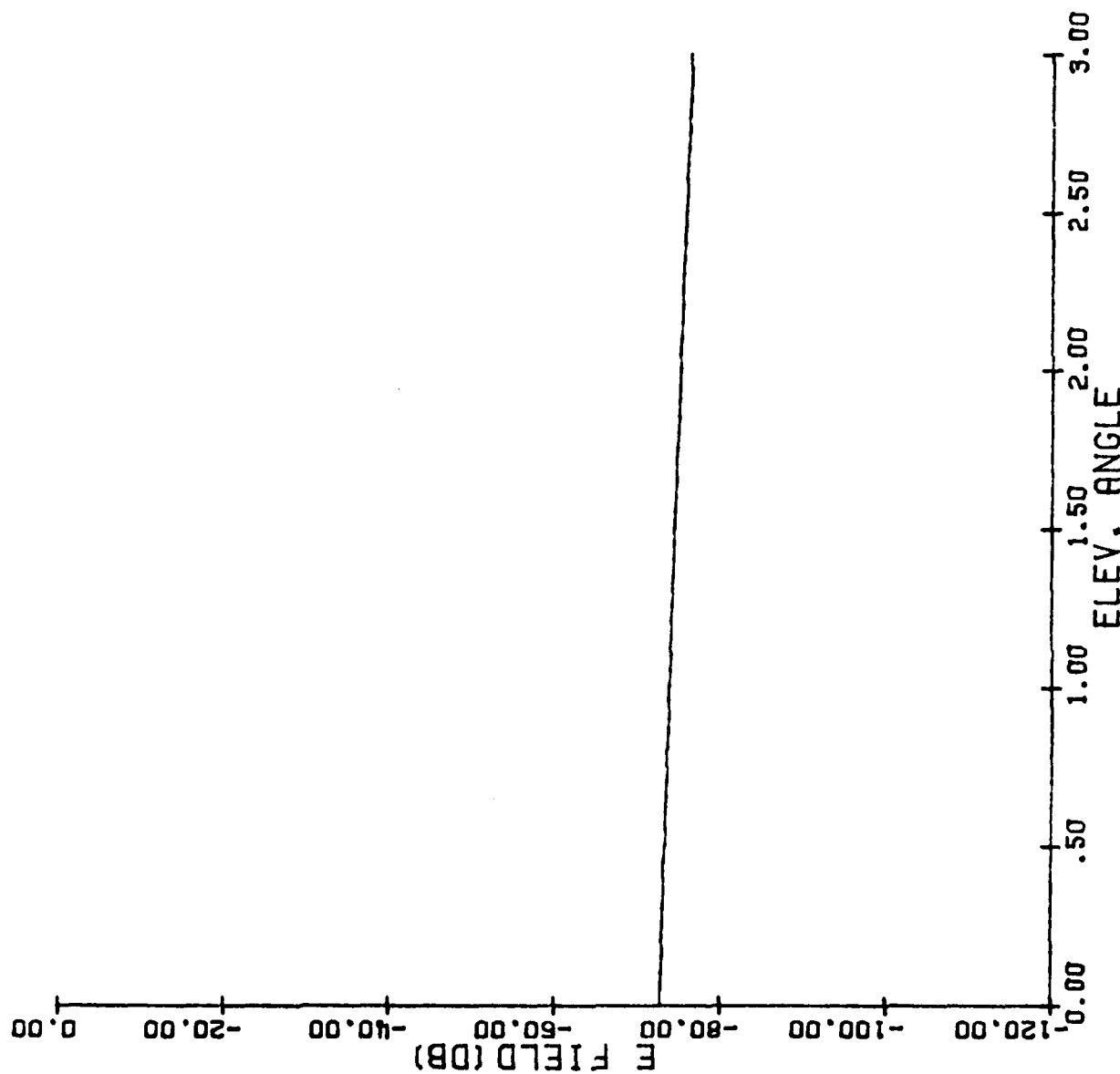
Figure 3-12. Contribution of Non-Plane Wave Contribution as a Function of Elevation Angle at a Range of 20 nm.

only partially block a signal), is not considered worthwhile for modeling tree effects. This conclusion is reached primarily due to the dependence of diffraction coefficients upon edge geometries, which are inherently irregular, and hence unpredictable, along forest boundaries. The modeling technique that has been successfully implemented by a GTD computer model is based upon an analysis of signal energy distribution with respect to forested areas. Accordingly, this section describes signal distribution in space; how such information is used in modeling is discussed in the following section.

Early work with light diffraction was facilitated by Huygen's principle which states: Each point on a wavefront acts as a new, or secondary, source of waves. This statement is shown to be a necessary consequence of the wave equation [42] and is thus consistent with theory. To illustrate Huygen's principle, consider Figure 3-13 which shows a signal being transmitted in free space from Point A to Point P. If the radiator is isotropic, a wavefront, or point of constant phase, will be represented by a circle around the radiator as shown in Figure 3-13. A 2-dimensional wavefront is represented by a circle in Figure 3-13 for simplicity; a 3-dimensional sphere representing a surface of constant phase is discussed later. According to Huygen's Principle, any point on this wavefront can be considered to be a new, or secondary, source of waves. The total signal strength observed at Point P is the complex sum of the contributions from the sources along the wavefront. One factor that must be considered in determining the amplitude of the contribution from these secondary sources is the obliquity factor [43] that accounts for the non-isotropic radiation patterns of the secondary sources. The obliquity factor specifies a radiation pattern of $1 + \cos\theta$, where θ is the angle with respect to the forward direction as shown in Figure 3-13.

Fresnel used Huygen's Principle to explain light intensity variations caused by passing light rays through circular apertures of different sizes. Although Fresnel's work specifically addressed phenomena in the visible spectrum, applications to VHF are valid because his theories are in agreement with the wave equation. Many of the theories and concepts developed by Fresnel are germane to the analysis of tree effects within line of sight at VHF and are therefore addressed below.

Consider an isotropic radiator located at a Point A and an observation point P as shown in Figure 3-14, which is a 3-dimensional version of Figure 3-13. The surface BCDE represents a section of a spherical wavefront, or surface of constant phase, radiated from Point A. According to Huygen's Principle, points on this wavefront act as secondary sources of waves. Thus, the resultant field at Point P can be determined by integrating the contributions from secondary sources over the entire wavefront surface. For the case of radiation in free space, such an integration process would clearly represent unnecessary complexity in making what would otherwise be a straightforward calculation. However, this calculation will enable the effects of apertures and obstructions to be calculated. To determine how a
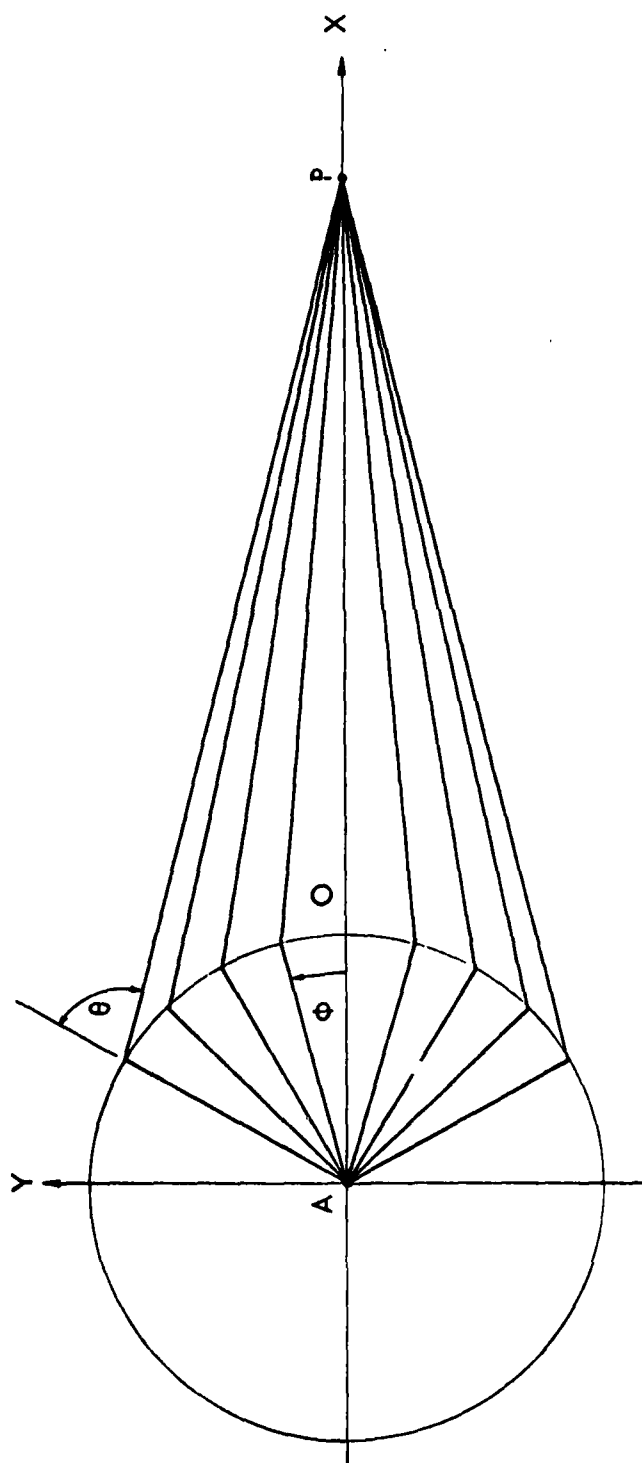
Figure 3-13. Illustration of Huygen's Principle.

-60-

Figure 3-14. Construction of Half-Period Zones on a Spherical
Wave Front.

particular secondary source will contribute in the integration, the phase from that source, as seen at Point P, must be determined. This phase is determined by the distance from the point on the wavefront to Point P. Figure 3-14 shows rings on the wavefront representing loci of points 180° out of phase with respect to the shortest path OP. The areas within these zones, labeled s_1, s_2,....s_n, are called Fresnel half-period zones, or, Fresnel Zones. The amplitude contributions of these Fresnel Zones as seen at Point P are proportional to the surface areas between successive zones denoted s_n. Additionally, because successive zones are 180° out of phase with each other, their amplitude contribution at point P will be of alternating sign as indicated below:

$$A = A_1 - A_2 + A_3 - A_4 + ...+ (-1)^{m-1}A_m \qquad (3-42)$$

where A_m is the amplitude contribution from the mth Fresnel Zone. Other factors affecting received signal at Point P from the mth zone will be obliquity and the distance from Point P to the mth zone, d_m. Thus the total contribution from any zone is:

$$A_m = \text{Constant} \times \frac{s_m}{d_m} (1 + \cos\theta) \qquad (3-43)$$

An exact calculation of s_m/d_m will show that the ratio remains constant for all m, leaving only the obliquity factor to affect A. The obliquity factor, and thus A_m, is shown to decrease non-uniformly with increasing m such that the contributions from any given zone will be less than the average of the contributions from the preceeding and following zones:

$$A_m < \frac{A_{m-1} + A_{m+1}}{2} \qquad (3-44)$$

Equation (3-42) can be re-written:

$$A = \frac{A_1}{2} + (\frac{A_1}{2} - A_2 + \frac{A_3}{2}) + (\frac{A_3}{2} - A_4 + \frac{A_5}{2}) + ...+ \frac{A_m}{2}$$

$$= A_1 - \frac{A_2}{2} - (\frac{A_2}{2} - A_3 + \frac{A_4}{2}) - (\frac{A_4}{2} - A_5 + \frac{A_6}{2}) - ...$$

$$- \frac{A_m - 1}{2} + A_m \tag{3-45}$$

Using the inequality of Equation (3-44) above, it is seen that the quantities in parentheses in Equation (3-45) are all positive, and thus the following inequalities must hold:

$$\frac{A_1}{2} + \frac{A_m}{2} < A < A_1 - \frac{A_2}{2} - \frac{A_{m-1}}{2} + A_m \tag{3-46}$$

Given that the contributions from any two adjacent zones are very nearly equal, the received amplitude can be approximated by:

$$A \approx \frac{A_1}{2} + \frac{A_m}{2} \tag{3-47}$$

However, as m becomes larger, A_m will approach zero as discussed above, allowing the received amplitude to be approximated by:

$$A \approx \frac{A_1}{2} \tag{3-48}$$

Thus, it is seen that the received signal amplitude is one-half of that which would be observed if only contributions from the first Fresnel half-period zone were received. This important result gives a clear indication of which regions should be considered in determining the effects of obstructions on the received signal. To further illustrate the Fresnel Zone concept, consider Figure 3-15 which is a 2-dimensional plot of the real part of the contribution to the received signal using the geometries of Figure 3-13. Because of symmetry, a 3-dimensional representation can be constructed by rotation about $\phi = 0$. As seen in Figure 3-15, the primary contribution to the received signal occurs within a small angular interval of ϕ which is defined by the first Fresnel Zone. Oscillations outside the first Fresnel Zone cause nearly equal reinforcement and cancellation, resulting in a small total contribution to the received signal.

Fresnel Zone sizes depend upon frequency, the distance between the transmitter and receiver, and the distance to the wavefront under consideration. The first Fresnel Zone is thus a volume enclosed by a locus of points representing a distance one-half wavelength longer
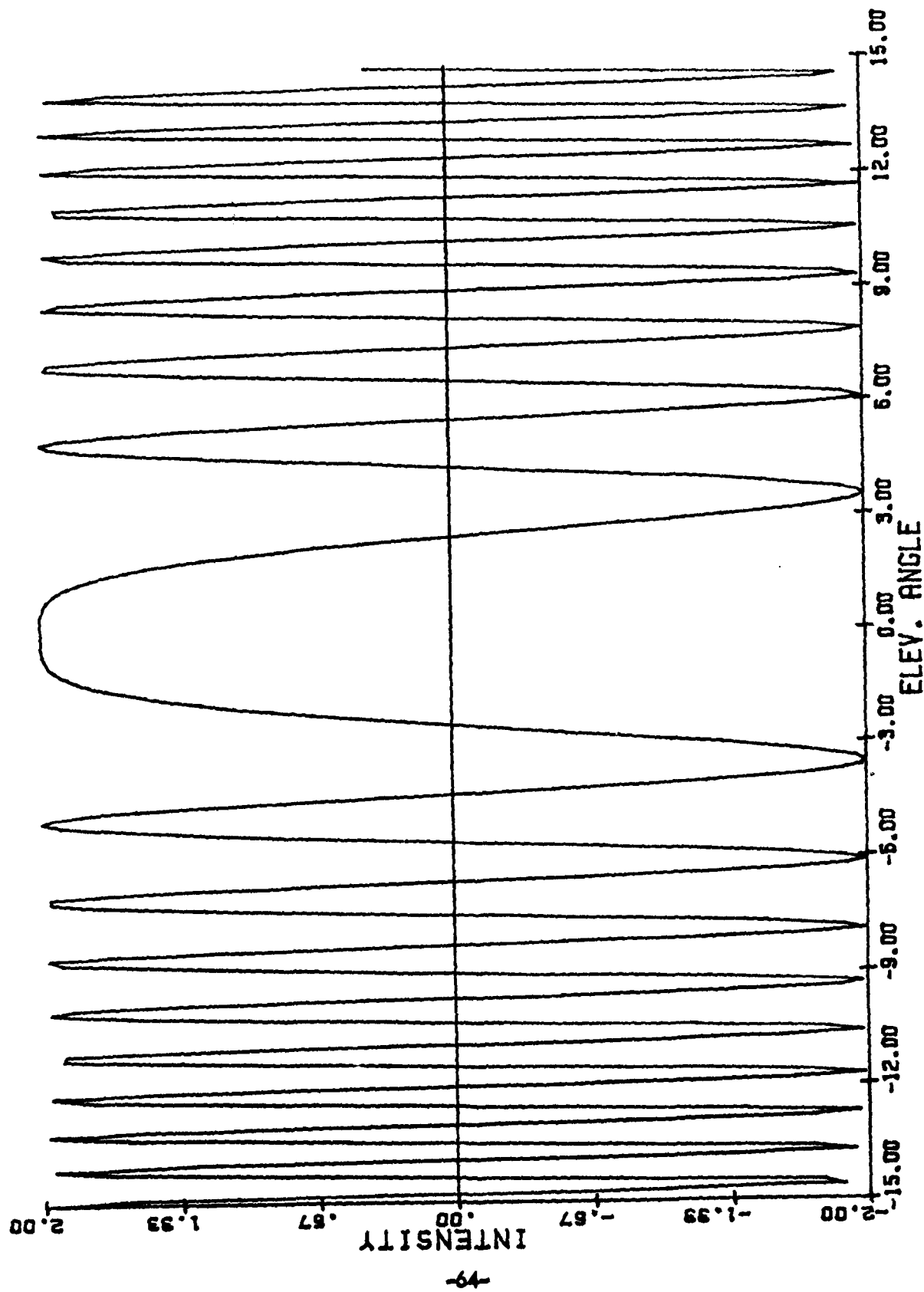
Figure 3-15. Plot of the Real Part of a Source Signal Contribution as a Function of the Angle Φ Using the Geometry of Figure 5-13.

-64-

than the shortest distance between the transmitter and receiver. These points form a symmetrical, 3-dimensional ellipse whose major axis is the line between the transmitter and receiver. The radius of that ellipse is defined by [44]:

$$R \approx \sqrt{\lambda \ \frac{ab}{a+b}} \qquad (3\text{-}49)$$

using variables described in Figure 3-14. The ellipse described above is called the first Fresnel Zone Fresnel ellipse, or more simply, the Fresnel Ellipse.

The above discussion indicates that there is a volume defined by the Fresnel Ellipse that is crucial in determining the amplitude of the received signal. Basically, if the Fresnel Ellipse does not contain any obstructions, line-of-sight propagation can be assumed. The effects of obstructions, particularly trees, within the Fresnel Ellipse are discussed later.

Former sections of this report consider reflection at boundaries only at the single point where the angle of incidence is equal to the angle of reflection. However, in view of the information presented in this section, it is clear that reflection actually occurs over an area, rather than a single point. To illustrate this area of reflection, consider Figure 3-16 which shows a source and its image with respect to a ground plane. As shown in Figure 3-16, the propagation path between the image and the receiver is intersected by the reflecting ground plane. The ellipses drawn on that ground plane represent loci of points 180° out of phase with the shortest path between the image and receiver; thus, those ellipses describe Fresnel Zones. The Fresnel Zones in Figure 3-15 are in the form of ellipses, rather than the circular Fresnel Zone representations of Figure 3-13, because the propagation path is intersected at an oblique angle.

The significance of Fresnel Zones on a reflecting surface is essentially the same as the significance of Fresnel Zones for free-space propagation. That is, the energy contribution of reflected signal is dominated by the first Fresnel Zone. If the terrain within the first Fresnel Zone is smooth, as per the Rayleigh Criterion discussed in Section IIIB, specular reflection can be assumed. If this area is not smooth, the composite reflection from that ground plane will be smaller than the reflection indicated by the reflection coefficient. Thus, the area defined by the first Fresnel Zone provides a good indication of the reflected signal contribution. The location and dimensions of the first Fresnel Zone can be calculated from the following equations using the notation shown in Figure 3-16 [45]:

$$x_0 = d \left[1 + \frac{h_2 - h_1}{2h_1[1 + (h_1+h_2)^2/\lambda(R+\lambda/4)]} \right]$$

-65-

z

y

P

(o,d,h₂)

$(0, d, h_2)$

Source
(o,o,h)

$(0, 0, h)$

b

(x_o, o, o)

$(x_o, 0, 0)$

ψ

(o,o,o)

$(0,0,0)$

x

$(x_o + x_1, o, o)$

$(x_o + x_1, 0, 0)$

a

$(x_o, -y, o)$

$(x_o, -y, 0)$

Image
$(o, o, -h_1)$

$(0, 0, -h_1)$
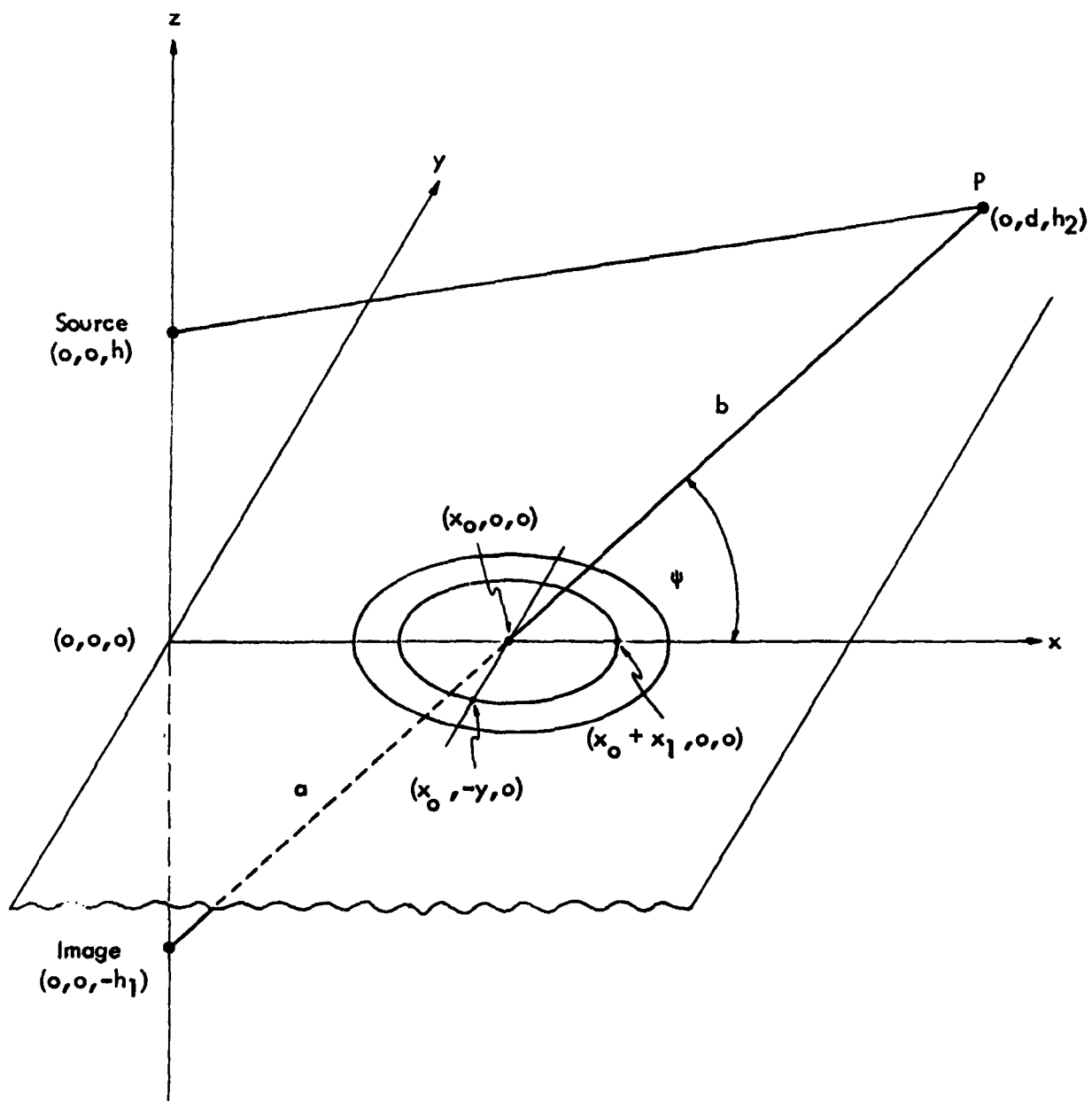
Figure 3-16. Construction of Fresnel-Zone Ellipses on Reflecting Ground Plane Surface.

$$x_1 = \frac{(1+\lambda/2R)(1+\lambda/4R)}{\sin\psi\left[1+\frac{\lambda(R+\lambda/4)}{(h_1+h_2)^2}\right]}\left(\frac{ab\lambda}{a+b+\lambda/4}\left[1+\frac{\lambda(R+\lambda/4)}{4h_1h_2}\right]\right)^{1/2}$$

$$y_1 = \left(1+\frac{\lambda}{4R}\right)\left[\frac{ab\lambda}{a+b+\lambda/4}\cdot\frac{1+\frac{\lambda(R+\lambda/4)}{4h_1h_2}}{1+\frac{\lambda(R+\lambda)}{(h_1+h_2)^2}}\right]^{1/2}$$

$$R = \sqrt{x^2+y^2+h_1^2} + \sqrt{(d-x)^2+y^2+h_2^2} \qquad (3\text{-}50)$$

E. Computer Implementation of Tree-Effect Modeling. Discussions of tree-related effects thus far have been concerned with canonic cases where tree cover is continuous and the ground plane supporting the trees is essentially flat. Measured data collected at a site with continuous trees over flat terrain support the theory of tree attenuation presented in this section. Consistent with the objective of modeling non-ideal sites, a method for applying this proven theory in practical situations is sought.

Section IIIB shows how tree-related attenuation can be accounted for by cancellation of the direct and reflected signals due to reflection from the air/forest boundary. Consequently, a rigorous approach to model implementation would be to examine the terrain in the first Fresnel Zone, as described in Section IIID, and determine the phase and amplitude of the signal reflected to the observation point. This process would involve an integration over the first Fresnel Zone, and would have to include blockage of the reflected signal for cases where the tree cover was not continuous in the first Fresnel Zone. Such a physical optics type approach (see Section IIE) would require considerable execution time, and would be difficult to implement in conjunction with existing software. For the above reasons, implementation of a rigorous solution to tree effects was not pursued.

The modeling technique that has been successfully implemented operates as a SUBROUTINE called by the GTD model discussed in Section IIF. Before describing how tree effects are modeled with the GTD program, it is necessary to discuss the GTD model's operation in greater detail than was given in Section IIF.

To provide further insight into the Ohio University GTD model used for this research, consider the simplified flow chart for that model presented in Figure 3-17. Referring to this flow chart, it is

Figure 3-17. Simplified Block Diagram for Ohio University GTD Model Operation Before Modification to Include Tree Effects.

seen that the first program step is to read the input data file. Input parameters to the GTD program include the 3-dimensional c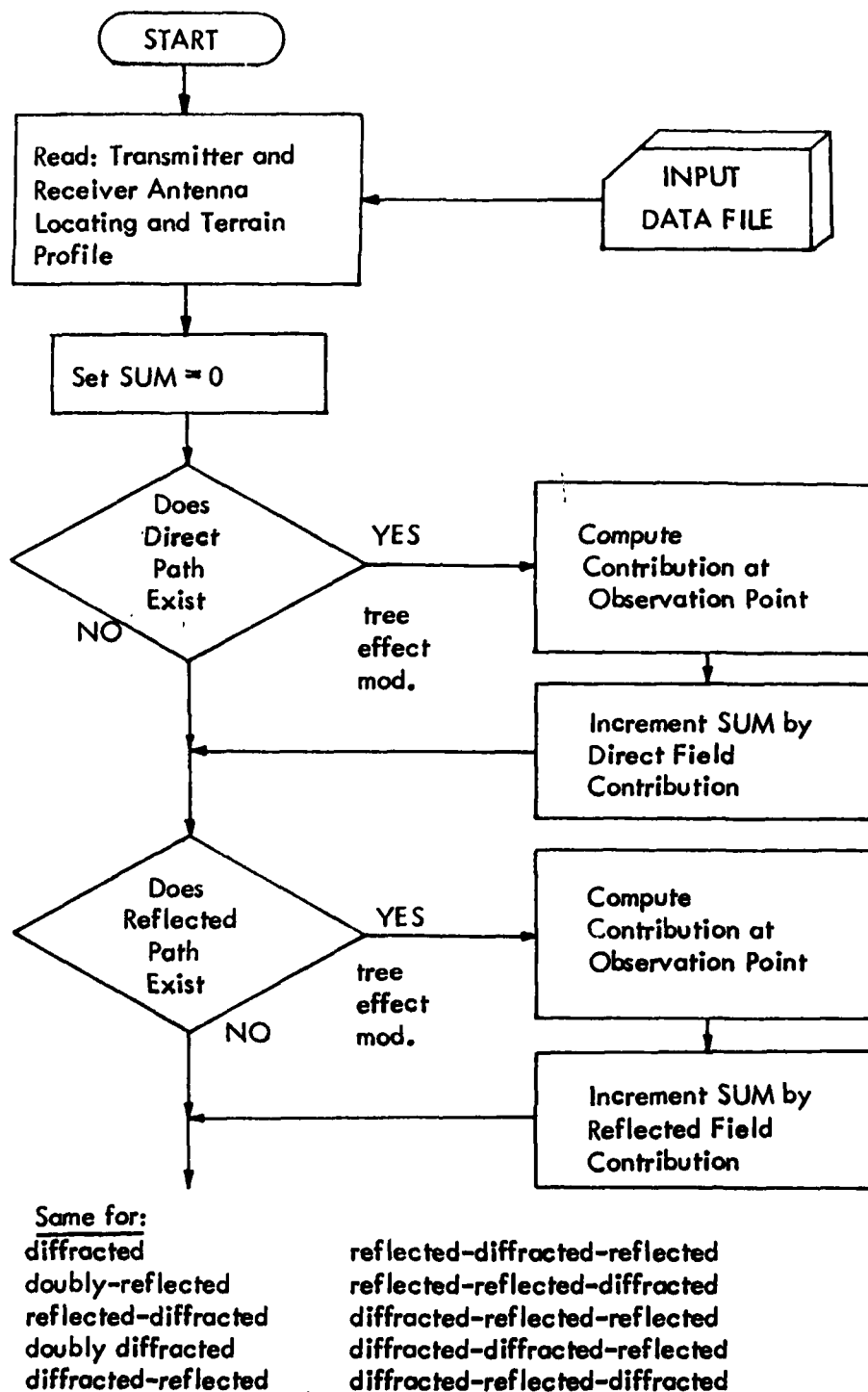oordinates of the transmitting source and observation point in addition to a contour of the intervening terrain. Subsequent program steps are to determine the existence of rays or ray combinations using the existence criteria described in Section IIF. If a ray or ray combination is found to exist, the contribution at the observation point is calculated using the 3-dimensional coordinates of all ground interaction points (e.g., reflection and diffraction points). The contribution at the observation point is calculated by multiplying the transmitted signal by a 1/R factor and a diffraction coefficient if diffraction is involved. Similarly, the phase of the signal at the observation point is determined by the propagation path distance multiplied by the phase constant plus any phase shift introduced by diffraction. The complex value representing the contribution at the observation point from a single ray or ray combination is then added to a running total (denoted as SUM in the flow chart of Figure 3-17) whereupon the contribution from the next ray or ray combination is calculated until all possible ray types are examined.

The computer model that does account for tree effects, referred to as the GTD/Forest model, uses the same input data file as described above in addition to data indicating what segments of the ground plane have tree cover. For example, consider the terrain profile of Figure 3-18, which includes a forested area. Using the terrain profile of Figure 3-18 as an example, it is worthwhile to consider the relative signal contributions at the observation point for the various ray paths. In Figure 3-18, the ground-reflected ray will not provide any significant contribution at the observation point for reasons discussed in Section IIIB. Furthermore, the diffracted ray, after passing through the lossy trees, will also not contribute much to the composite signal strength. Thus, only the direct ray is left to influence the received signal strength. Reflection from the air/forest boundary is shown to exist; however, accounting for its contribution by treating it as the other rays in Figure 3-18 are treated is inappropriate for the following reasons:

(1) forested areas may not be large compared to the first Fresnel Zone, invalidating the assumption of specular reflection, and

(2) diffractive behavior along forest boundaries is not known, and thus signal discontinuities for the crossing of such boundaries cannot be compensated for.

In order to explain how the reflection from the air/forest boundary is accounted for in the model, an important distinction must be made. As the elevation angle of the observation point approaches grazing incidence, the Fresnel Ellipse of the direct path will at some point intersect the trees. At that point, there is no true direct path signal, because only some of the energy will reach the observation point via free space; the remainder of the direct signal will arrive via an air/forest-reflected path. In addition, signals
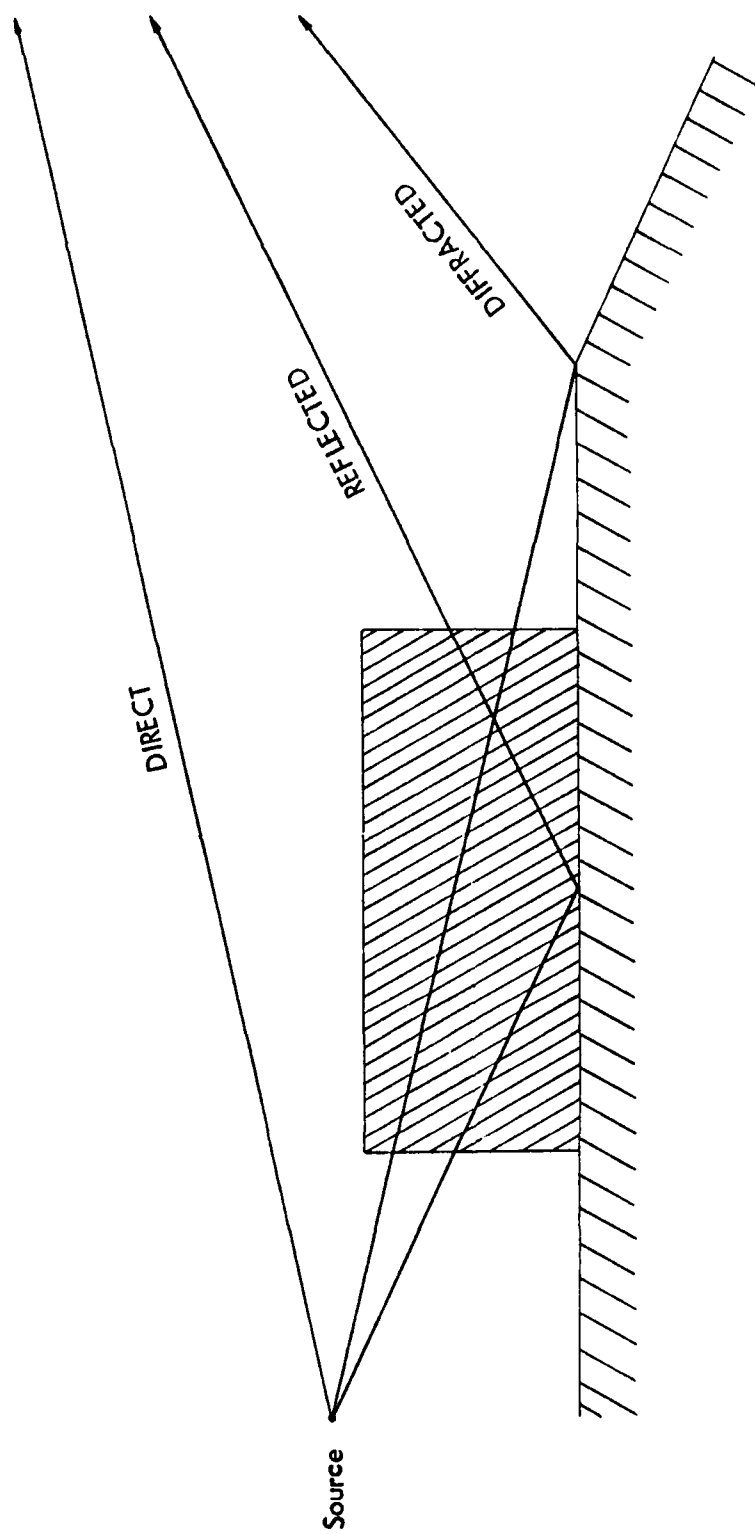
Figure 3-18. Sample Terrain Profile to Illustrate Tree Effect Modeling.

-70-

arriving along the reflected path will tend to cancel due to a reflection coefficient that will be close to -1. Thus, for near-grazing incidence, it is no longer valid to treat the direct and reflected paths separately.

The modeling approach used to account for a combined direct and reflected path is to apply a correction to the direct path proportional to the distance that the Fresnel Ellipse intersects a forested area. Application of this correction factor is illustrated in Figure 3-19 where the Fresnel Ellipse is seen to intersect a forested area for a distance d. The correction factor applied to the direct path for this case would be $e^{-\delta d}$, where δ is a real, empirically-determined variable. A value of corresponding δ to 0.69 dB/100' was determined from the data collected.

Cognizant of the above information, a detailed description of tree-effect modeling is presented. Again, using the terrain profile of Figure 3-17 as an example, a step-by-step discussion of model operation is given. The location of forested areas is read by the program along with the terrain profile data; if no forested areas are present on the profile, the program will execute exactly as shown in the flow diagram of Figure 3-17. For the forested terrain profile of Figure 3-18, the program will determine that the direct ray does exist and that a forested area is present on the profile (at this point in the program, blockage by trees is not considered). Given the existence of a ray and the presence of trees, a SUBROUTINE is called to determine the effects of the forested area. The location of this SUBROUTINE call is denoted as tree-effect modification in the flow chart in Figure 3-17. The SUBROUTINE called has access to the original terrain profile in addition to the coordinates of forested areas and points of ground interaction via a COMMON statement. With this information, the SUBROUTINE first determines if the ray is blocked by trees. If tree blockage does exist, the distance of propagation through the trees is calculated and is used to determine the losses incurred via propagation through the lossy trees. Next, the SUBROUTINE determines the distance that the ray's Fresnel Ellipse intersects the forest, as illustrated in Figure 3-19 and assigns a correction factor as described above. The SUBROUTINE then combines the two loss correction factors into a composite correction factor and returns it to the GTD program. The GTD program multiplies this correction factor by the signal contribution computed without tree effects to SUM as indicated in the flow chart. The GTD program then increments to the next ray as described earlier. The SUBROUTINE that determines tree effects does not discriminate between ray types; a diffracted ray propagating within or near the trees will be assigned the same attenuation as a direct or reflected ray.

A listing of the MAIN program and supporting SUBROUTINES used to perform the above operations is given in Appendix C along with a flow diagram indicating program sequence and data transfer. In addition, Appendix D details the input data requirements for GTD/Forest model operation.
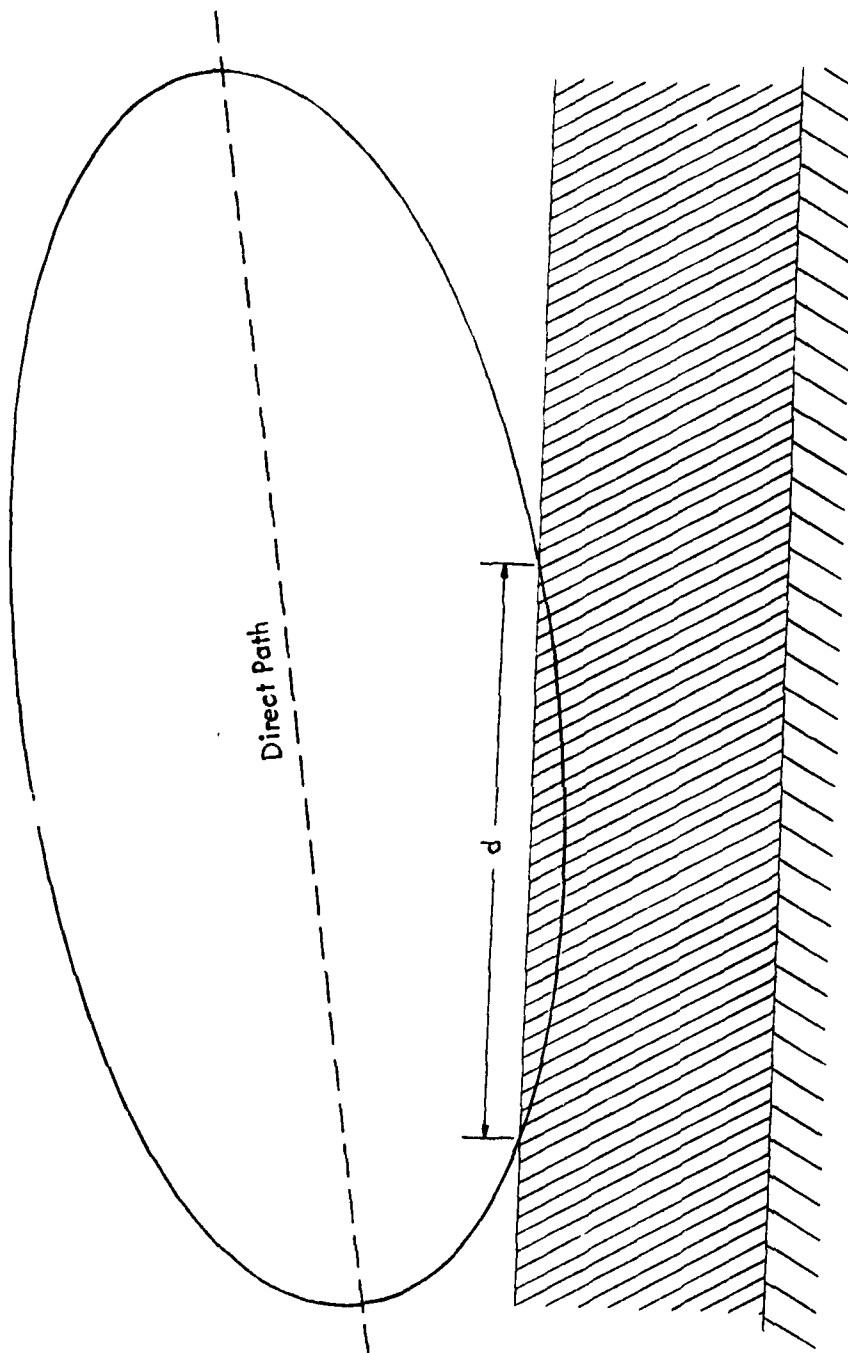
Figure 3-19. Application of the Fresnel Ellipse Correction Scheme.

An additional aspect of model operation of interest is model response to variations in input parameters. Although such an analysis is implicit in model evaluation with respect to measured data, an explicit sensitivity analysis is necessary to verify that unrealistic discontinuities do not exist in model response. Such discontinuities were observed in Keller's GTD model near shadow and reflection boundaries, as discussed in Section IIF, which lead to the development of the UTD model.

Previous work to eliminate discontinuities in the terrain scattering portion of the GTD/Forest model, as referenced in Section II, indicates that continuous operation can be assumed for that function of the model. Therefore, only model response with respect to tree-related parameters needs to be addressed.

Of particular interest for any sensitivity analysis are regions where a transition occurs between modeling regimes; for GTD modeling, such a transition occurs in the vicinity of both the shadow and reflection boundaries. For tree-effect modeling, transition occurs at the point where tree attenuation calculations begin or end with respect to a given model variable. For example, consider the situation where the propagation path between aircraft and ground-based antenna is such that the Fresnel Ellipse of that propagation path intersects trees. Transition occurs when either aircraft altitude, tree height, or antenna height are varied so as to position the Fresnel Ellipse above the trees. For changes in the three variables given above, a continuous model response is necessary to be consistent with observed response.

Figure 3-20 plots the GTD/Forest model response to variations in antenna height for flat, level terrain forested with continuous, 38' trees (an equivalent analysis could have been performed by varying aircraft elevation). The modeled airborne receiver is at 20 nm, 3000' altitude; simulated parameters were chosen to represent conditions for which measured data are available. These measured data were obtained at the FAATC experimental RCAG site, and are presented in Section V. Referring to Figure 3-20, it is seen that signal strength increases monotonically and continuously with ground-based antenna height until the antenna height exceeds 59', whereupon signal strength becomes invarient to antenna height. This type of behavior is consistent with the theory of tree attenuation posed in Section III and with observations. Further, points at which comparisons with measured data can be made to show close agreement. Based upon the above information, it is concluded that tree-effect modeling, as described here, is not degraded by unrealistic, discontinuous response.

Another potential cause of unrealistic discontinuities in model response is the quantization of terrain profiles into 5° increments. With this quantization, the model determines signal strength based upon terrain data that is described by a single contour every 5° in azimuth. An obvious shortcoming of this terrain representation is that, for reasons described in this section, wave interactions with
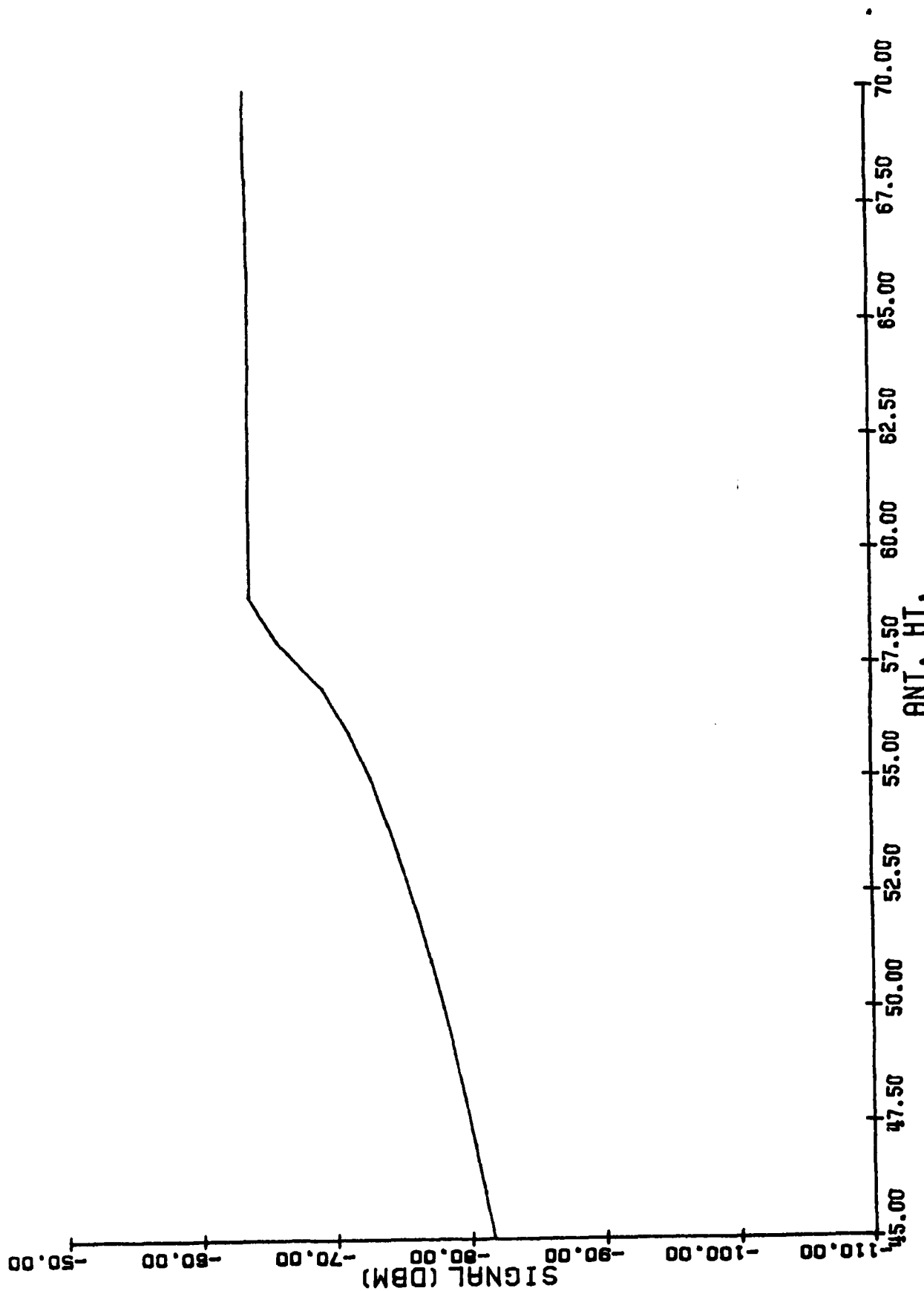
Figure 3-20. GTD/Forest Model Prediction of Signal Strength Changes Resulting from Varying the Ground-Based Antenna Height in the Presence of 38' Trees When the Aircraft Is at 20 NM, 3000' Altitude; Transmitter Power 4 Watts.

the ground occur over an area, defined by Fresnel Zones, rather than the single-point interactions assumed by the model. Consequently, signal strength variations between adjacent terrain profiles calculated by the model tend to be greater than those measured. The GTD/Forest model compensates for these unrealistically-large variations by averaging raw modeled signal strength over three 5° sectors to generate an estimated signal strength for a single azimuth sector. For example, the model estimate for the 5° azimuth sector is the average value of the signal strength calculated for the 0°, 5° and 10° azimuth sectors. The theoretical rationale for the above averaging process is that the minor axis of the first Fresnel Zone covers an azimuth interval of several degrees for propagation paths of interest, and averaging adjacent profile signal strength calculations enables this factor to be included into the final estimate. The empirical rationale for averaging is that closer agreement with measured data is realized with averaging than is realized without averaging.

The modeling technique described above represents engineering approximations to a complex modeling problem. The assumptions made in developing those approximations have clearly ignored some known phenomena, such as refraction; however, the trends predicted by those approximations are in the same direction as theory would indicate. Most importantly, comparisons of measured data with predictions made using the above modeling approximations show outstanding agreement.

IV. SIGNAL STRENGTH MEASUREMENT EQUIPMENT, CALIBRATION, AND DATA COLLECTION

A. Introduction. The collection and analysis of measured signal strength data is of paramount importance to the work presented in this report, for without such data no realistic evaluation of a communication coverage model could be made. Accordingly, much effort has been dedicated to a thorough study of signal strength measurements and factors affecting those measurements. The results of the study presented here are well documented and repeatable signal strength data from several sites which give a clear indication as to the effects of local obstructions, trees, and terrain scattering.

Ground-air signal strength data have been collected prior to the measurement effort reported here, although all such data obtained have been either for conditions outside of the range of interest, poorly-documented, or, of insufficient resolution to afford meaningful analysis. For example, the FAA routinely measures signal strength from RCAG sites for certification purposes, although flight records from these measurements seldom contain information relating signal strength values to aircraft position. Thus the data presented in this section represents the most accurate, well-documented signal strength data available to date for the frequency range and distances under consideration.

Signal strength data were mostly collected during constant-altitude orbits around a site with some data collected during flights along radials to the site. Minimum enrouted altitudes were typically used for these measurements to represent worst-case signal strength conditions. Data from orbital flights represent signal strength as a function of azimuth, and, as a function of distance for radial flights. The radius for orbital flights ranged from 8 to 40 nm and was determined for a particular site based upon conditions and the phenomenon being investigated. All of the measurements reported here were made by either Ohio University or the FAA Technical Center (FAATC), using three different type aircraft, a Convair 580, a Bonanza V-35, and a Piper Cherokee. All three proved capable of providing repeatable measurements and, in the one instance where a comparison was made, showed good agreement for measurements taken with two different aircraft at the same site. Measurement degradation due to aircraft antenna lobing effects during roll or pitch maneuvers was not found to be significant for the aircraft during orbital flights.

The FAA requirements for minumum signal strength values at the edge of a coverage area are specified in terms of power available from a matched dipole delivered to a 50 Ohm load. Such a power value is typically expressed in dBm which is a measure of power referenced to one miliwatt given in decibels; this power value is directly proportional to the square of the incident electric field. Data were collected in dBm to be consistent with FAA specifications and for convenience in equipment calibration due to most signal standards being calibrated in dBm. Therefore, all measured data presented in

this section are expressed in dBm. As stated previously, minimum permissable signal power at the edge of a coverage area is -87 dBm.

B. Measurement Equipment and Calibration. FAATC signal strength data were collected using the Convair 580 aircraft pictured in Figure 4-1. The measurement antenna, a Collins blade antenna, is mounted on the underside of the aircraft as shown in Figure 4-2. The intensity of the incoming signal is determined from the AGC voltage of calibrated AN/GRR-23(v)10 receivers pictured in Figure 4-3. The AGC voltage is recorded on Hewlett-Packard Model 9280 strip-chart recorders, also pictured in Figure 4-3. The signal standard used for calibration is a Hewlett Packard Model 86408 signal generator. As will be discussed later, some measurements were performed with the receiver in the aircraft while others were performed with a transmitter in the aircraft and the receiving equipment on the ground.

Ohio University measurements were performed using a Piper Cherokee, pictured in Figure 4-4, and a Bonanza V-35, pictured in Figure 4-5. Both aircraft use Antenna Specialists Model AV-529 vertical whip antennas, and the Piper Cherokee uses a Collins blade antenna as a second antenna. Specific tests to measure the effects of antenna lobing due to roll and pitch for the antennas pictured in Figures 4-4 and 4-5 indicate that less than a decibel variation will result from + 5° roll, and almost no variation for typical pitch angles. It should be noted that work by FAATC has shown that significant lobing due to roll and pitch can occur with certain antenna placements [46]. Hence, the small lobing effects reported here cannot be assumed for every aircraft, but rather must be measured in each case. The Ohio University measurements were performed with the transmitter in the aircraft and the receiving equipment on the ground. The receiver employed is the same as is used by FAATC; a Heath-Schlumberger Model SR-206 strip-chart recorder is used to record the receiver AGC output voltage. In order to achieve maximum resolution on the chart recorder, a calibration unit, shown schematically in Figure 4-6, is used to offset the recorder and vary the magnitude of the AGC voltage. A Wavetek Model 3000 signal generator is used as a signal standard.

Calibration for both Ohio University and FAATC measurement equipment are performed in the same manner as is described below. Before and after any measurement sequence, such as an orbital or radial flight, equipment response to known signal strength values, as observed on the strip chart recorders, is checked. The known signal strength is provided by the signal standards listed above and is input to the receiver at the antenna input during the calibration procedure. The signal standard output power is then varied over the range of values expected to be received during the measurement. Typical ranges are from -50 to -100 dBm. Sample chart recordings obtained during calibration are shown in Figures 4-7 and 4-8 for FAATC and Ohio University equipment. Non-linearities in receiver AGC response with respect to input power is evident in Figures 4-7 and 4-8; these non-linearities would prevent meaningful linear extrapolation of inter-

-77-
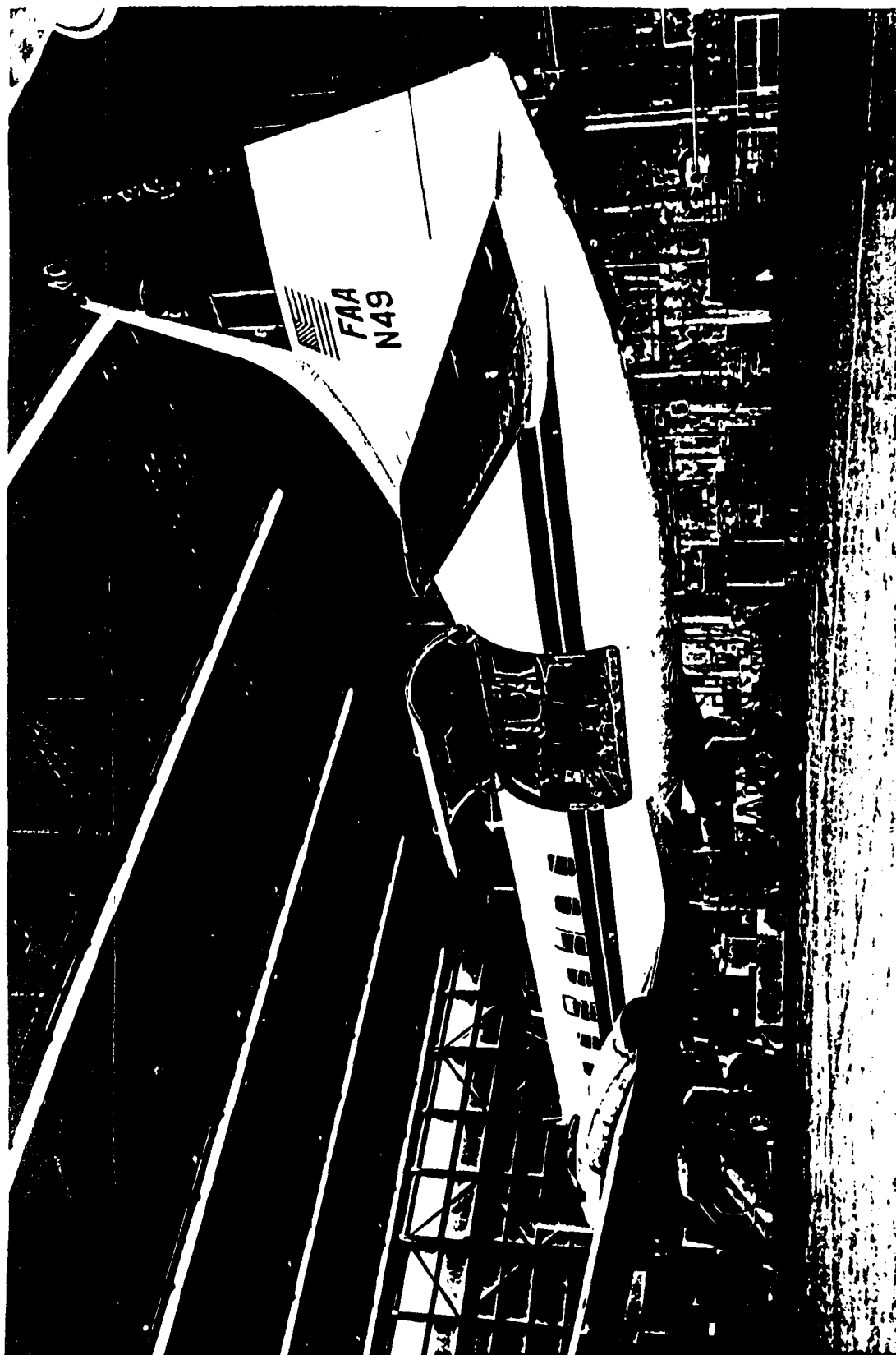
Figure 4-1. FAATC Convair 580 Signal Strength Measurement Aircraft.

Figure 4-2. Measurement Antenna on FAATC Convair 580.
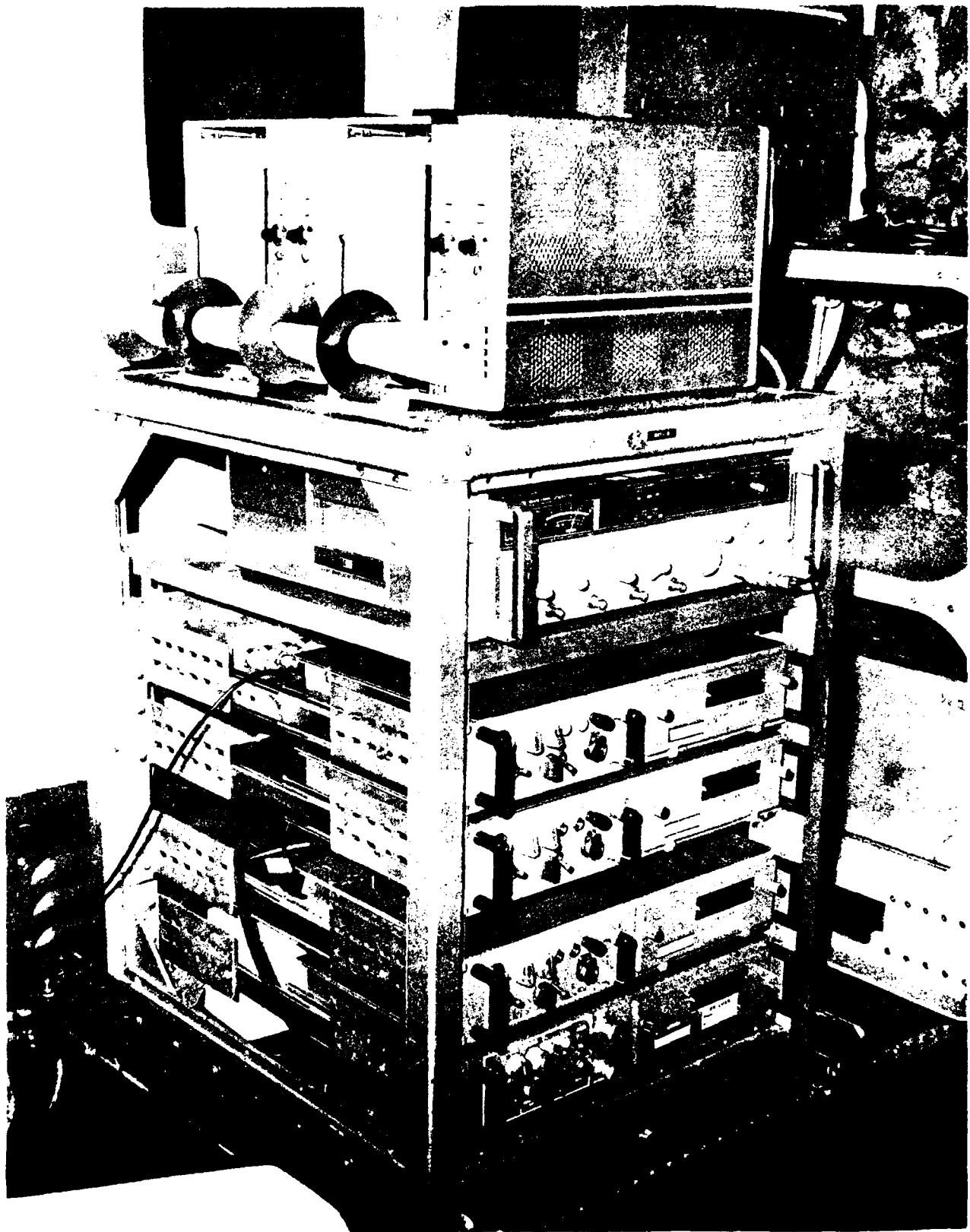
Figure 4-3. FAATC Signal Strength Measurement Receivers, Strip Chart Recorders, and Signal Standard.
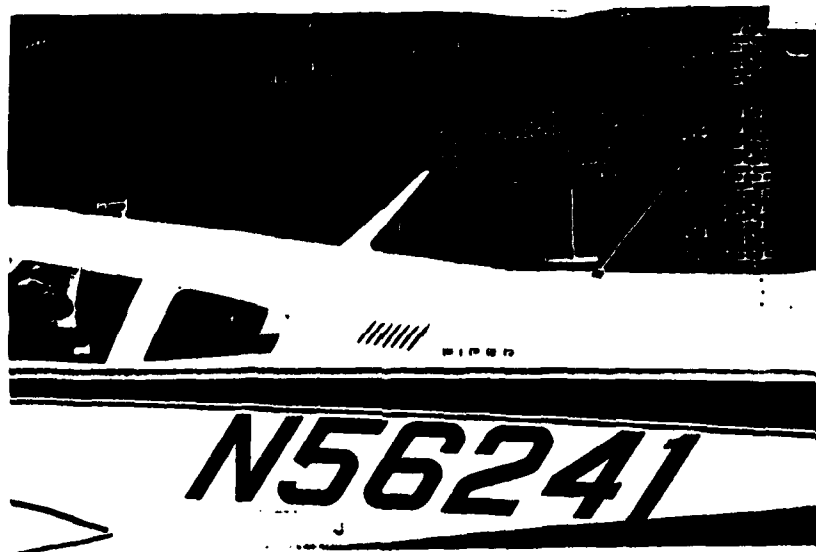
Figure 4-4. Piper Cherokee Used by Ohio University for Signal Strength Measurements.
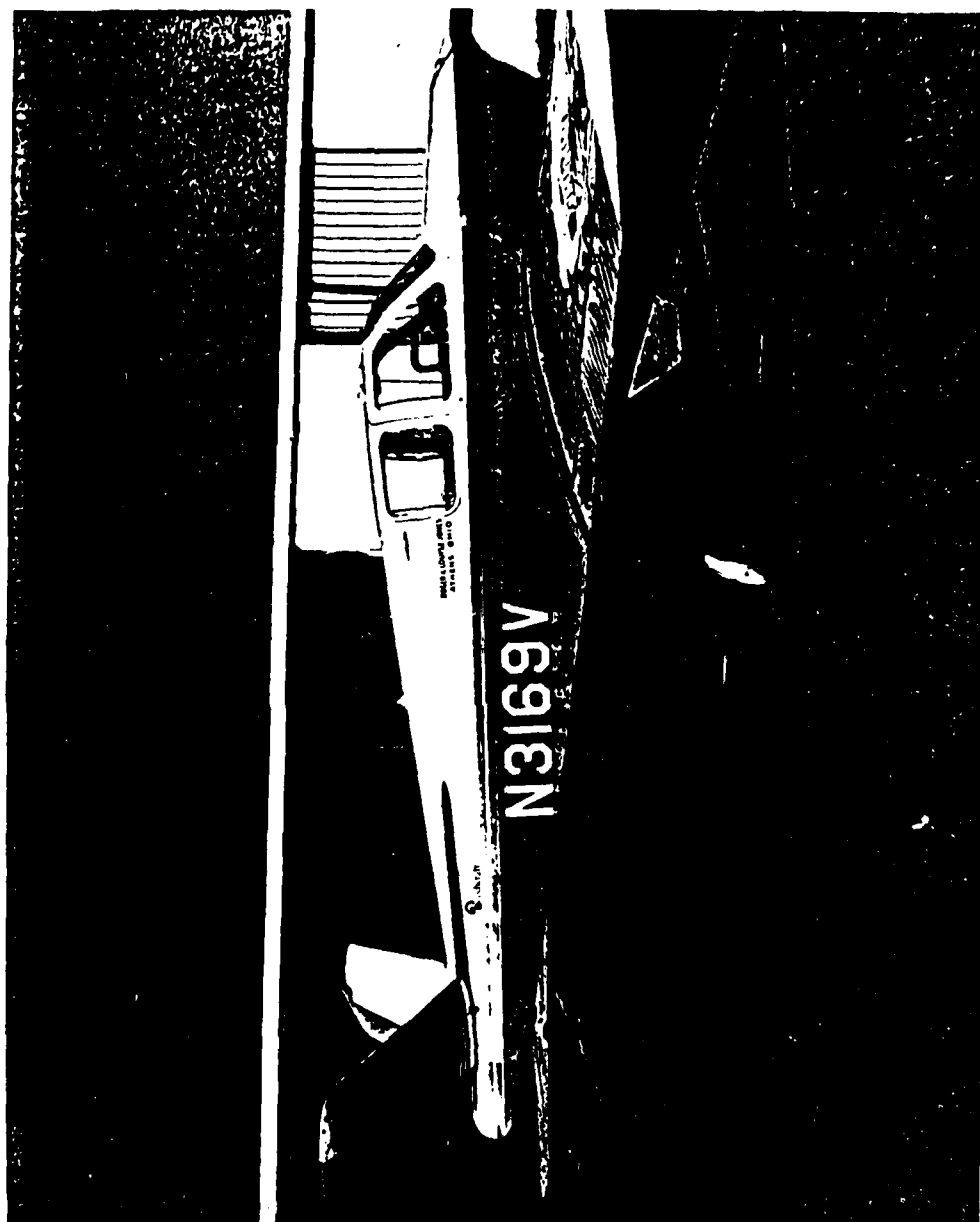
Figure 4-5. Bonanza V-35 Used by Ohio University for Signal Strength Measurements.
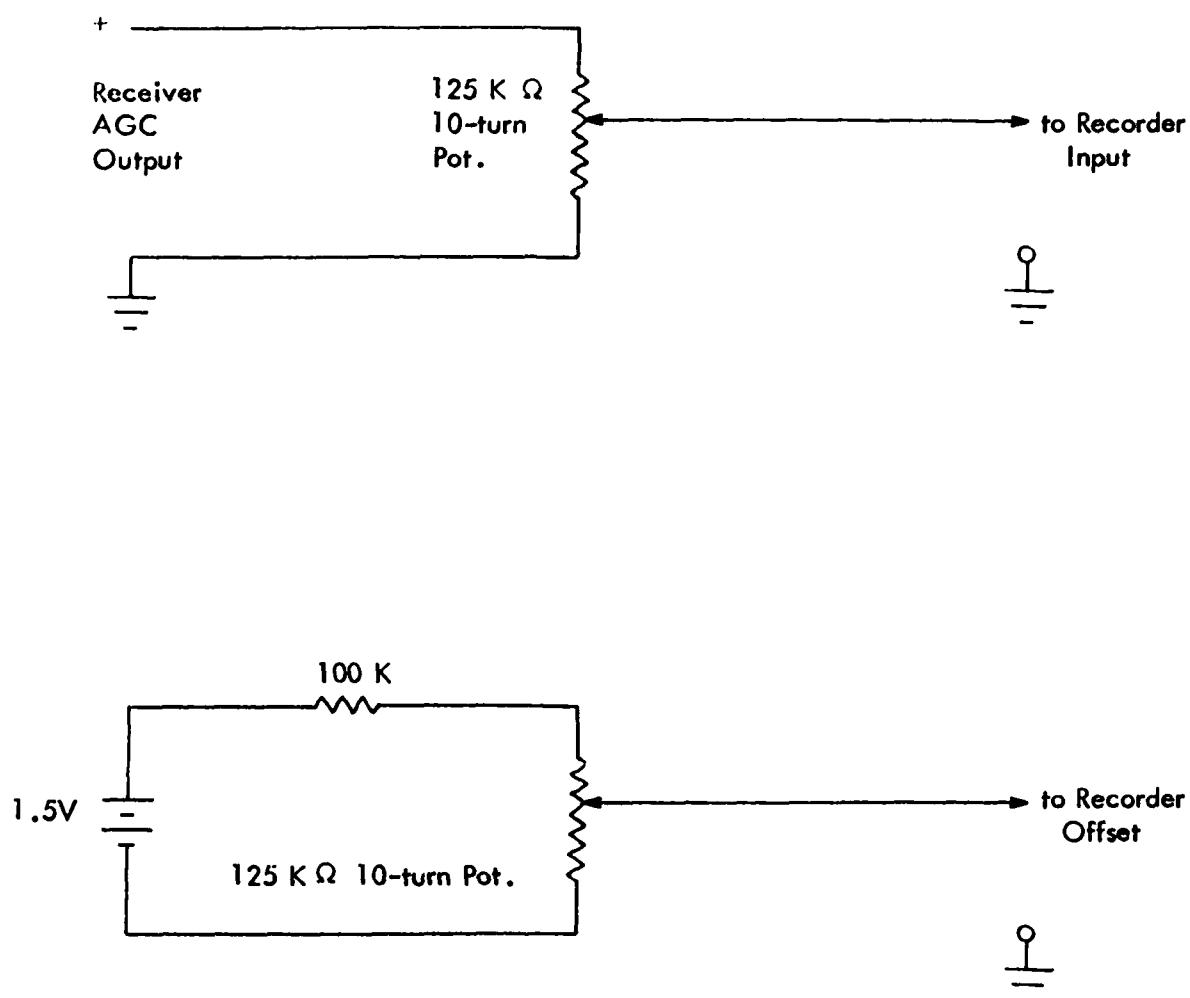
Figure 4-6.   Calibration Unit Used by Ohio University to Condition Receiver AGC and
Offset Recorder so as to Obtain Maximum Resolution.
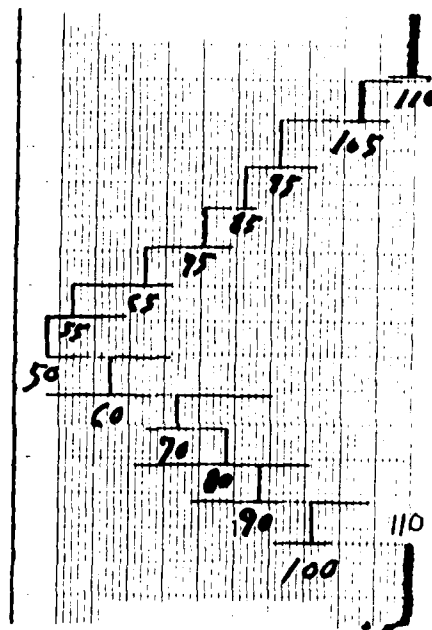
Figure 4-7. Calibration Values for FAATC Data. (Values shown represent input signal power in dBm.)
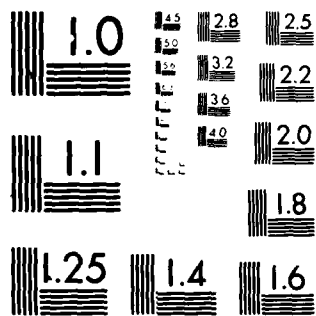
MICROCOPY RESOLUTION TEST CHART

NATIONAL BUREAU OF STANDARDS-1963-A
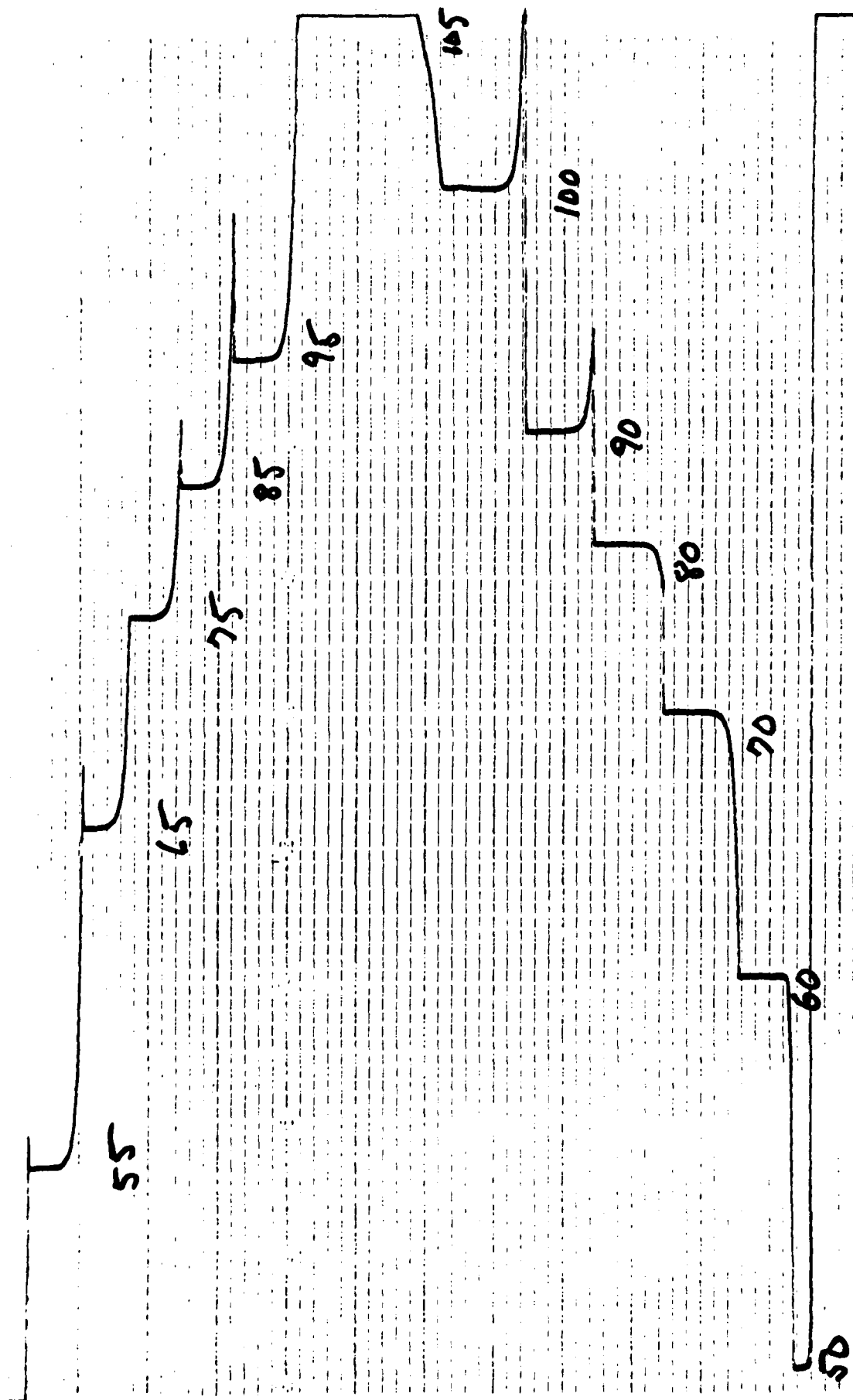
Figure 4-8. Calibration Values for Ohio University Data. (Values shown represent input signal power in dBm.)

mediate values if the interval between calibration points were too large. However, with calibration points available every 5 dBm as shown in Figures 4-7 and 4-8, resolution within one dBm has been routinely obtained. As stated, calibration was performed both before and after a measurement sequence, thus providing information on the equipment drift that had occurred during the measurement. Although such drift was typically small, on the order of a decibel, the effects of drift were minimized by graphically averaging post and pre-measurement calibration values for use in data reduction.

C. Data Reduction. During data collection flights, event marks are placed on flight records concurrent with passage over ground fixes. Typical ground fixes include highways, rivers, towns, and power lines and are used to correlate signal strength values with aircraft position. Actual position is determined from ground fixes using aeronautical sectional charts. To illustrate the information contained on a flight record, consider a portion of a flight record obtained during an orbital flight around a temporary site at Washington Court House, Ohio shown in Figure 4-9. The circled number 11, referring to Figure 4-9, indicates passage over the eleventh ground fix, which is a readily-identifiable highway at 160° azimuth to the site. The previous, or tenth, event mark (not shown) provides another azimuth reference angle; using these two known azimuth angles, intermediate angles are estimated assuming constant aircraft speed. As seen in Figure 4-9, azimuth angles are calculated in 5° increments, and the portion of the flight record shown covers the azimuth sector of 140° to 195°. Angle values given represent azimuth with respect to true north. The signal strength scale shown to the right of the flight record in Figure 4-9 was derived from the calibration data of Figure 4-8.

The high degree of noise evident in the signal strength trace of Figure 4-9 is characteristic of the noise observed during all of the airborne measurements reported here. The separation of noise from actual signal strength variations is not readily apparent by analysis of a single measurement. However, a side-by-side comparison of two or more measurements of the same site show noise variations to be uncorrelated while true signal strength trends tend to be correlated from measurement to measurement. A general conclusion reached sub-sequent to the reduction of a large body of airborne data is that variations within a 5° sector typically do not correlate from measurement to measurement, thus suggesting that filtering, or averaging the raw data over a 5° sector will result in data representative of actual signal strength variations. The reduced data presented in this section have been derived from raw airborne data using such an averaging process. To illustrate how the data reduction process is accomplished, again refer to the raw signal strength data of Figure 4-9. As was stated earlier, azimuth angles are available every 5° and are identified on the strip chart as vertical marks as seen in Figure 4-9. The horizontal line at each azimuth is an estimate of the average signal strength value within a + 2.5° sector. Thus, all data collected during a measurement are considered during data reduction,
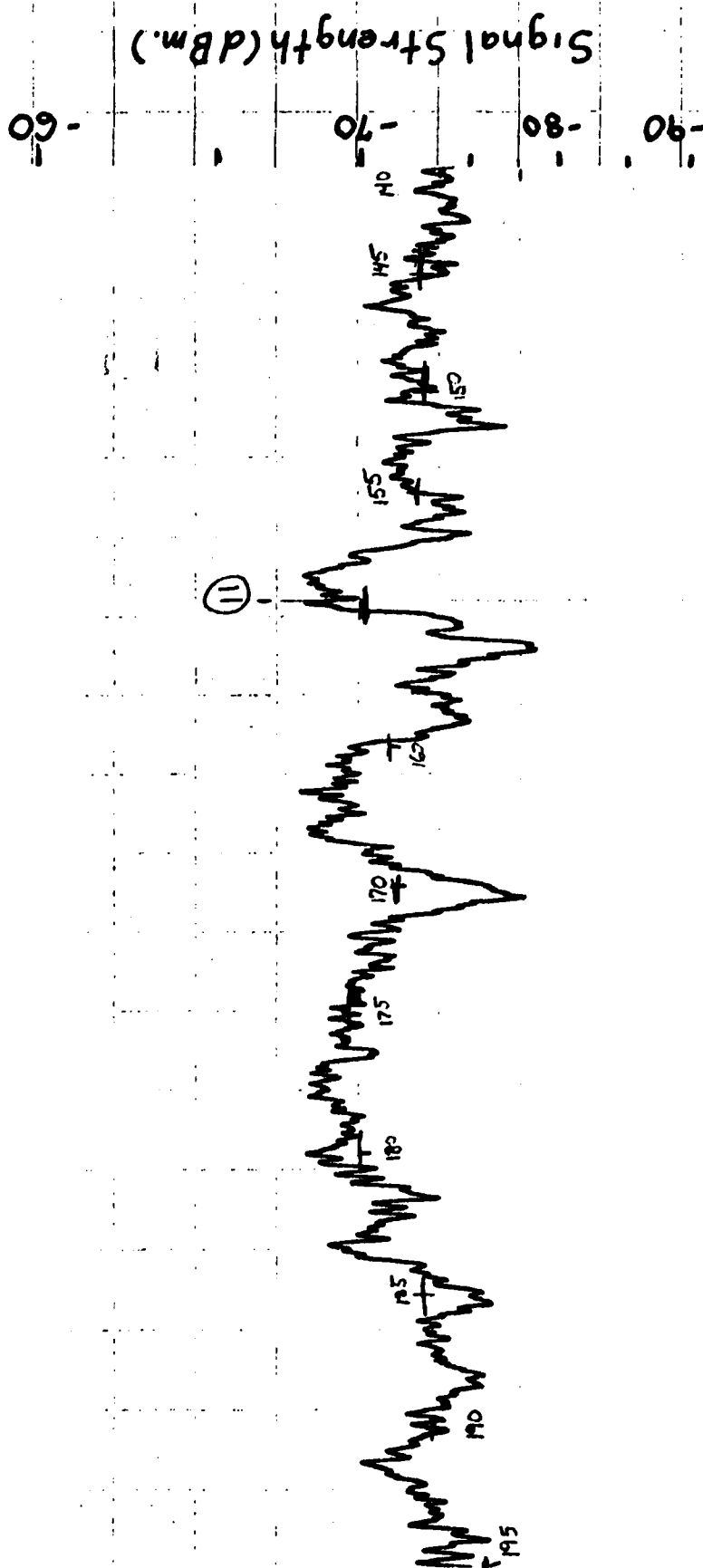
Figure 4-9. Portion of Flight Record Obtained During Signal Strength Measurements at Washington Court House, Ohio.

rather than only recording signal strength at specific azimuth values. The final result of data reduction is a signal strength value every 5° representing an average of raw data over a 5° sector for an orbital measurement; a similar result is obtained for radial flights as will be discussed later. It should be noted that the averaging process described above was performed several times on one set of raw data to determine the repeatability of the process. The results of that test showed a maximum deviation of one decibel, which occurred 3 times over an entire orbit. The data presented in the following section show that an uncertainty of one decibel is insignificant compared to other errors.

Aircraft navigation during measurements was accomplished mainly by pilotage, where ground fixes are used to determine position and desired heading. Cross-checks were occasionally provided by VOR fixes, although such fixes were considered secondary to ground references. Measurements taken at the FAATC experimental RCAG facility in Atlantic City, New Jersey were supported by data supplied by the FAATC discrete address beacon system (DABS). Although these measurements were collected using pilotage for navigation, DABS simultaneously recorded the aircraft position at periodic time intervals. During data reduction, DABS fixes were used to determine aircraft position at particular time fixes, which were also recorded on the flight records. A plot of a 20 nm orbital flight made by Ohio University in a Bonanza V-35, as recorded by DABS, is presented in Figure 4-10. The outer ring in Figure 4-10 is a 25 nm reference centered at the DABS site which is offset from the RCAG site being measured accounting for the offset in the aircraft orbit. The obvious deviation from the orbit in the North-East sector was made to avoid a restricted area. Such a deviation in course is not considered to significantly degrade the data due to the predominantly inverse relationship of signal strength to distance.

Figure 4-10.   DABS Plot of Orbit Made by Ohio University During a Signal
Strength Measurement at the FAA Technical Center.

V. MEASURED AND MODELED DATA COMPARISONS

A. Introduction. Using techniques described in the previous section, accurate and repeatable signal strength records have been collected. These measured data, in addition to data provided by some of the computer models discussed previously, are presented in this section to provide a meaningful evaluation of model performance.

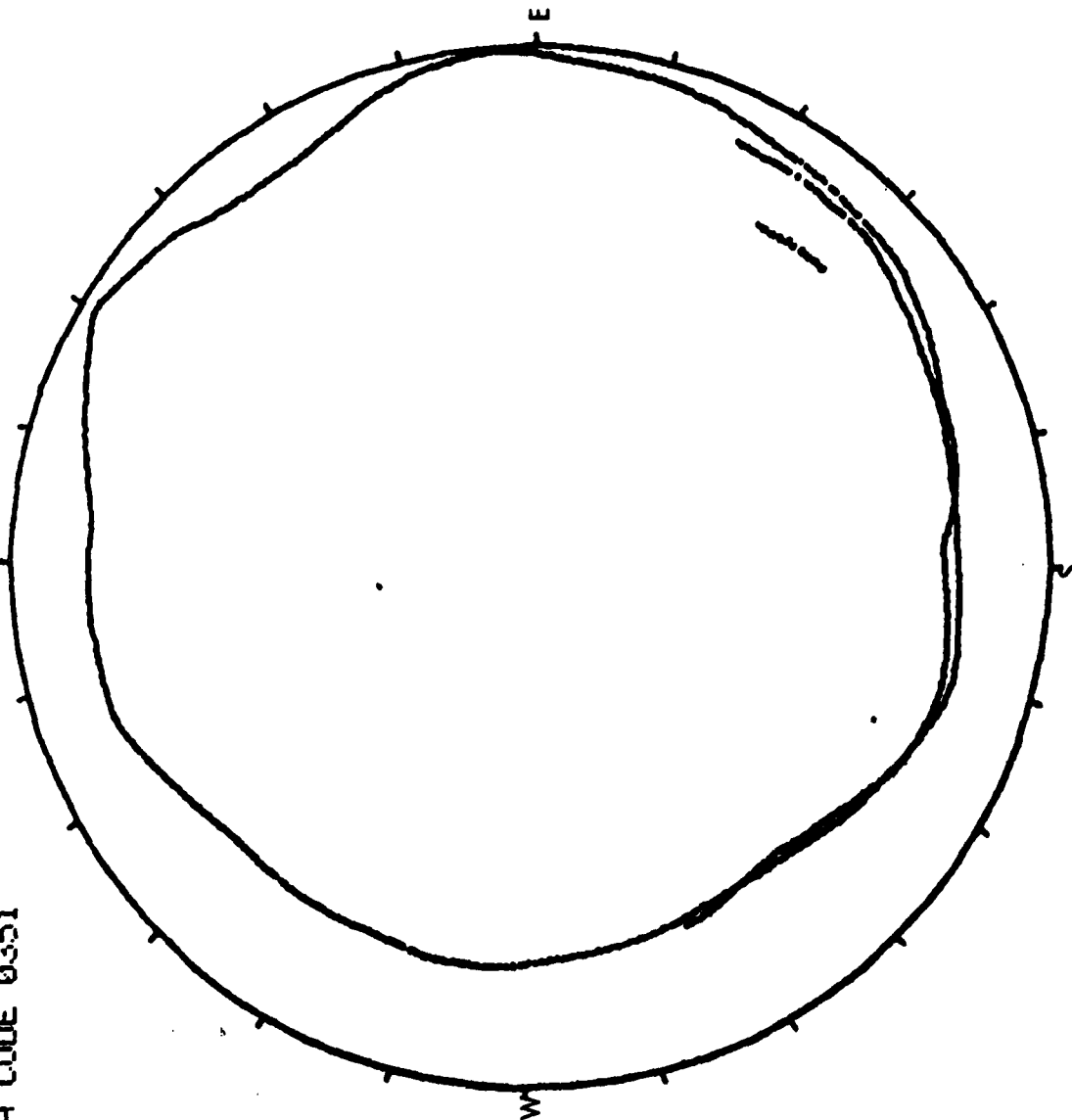Prior to the research presented here, which began in September 1978, few data were available that provided insight into the collection of airborne signal strength data or into factors that influence propagation for short-range, air-ground propagation paths. Consequently, the first phase of data collection was aimed at providing an understanding of airborne signal strength measurements in general, in addition to isolating the predominant factors affecting propagation, and hence signal strength. Pursuant to that objective, signal strength data were collected at two sites, Charlottesville, Virginia and South-Raleigh, North Carolina, for the purpose of determining measurement repeatability and the effects of scattering by parasitic elements on the antenna tower. Two major findings from those preliminary measurements were that: (1) repeatable signal strength data could be collected, and (2) scattering due to parasitic elements on the tower could be ignored. In addition, it was found that appreciable variations in measured signal strengh were observed in areas where such variation would not be expected based upon existing propagation theory. This observation prompted further measurements to be performed to prove or disprove hypotheses that had been formed based upon the limited data available. Accordingly, data collection was performed at the FAATC Experimental RCAG Site to enable an evaluation of propagation factors not caused by rough terrain (the terrain in the vicinity of that site is essentially flat). However, the results of those measurements again showed appreciable variation in signal strength for a constant-radius orbital flight, variations that only appeared to correlate with areas of tree cover. Based upon this discovery a computer model was developed, implemented as a modification to a GTD terrain scattering model, that considered tree effects in estimating signal strength. Results from this model showed excellent agreement with the FAATC site measured data, although further validation was considered necessary before any conclusions could be formulated regarding model performance. Consequently, a data collection effort was performed at a temporary site installed at Washington Court House, Ohio, a generally flat site with well-defined forest boundaries. Measured data from that site provided new information about the electrical properties of trees at VHF enabling the model to be upgraded; this upgraded version of the model, called the GTD/Forest model, provided output data in close agreement with the FAATC site and the Washington Court House site measured data. In order to evaluate the GTD/Forest model's prediction capability, model results were obtained for a second site at Washington Court House prior to data collection. Because measured and model-predicted data showed close agreement, it was concluded that the capability to predict tree effects had been established.

Accurate modeling results are expected at sites where terrain elevation and forest boundaries are well defined and slowly varying within the first Fresnel Zone. The site types selected to verify tree attenuation theory met these criteria, and consequently close agreement between measured and modeled data was realized. However, many sites that may be of interest for modeling purposes may not be well defined or well behaved in terms of terrain or tree cover. To establish a bound on modeling error, two sites, South Raleigh, North Carolina and Albany, Ohio, were selected that showed substantial terrain elevation variation within the first Fresnel Zone in addition to some areas of sparese, poorly-defined tree cover. Modeling error was further exacerbated due to the use of terrain elevation data that were quantized to 10-foot intervals in one case, and 20-foot intervals in the other. Such terrain elevation quantization results from the use of readily-available, low-cost, Geological Survey topographical maps to obtain terrain elevation data. Some improvement in modeling accuracy may result by obtaining terrain data with a smaller quantization interval, however, the cost of obtaining such data is usually prohibitively high. For this reason, and because Geological Survey data are available for the entire continental United States, the only terrain data used for the modeling work presented in this section were reduced from Geological Survey maps. It should be noted however, that large quantization intervals will not degrade modeling accuracy at sites where terrain elevation variations are reasonably linear and monotonic between contour lines. The work with worst-case type sites showed the expected result that as the factors affecting propagation become less well defined, modeling accuracy declines.

Previous empirical validation of the GTD model used in this study had been performed only with horizontal polarization; hence, an essential facet of the evaluation phase of this effort has been to demonstrate proper operation of the GTD model for vertical polarization. To meet this objective, a site was selected in Athens, Ohio that contained a well-defined ridge. Partial orbits were flown with respect to that ridge, and at several different altitudes, to provide complete documentation on diffractive effects above, near, and below shadow boundaries. Predictions from the GTD/Forest model, made prior to data collection, showed excellent agreement with measured data. Thus, proper operation of the GTD model for vertical polarization is verified.

Computer model outputs presented in this chapter were obtained from the thin-wire model, discussed in Section IIC, the ITS Longley-Rice model, discussed in Section IID, and the GTD/Forest model discussed in Section IIIE. Signal strength estimates from all three models were not obtained for each site due to insensitivity of some of the models to certain site parameters. For instance, the ITS model does not calculate tree effects, and responds only to rather large variations in terrain elevation. Thus, the ITS model will predict an isotropic radiation pattern for relatively flat sites such as the FAATC experimental RCAG, the South Raleigh RCAG, and the Washington Court House site.

The data reported here are categorized according to site rather than by model. Thus, each site investigated is discussed with regards to salient characteristics suspected of affecting propagation, followed by a presentation of measured and modeled data.
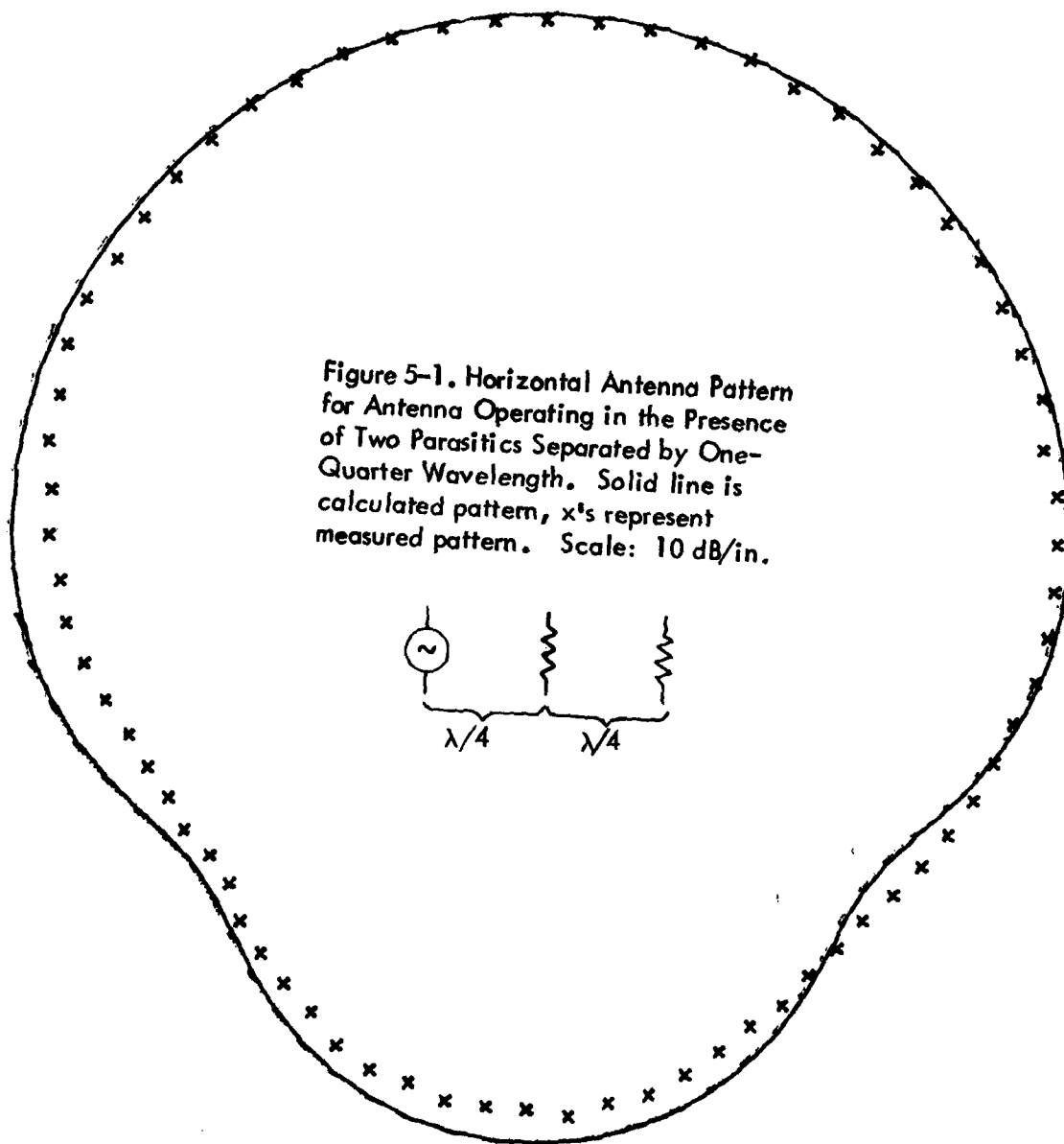
B. Discussion of Data.

1. FAATC Antenna Pattern Range. One of the first phenomena investigated at Ohio University relating to propagation prediction was scattering from parasitic structures. Accordingly, the thin-wire scattering model was implemented to study scattering effects. To insure that this scattering model was operating properly, a simple radiator-scatter configuration was simulated and compared with respect to measured data collected at the FAATC antenna pattern range. The results of this effort are plotted in Figure 5-1 showing both measured and modeled data for an antenna radiating in the presence of two loaded parasitic elements separated by a quarter wavelength as shown in the figure. Although the configuration shown is not typical of an RCAG tower configuration, the data obtained do provide insight into model accuracy. Referring to Figure 5-1, it is seen that thin-wire data match measured data quite closely. The slight asymmetry in the measured data indicates errors in data collection, because the symmetrical radiator-scatter configuration should produce a perfectly symmetrical radiation pattern.

Once proper operation of the thin-wire model had been determined, practical RCAG tower configurations were modeled. Calculated antenna pattern distortion for typical RCAG tower configurations are presented in Figure 5-2. As seen in this figure, calculated distortion for standard separations is at most in the neighborhood of 3 decibels. More detailed modeling, in which nearby towers, tower railing, and guy wires are included, shows nearly the same results as indicated in Figure 5-2. Signal strength data were collected to measure explicitly some of the configurations shown in Figure 5-2; these data, which are presented in Section VB4, indicate that thin-wire model results are realistic.

Because of the small degree of antenna pattern distortion measured and calculated for standard RCAG antenna configurations, it was decided that further study into thin-wire modeling be aborted for general site modeling. However, the thin-wire model should be considered as a viable tool for calculating scattering effects in cases where parasitic structures are suspected of causing deficient communications coverage.

2. Charlottesville, Virginia. A portion of a VFR sectional showing Charlottesville and vicinity is shown in Figure 5-3. This site was the first to be investigated and was selected because of its varied terrain, mountains to the West and plains to the East. A picture of the transmitting antenna with respect to local obstructions is pictured in Figure 5-4; an enlarged picture of the transmitting antenna is shown in Figure 5-5. The Swastika antenna pictured in

Figure 5-1. Horizontal Antenna Pattern
for Antenna Operating in the Presence
of Two Parasitics Separated by One-
Quarter Wavelength. Solid line is
calculated pattern, x's represent
measured pattern. Scale: 10 dB/in.

1.5 dB Distortion

2.5 dB Distortion

3.2 dB Distortion

1.7 dB Distortion

1.0 dB Distortion
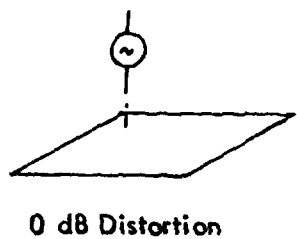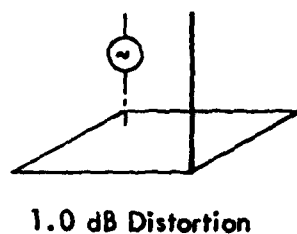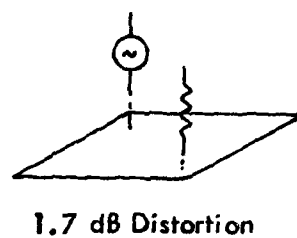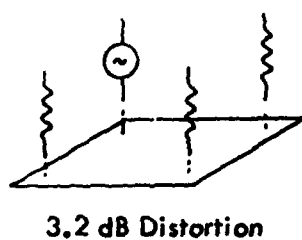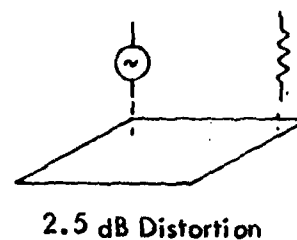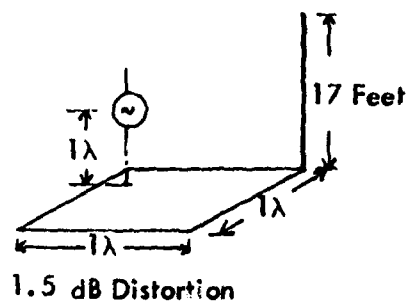
0 dB Distortion

Figure 5-2. Predicted Antenna Pattern Distortion for Various
Antenna-Lightning Rod Configurations Operating
Above a Typical Ground Plane.
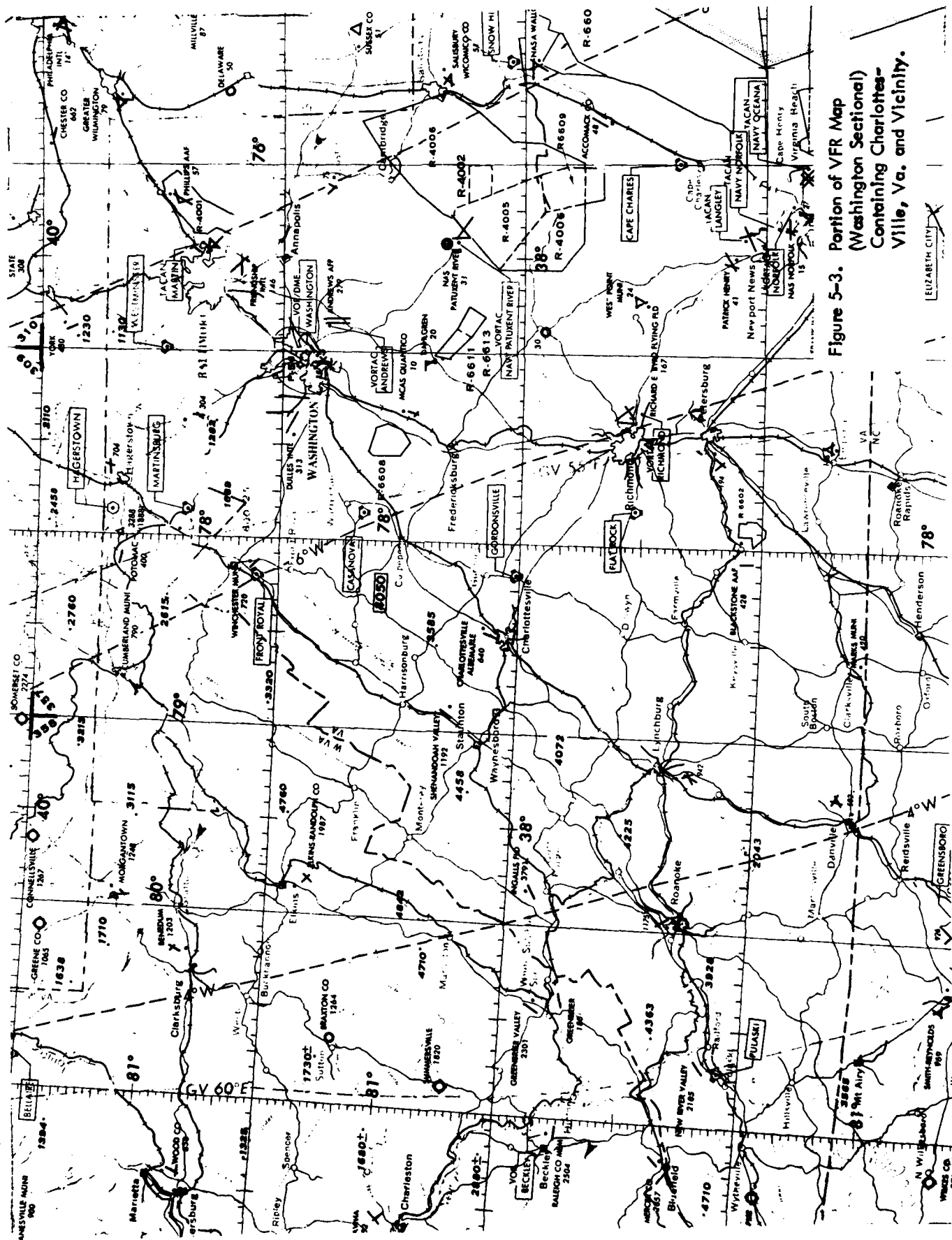
Figure 5-3. Portion of VFR Map (Washington Sectional) Containing Charlottesville, Va. and Vicinity.
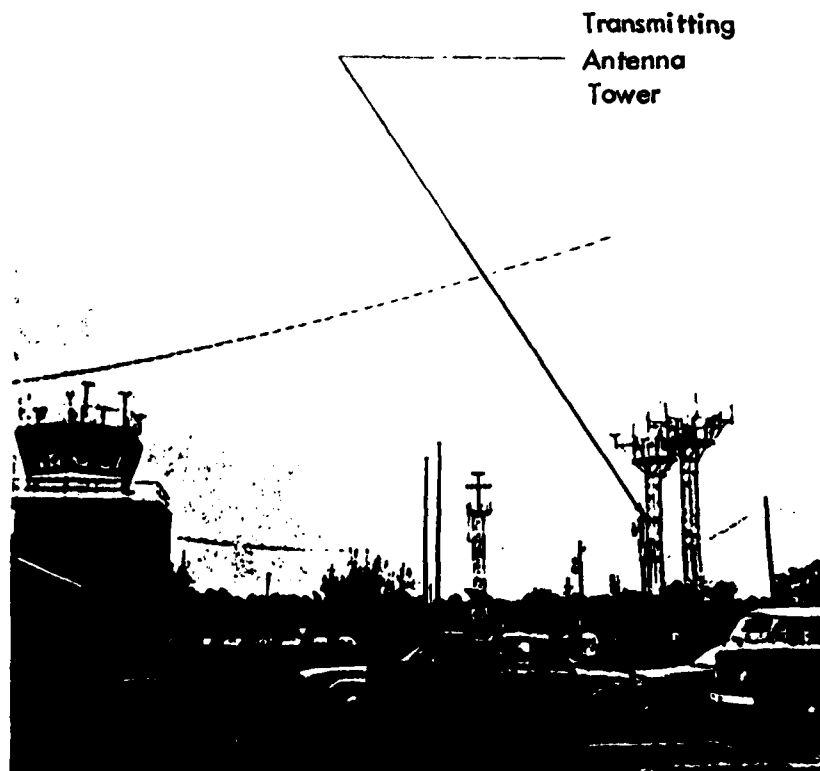
Figure 5-4. Picture of Transmitter Antenna Tower at Charlottesville, Virginia

Transmitting Antenna
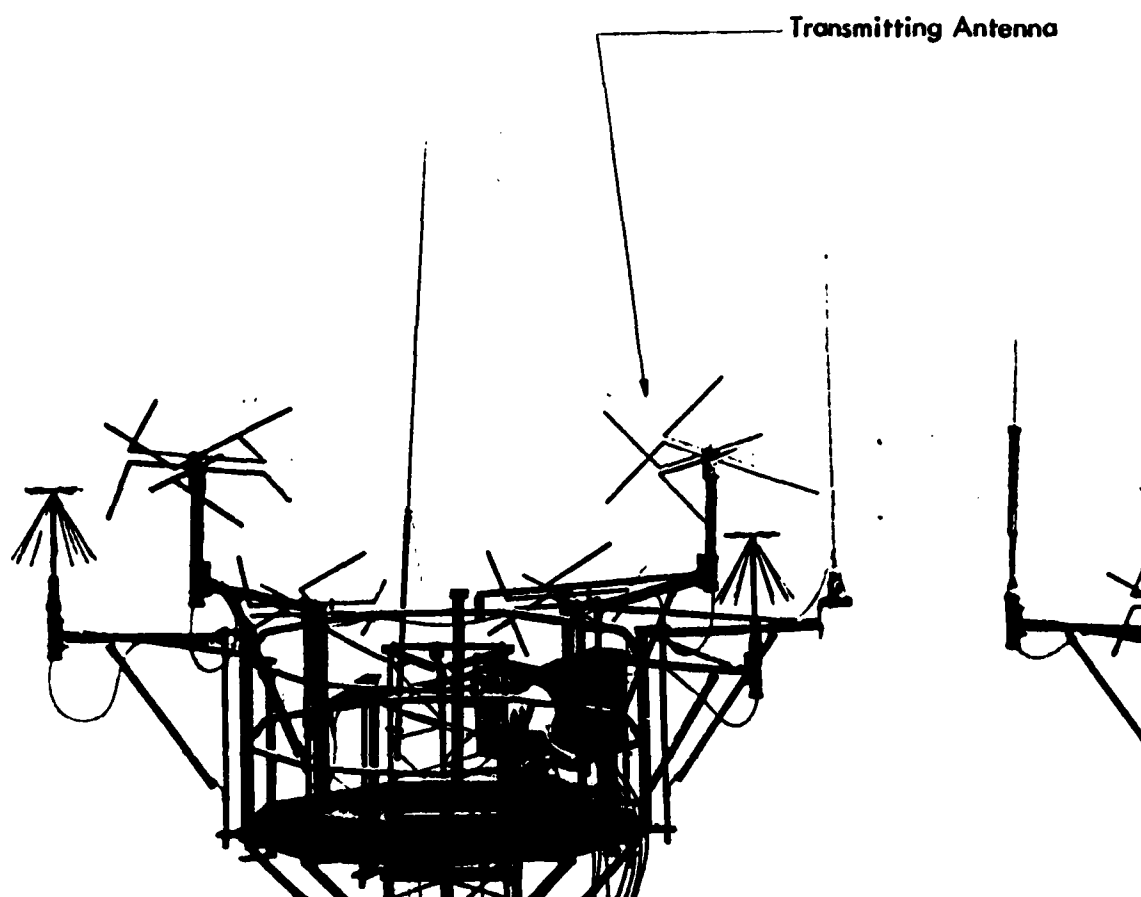
Figure 5-5. Charlottesville, Virginia RCAG Tower Used for These Measurements. Tower height is 40' and antenna configuration is non-standard.

Figure 5-5 was used as the transmitting antenna for one set of flight measurements, and was replaced by a TACO Model D-2267 antenna for a second set of measurements; a rigorous field evaluation of these antennas with respect to each other had not been performed previously. The result of that comparison is that the antennas perform essentially equally.

Pertinent site parameters for the Charlottesville site are as follows: antenna height 40', operating frequency 122.65 MHz., foreward power (measured at the antenna) 22.0 Watts, and reflected power 0.25 watts. Measurements were performed by FAATC on both June 18 and October 5, 1979.

The picture shown in Figure 5-5 was taken with a 180 mm telephoto lens from the second floor of the terminal building; clearly, the propagation path from the antenna shown is blocked by the building for low-elevation angle reception. Further, the separation between the transmitting antenna and parasitic structures, such as lightning rods, other antennas, and near-by towers, is considerably less than the separation specified for a standard RCAG site. A modeling effort using the thin-wire model could have been undertaken to characterize scattering due to these local obstructions; however, it was decided that only scattering from standard sites be considered. Cognizant of nonstandard scattering at the Charlottesville site, measured data were collected to evaluate the vertically-polarized TACO antenna with respect to the circularly-polarized Swastika antenna in addition to providing general insight into signal strength data collection.

Signal strength data were collected along the 55° and 240° radials at the Charlottesville site in addition to numerous orbital measurements. These two radials were selected in particular due to their relative terrain roughness and smoothness. A plot of terrain profiles along these radials are presented in Figures 5-6 and 5-7; data for these plots were obtained from the ITS terrain data base as described in Section IID. If terrain roughness were a major factor in propagation path loss, a noticeable difference would be expected in signal strength along the two radials shown in Figures 5-6 and 5-7. However, measurements taken along these two radials, shown in Figure 5-8, reveal little difference within a 40 nm range. It should be noted that the aircraft is within line of sight at 40 nm along both radials, and thus edge diffraction is not a significant factor. The lack of repeatability evident in Figure 5-8 was attributed to aircraft antenna lobing at first; however, subsequent radial measurements showed that repeatability can be achieved if the azimuth angle with respect to the site is accurately maintained during the measurement. The reason that maintaining a constant angle is critical to repeatability is readily apparent from orbital measurements, where signal strength is shown to vary rapidly over a narrow azimuth sector for the Charlottesville site. A repeatable radial measurement at Charlottesville along the 55° radial is shown in Figure 5-9. Divergence of inbound and outbound traces beyond 50 nm resulted from deviation from course as requested by traffic controllers. A very
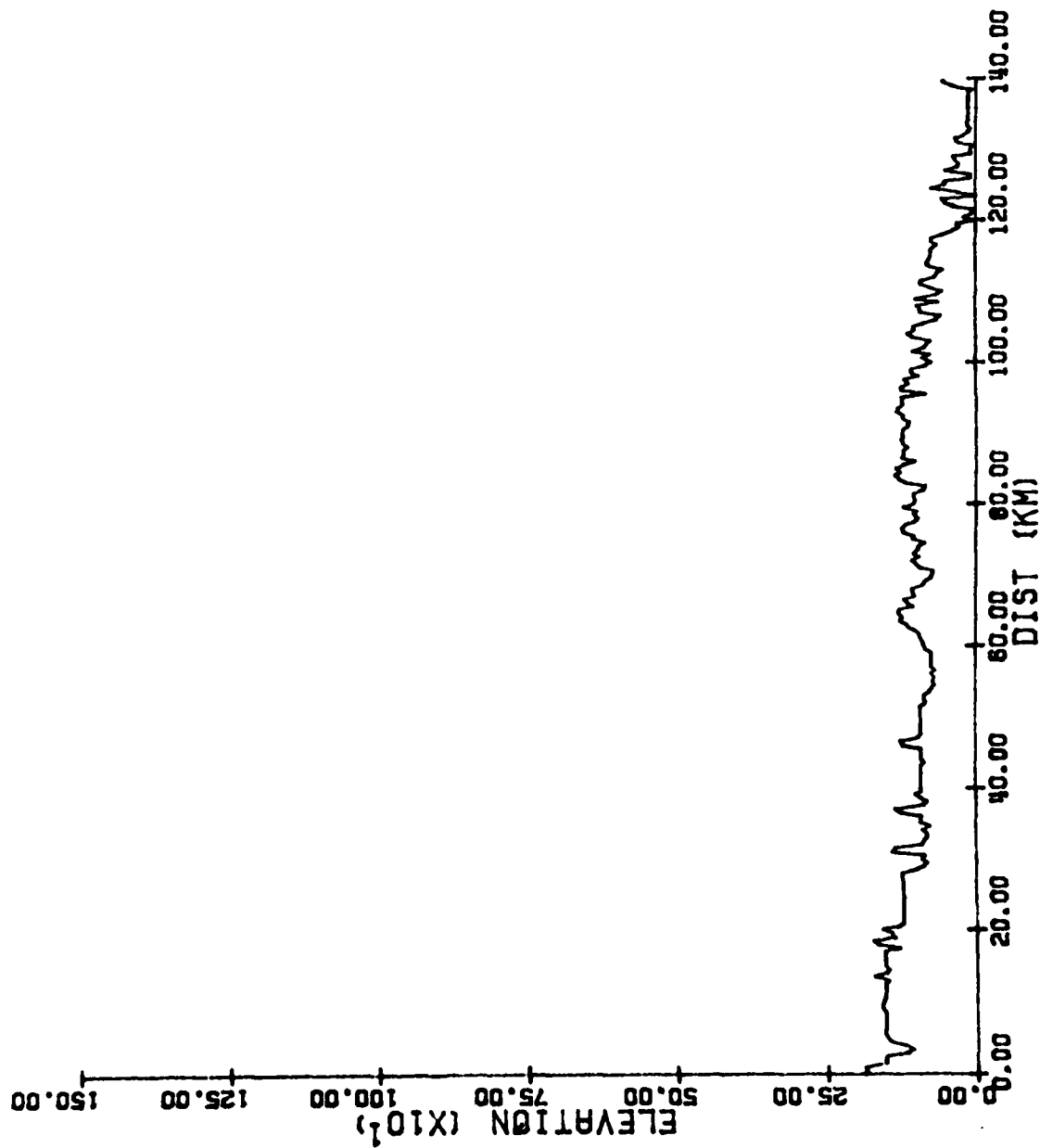
Figure 5-6. Terrain Profile along the 060° Radial from the Charlottsville, Virginia Site.
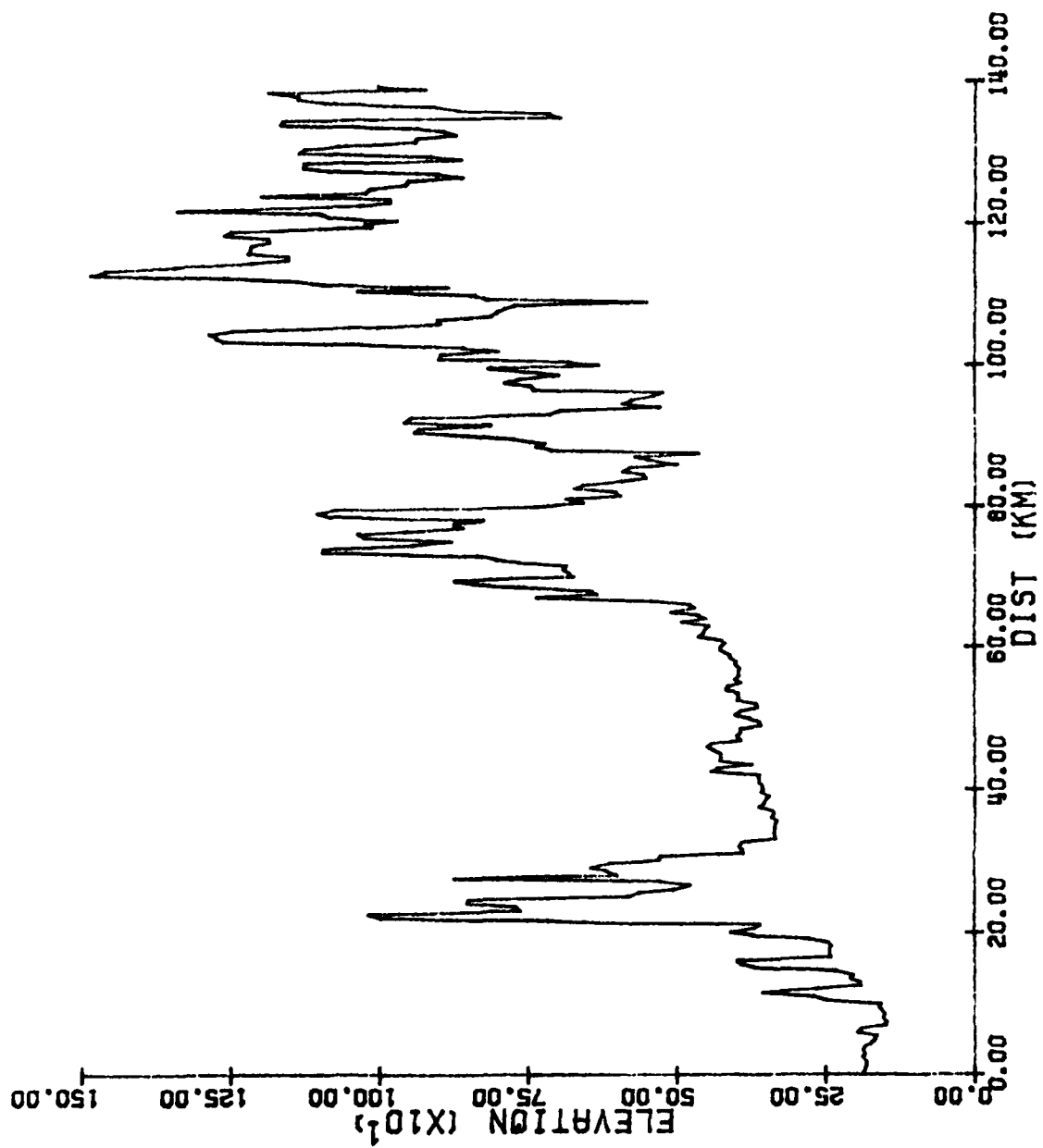
Figure 5-7. Terrain Profile along the 305° Radial from the Charlottsville, Virginia Site.
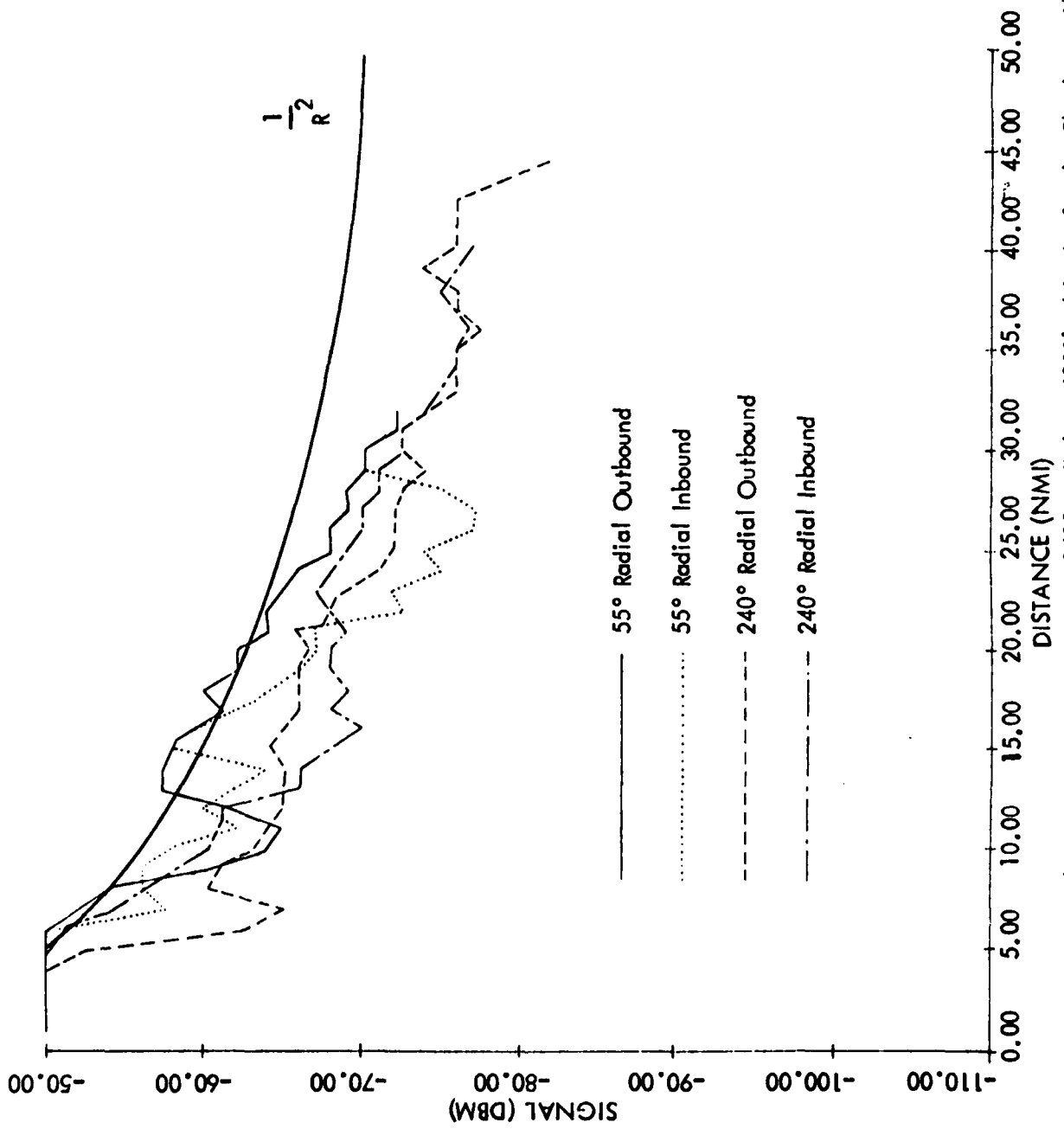
Figure 5-8. Measured Signal Strength Along the 55° and 240° Radials at 6000' Altitudes for the Charlottesville, Virginia RCAG Site.
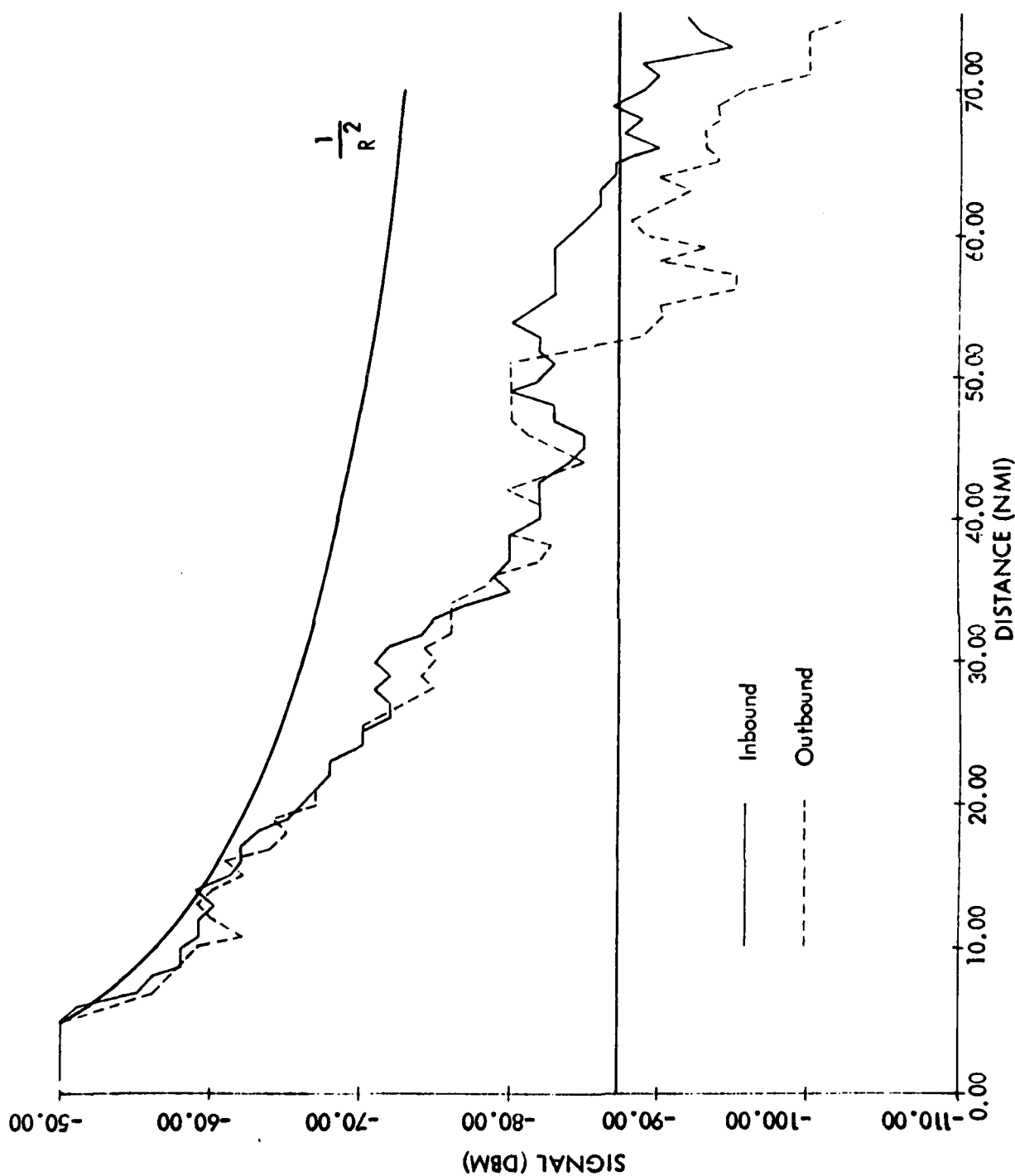
Figure 5-9. Measured Signal Strength along the 55° Radial of the Charlottesville, Virginia RCO Site Inbound and Outbound at 5800' Altitude.

important observation that can be made from Figure 5-9 is that there are no pronounced effects of vertical lobing; signal strength intensity tends to decrease inversely with distance over the range shown which covers elevation angles ranging from 90° to almost 0°. This lack of vertical lobing was observed on all other radial measurements collected for this report. Such an observation is consistent with the information presented in Section III.

Orbital airborne measurements were collected at 10 nm, 3000' altitude, and 40 nm, 6000' altitude. The 10 nm orbit was performed to determine the effects of local obstruction scattering in addition to providing information on Swastika versus TACO antenna performance within clear line of sight; the Fresnel Ellipse, as defined in Section III, did not intersect the terrain for the 10 nm orbit. Measured signal strength is presented in Figure 5-10. Referring to Figure 5-10, the similarity between the Swastika and TACO antenna is apparent. The large signal strength variation seen in Figure 5-10, which is in excess of 20 dB, is considered to be caused by local obstruction scattering and multipath.

Measured signal strength obtained during 40 nm orbits around the Charlottesville site are plotted in Figure 5-11 along with ITS model data for the Charlottesville site. As seen in Figure 5-11, signal strength variation is approximately 40 dB over the entire orbit. To provide insight into the conditions under which the orbit was flown, it is instructive to plot out the depression angle of the aircraft during the orbit with respect to the terrain horizon as seen by the transmitting antenna; a plot of depression angle is given in Figure 5-12. The depression angle is positive if the aircraft is above the physical horizon seen at the transmitting antenna, and hence is within line of sight. Conversely , a negative depression angle indicates that the aircraft is below the physical horizon. The plot of Figure 5-12 was made using the ITS terrain data base and does consider earth curvature. As expected, measured signal strength does tend to be lower for aircraft positions beyond line of sight.

The high degree of noise and lack of repeatability evident in the measured data of Figure 5-11 in conjunction with unknown local-obstruction scattering effects makes it difficult to draw meaningful conclusions regarding ITS model performance at the Charlottesville site. However, it is clear that some of the correlated trends in the measured data are also evident in the modeled data.

3. FAATC Experimental RCAG Facility. The FAATC Experimental RCAG Facility, pictured in Figure 5-13, is located near Atlantic City, New Jersey and is maintained by FAATC to investigate various facets of RCAG operation. The terrain in the vicinity is essentially flat, and there are well-defined areas comprised of hardwood-evergreen forests. Additionally, there are no nearby obstructions to interfere with propagation. The transmitting antenna height is 54', and the mean tree height is 38'.
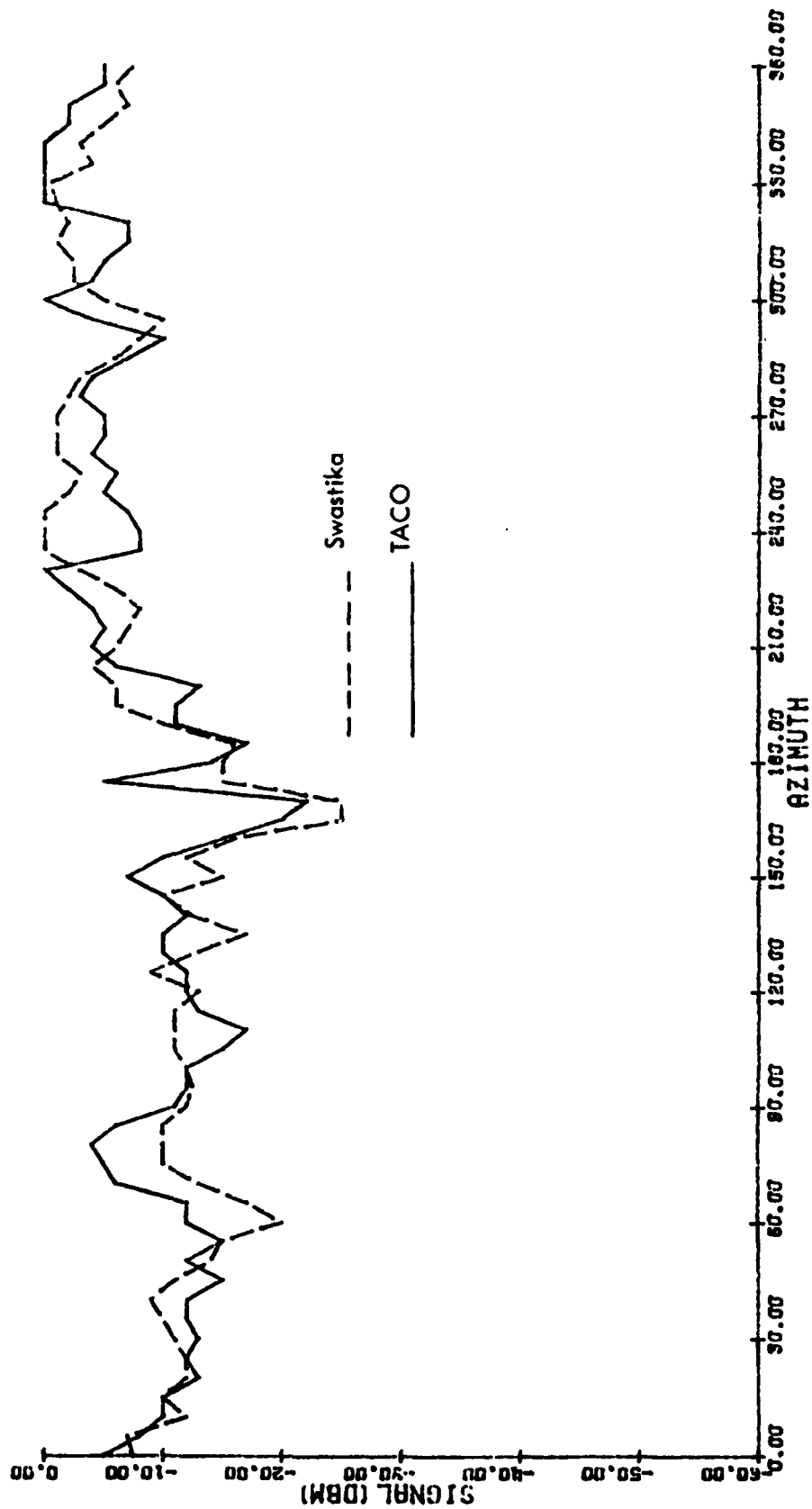
Figure 5-10. Measured Signal Strength for a 10 NM, 3000' Altitude Orbit around the Charlottesville, Virginia RCO Site for both a Swastika and a TACO Transmitting Antenna.
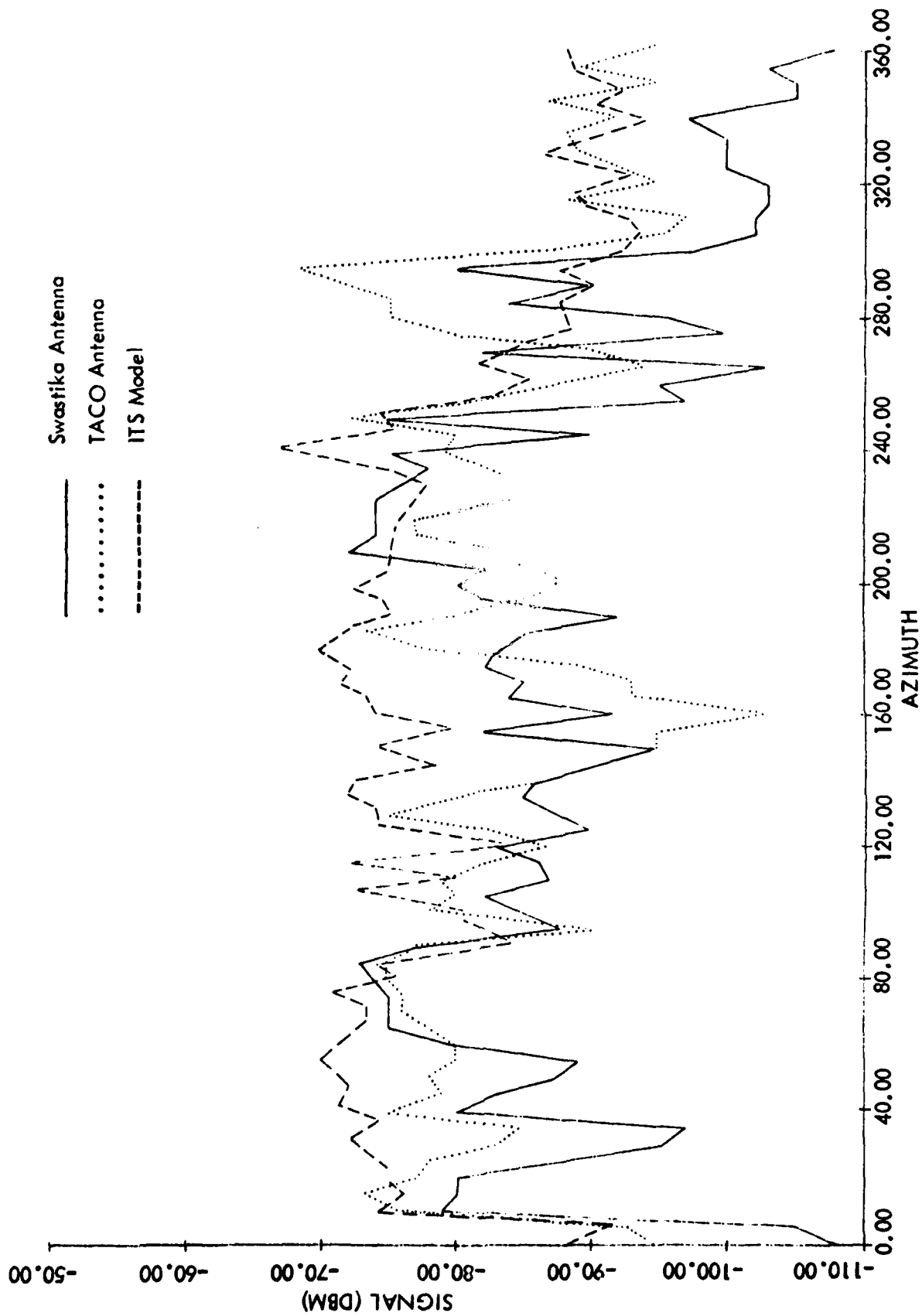
Figure 5-11. Modeled and Measured Data for a 40 nm, 6000' MSL Altitude Orbit Around the Charlottesville, Virginia Site.

Swastika Antenna
TACO Antenna
ITS Model

SIGNAL (DBM)

AZIMUTH
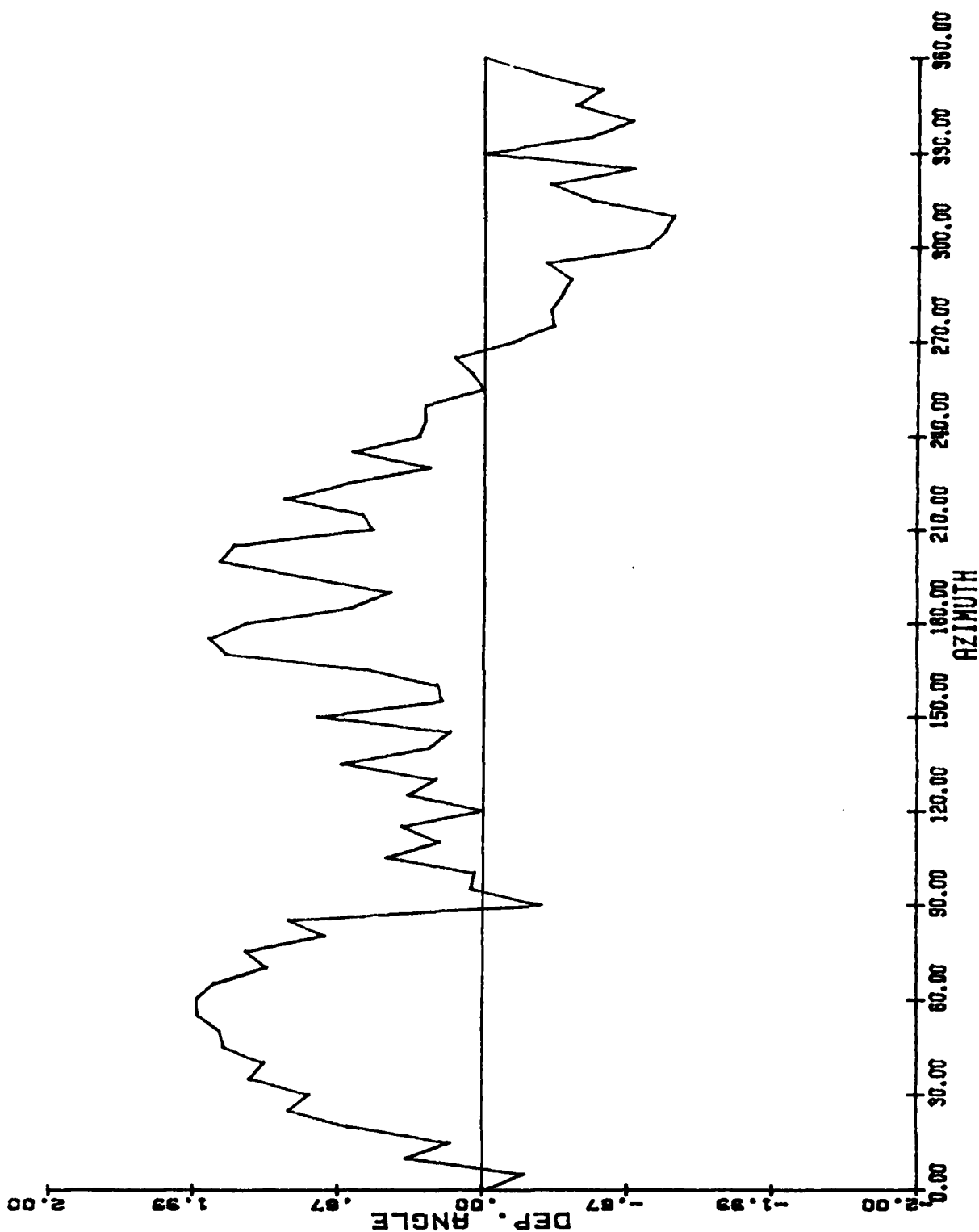
Figure 5-12. Elevation Angle of Aircraft with Respect to Horizon as seen by Transmitting Antenna at the Charlottesville, Virginia RCAG Site for Aircraft Making 40 nm , 6000' Altitude Orbit. The plotted values were determined from the terrain data base.

Figure 5-13. Picture of NAFEC RCAG Site.

Two series of measurements were performed for this task at the
FAATC facility, the first by FAATC on October 5, 1979, and the second
by Ohio University on March 4, 1980; FAATC measurements were collected
at 126.25 MHz with a transmitter power of 10 watts, and the Ohio
University measurements at 123.2 MHz with a transmitter power of 5
watts. All data were collected during 20 nm, 3000' altitude orbits.

The first series of measurements were performed to determine the
effects of scattering caused by the supporting tower in addition to
examining tree effects. To meet the former objective, four identical
TACO VHF antennas were mounted symmetrically on the same tower;
received signal strength from each antenna was recorded as the
aircraft, with transmitter aboard, flew orbits around the site. If
scattering from the supporting tower were a significant factor,
effects from that scattering would be expected to be seen by each
antenna on the tower displaced angularly by the angular separation of
the antennas with respect to the center of the tower. Figures 5-14
through 5-17 plot the measured signal strength as a function of azi-
muth from each of the four antennas; clearly, all four of these plots
exhibit the same basic trends, indicating that tower. This conclusion
is consistent with the results predicted by the thin-wire model.

The trends that are evident in Figures 5-14 through 5-17 appear to
correlate only with tree boundaries. The polar plot of Figure 5-18
presenting a representative measured signal strength superimposed upon
a layout of the site clearly shows that the signal strength trends do
not correlate with site structures such as the other towers or the
building. Appreciable correlation with tree boundaries is evident in
Figure 5-19 which shows a polar plot of signal strength superimposed
on a map of tree boundaries. Consistent with the theory posed in
Section III, an appreciable decrease in received signal strength is
observed in azimuth sectors where tree cover comprises the reflecting
zone.

A plot of measured and GTD/Forest-modeled data are presented in
Figure 5-20. Close agreement between measured and modeled data is
evident in this figure. It should be noted here that all of the non-
site model variables, such as the Fresnel Ellipse attenuation
constant, the Fresnel Ellipse ratio, and the conductivity and per-
mitivity of the forest medium, were determined empirically from the
Washington Court House, Ohio measured data. All GTD/Forest model data
presented in this report were obtained using the same values for these
non-site variables. The only parameters changed in modeling different
sites are those parameters relating to the site itself, such as
terrain profiles and the height of the transmitting antenna and trees.

The first series of measurements were performed in early Fall
when the deciduous trees were in leaf; the second series of measure-
ments were performed in the Winter when deciduous trees were not in
leaf. If scattering from leaves were a significant factor affecting
signal strength, an appreciable difference between in-leaf and out-of-
leaf signal strength would be expected. However, referring to Figure
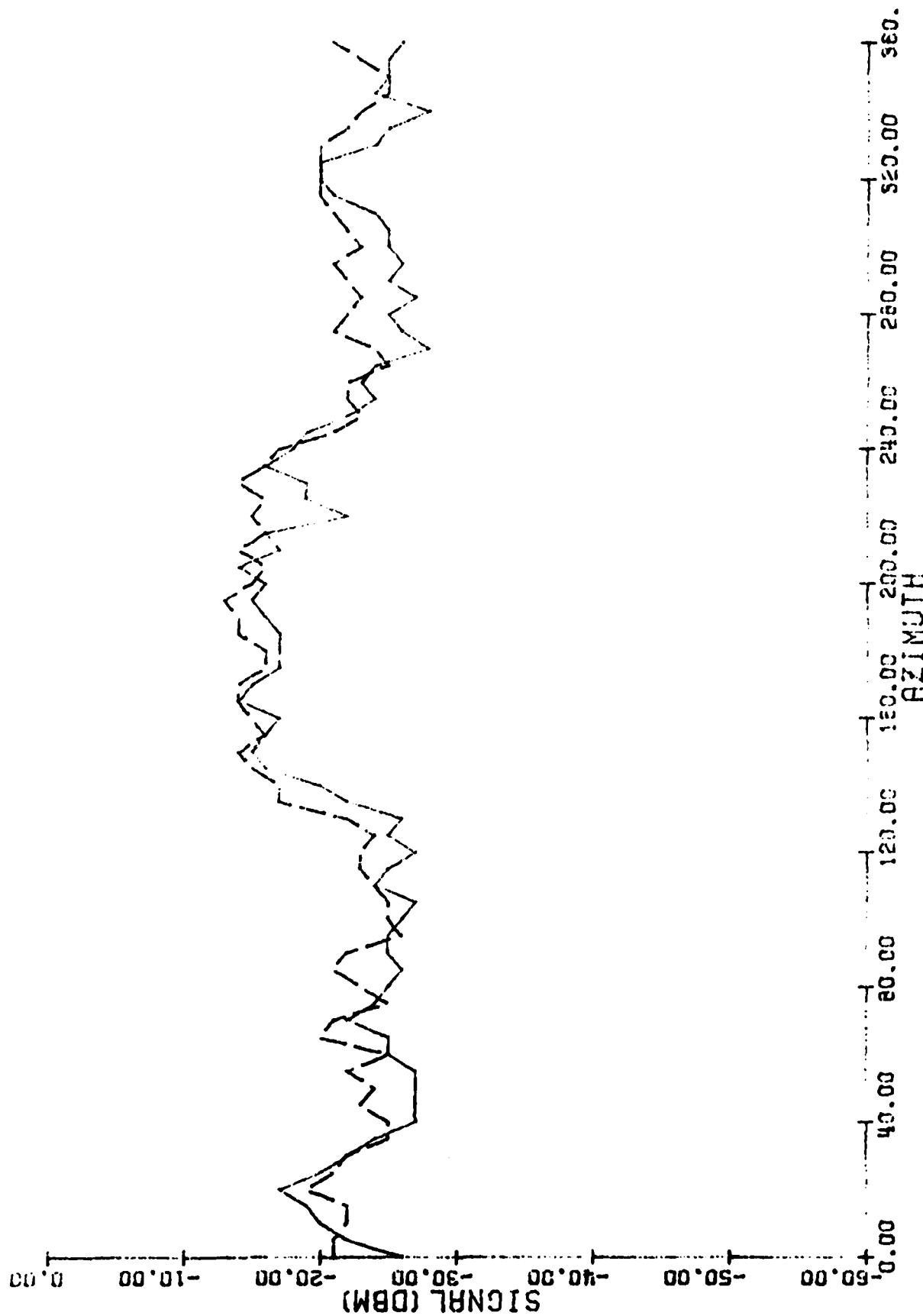
Figure 5-14. Measured Signal Strength for Antenna #1 for a 20 nm , 3000' Orbit around the NAFEC RCAG Site.
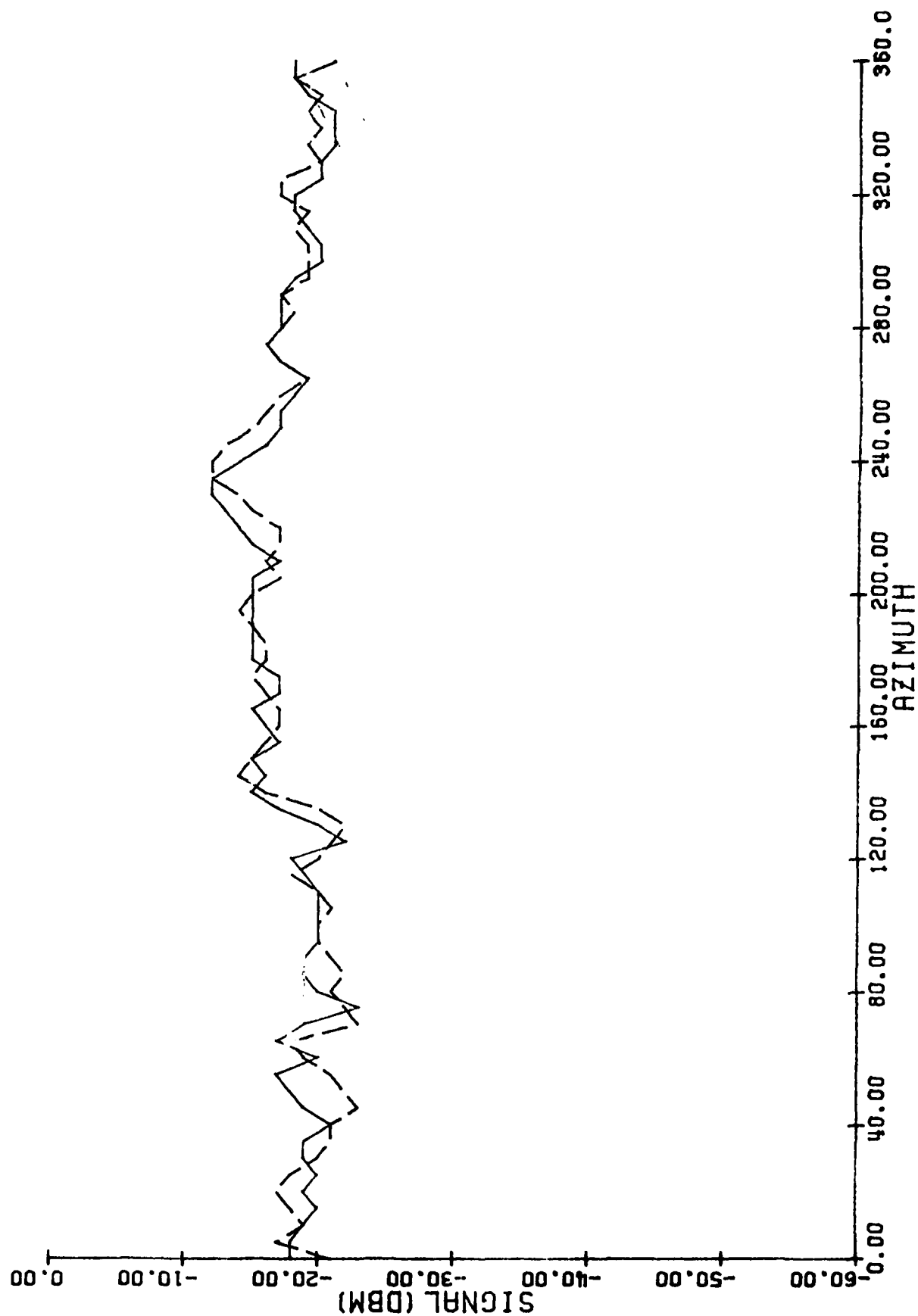
Figure 5-15. Measured Signal Strength for Antenna #2 for a 20 nm, 3000' Orbit around the NAFEC RCAG Site.
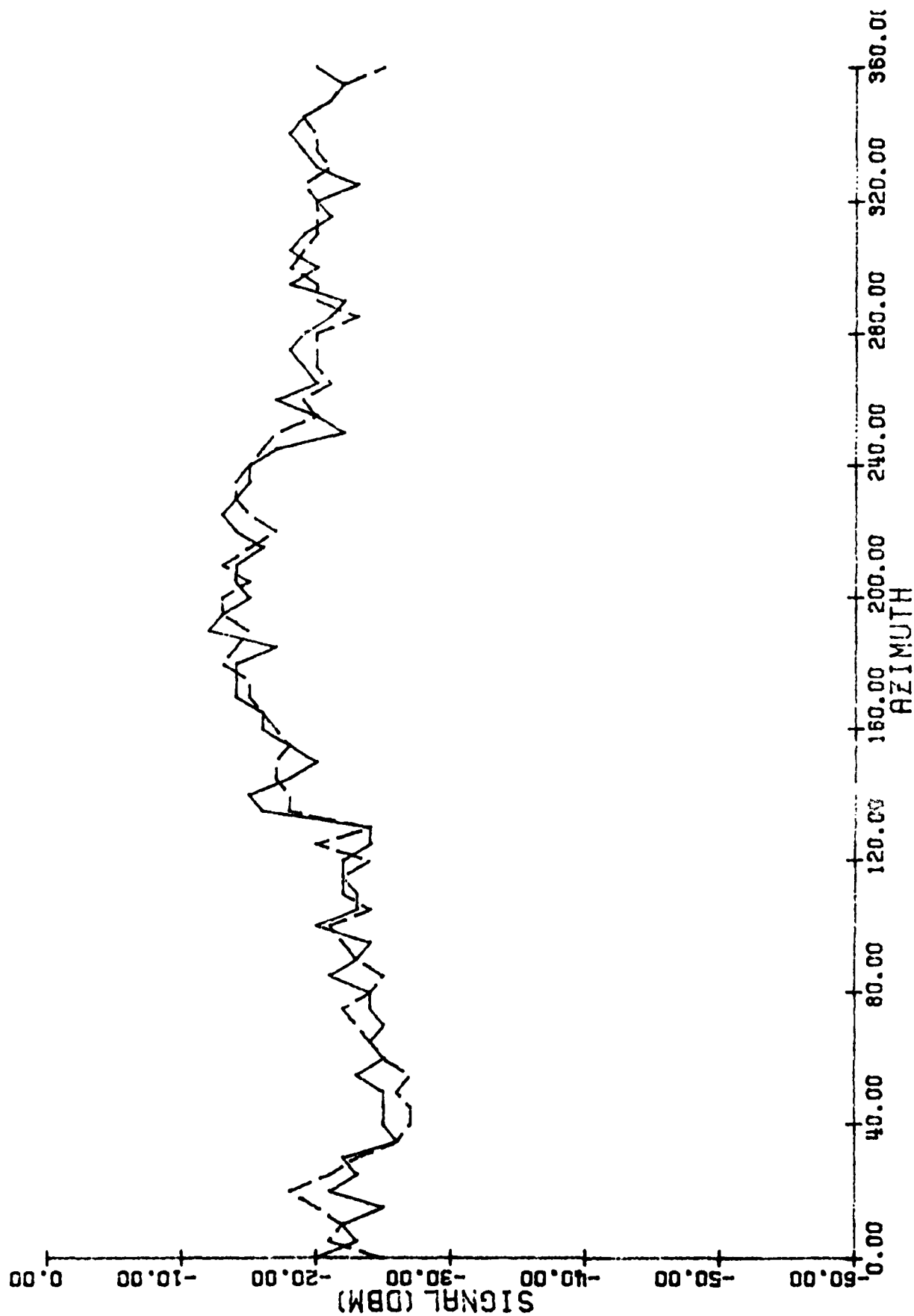
Figure 5-16. Measured Signal Strength for Antenna #3 for a 20 nm, 3000' Orbit around the NAFEC RCAG Site.
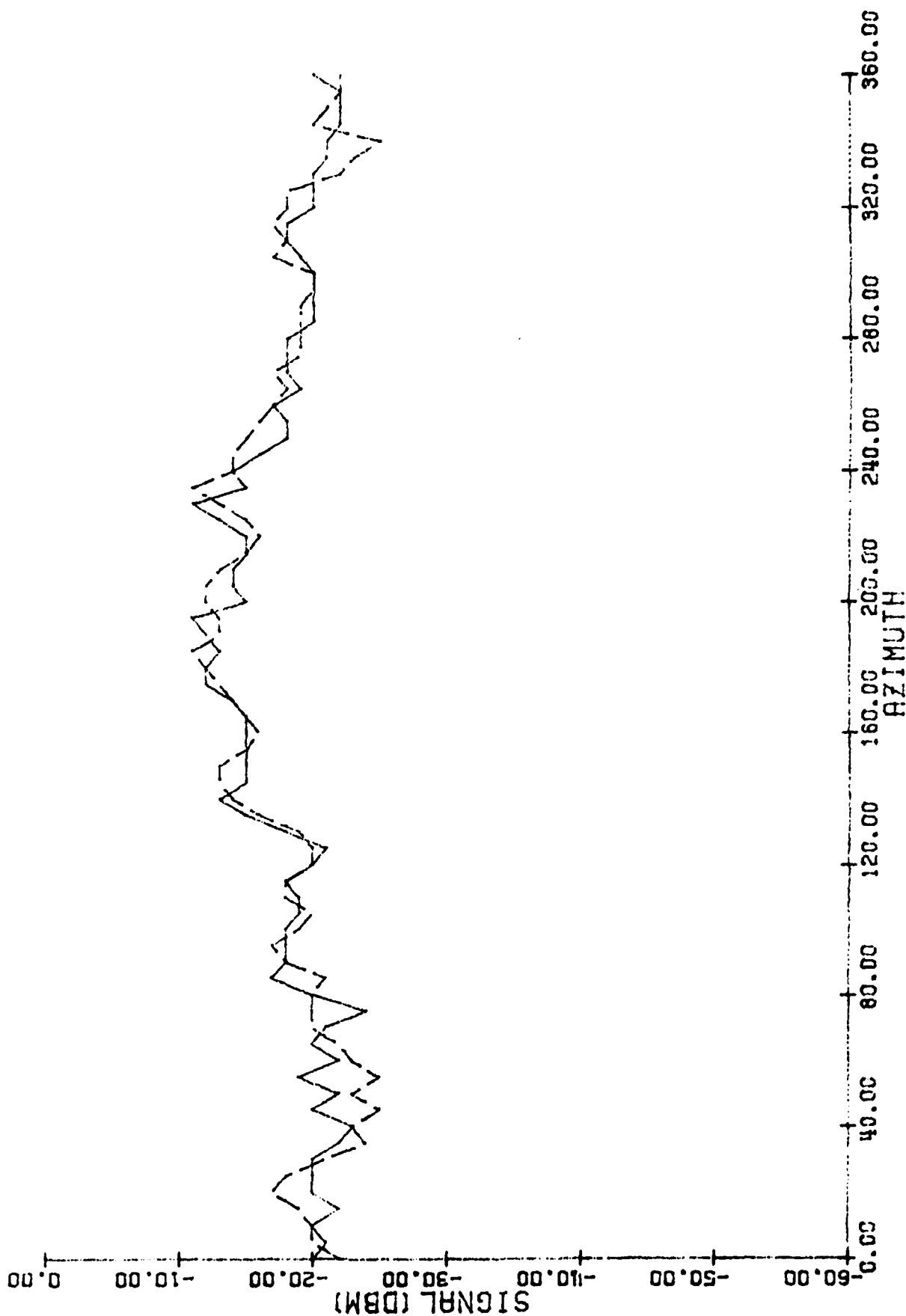
Figure 5-17. Measured Signal Strength for Antenna #4 for a 20 nm , 3000' Orbit around the NAFEC RCAG Site.
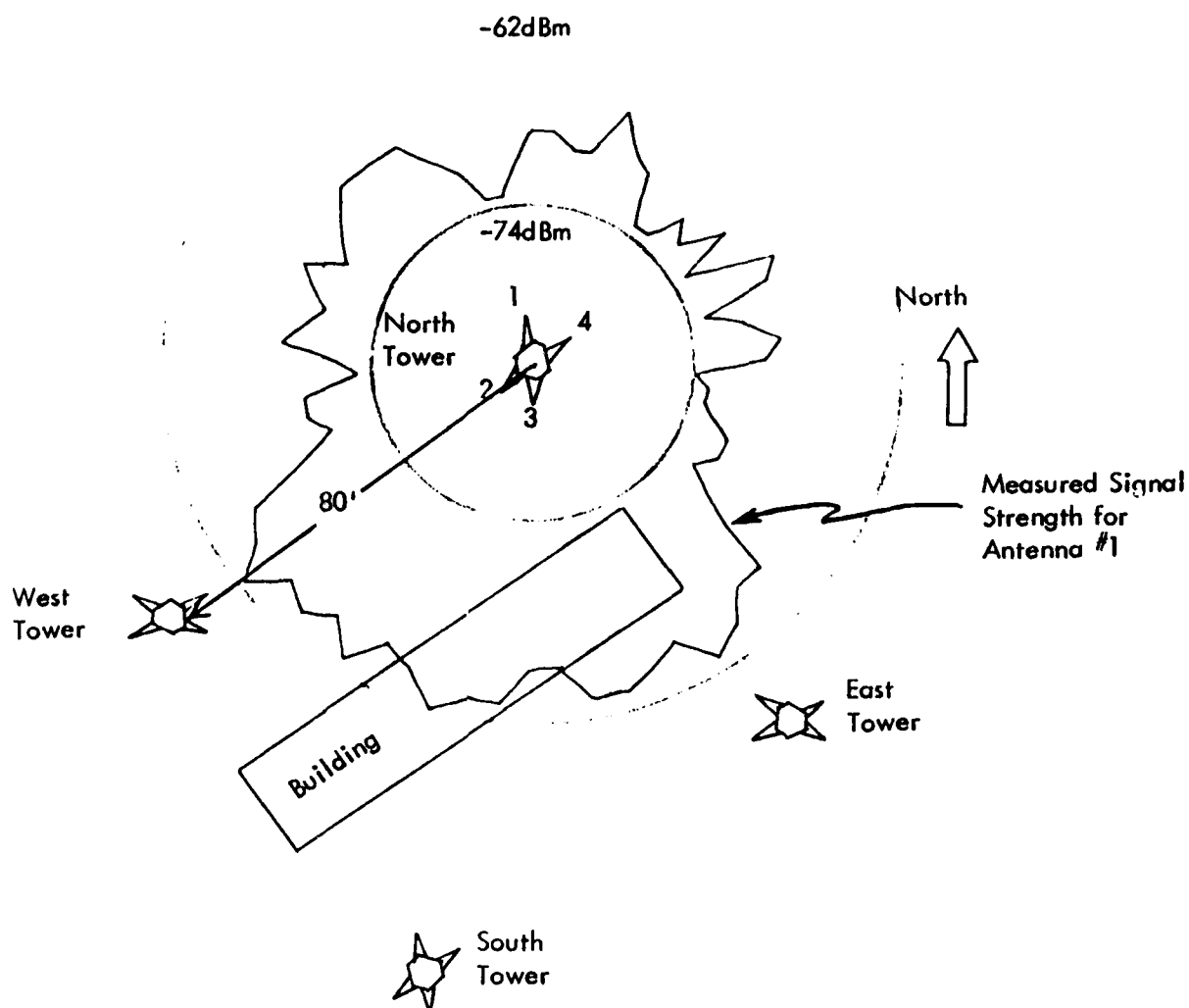
Figure 5-18. Layout of NAFEC RCAG Site with Relative Radiation Pattern for
the #1 Antenna on the North Tower. Scale for the radiation pattern
is 10 dB/inch.
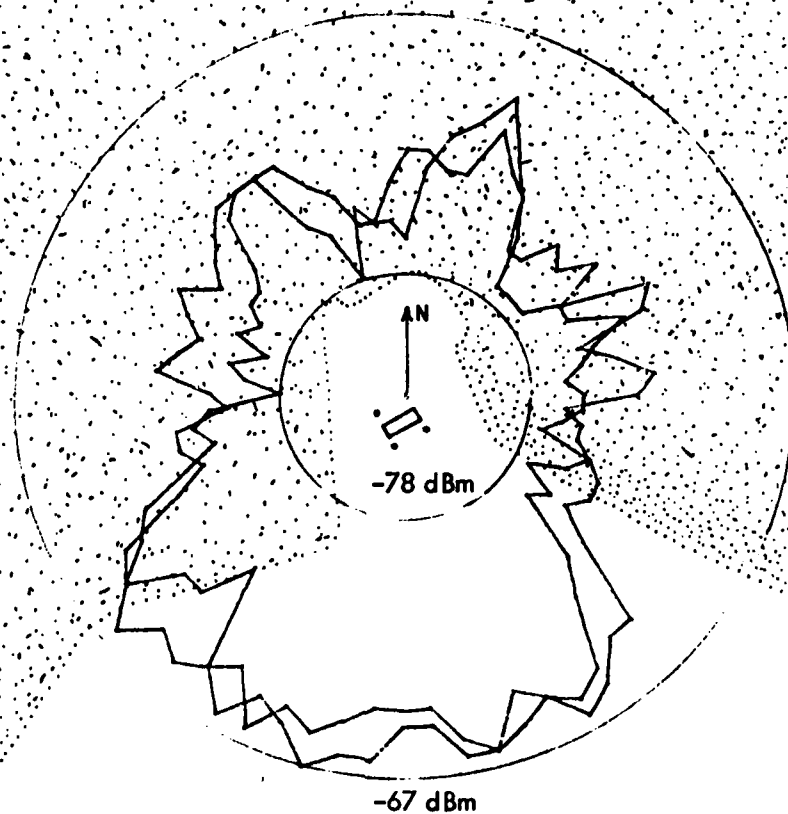
Figure 5-19. Sketch of Area Surrounding the NAFEC RCAG Site Showing Tree Boundaries. The superimposed signal strength was measured at 20 nm , 3000' elevation by NAFEC. (Scale: 1" = 400')
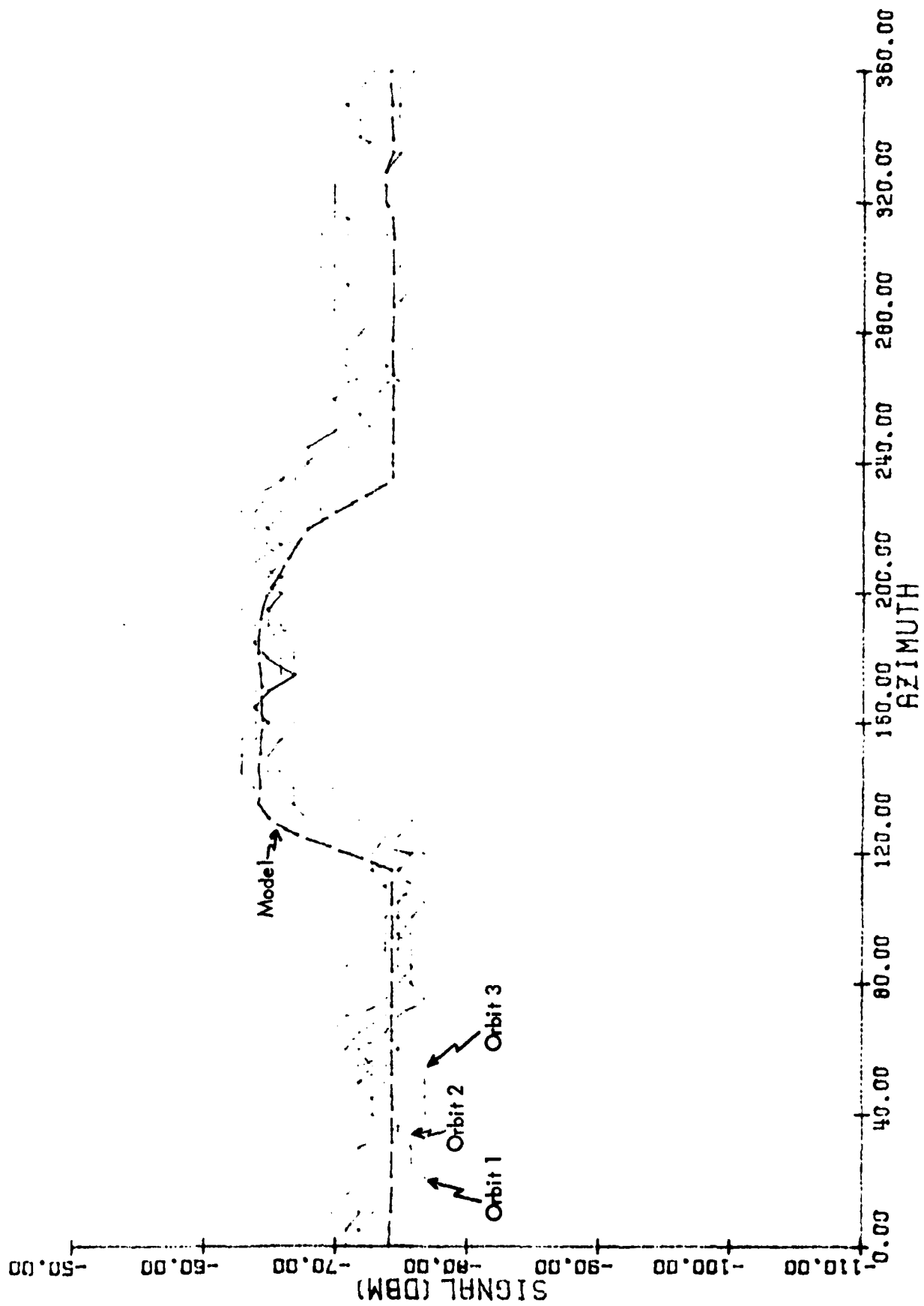
Figure 5-20. Measured and Modeled Signal Strength Values for a 3000' Altitude, 20 nm Orbit Around the Experimental NAFEC RCAG Site. Modeled values are plotted with dashed line.

5-21, which plots received signal strength values for both Fall and Winter, no discernable difference is seen. Based upon this observation, it is concluded that the vertical, finitely-conducting tree trunks, that are large with respect to a wavelength, rather than leaves, which are considerably smaller than a wavelength, are the predominant reflectors of electromagnetic radiation for vertically-polarized VHF waves.

An additional observation that can be made based upon the two series of measurements at the FAATC site is that even though the two series of measurement were collected using completely different airborne equipment by different personnel, the same measured values were obtained, thus indicating that neither equipment nor personnel biased the data.

4. South-Raleigh RCAG. The South-Raleigh RCAG site is a standard RCAG facility located approximately 10 miles south of Raleigh-Durham, North Carolina in an area of rolling farmland with occasional groves of trees. The type of topography and tree cover at the South Raleigh site, depicted in Figures 5-22 and 5-23, is among the most challenging for the GTD/Forest model. This challenge arises because terrain elevation and tree cover fluctuate within the area of the first Fresnel Zone. As discussed in Section IIF, which describes GTD model operation, the GTD model assumes ground reflection from a single point; if terrain variations within the first Fresnel Zone are relatively constant, accurate modeling results can be expected. As terrain variations become increasingly erratic within the first Fresnel Zone, model accuracy decreases. Some of the error introduced by erratic terrain is compensated for by including the contribution from diffractive edges, although, depending upon the extent of terrain variations, there still may be appreciable net errors. Additionally, some of the forested areas at the South Raleigh site are small with respect to the first Fresnel zone. The assumptions made in Section III regarding reflection from trees are based upon forested areas that are greater in area than the first Fresnel Zone. The effect of small forested areas at South Raleigh is that modeling results are less accurate than modeling performed at sites with larger forested areas. Fortunately, the above factors that make modeling difficult also tend to diffuse and block an appreciable part of the reflected signal, thus minimizing the probability of signal deficiencies caused by cancellation from a strong, out-of-phase reflection.

In addition to model evaluation, a secondary objective of the measurements at the South-Raleigh site was to determine explicitly the effects of lightning rods, the supporting tower, and other antennas on the radiation pattern of the transmitting antenna. The transmitting antenna is 44' above local terrain, transmitter power is 10 watts, and operating frequency is 135.95 MHz. Measurements at the South-Raleigh RCAG site were performed by FAATC from June 19 through June 21, 1979.

To investigate the effects of other antennas and lightning rods, four 20 nm, 3000' altitude orbits were flown around the site with four
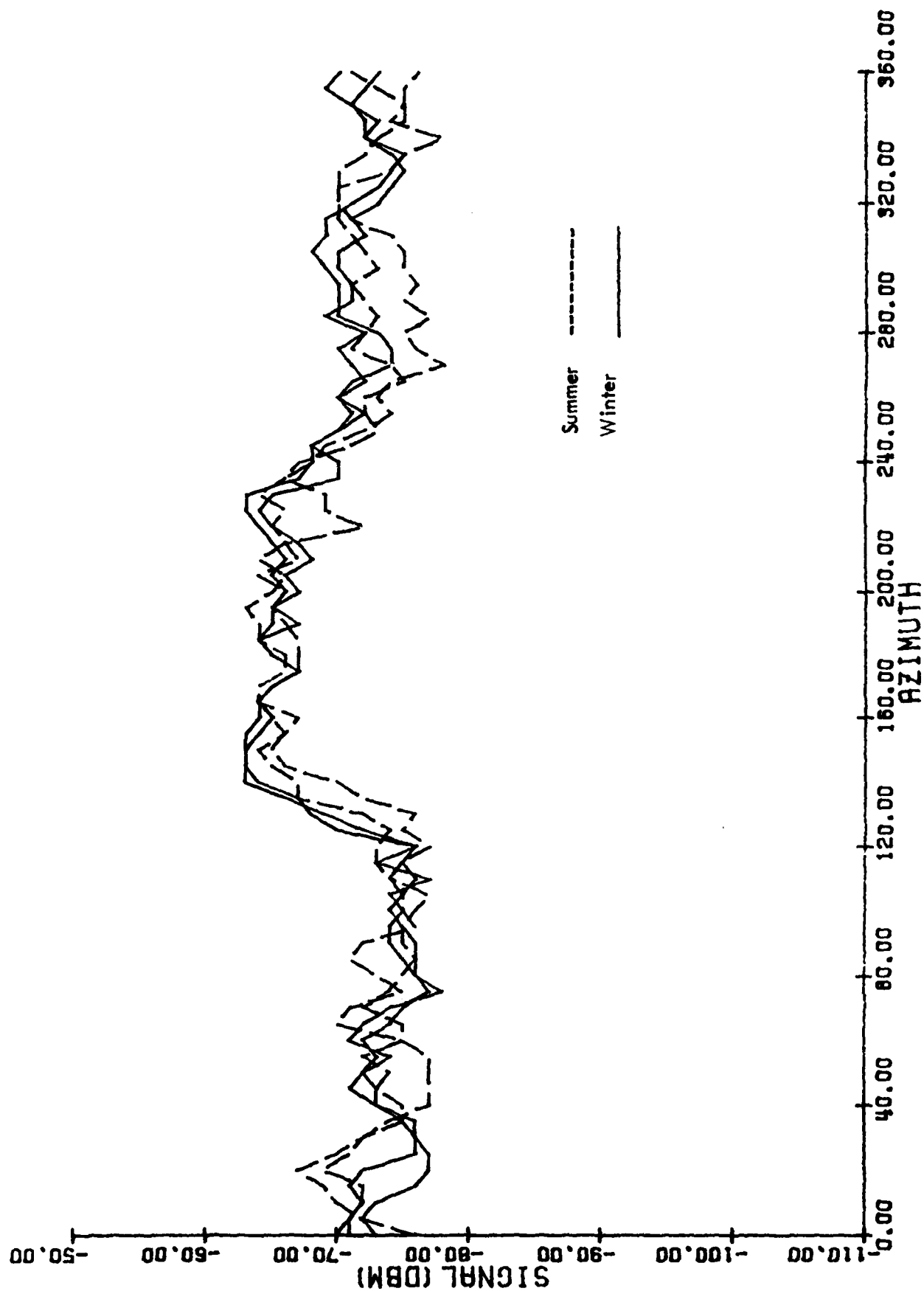
Figure 5-21. Measured Signal Strength for Both Fall and Winter Obtained During 20 nm, 3000' Altitude Orbits Around the FAATC Experimental RCAG Site.

CONTOUR INTERVAL 10 FEET
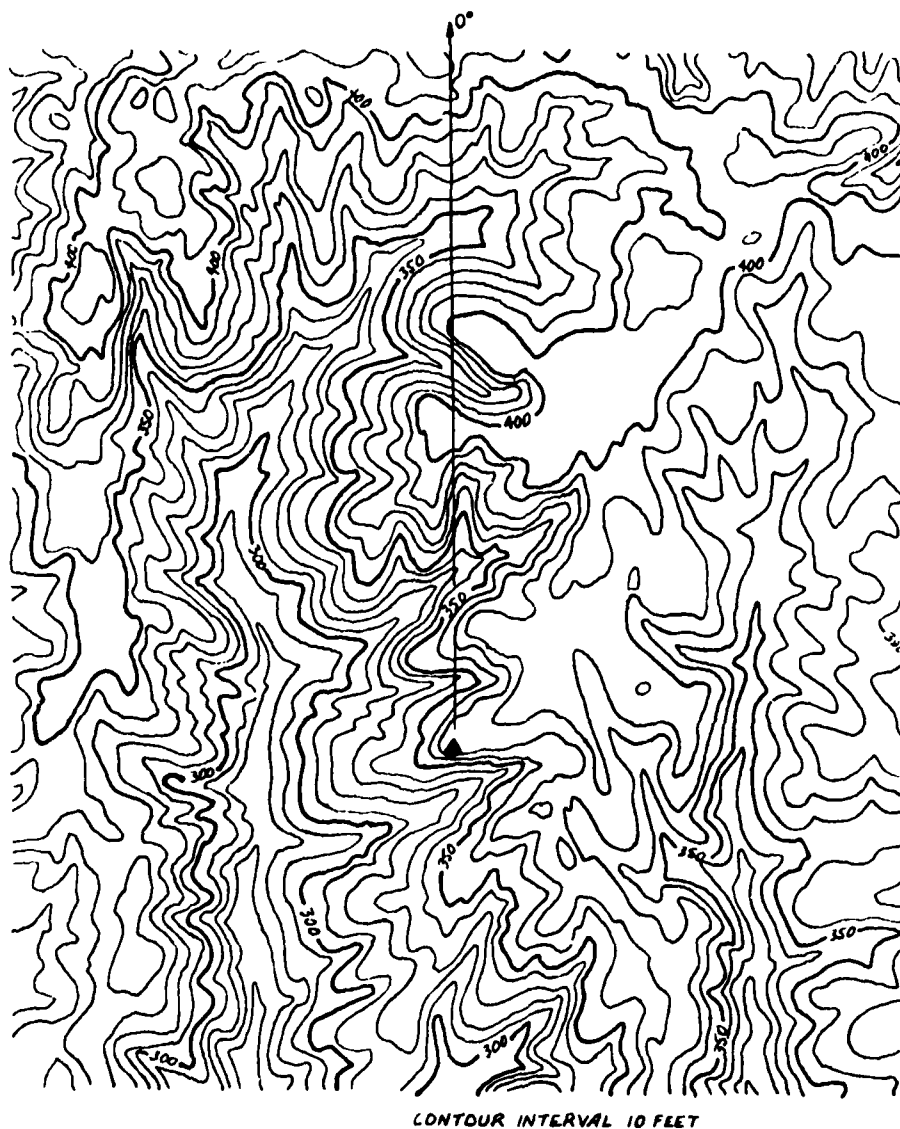
Figure 5-22. Topography of Terrain in the Vicinity of the South
Raleigh RCAG Site (Scale 1:24000).
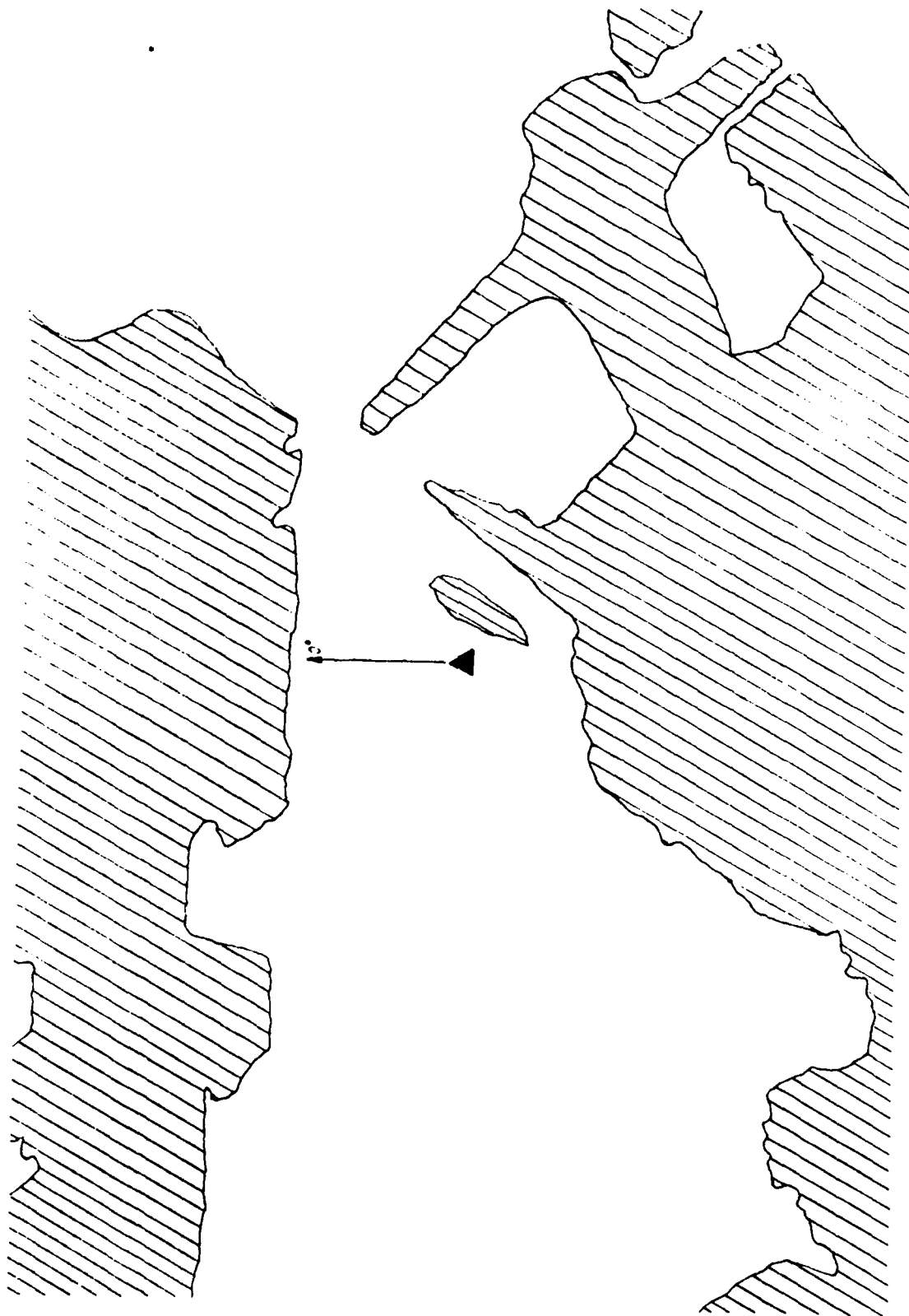
Figure 5-23. Location of Tree Cover in the Vicinity of the South Raleigh RCAG Site (Scale 1:2940).

different antenna/lightning rod configurations. The results of those orbits show that variations in transmitting antenna pattern due to other antennas or lightning rods in a standard configuration are immeasurable. Because these measurements were performed using TACO VHF and UHF antennas, the above statement applies strictly to cases where TACO antennas are used, however indications are th the statement will be true for other antennas as well.

A picture of the transmitting tower and antenna used for these measurements is given in Figure 5-24 which shows all parasitics (non-transmitting antennas and lightning rods) removed. A top view showing the location of these parasitics is shown in Figure 5-25.

Measured signal strength for the four antenna/lightning rod configurations are plotted in Figure 5-26. The first orbit was performed with a single TACO VHF antenna on the tower with the support arm holding the antenna in (Figure 5-24 shows the support arm extended in the normal position). The support arm was in on the first orbit to determine the effects of antenna/tower coupling. As can be seen from Figure 5-26, having the support in was the only condition that resulted in a measurable variation in the antenna pattern. On the second orbit, the support was extended, and the lightning rods added. Two TACO UHF antennas were added for the third orbit, and a full complement was measured on the fourth orbit with the addition of a second TACO VHF antenna. From these orbital measurements, it is seen that the effects of parasitics in a standard tower configuration are insignificant with respect to measurement error and other factors affecting propagation variability.

A polar plot of signal strength from an orbital measurement is superimposed on a layout of the South-Raleigh site in Figure 5-27. This plot is presented to illustrate the lack of correlation between signal strength variations and local obstructions, viz., the other towers, or the building.

GTD/Forest model results are plotted in Figure 5-28 along with measured data. Some of the actual signal strength trends are calculated by the model, although generally, the agreement between measured and modeled data is less for this site than for the other sites modeled. Of particular interest is the azimuth sector between 120° and 160° where the model estimates a slight drop in signal strength for a region where an increase is observed. Referring to that azimuth sector in the tree-cover map of Figure 5-23 shows a small cluster of trees close to the antenna. The model calculates a decrease in signal strength resulting from reflection from these trees, whereas this small group of trees apparently increases the received signal by scattering the out-of-phase reflected signal. The incapability to discern between a reflective and a scattering surface does represent a deficiency in the present GTD/Forest model, however measured data in excess of what is currently available would be necessary to make appropriate modifications.
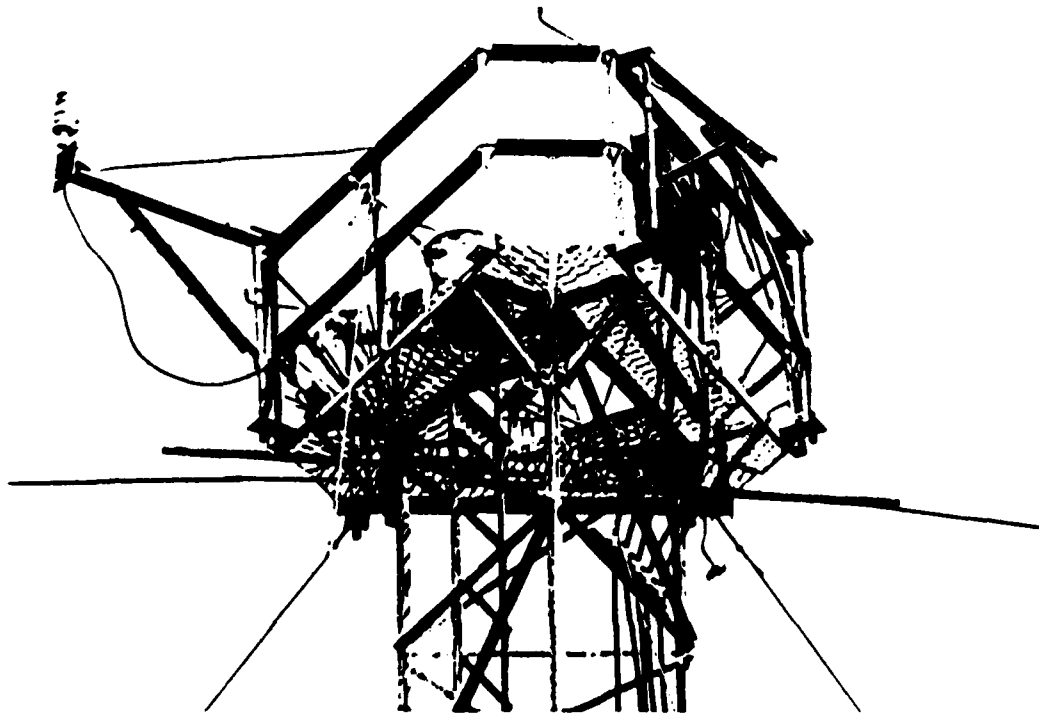
Figure 5-24. South Raleigh RCAG Tower with TACO VHF Antenna Pictured with Support Arm Extended. The support arm was moved in for the first measurement to determine coupling effects with the tower.
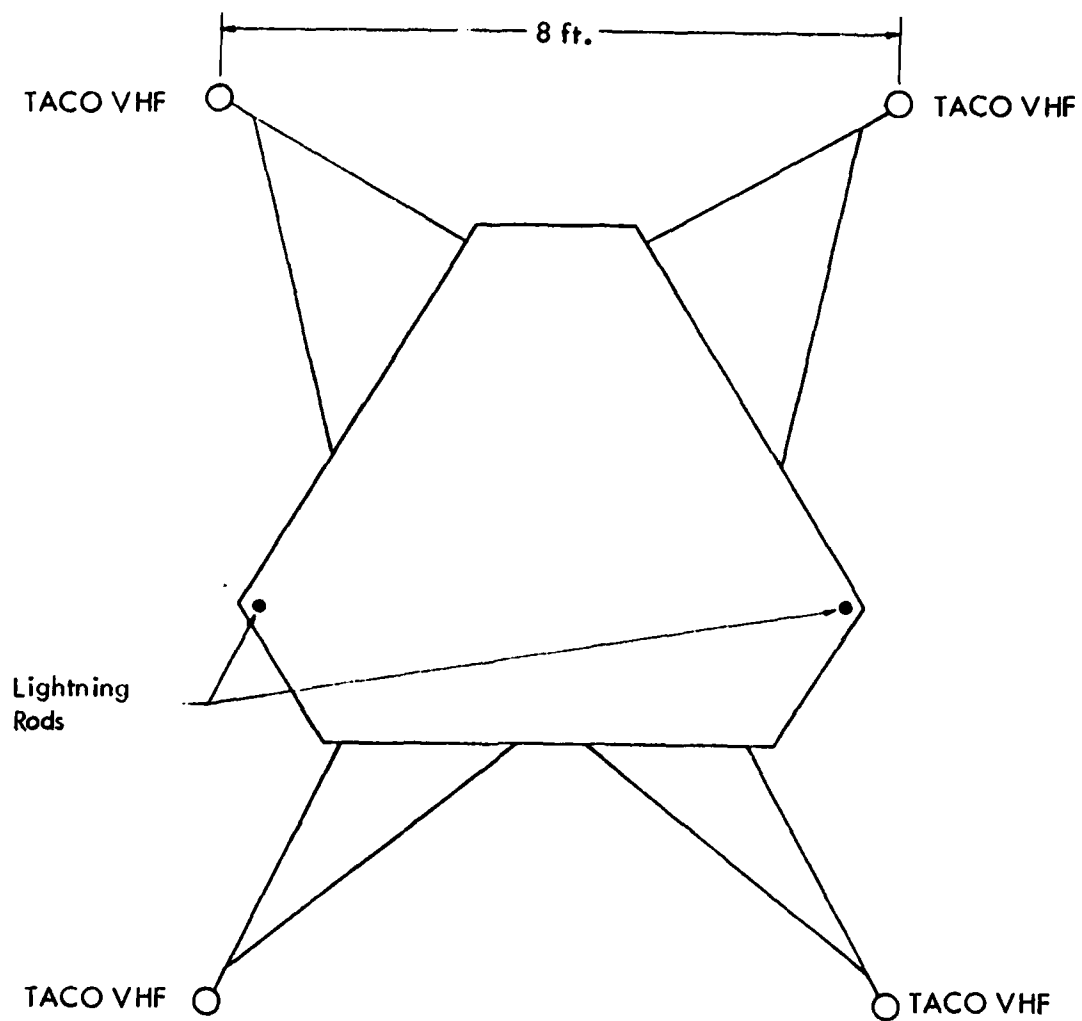
Figure 5-25. Layout of South-Raleigh RCAG Antenna Platform.
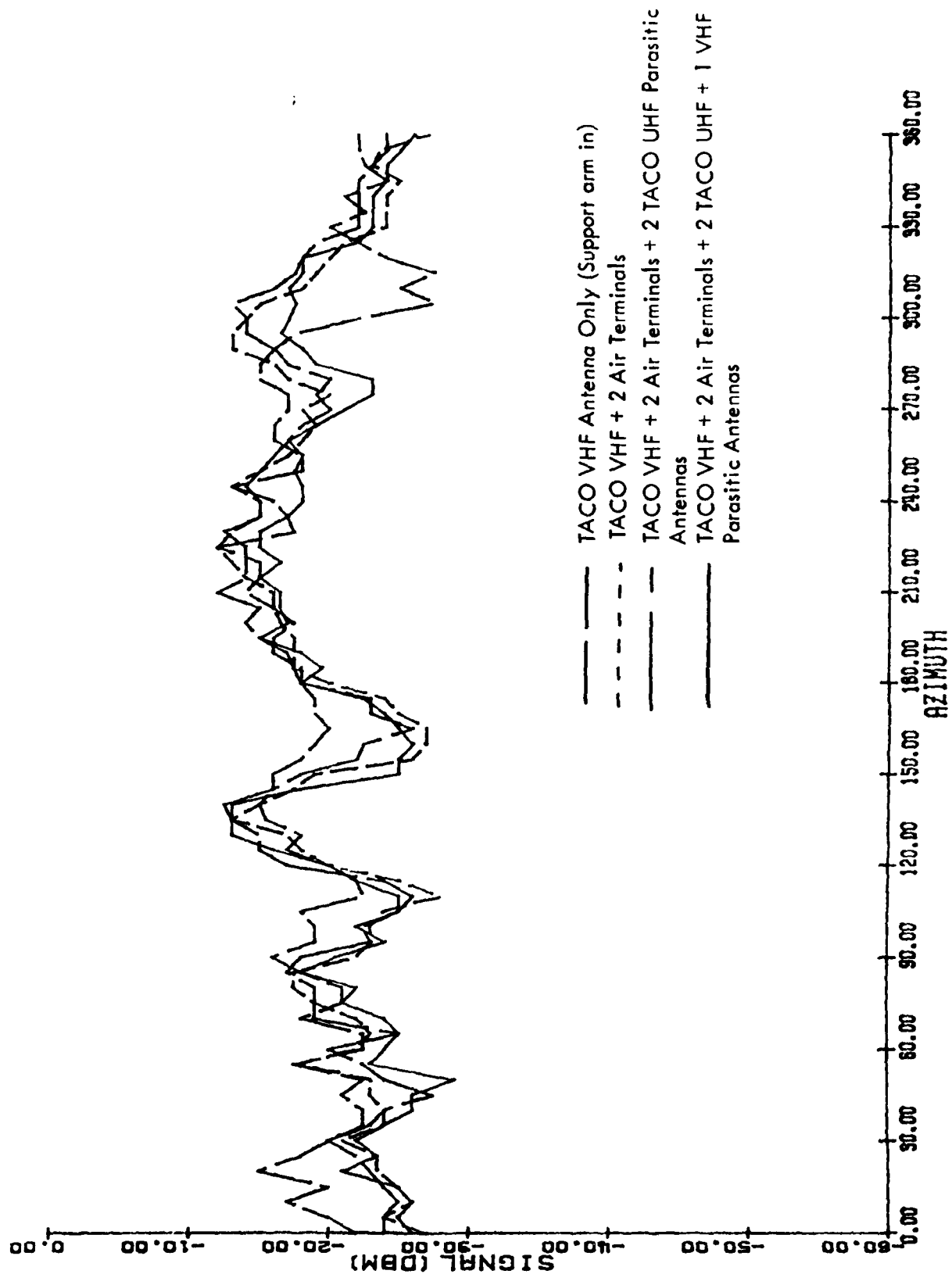
Figure 5-26. Measured Signal Strength for a 20 nm, 3000' Altitude Orbit Around the South Raleigh, RCAG Site for 4 Air Terminal/Antenna Configurations.

TACO VHF Antenna Only (Support arm in)

TACO VHF + 2 Air Terminals

TACO VHF + 2 Air Terminals + 2 TACO UHF Parasitic Antennas

TACO VHF + 2 Air Terminals + 2 TACO UHF + 1 VHF Parasitic Antennas

-123-
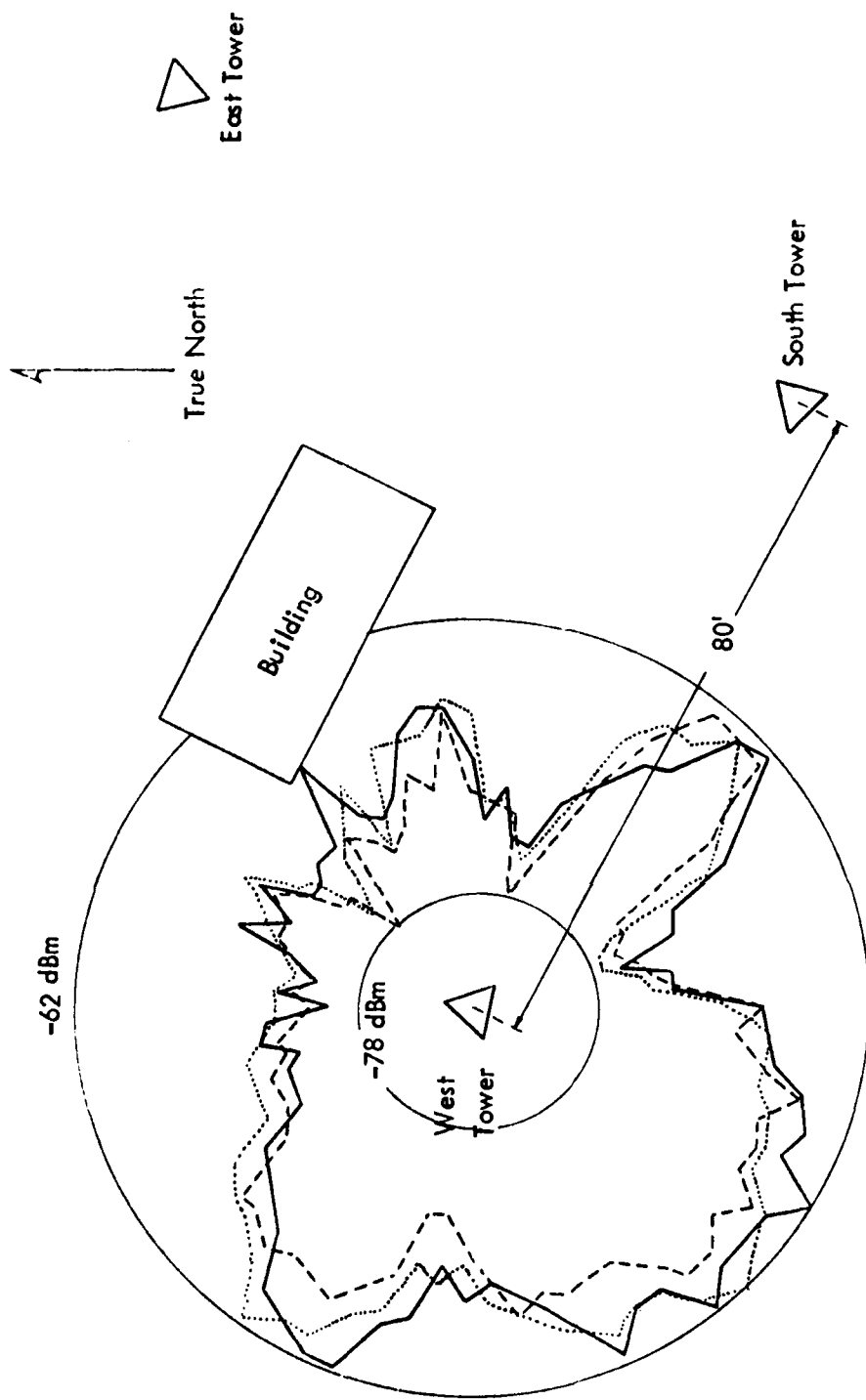
Figure 5-27. Layout of South Raleigh RCAG Site. Scale – 1" equal to 20'
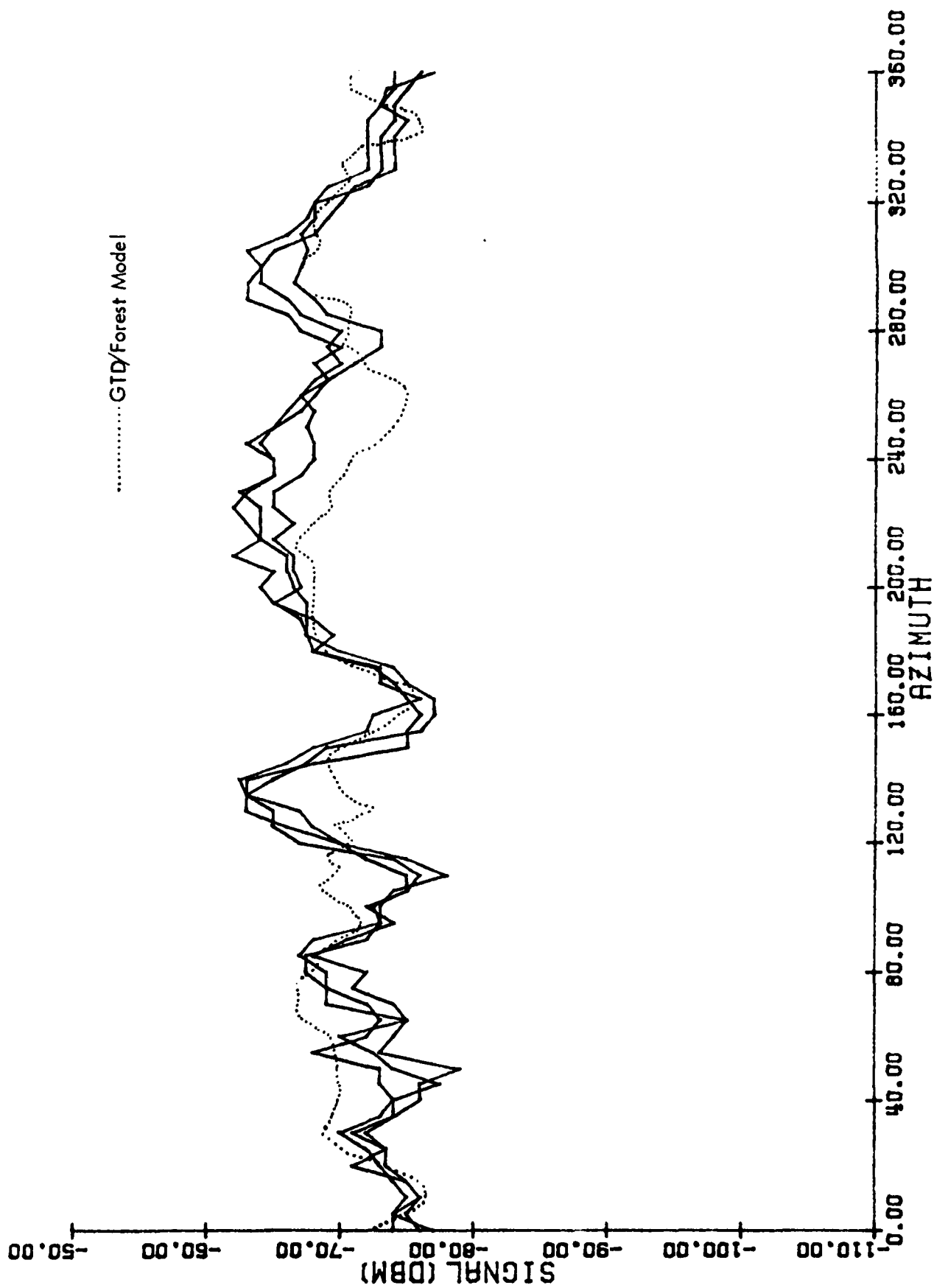
Figure 5-28. Measured and GTD/Forest Modeled Signal Strength for a 20 nm, 3000' Altitude Orbit Around the South Raleigh RCAG Site.

5. Washington Court House, Ohio. Washington Court House is located in South-Central Ohio and was selected for analysis because of well-defined forested areas in addition to generally level terrain. A topographical map of the area where two temporary sites were established are shown in Figure 5-29. Trees near the site, shown as dotted areas in Figure 5-29, are approximately 65 feet high and are primarily comprised of silver maple, locus, black walnut, and tulip poplar. The purpose of signal strength measurements at Washington Court House was to gain further insight into the mechanisms affecting tree-related attenuation and GTD/Forest model performance. Consistent with this objective, two temporary sites were established in strategic locations so as to test specific hypotheses regarding tree attenuation; one of the temporary sites installed is pictured in Figure 5-30. As seen in Figure 5-30, a TACO VHF antenna is supported on a guyed, 45' tower. The received signal is fed through low loss cable to the van, which contains the calibrated receiver and recording equipment. Data is collected as the aircraft, with transmitter aboard, flies 8 nm, 1200' AGL orbits around the site. Measured data were collected on two occasions, the first on August 13, 1981 and the second on September 4, 1981. Both measurements were performed by Ohio University using a Piper Cherokee aircraft; transmitter power was 4 Watts at 123.2 MHz.

Measured and GTD/Forest-modeled data are presented in Figures 5-31 and 5-32 for both temporary sites at Washington Court House. As seen in these figures, good agreement between modeled and measured data is evident. It should be noted here that, as with the FAATC experimental site, the ITS model will model the radiation pattern for both Washington Court House sites as being isotropic, due to the relatively flat terrain and the model's insensitivity to forested areas.

Measured data collected at the first temporary site were used to optimize the GTD/Forest model. Specifically, values of the Fresnel Ellipse attenuation constant, the Fresnel Ellipse ratio, and the electrical properties of the trees were varied until modeled data reached closest agreement with measured data. Once the model had been optimized, no additional changes were made to the model. The second temporary site at Washington Court House was modeled prior to measurement taking in order to demonstrate the model's prediction capability. Measured and modeled results from that effort are shown in Figure 5-32, again showing good agreement between measured and modeled data. It should be noted here that the GTD model without the forest modification would predict a nearly isotropic radiation pattern for this site due to the relatively-level terrain.

6. Ohio University Airport. The Ohio University Airport is located in Albany, Ohio and was selected for investigation due to its irregular and poorly-defined terrain. The Ohio University Airport site also represents a worst-case type site for modeling purposes. The terrain in the vicinity of the airport is shown topographically in Figure 5-33, with terrain elevation depicted by 20-foot terrain contours. The terrain features that make the Ohio University airport
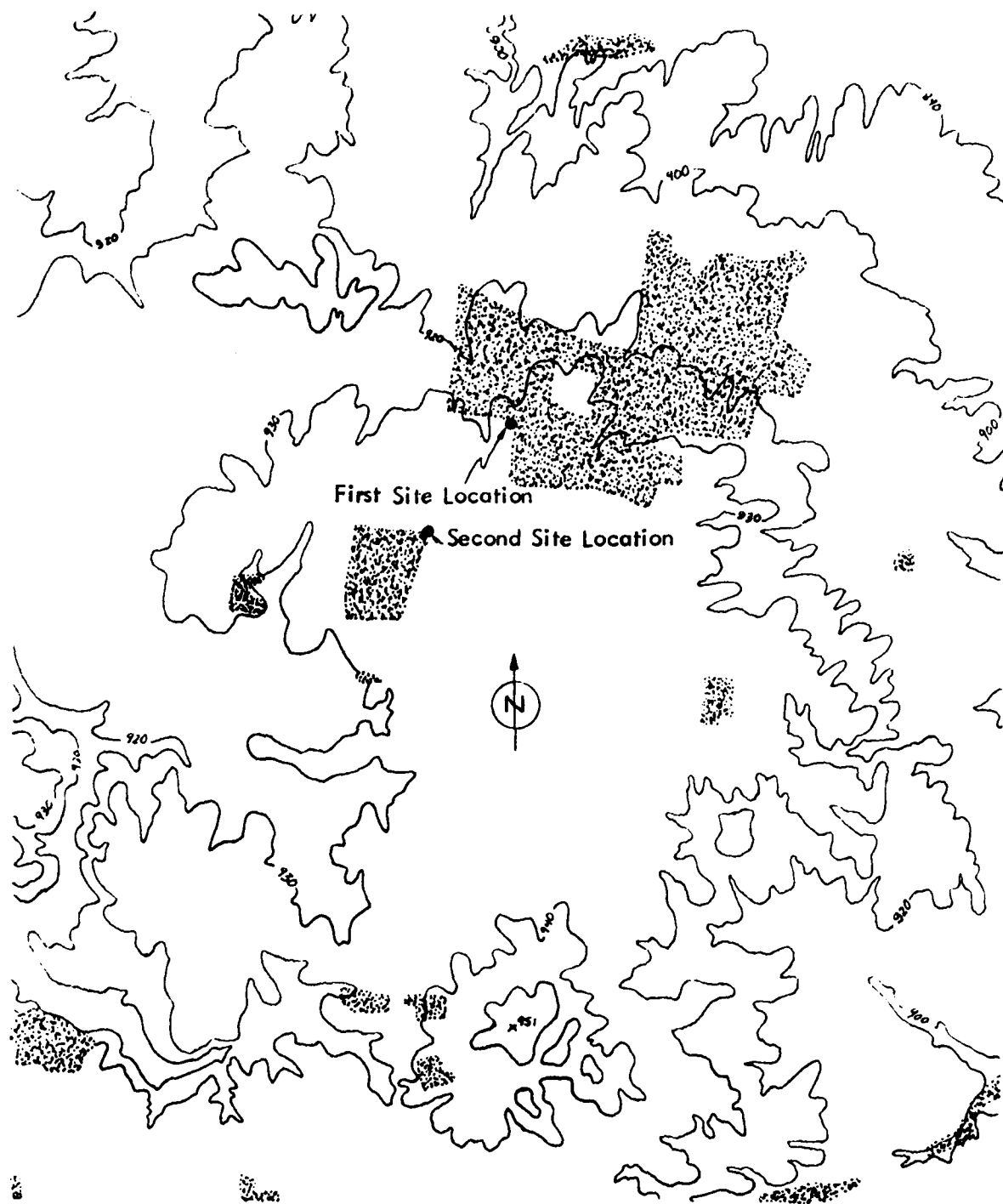
Figure 5-29. Topology and Tree Boundaries for the Temporary, Experimental
Washington Court House, Ohio, Communications Site.

Figure 5-30. Temporary Site Set Up by Ohio University for Signal Strength
Measurements at Washington Court House, Ohio.
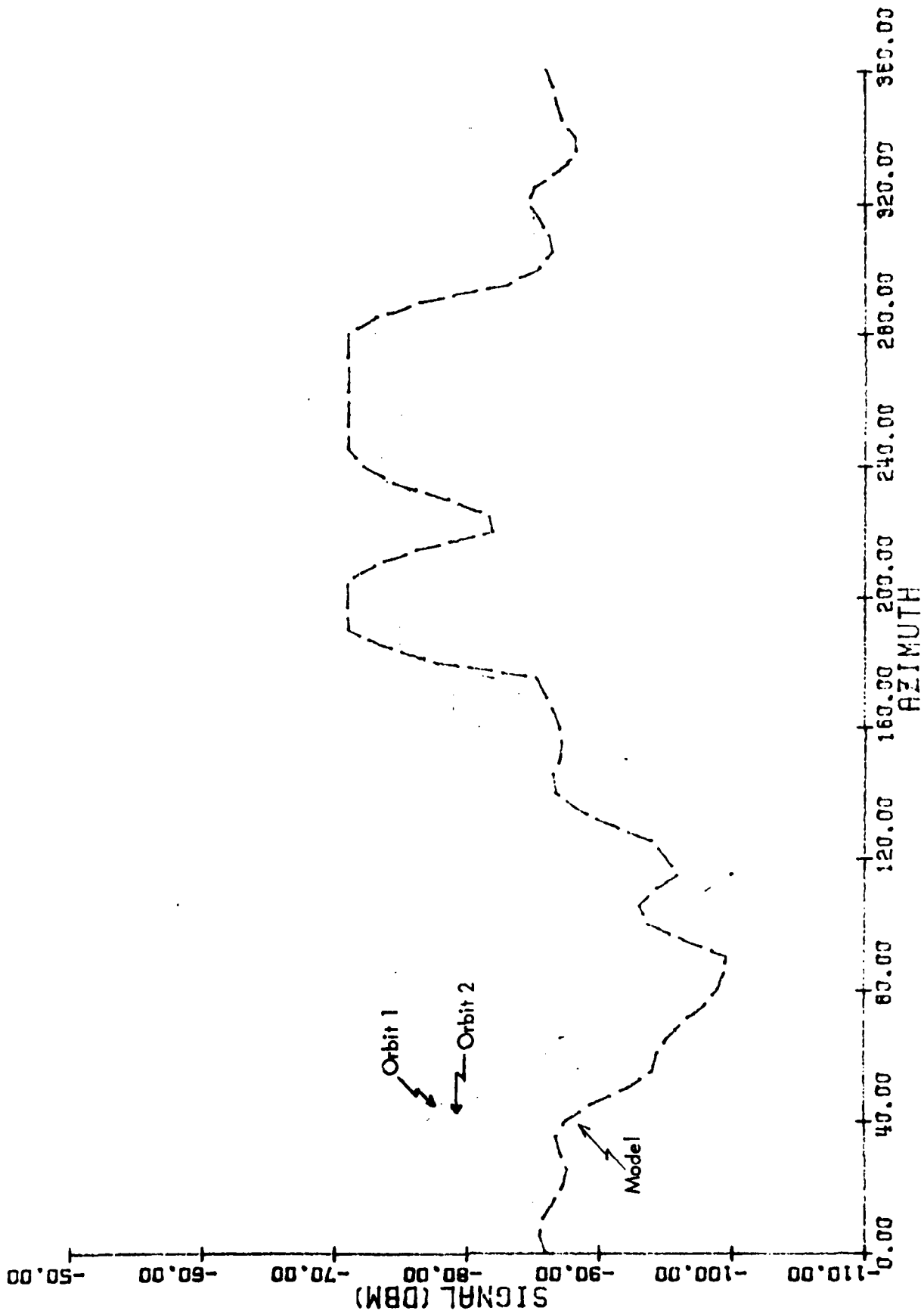
Figure 5-31. Measured and Modeled Signal Strength Values for two 1200' AGL, 8 nm Orbits Around the Experimental Washington Court House, Ohio Site. Modeled values are plotted with the dashed line.

-129-
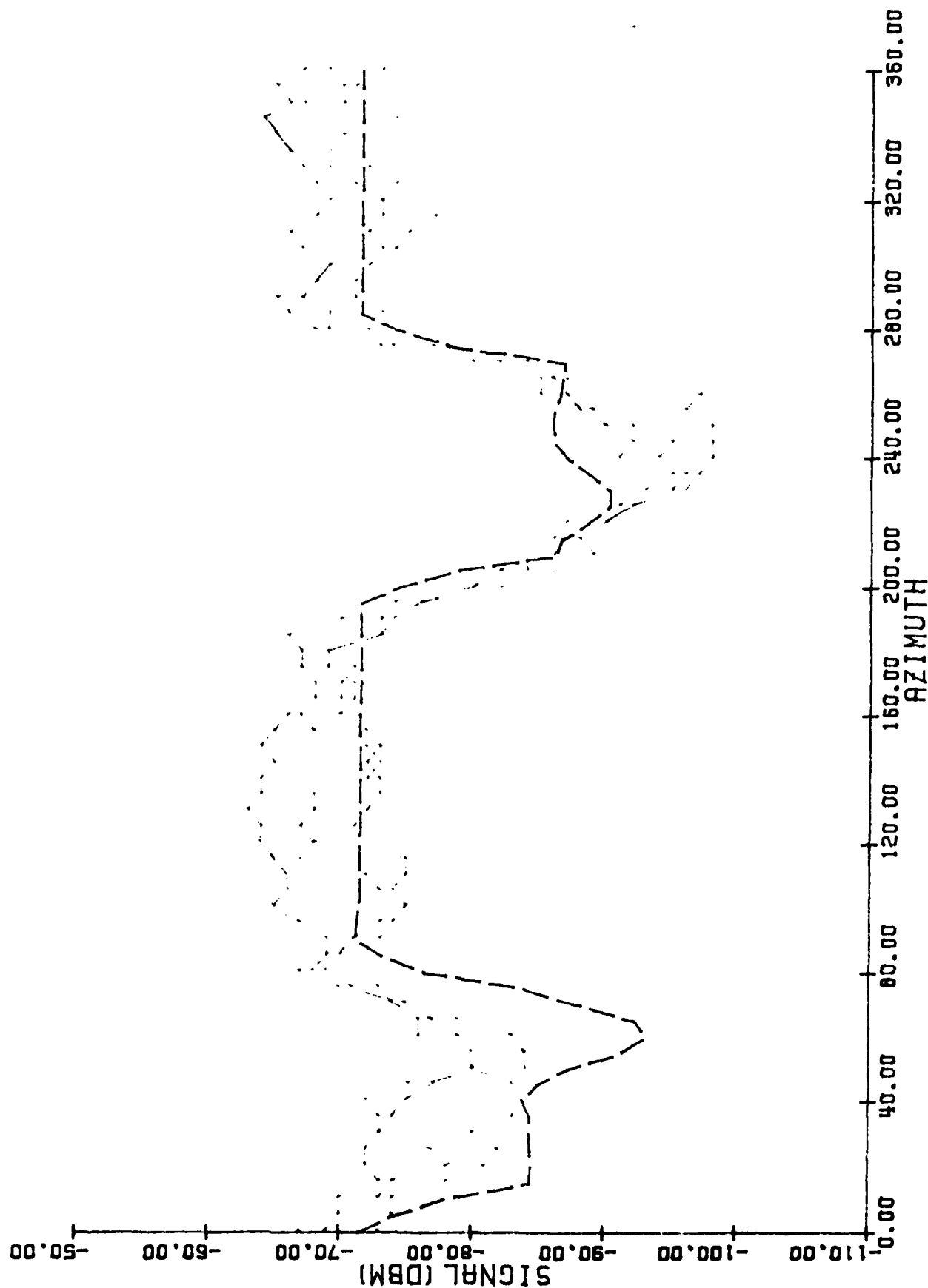
Figure 5-32. Measured and Predicted Signal Strength for a Second Site Location at Washington Court House, Ohio, for 1200' AGL, 8 nm Orbit. The Prediction, shown with the dotted line, was made prior to the measurements.

CONTOUR INTERVAL 20 FEET

Figure 5-33. Topographical Map of the Ohio University Airport and Vicinity.

site difficult to model, referring to the map of Figure 5-33, are those terrain variations between contour lines that are now shown on the topographical map as a result of quantization. In fact, an on-site inspection shows terrain elevation variations of nearly 20 feet in places where the topographical map shows flat terrain; this is an obvious consequence of quantization. Further confounding of the modeling effort results from areas of sparse tree cover that are difficult to define in terms of the phenomenon addressed in Section III.

Measured data were collected at the Ohio University Airport site on March 9, 1981 during two 8 nm, 2500' MSL altitude orbits around the site; transmitting frequency was 123.2 MHz. The ground-based antenna was temporarily positioned above a hanger at the airport 45' above ground level. Transmitter power was 4 Watts, and a Piper Cherokee aircraft was used for data collection.

Measured and GTD/Forest modeled data for the Ohio University Airport site are presented in Figure 5-34. Clearly, close agreement between modeled and measured data is not achieved at this site, although a more realistic estimate is provided by the GTD/Forest model than would be realized by the inverse-square, free-space estimate shown in Figure 5-34.

Also seen in Figure 5-34 is an unrealistically low estimate of signal strength by the GTD/Forest model. The reason for this low estimate is that the model input data indicates that the terrain is considerably smoother than it actually is, and hence the model will calculate a more coherent, specular reflection than actually exists. Such a modeling deficiency can be compensated for by assigning a terrain roughness factor to each terrain profile to account for diffuse scattering by rough terrain; however, such an empirically-based effort would require considerably more measured data than is presently available.

Present indications are that the actual signal strength for a site containing rough, rapidly-varying terrain elevation within the reflecting zone will be bounded from above by the free-space estimate, and from below by the GTD/Forest estimate. Further work into a study of irregular terrain will likely provide insight into the modeling deficiency addressed here.

7.   Athens, Ohio. Athens, Ohio is located in the foothills of the Appalachian Mountains in Southeastern Ohio. A temporary site was strategically located in Athens, Ohio in order to enable an evaluation of GTD model performance for vertical polarization in the vicinity of diffractive ridges for vertical polarization. A topographical map of the area near the temporary site is shown in Figure 5-35. Because all of the terrain characteristics of interest are located within a 90° azimuth sector, only partial orbits ranging from 90° to 180° azimuth were flown. Four aircraft altitudes, from 2500' MSL to 3500' MSL in 500' increments were investigated. With a 15' ground-based antenna height above a 635' MSL site elevation, these
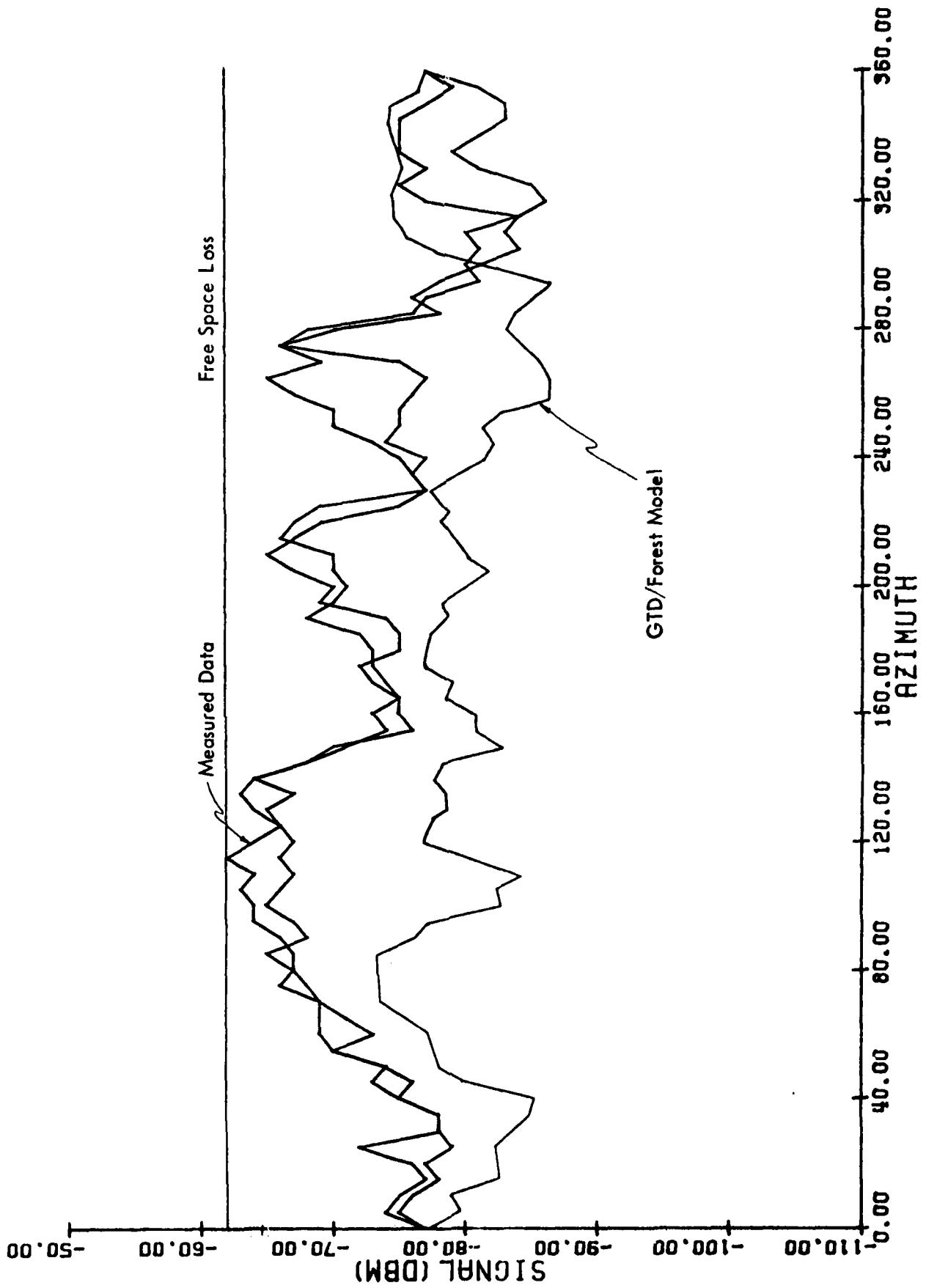
Figure 5-34. Modeled and Measured Signal Strength Data for an 8 NM, 2500' Orbit Around a Temporary Site Located at the Ohio University Airport.

-133-
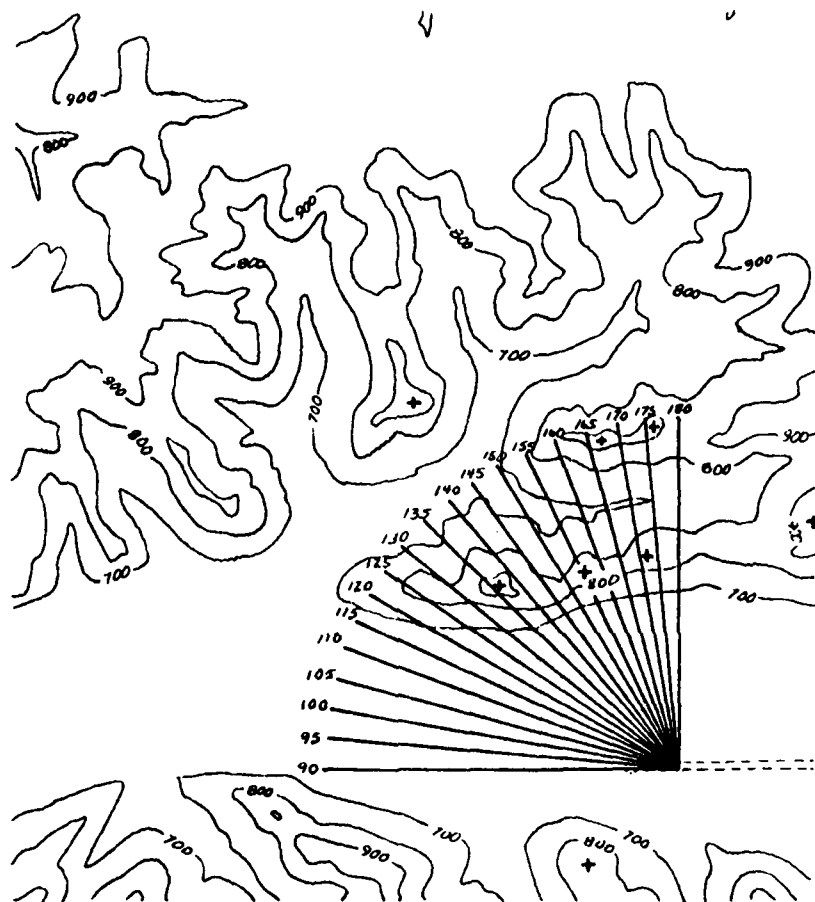
Figure 5-35. Topographical Map of the Vicinity of the Temporary Site Installed at Athens, Ohio. Terrain Contours are in 100' intervals; scale 1:24000.

-134-

aircraft elevations correspond to elevation angles of 1.59°, 2.18°,
2.77° and 3.35° with respect to the ground-based antenna. Referring
to the topographical map of Figure 5-35, it is seen that the local
horizon elevation angle with respect to the ground-based antenna
varies from 0.15° at 90° azimuth, to 5.83° at 135° azimuth. Thus, the
orbits flown place the aircraft above, near, and beyond the shadow
boundary of the diffractive ridge.

Measured and modeled data from both the ITS and GTD/Forest models
are presented in Figures 5-36 through 5-39 for all four altitudes
given above. As seen in these figures, close agreement between the
GTD/Forest model data and measured data except for the 2000' altitude
orbit, where a significant divergence is observed beyond 150° azimuth.
The source of the error is in the GTD routine that calculates diffrac-
tion coefficients. As stated, the measurements presented here enable
the first evaluation of the GTD model to be performed for vertical
polarization; it is likely that this new information can be used to
correct the deficiency observed for the 2000' orbit. However, the
existing deficiency indicated by the 2000' altitude orbit data is not
considered critical for practical site modeling, because a 2000' alti-
tude orbit with respect to the temporary site at Athens does not
represent conditions that would be encountered at an operational faci-
lity.

The piecewise linear approximations to the terrain at the Athens
site are depicted in Figure 5-40(a) and (b). Referring to this
figure, it is seen that for azimuth sectors between 90° and 110°, the
terrain is modeled as perfectly flat and level. Terrain in azimuth
sectors from 115° to 180° is modeled as flat and level up to the base
of the hill, rising linearly to the peak of the ridge, and then
descending linearly beyond the peak. Although the coordinates of
points 2 through 4, using the notation of Figure 5-40(b)m, vary from
profile to profile within the azimuth sector indicated, the general
trends shown in the figure are characteristic of the terrain. Also
shown in Figure 5-40(b) is the actual terrain contour, and the modeled
contour in the vicinity of Point 2. The coordinates of Point 2 were
chosen such that the modeled wedge angle, denoted Ψ_w in Figure
5-40(b), was the same as the wedge angle of the terrain. The location
of Point 3 was taken directly from the topographical map; Point 4 was
selected to be representative of the slope along the descent from the
peak, again with the intent of defining the modeled wedge angle
accurately. Care is taken to insure that the modeled wedge angle is
accurate because the value of the wedge angle is a parameter in the
GTD model calculation of diffraction coefficients.

Tree attenuation was not considered by the GTD/Forest model at the
Athens site even though significant tree cover does exist within the
azimuth sectors containing the diffractive ridge. Tree effects were
not calculated because the only significant propagation path affecting
received signal strength for beyond line-of-sight reception is the
diffracted ray which propagates from the ground-based antenna to the
local horizon, and is then re-radiated to the aircraft. Because the
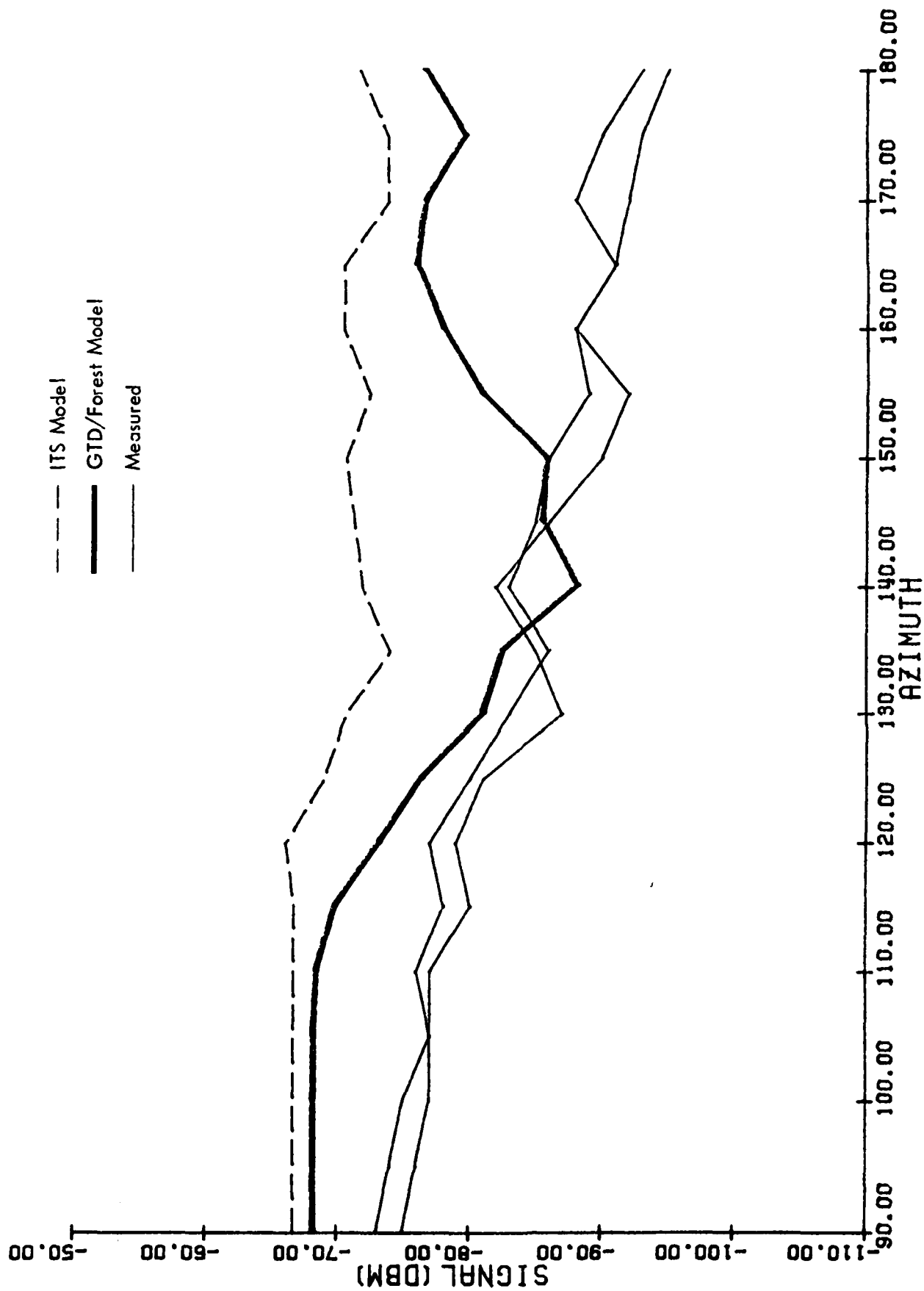
Figure 5-36. Measured and Modeled Data for an 8 NM, 2000' Altitude Orbit Around a Temporary Site in Athens, Ohio.
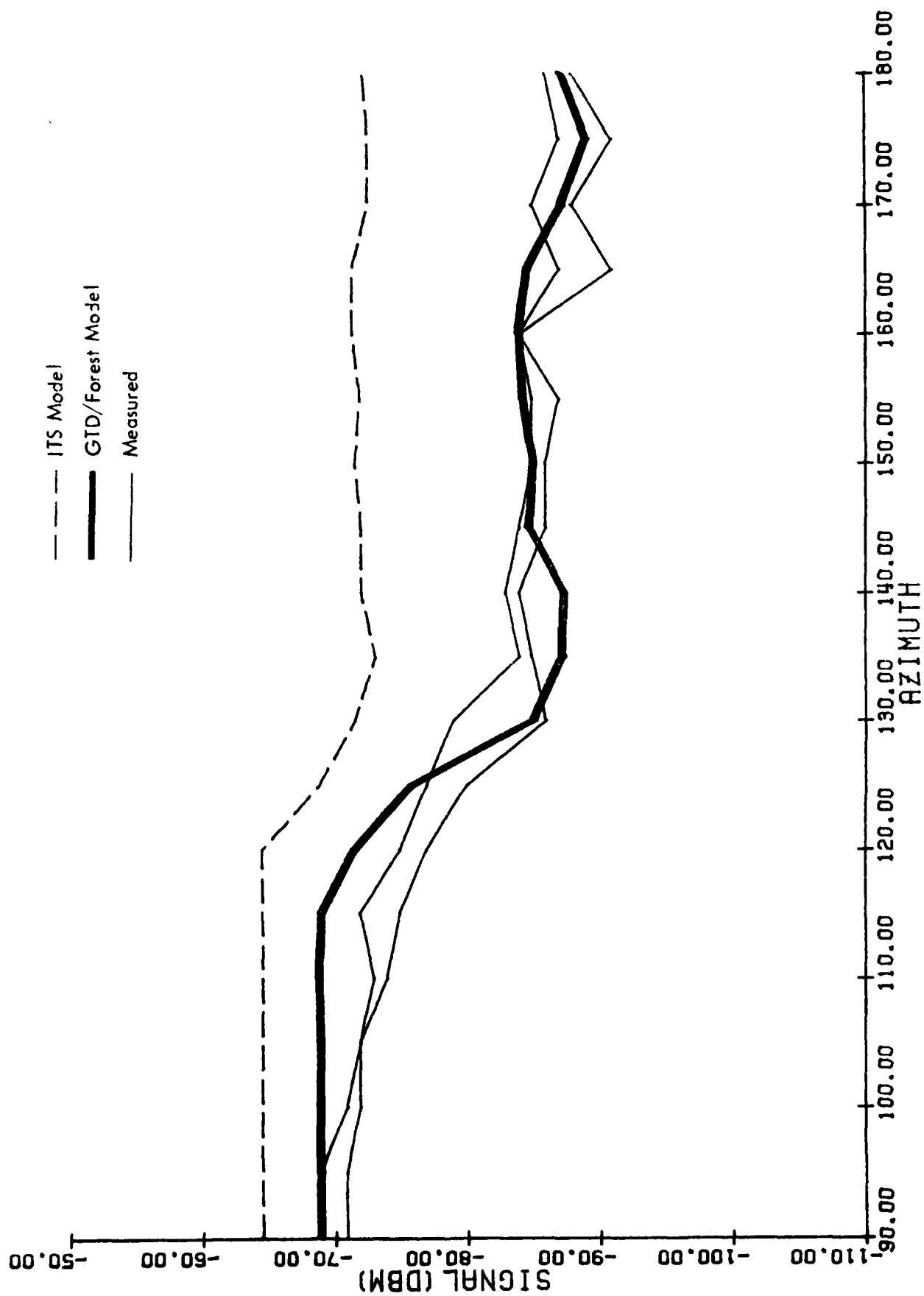
Figure 5-37. Measured and Modeled Data for an 8 NM, 2500' Altitude Orbit Around a Temporary Site in Athens, Ohio.
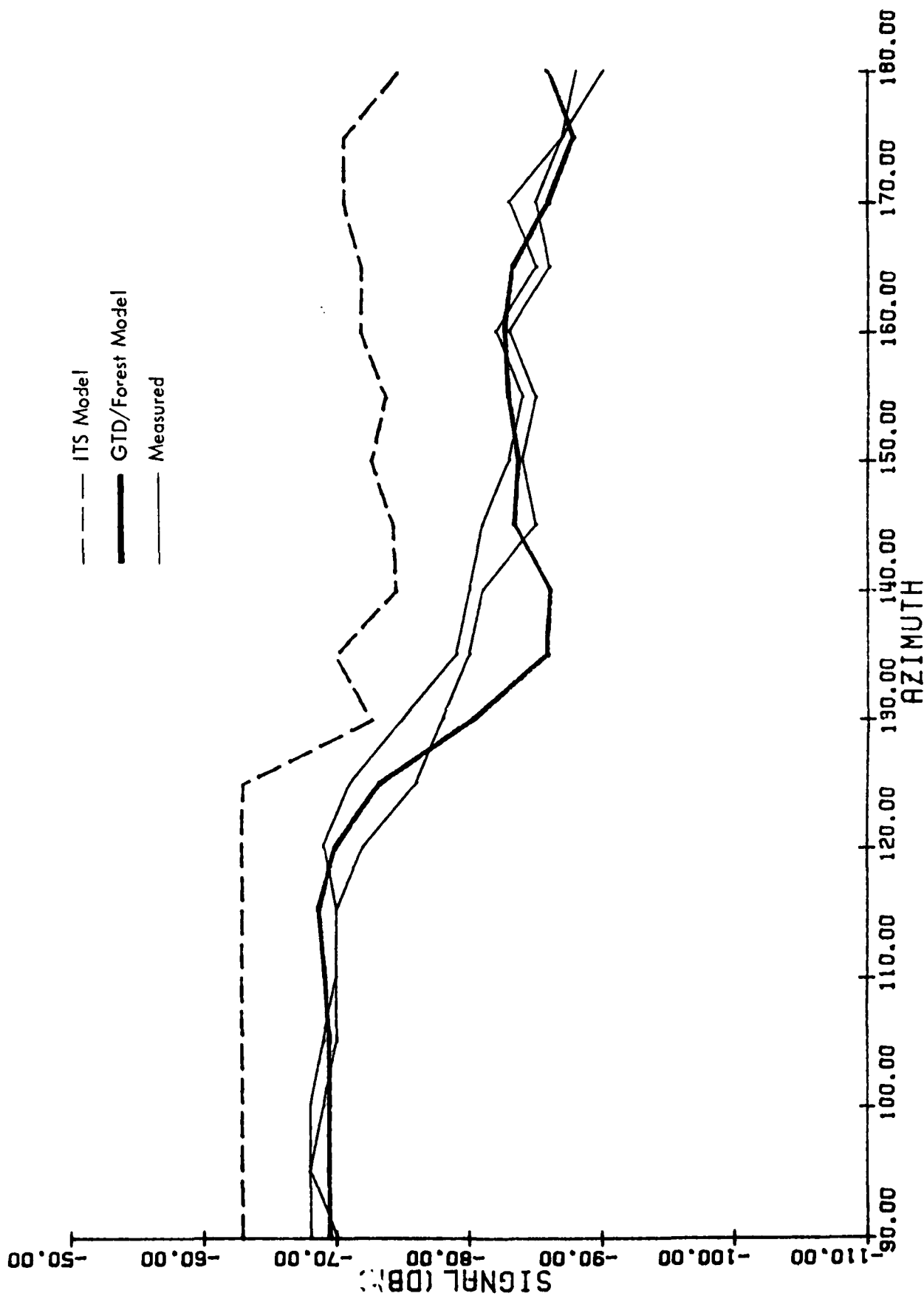
Figure 5-38. Measured and Modeled Data for an 8NM, 3000' Altitude Orbit Around a Temporary Site in Athens, Ohio.

-138-
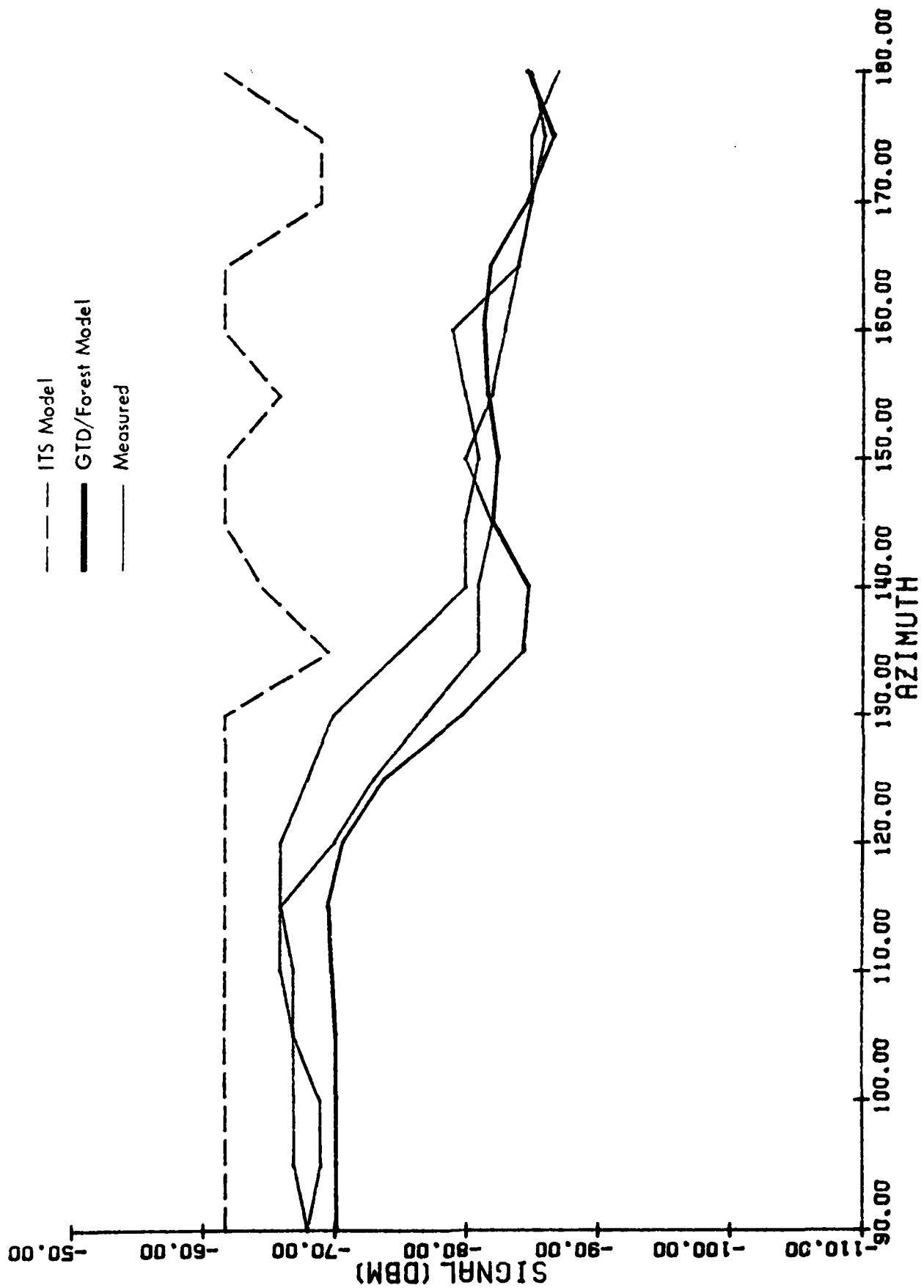
Figure 5-39. Measured and Modeled Data for an 8NM, 3500' Altitude Orbit Around a Temporary Site at Athens, Ohio.

-139-

Ground-Based
Antenna

Modeled Terrain Profile
(Azimuth Sectors 90°→110°)

(1)

(2)

4000'

(a)

Actual Terrain
Profile

Modeled Terrain Profile
(Azimuth Sectors 115°→180°)

ψ_ω

(3)

(4)

(1)

(2)
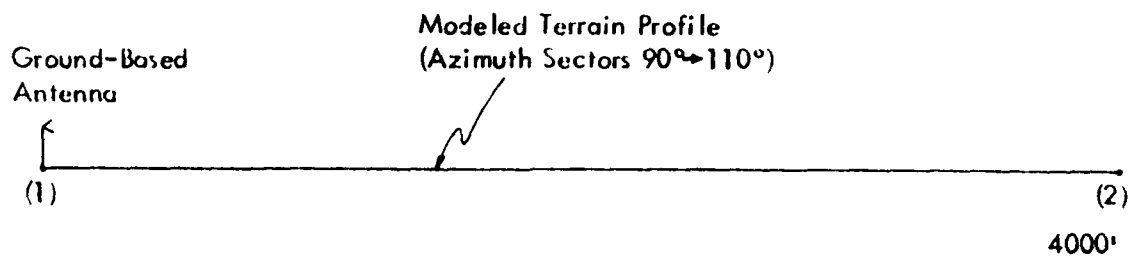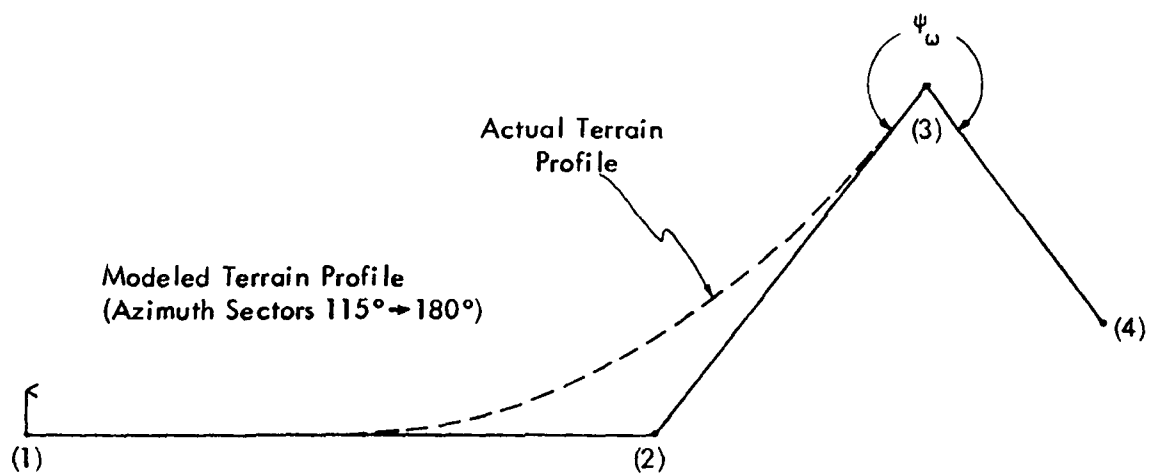
(b)

Figure 5-40. Terrain Data Used to Model the Athens, Ohio Site with
the GTD/Forest Model.

local horizon at the Athens site is in excess of 3° for azimuth sectors containing significant tree cover, the criterion of near-grazing incidence, as discussed in Section III, is not met. Consequently, signals cancellation due to tree reflections is not predicted by the theories presented in this report; the measured data presented in Figures 5-36 through 5-39 support this claim.

The ITS model requires that input data defining terrain contours be specified in regular intervals. The input data used to generate the ITS model presented in Figures 5-36 through 5-39 were created using 1750' intervals between data points. For azimuth sectors where the terrain is generally flat (90° to 110° azimuth), the ITS terrain data indicate perfectly flat terrain extending to 3500' followed by terrain that varies 100' in elevation every 1750' for the extent of the profile. The 100' variations in terrain elevation are included in the data file to enable a reasonable estimate of terrain roughness, necessary for ITS model operation, to be made. Terrain profiles containing diffractive ridges are modeled as flat to 1750' from the ground-based antenna, and then rising to a peak at 3500'. The height of this peak at 3500' is calculated so that its elevation angle with respect to the ground-based antenna is the same as the true elevation angle. This modeling procedure was followed because the ITS model estimate of below line-of-sight loss is based upon the angle below the shadow boundary. Measured data at the Athens, Ohio site were collected by Ohio University on March 12, 1981 using a Beechcraft Model-35 aircraft. Transmitter power was 4 Watts at a frequency of 123.2 MHz.

The measured and modeled results obtained at the Athens site verify proper operation of the GTD model for vertical polarization in addition to validating some of the assumptions presented in Section III regarding tree effects. ITS model results do not show as close an agreement with measured data as is realized with the GTD/Forest Model, however, this is an expected result for reasons discussed in Section III. Finally, it should be noted that all model results were generated prior to data collection.

VI. CONCLUSIONS

The work presented in this report represents an in depth study of coverage-area prediction at VHF for low power, short range, ground-to-air propagation. An extensive data collection effort has been performed to obtain accurate signal strength data in order to isolate predominant factors affecting signal strength. In addition, propagation modeling techniques have been evaluated with respect to measured data to provide insight into model capabilities and limitations. Based upon this work, the following conclusions are offered:

1. Significant attenuation of the received signal (10-15 dB) due to tree effects within line of sight is observed for low elevation angle reception. Based upon this finding, RCAG facility antennas should be positioned so that the Fresnel Ellipse of the propagation path between the ground and airborne antennas does not intersect trees.

2. Existing modeling techniques do not consider tree effects when estimating received signal strength, which may result in significant errors.

3. A GTD terrain scattering model, modified for this task to account for tree attenuation, has provided modeled data which are in close agreement with measured data for several typical sites. This new model, called the GTD/Forest model, has a demonstrated prediction capability for both within and beyond line-of-sight propagation paths.

4. Accurate and repeatable airborne signal strength measurements can be performed using both large and small aircraft and standard antennas.

5. Antenna pattern distortion caused by scattering from the supporting tower, lightning rods, and other antennas on the tower is negligible for a standard RCAG tower configuration.

6. There is no measurable difference in performance characteristics between the circularly-polarized Swastika antenna and the vertically-polarized TACO antenna.

7. No discernable variation in coverage area is observed with seasonal changes.

8. Indications are that modeling capability can be enhanced further by the inclusion of a terrain-roughness factor into the GTD/Forest model. Such an effort will require more measured data than is available at present.

VII. RECOMMENDATIONS

The newly-developed propagation model presented in this report has provided accurate estimates of signal strength for several sites representing a variety of propagation path conditions. The means to determining confidence levels for the model's predictions is to obtain additional validations through measured and modeled data. Such an effort will enable a figure of merit to be assigned to the model output as well as to expose any remaining deficiencies in the model.

The model presented here is designed specifically for estimating signal strength near the horizon. For receiver locations near the horizon, the assumption is made that specular reflection occurs from tree tops and the ground plane; measured and modeled data comparisons show that this assumption is correct. However, this assumption is not correct for receiver locations well above the horizon, where modeled data will be influenced by non-existent vertical lobing effects. Thus, if modeled results are desired for receiver locations above the horizon, further work into diffusion or scattering from irregular surfaces should be performed to determine an appropriate correction factor for the reflection coefficient to account for non-specular reflected signal energy.

VIII.   ACKNOWLEDGEMENTS

IX.   REFERENCES

[1]   U. S. National Aviation Standard for the VHF Air-Ground
        Communication System, FAA Order 6510.6, November, 1977.

[2]   Enroute Communications ARTCC Installation Standards Handbook,
        Department of Transportation, Federal Aviation
        Administration.

[3]   Electronics Engineers' Handbook, Fink, G., McGraw-Hill, 1975,
        Section 18.

[4]   Advances in Radio Research, edited by J. Saxton, Academic
        Press, Volume 1, 1964.

[5]   Smith, Robert D., A Comparison of Measured Data and ITS Model
        Predictions, FAA Report RD-77-106, January, 1978.

[6]   Weeks, W. L., Antenna Engineering, McGraw-Hill, 1968.

[7]   Kraus, J. D., Antennas, McGraw-Hill, 1950.

[8]   Beckmann and Spizzichino, The Scattering of Electromagnetic
        Waves from Rough Surfaces, Volume 4, MacMillian, 1963,
        p. 3 and Chapter 5.

[9]   Op. Cit., Beckmann and Spizzichino, p. 32.

[10]   Richmond, J. H., Radiation and Scattering By Thin-Wire
        Structures in the Complex Frequency Domain,

[11]   Perini, J., Users Manual for the Antenna Pattern Distortion
        Computer Program-Version IV, Rome Air Development Command
        Report RADC-TR-78-263, January, 1979.

[12]   Conversation with Dr. J. Perini on December 10, 1979.

[13]   Coyle, James J., Test and Evaluation of Air/Ground
        Communications Antennas, FAA Report NA-77-39, June, 1978.

[14]   Harrington, Roger F., Field Computation by Moment Methods
        Macmillian Series in Electrical Engineering

[15]   Gierhart and Johnson, Computer Programs for Air/Ground
        Propagation and Interference Analysis 0.1-20 GHz., FAA
        Report RD-703-103, September, 1973.

[16]   Gierhart and Johnson, Propagation Model (0.1 to 20 GHz.)
        Extensions for 1977 Computer Programs, FAA Report RD-77-129,
        May, 1978.

[17]   Hufford, G. and Longley, A., Characterization of a VHF
        Air-Ground Channel, OT Report 74-47, October, 1974, p. 15.

[18]   Op. Cit., Hufford and Longley, pp. 17-21.

[19]   Op. Cit., Smith, Robert D.

[20]   Kraus, J. D., Electromagnetics, McGraw-Hill, Second
        Edition, 1973, pp. 465-472.

[21]   Stratton, J. A., Electromagnetic Theory, McGraw-Hill,
        1941, pp. 460-468.

[22]   ILS Glide Slope Performance Prediction, Volume B,
        S. Morin et. al., FAA Report RD-74-157-B, September, 1941.

[23]   Rondini, R., A Study of Diffraction of Electromagnetic
        Waves Around Large Stationary Aircraft and Its Effects
        on Instrument Landing System Guidance Signals, Ph.D.
        dissertation, Ohio University, June, 1976.

[24]   Sommerfield, A., Mathematische Theorie der Diffraktion,
        Math. Ann. Vol. 47, 1896.

[25]   Keller, J. B., Geometrical Theory of Diffraction, Journal
        Optical Society of America, Vol. 52, pp. 116-130, 1962.

[26]   Kouyoumjian, R. G., and P. H. Pathak, A Uniform Geometrical
        Theory of Diffraction for an Edge in a Perfectly
        Conducting Surface, IEEE Proceedings, Vol. 62, No. 11,
        pp. 1448-1461, November 1974.

[27]   Luebbers, R. J. et al, the Ohio University ILS Modeling
        Center, Technical Memorandum #S-46, November, 1977.

[28]   Wait, Ott, and Telfer, Workshop on Radio Systems in
        Forested and/or Vegetated Environments, Army communications
        command, Fort Huachuca, Arizona AD-780 712, February, 1974.

[29]   Johnk, Carl T. A., Engineering Electromagnetic Fields and
        Waves, Wiley, 1975, p. 173.

[30]   Jansky and Bailey Research and Engineering Department,
        Tropical Propagation Research, Final Report, Volume 1,
        Atlantic Research Corp., Alexandria, Va., 1966.

[31]   Parker, H. W., and Makarabhiromya, W., Electric Constants
        Measured in Vegetation and in Earth at Five Sites in
        Thailand, Stanford Research Institute Special Technology
        Report 43, Menlo Park, California, 1967.

[32]   Pounds, D. J. and LaGrone, A. H., Considering Forest
        Vegetation as an Imperfect Dielectric Slab, Electrical
        Engineering Research Laboratory, University of Texas, Austin,
        Report 6-53, May, 1963.

[33]   Beckmann, P. and Spizzichino, A., The Scattering of Electro-
        magnetic Waves from Rough Surfaces, MacMillian, International
        Series of Monographs on Electromagnetic Waves, Volume 4,
        1963, pp. 9-10.

[34]   Harrington, Roger F., Time-Harmonic Electromagnetic Fields,
        McGraw-Hill, 1961, p. 58.

[35]   Dence, D. and Tamir, T., Radio Loss of Lateral Waves in
        Forest Environments, Radio Science, Volume 4, Number 4,
        pp. 307-318, April, 1969.

[36]   Tamir, T., On Radio-Wave Propagation in Forest Environments,
        IEEE Transactions on Antennas and Propagation, Volume AP-15,
        Number 6, November, 1967.

[37]   Brekhovskikh, L. M., Waves in Layered Media, Second Edition,
        Academic Press, 1980, Chapter 4.

[38]   Op. Cit., Brekhovskikh, p. 3.

[39]   Arfken, G., Mathematical Methods for Physicists, Second
        Edition, Academic Press, 1970, p. 373.

[40]   Op. Cit., Brekhovskikh, Section 27.

[41]   Tamir, T., Inhomogeneous Wave Types at Planar Structures:
        I. The Lateral Wave, Optik, Sonderabdruck 36. Band (1972)
        Seite 209-232.

[42]   Bueche, F., Introduction to Physics for Scientists and
        Engineers, Second Edition, McGraw-Hill, 1975, p. 632.

[43]   Jenkins, F. and White, H., Fundamentals of Optics, Third
        Edition, McGraw-Hill, 1957, p. 354.

[44]   Reference Data for Radio Engineers, Howard Sams & Co.,
        Fifth Edition, 1972, Section 26-16.

[45]   Fink, D., Electronic's Engineers Handbook, First Edition,
        McGraw-Hill, 1975, Section 18-66.

[46]   Coyle, J., Test and Evaluation of Air/Ground Communications
        for Helicopter Operations in the Offshore New Jersey,
        Baltimore Canyon Oil Exploration Area, FAA Report
        No. RD-79-123, January, 1980.

[47]   Hansen, J. and Webster, A., Advanced Communications Systems
        Support, FAA Report RD-78-11, January 1978.

[48]   Johnk, Carl, Engineering Electromagnetic Fields and Waves,
        Wiley, 1975.

[76] Geological Survey Maps can be ordered from: Branch of
Distribution, U.S. Geological Survey, Box 25286, Federal
Center, Arlington, Virginia 22202.

X. APPENDICES

A. __Calculation of the Complex Reflection Coefficient for__
__Vertical Polarization.__ As a vertically polarized wave strikes fini-
tely-conducting ground, a certain amount of energy is transmitted into
the ground, and the remainder is reflected. Further there will be a
phase delay experienced by the reflected ray; the magnitude and phase
of the reflected wave is determined by the complex reflection coef-
ficient Γ. The geometry of the problem is presented in Figure A-1.
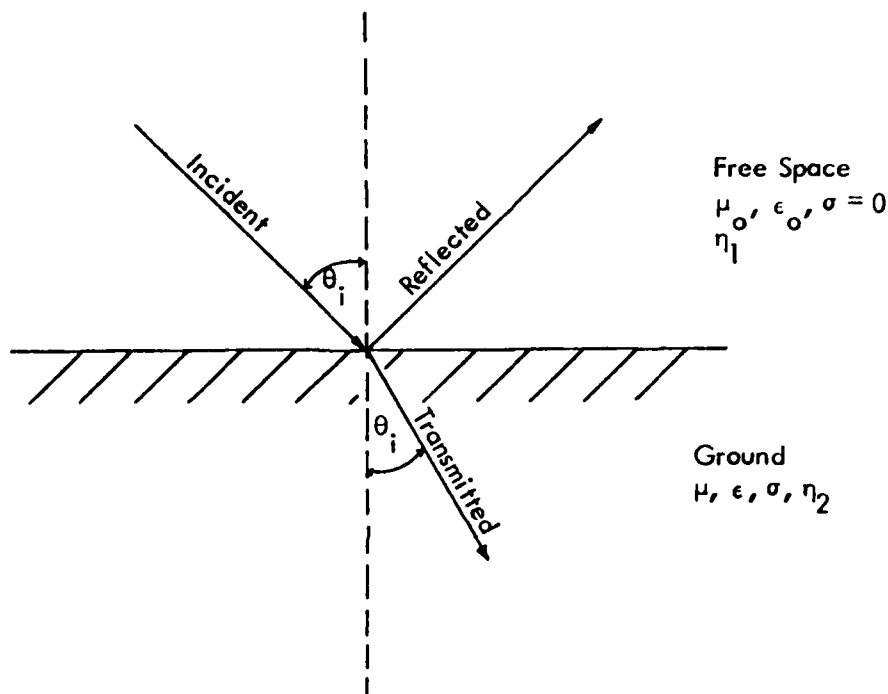
Figure A-1. Reflection at Free-Space, Ground Boundary.

The reflection coefficient is determined by [48]:

$$\Gamma = \frac{n_2 \cos\theta_t - n_1 \cos\theta_i}{n_2 \cos\theta_t + n_1 \cos\theta_i} \qquad\qquad (A-1)$$

where n_1 and n_2 are the intrinsic impedances of free-space and the
particular ground under consideration, respectively; these are typi-
cally complex numbers.

The intrinsic impedance is defined by:

$$\eta = \frac{\dfrac{\mu}{\epsilon'}}{[1 + (\frac{\epsilon''}{\epsilon'})^2]^{1/4}} \; e^{j(1/2 \, arc \, tan(\epsilon''/\epsilon'))} \; \Omega \tag{A-2}$$

where $\epsilon' = \epsilon$ and $\epsilon'' = \sigma/\omega$

Subroutine KCGAM, shown in Figure A-2, computes the reflection co-efficient for a given incident angle, given in the call statement, and ground constants, transferred in COMMON BLOCK PARAM.

```
      SUBROUTINE KCGAM(THETAI,CGAMAV)
C KCGAM CALCULATES THE COMPLEX REFLECTION COEFFICIENT (CGAMMA) CORRES-
C PONDING TO INPUT PARAMETERS THETAI, THE INCIDENCE ANGLE IN DEGREES,
C RHO, THE CONDUCTIVITY IN MHOS/METER, AND DIE, THE RELATIVE DIELECTRIC
C CONSTANT, AND FREQ IS THE FREQUENCY IN HERTZ.
      IMPLICIT COMPLEX*16(C)
      IMPLICIT REAL*8 (A,B,D-H,O-Z)
      COMMON /PARAM/ RHO,DIE,FREQ
      PI=3.14159265358979
      THETA=THETAI*PI/180.
      FREQ=125.D6
      OMEGA=2.*PI*FREQ
      UO=PI*4.D-7
      EO=8.85419D-12
      EP=DIE*EO
      EPP=RHO/OMEGA
      PHS=DATAN(EPP/EP)*.5
      CPHS=DCMPLX(0.DO,PHS)
      FNUM=DSQRT(UO/EP)
      DENOM=(1.+(EPP/EP)**2)**.25
      CNHAT=(FNUM/DENOM)*CDEXP(CPHS)
      XNO=DSQRT(UO/EO)
      STHETI=DSIN(THETA)
      XTHETI=DCOS(THETA)
      XTHETT=DSQRT(1.-(STHETI**2)/DIE)
      CGAMAV=-(CNHAT*XTHETT-XNO*XTHETI)/(CNHAT*XTHETT+XNO*XTHETI)
      RETURN
      END
```

Figure A-2.   Subroutine KCGAM.

B. Calculation of the Complex Propagation Constant. A SUBROUTINE to calculate the complex propagation constant, γ, as determined from Equations (3-2) through (3-4) is listed in Figure B-1. As seen in the COMMENT statements in SUBROUTINE CEXPON, input parameters are frequency, relative dielectric permitivity, and conductivity in mhos/meter. The output variable, CALBT, is a complex variable representing the complex propagation constant, γ.

```
      SUBROUTINE CEXPON(CALBT,EF,RHOF)
C SUBROUTINE CEXPON DETERMINES THE COMPLEX PROPAGATION CONSTANTS FOR A
C MEDIUM FROM INPUT PARAMETERS EF, THE RELATIVE DIELECTRIC PERMITIVITY,
C AND RHOF, THE CONDUCTIVITY IN MHOS/METER.  THE FREQUENCY IS SPECIFIED
C VIA THE COMMON BLOCK /ANTNNA/.  THE OUTPUT VARIABLE CALBT IS A
C DOUBLE-PRECISION, COMPLEX VARIABLE EQUAL TO ALPHA+J BETA.
      IMPLICIT REAL*8 (A,B,D-H,K,O-Z)
      IMPLICIT COMPLEX*16 (C)
      COMMON /ANTNNA/ XP(40),YP(40),ZP(40),K,FREQ,N
      PI=3.14159265358979
      EO=8.85419D-12
      UO=PI*4.D-7
      OMEGA=FREQ*PI*2.DO
      EP=EF*EO
      EPP=RHOF/OMEGA
      SQ2=DSQRT(2.DO)
      FACT=DSQRT(1.DO+(EPP/EP)**2)
      FACT2=DSQRT(FACT-1.DO)
      KONST=(OMEGA*DSQRT(EP*UO)/SQ2)
      ALPHA=KONST*FACT2
      FACT3=DSQRT(FACT+1.DO)
      BETA=KONST*FACT3
      CALBT=DCMPLX(ALPHA,BETA)
      RETURN
      END
```

Figure B-1. Listing of SUBROUTINE CEXPON.

C.   Program Listing and Flow Diagram for GTD/Forest Model
Implementation.   A flow diagram showing program sequence and data
transfer is shown in Figure C-1. The GTD/Forest computer model is
written in modular form with specific operations performed by
SUBROUTINES rather than the MAIN program whenever possible. For this
reason, the MAIN program, listed in Figure C-2, is relatively small
when compared to some of the SUBROUTINES.

Referring to the flow diagram and program listing of Figures C-1
and C-2, it is seen that the first program operation is to initialize
constants, such as frequency, wavelength, phase constant, and, and to
set in values for the observation point (x,y,z). The particular
program shown calculates signal strength for a constant-radius orbit
around a site. This is accomplished in the program by positioning the
observation point at a fixed altitude and distance and computing
signal strength for terrain profiles along sampled radials to the
site. The sampling interval for all orbital data presented in this
report, both measured and calculated, is 5 degrees in azimuth. Thus,
to calculate the signal strength for an entire orbit, 72 radial pro-
files must be evaluated to cover the entire 360° sector.

After initializing constants and setting the observation point,
the next step in the program sequence is to read the non-terrain site
parameters such as transmitting antenna height, effective radiated
power, tree height, conductivity and permitivity of the trees, the
Fresnel Ellipse correction factor, and the fraction of the Fresnel
Ellipse to be considered in calculating the correction factor. The
above parameters remain constant for all azimuths with respect to the
site and hence only need to be read once. The program that reads site
data is KCDTCL and is listed in Figure C-3.

Continuing with the flow diagram of Figure C-1, the program reads
terrain profile data using SUBROUTINE KCDTCL. KCDTCL then calls a
SUBROUTINE BUILD, also listed in Figure C-3, which creates a second
terrain profile which includes forested areas. Both of these profiles
are made available to the MAIN program and SUBROUTINES via COMMON
BLOCK statements as indicated in the flow diagram. Subsequent to
reading the terrain profile and creating a forested profile, the GTD
SUBROUTINE, VOUILS, is called to perform the signal strength calcula-
tion. VOUILS in conjunction with KCTREE, which is listed in Figure
C-4, determines received signal strength based upon both terrain pro-
files.

The azimuth angle of the profile and signal strength value are stored
after VOUILS returns to the MAIN program.   A check is then made to
determine if there are additional terrain profiles to be read; if
there are, the program jumps back to KCDTCL to read the additional
files and then computes signal strength for that profile as described
above. If there are no additional profiles, the MAIN program converts
the signal strength values to decibels and creates data arrays com-
patible with plot routines. After these arrays have been created, the
program terminates.

With only minor modifications, the above program can compute coverage area, rather than signal strength at a particular location as is done presently, by incrementing the observation point distance from the transmitter until a below-threshold signal strength is calculated. The model output for coverage-area prediction is the maximum distance from the site for which sufficient signal strength is calculated versus azimuth angle.

Raw data from the GTD/Forest model representing signal strength versus azimuth or coverage area are plotted graphically under program control on a Hewlett-Packard Model 7203A Graphic Plotter. Examples of signal strength versus azimuth, both in rectangular and polar form, are seen in Section V of this report. Plots of coverage area as a function of azimuth are made in polar form with radial distances on the plot adjusted so that a one-to-one correspondence betweena specified map scale and the plotted scale is obtained. An overlay of the coverage-area plot can be placed over a map of the same scale, with the origin of the coverage-area plot centered over the modeled-site, revealing the predicted coverage area for that site.
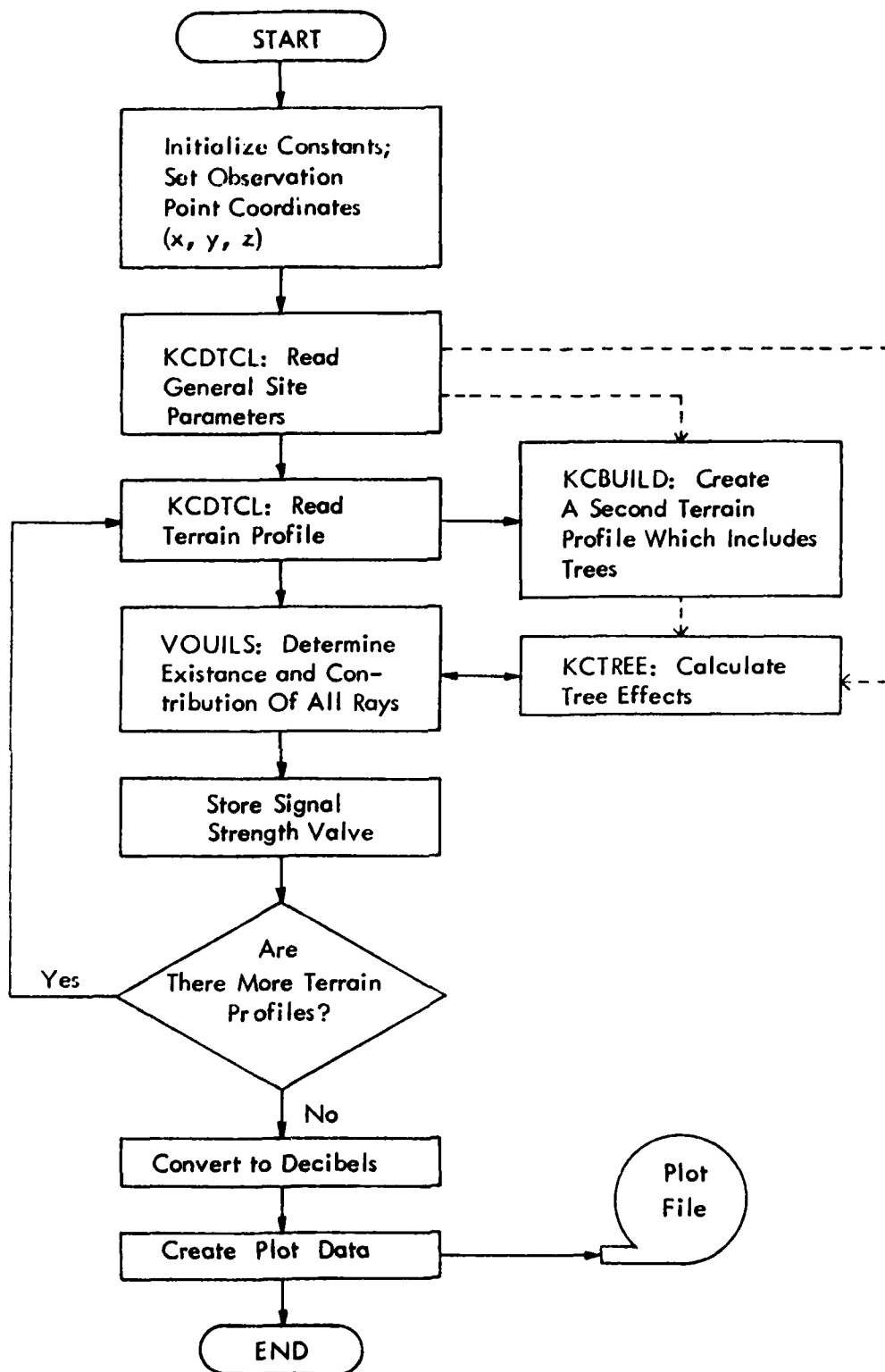
Figure C-1. Flow Diagram For GTD/Forest Computer Model: Dotted Lines Indicate Common Block Data Transfer.

```
      IMPLICIT REAL*8 (A,B,D-H,K,M,O-Z,$)
      IMPLICIT COMPLEX*16 (C)
      COMPLEX*16 ATTENU
      DIMENSION JANGLE(75),XMAG(75),DB(75)
      COMMON /TREE/ ATTENU,JPLATE(5),JCOR(5),JCOR2(5)
      COMMON /OBSVER/X,Y,Z
      COMMON /W/ ICON
      COMMON/ANTNNA/ XP(40),YP(40),ZP(40),K,FREQ,N
      COMMON /AZP/ AZD
      COMMON /PLATE/ XO(30),YO(30),ZO(30),NE
      LOGICAL MORE
C     ******************************************************************
C THIS IS THE MAIN PROGRAM THAT IMPLEMENTS THE GTD/FOREST MODEL.
C SITE PARAMETERS INCLUDING TERRAIN PROFILES ARE READ BY KCDTCL.
C THESE PARAMETERS ARE TRANSFERRED TO SUBROUTINES VIA THE ABOVE COMMON
C BLOCKS.  TREE EFFECTS ARE DETERMINED BY KCTREE WHICH IS CALLED FROM
C SUBROUTINE VOUILS.
C
C     ******************************************************************
C ICON IS A PRINT CONTROL WORD INDICATING IF A PRINTOUT IS DESIRED
      ICON=0
C ATTENU IS AN ATTENUATION CONSTANT USED BY THE GTD PROGRAM;
C IT IS SET TO (1,0) HERE SINCE ATTENUATION IS TO BE DETERMINED
C BY SUBROUTINE KCTREE.
      ATTENU=(1.,0.)
      N=1
      SPEED=9.8425197E8
      DPI=3.1415926535898*2.
      FREQ=125.E6
      XLAMDA=SPEED/FREQ
      K=DPI/XLAMDA
C (X,Y,Z) ARE THE COORDINATES OF THE OBSERVER
      X=0.
      Y=48.64D3
      Z=2.00D3
C KCDTCL READS TERRAIN DATA; AZ IS THE AZIMUTH OF THE TERRAIN
C PROFILE; MORE=.TRUE. INDICATES ADDITIONAL PROFILES.
10    CALL KCDTCL(AZ,MORE)
      IF(.NOT.MORE) GO TO 20
C VOUILS AND VGROUN ARE THE GTD ROUTINES
      CALL VOUILS(CET,CEPSI)
C CET IS THE VERTICAL ELECTRICAL FIELD AT (X,Y,Z)
      CALL VGROUN(CET,1,1)
15    JAZ=AZ/5.+1.
      XMAG(JAZ)=CDABS(CET)
      JANGLE(JAZ)=AZ
      DB(JAZ)=-78.+20.*DLOG10(XMAG(JAZ))
```

Figure C-2. Program Listing for MAIN Program.

```
C  JANGLE AND DB ARE OUTPUT ARRAYS OF AZIMUTH ANGLE AND SIGNAL STRENGTH
      WRITE(8,3) JANGLE(JAZ),DB(JAZ)
3     FORMAT(I3,F5.1)
      GO TO 10
20    STOP
      END
```

Figure C-2. (Continued).

```fortran
      SUBROUTINE KCDTCL(AZ,MORE)
      IMPLICIT REAL*8 (A,B,D-H,O-Z)
      IMPLICIT COMPLEX*16 (C)
      REAL*8 K
C KCDTCL READS A TERRAIN DATA FILE AND RETURNS THE INFORMATION IN
C /PLATE/, AZ IS THE AZIMUTH OF THE PROFILE, NE IS THE NUMBER OF
C DATA POINTS, AND MORE=FALSE INDICATES AN EOF
      COMMON /PLATE/ XO(30),YO(30),ZO(30),NE
      COMMON /OBSVER/ X,Y,Z
      COMMON /ANTNNA/ XP(40),YP(40),ZP(40),K,FREQ,N
      COMMON /AZP/ AZD
      COMMON /KTREE/ THT,EF,RHOF,YONEW(30),ZONEW(30),TYPE(30),NEW
      COMMON /CLAT/ XNEP,RATIO
      COMMON /CGAMMA/ CALBTO,CALBT
      DATA JSET/0/
      LOGICAL MORE
      XP(1)=0.
      YP(1)=0.
      IF(JSET.NE.0) GO TO 10
C READ ANTENNA DATA, ZP=ANTENNA HEIGHT(FEET MSL), ERP=EFFECTIVE
C RADIATED POWER(WATTS),THT IS THE TREE HEIGHT (FEET), EF IS THE
C RELATIVE DIELECTRIC PERMITIVITY OF THE FOREST MEDIUM, RHOF IS THE
C CONDUCTIVITY OF THE FOREST, XNEP IS THE FRESNEL ELLIPSE CORRECTION
C FACTOR, AND RATIO IS AMOUNT OF THE FIRST FRESNEL ELLIPSE TO BE
C CONSIDERED.
      MORE=.TRUE.
      READ 1, ZP(1),ERP,THT,EF,RHOF,XNEP,RATIO
1     FORMAT(7F8.0)
      RHOF=RHOF*1.D-7
      CALL CEXPON(CALBTO,1.D0,0.D0)
      CALL CEXPON(CALBT,EF,RHOF)
      WRITE(7,999) CALBT
999   FORMAT(2F15.8)
      WRITE(7,2) ZP(1),ERP,THT,EF,RHOF
2     FORMAT(1X,'THE ANTENNA IS AT',F6.1,' FEET MSL WITH AN ERP OF',
     ,F4.1,' WATTS'/' TREE HEIGHT=',F4.0,' FEET, REL.DIE.CONST.=',
     ,F10.7,'CONDUCT.=',D12.5)

      JSET=1
10    READ(5,3,END=30) XN,AZ
3     FORMAT(2F6.0)
C NE IS THE NUMBER OF DATA POINTS AND AZ IS THE AZIMUTH(DEGREES)
      NE=XN
C ********************************************************************
      WRITE(7,4)
4     FORMAT(1X/'   DISTANCE   ELEVATION   TYPE'/)
      DO 20 I=1,NE
C READ TERRAIN DATA: YO=DISTANCE FROM ANTENNA(FEET), ZO=TERRAIN
C ELEVATION MSL(FEET), TYPE=T(TREES)-C(CLEAR)-W(WATER)
```

Figure C-3.   Listing for SUBROUTINE KCDTCL.

```
          READ 5, YO(I),ZO(I),TYPE(I)
          YO(I)=YO(I)/1.0000
          ZO(I)=ZO(I)/1.0000
5         FORMAT(2F10.2,1X,A2)
          WRITE (7,6) YO(I),ZO(I),TYPE(I)
6         FORMAT(1X,2F10.1,A2)
20        CONTINUE
          CALL BUILD(AZ)
          RETURN
30        MORE=.FALSE.
          RETURN
          END
          SUBROUTINE BUILD(AZ)
C  BUILD CREATES A NEW TERRAIN PROFILE (YONEW(30), ZONEW(30)) THAT
C  INCLUDES FORESTED AREAS WHICH ARE REPRESENTED BY AREAS ELEVATED
C  BY THT ABOVE THE ORIGINAL PROFILE.  THE NEW NUMBER OF PLATES,
C  NEW, IS GREATER THAN NE BECAUSE OF THE VERTICAL SIDES OF
C  FORESTED AREAS.
          IMPLICIT REAL*8 (A,B,D-H,O-Z)
          DIMENSION XP(3),YP(3),ZP(3),RN(3),RN1(3)
       .  COMMON /KCB/ UPLAT(50,3),UN(3),US(3),NPLATE
          COMMON /AZP/ AZD
          COMMON /PLATE/ XO(30),YO(30),ZO(30),NE
          COMMON /KTREE/ THT,EF,RHOF,YONEW(30),ZONEW(30),TYPE(30),NEW
          COMMON /KTRANS/ DRV(50,3),NSKIP
          DATA T/'T'/,C/'C'/
          NADD=0
C  KCPFPT PLOTS THE TERRAIN PROFILE
C      IF(AZ.EQ.AZD) CALL KCPFPT(NE,YO,ZO,0)
          YONEW(1)=YO(1)
          ZONEW(1)=ZO(1)
          DO 20 N1=2,NE
          YONEW(N1+NADD)=YO(N1)
          ZONEW(N1+NADD)=ZO(N1)
          IF(TYPE(N1).NE.T.AND.TYPE(N1-1).NE.T) GO TO 20
          IF(TYPE(N1).EQ.T.AND.TYPE(N1-1).EQ.T) GO TO 10
          IF(TYPE(N1-1).EQ.T) ZONEW(N1+NADD)=ZO(N1)+THT
          NADD=NADD+1
          YONEW(N1+NADD)=YO(N1)
          ZONEW(N1+NADD)=ZO(N1)+THT
          IF(TYPE(N1-1).EQ.T) ZONEW(N1+NADD)=ZO(N1)
          GO TO 20
10        YONEW(N1+NADD)=YO(N1)
          ZONEW(N1+NADD)=ZO(N1)+THT
20        CONTINUE
          NSKIP=0
          NEW=NE+NADD
C  IF THERE ARE NO TREES ON THE PROFILE, NSKIP=1
          IF(NE.EQ.NEW) NSKIP=1
          IF(NSKIP.EQ.1) RETURN
C  SCALE IS AN ENTRY POINT TO KCPFPT
```

Figure C-3. (Continued).

```
C       IF(AZ.EQ.AZD) CALL SCALE(NEW,YONEW,ZONEW,1)
        I1=1
        I2=2
        I3=3
        I4=4
        NP=NEW*2
        DO 30 I=1,NP
        J=(I+1)/2
C DRV IS A 3-DIMENSIONAL TERRAIN PROFILE USED BY THE
C MAIN PROGRAM; THE FOLLOWING TAKES THE NEW 2-DIMENS-
C IONAL PROFILE AND CREATES A FLAT 3-D PROFILE.
        DRV(I,2)=YONEW(J)
        DRV(I,3)=ZONEW(J)
        DRV(I,1)=(-1)**I*(-1)**J*50000.
30      CONTINUE
        NPLATE=(NEW*2-2)/2
        DO 90 I=1,NPLATE
        ODD=I/2.
        IEVEN=ODD
        IEVEN=IEVEN*2
        DO 40 J=1,3
        XP(J)=DRV(I1,J)-DRV(I3,J)
        YP(J)=DRV(I2,J)-DRV(I4,J)
        RN(J)=DRV(I3,J)-DRV(I1,J)
40      RN1(J)=DRV(I4,J)-DRV(I2,J)
        IF(IEVEN.NE.I) GOTO 50
C VECTOR(IOP,A,B,C) PERFORMS VECTOR OPERATIONS: IOP=1, C WILL
C BE THE CROSS PRODUCT OF 1X3 VECTORS A AND B; IOP=2, C IS THE
C NORMALIZED CROSS PRODUCT; IOP=3, C IS THE UNIT VECTOR DEFINED
C BY THE ENDPOINTS OF A AND B; IOP=4, C(1) IS THE DOT PRODUCT
C OF A AND B (C(2)=C(3)=0).
C THE FOLLOWING CHECKS TO INSURE THAT 3-D PLATES ARE CO-PLANAR.
        CALL VECTOR(2,RN1,RN,UN)
        CALL VECTOR(2,YP,XP,ZP)
        CALL VECTOR(4,ZP,UN,XP)
        GO TO 60
50      CALL VECTOR(2,RN,RN1,UN)
        CALL VECTOR(2,XP,YP,ZP)
        CALL VECTOR(4,ZP,UN,XP)
60      CONTINUE
        IF(DABS(XP(1)-1.D0).LT.1.D-10) GOTO 70
        WRITE(7,44) I
44      FORMAT(1X,'VERTICIES NONPLANAR AT PLATE', I3)
        STOP
70      DO 80 L1=1,3
```

Figure C-3.   (Continued).

```
80   UPLAT(I,L1)=UN(L1)
     I1=I1+2
     I2=I2+2
     I3=I3+2
     I4=I4+2
90   CONTINUE
     RETURN
     END
```

Figure C-3.   (Continued).

```
            SUBROUTINE KCTREE(PT1,L1,PT2,L2,PT3,L3,CTREE,IOP)
C  SUBROUTINE KCTREE IS CALLED BY THE GTD MAIN PROGRAM WHENEVER A RAY OR
C  RAY COMBINATION IS DETERMINED TO EXIST.  PT1, PT2, AND PT3 ARE GROUND
C  POINTS OF INTERACTION (I.E., REFLECTION OR DIFFRACTION POINTS)
C  EXPRESSED IN WAVELENGTHS.  IOP INDICATES THE RAY TYPE.
C  THE POSITION OF THE TRANSMITTING ANTENNA, XP,YP, AND ZP ARE
C  SPECIFIED IN THE COMMON BLOCK /ANTNNA/.  THE COORDINATES OF THE
C  OBSERVER (X,Y,Z) ARE GIVEN IN COMMON BLOCK /OBSVER/. THE TERRAIN
C  PROFILE WITHOUT TREES IS DRV(50,3) AND IS TRANSFERRED IN COMMON
C  BLOCK /KTRANS/.  THE PROFILE INCLUDING TREES IS IN YONEW AND
C  ZONEW, TRANSFERRED IN COMMON BLOCK /KTREE/. CTREE IS THE COMPLEX
C  VARIABLE OUTPUT OF THE SUBROUTINE REPRESENTING THE PHASE SHIFT AND
C  ATTENUATION EXPERIENCED BY THE RAY AS A RESULT OF INTERACTIONS WITH
C  THE TREES.
            IMPLICIT REAL*8 (A,B,D-H,P-Z)
            IMPLICIT COMPLEX*16 (C)
            REAL*8 K
            DIMENSION PT1(3),PT2(3),PT3(3),PTA(3),PTB(3)
            COMMON /ANTNNA/ XP(40),YP(40),ZP(40),K,FREQ,N
            COMMON /OBSVER/ X,Y,Z
            COMMON /KCDUM/ DUM(3),KM
            COMMON /KTREE/ THT,EF,RHOF,YONEW(30),ZONEW(30),TYPE(30),NEW
            COMMON /KTRANS/ DRV(50,3),NSKIP
C  SUM AND SUMCL ARE THE DISTANCES THAT RAYS TRAVEL THROUGH AND
C  WITHIN THE FRESNEL ELLIPSE CLEARANCE OF THE TREES,RESPECTIVELY.
C  THESE VARIABLES ARE INITIALIZED TO ZERO.
            SUM=0.
            SUMCL=0.
            PI=3.14159265358979
C  XLAMDA IS THE WAVELENGTH = 2*PI/PHASE CONSTANT
            XLAMDA=(PI*2.DO)/K
            CTREE=CMPLX(1.0,0.)
C  NSKIP=1 INDICATES NO TREES ON PROFILE, THUS RETURN TO MAIN.
99          IF(NSKIP.EQ.0) GO TO 10
            RETURN
C  THE 3-DIMENSIONAL VECTOR PTA IS SET TO THE VECTOR OF THE XMITTING
C  ANTENNA
10          PTA(1)=XP(1)
            PTA(2)=YP(1)
            PTA(3)=ZP(1)
C  VECTOR PTB IS SET EQUAL TO THE FIRST GROUND POINT OF INTERACTION.
            DO 20 I=1,3
20          PTB(I)=PT1(I)*XLAMDA
C  IF THE RAY IS NOT A DIRECT RAY, GO TO 30
            IF(IOP.NE.1) GO TO 30
C  VECTOR PTB IS SET EQUAL TO THE FIRST GROUND POINT OF INTERACTION.
            PTB(1)=X
            PTB(2)=Y
            PTB(3)=Z
```

Figure C-4.   Program Listing of SUBROUTINE KCTREE.

```
C  CLEAR DETERMINES PATH DISTANCE WITHIN FRESNEL ELLIPSE
30     CALL CLEAR(PTA,PTB,SUMCL)
C  TOTAL DETERMINES PATH DISTANCE WITHIN FOREST
       CALL TOTAL(PTA,PTB,SUM)
C  SUBTRACT COMMON DISTANCE
       SUMCL=SUMCL-SUM
       IF(SUMCL.LT.0.) SUMCL=0.
       IF(IOP.NE.1) GO TO 40
C  COMPLEX FUNCTION CKTR DETERMINES ATTENUATION AND PHASE SHIFT DUE
C  TRAVELING SUM DISTANCE THROUGH TREES.
       CTREE=CKTR(SUM)
C  CLATT DETERMINES ATTENUATION DUE TO PASSING A DISTANCE SUMCL
C  WITHIN THE FRESNEL ELLIPSE OF THE FOREST.
       CALL CLATT(SUMCL,CTREE)
       WRITE(7,1) IOP,SUM,SUMCL,CTREE
1      FORMAT(1X,' RAY ',I3,' WITHIN=',F6.0,' WITHIN CLEARANCE=',F6.0,'
      , CTREE=',2F10.7)
       RETURN
C  SET THE FIRST GROUND POINT OF INTERACTION AS THE SOURCE PTA
40     DO 50 J=1,3
50     PTA(J)=PT1(J)*XLAMDA
C  IF MORE THAN ONE GROUND POINT OF INTERACTION, GO TO 60; OTHERWISE
C  SET PTB TO OBSERVATION POINT
       IF(IOP.NE.2.AND.IOP.NE.8) GO TO 60
       PTB(1)=X
       PTB(2)=Y
       PTB(3)=Z
       GO TO 80
C  SET PTB EQUAL TO THE SECOND GROUND POINT OF INTERACTION
60     DO 70 IK=1,3
70     PTB(IK)=PT2(IK)
80     CALL CLEAR(PTA,PTB,SUMCL)
       CALL TOTAL(PTA,PTB,SUM)
       SUMCL=SUMCL-SUM
       IF(SUMCL.LT.0.) SUMCL=0.
C  IF THERE ARE ONLY TWO GROUND POINTS OF INTERACTION, COMPUTE LOSSES
C  AND THEN RETURN
       IF(IOP.NE.2.AND.IOP.NE.8) GO TO 90
       CTREE=CKTR(SUM)
       CALL CLATT(SUMCL,CTREE)
       WRITE(7,1) IOP,SUM,SUMCL,CTREE
       RETURN
C  SET PTA EQUAL TO THE SECOND GROUND POINT OF INTERACTION
90     DO 100 L=1,3
100    PTA(L)=PT2(L)*XLAMDA
C  IF THERE IS A THIRD GROUND POINT OF INTERACTION, GO TO 110
       IF(IOP.GT.4.AND.IOP.LT.8) GO TO 110
       IF(IOP.EQ.10.OR.IOP.EQ.12) GO TO 110
```

Figure C-4. (Continued).

```fortran
         PTB(1)=X
         PTB(2)=Y
         PTB(3)=Z
         GO TO 130
C  SET PTB TO THE THIRD GROUND POINT OF INTERACTION
110      DO 120 IM=1,3
120      PTB(IM)=PT3(IM)*XLAMDA
130      CALL CLEAR(PTA,PTB,SUMCL)
         CALL TOTAL(PTA,PTB,SUM)
         SUMCL=SUMCL-SUM
         IF(SUMCL.LT.0.) SUMCL=0.
         IF(IOP.GT.4.AND.IOP.LT.8) GO TO 140
         CTREE=CKTR(SUM)
         CALL CLATT(SUMCL,CTREE)
         WRITE(7,1) IOP,SUM,SUMCL,CTREE
         RETURN
C  SET PTA TO THE THIRD GROUND POINT OF INTERACTION
140      DO 150 IN=1,3
150      PTA(IN)=PT3(IN)
         PTB(1)=X
         PTB(2)=Y
         PTB(3)=Z
         CALL CLEAR(PTA,PTB,SUMCL)
         CALL TOTAL(PTA,PTB,SUM)
         SUMCL=SUMCL-SUM
         IF(SUMCL.LT.0.) SUMCL=0.
         CTREE=CKTR(SUM)
         CALL CLATT(SUMCL,CTREE)
         WRITE(7,1) IOP,SUM,SUMCL,CTREE
         RETURN
         END
         SUBROUTINE CLEAR(PTA,PTB,SUMCL)
C  SUBROUTINE CLEAR DETERMINES THE DISTANCE THAT THE FIRST FRESNEL
C  ELLIPSE INTERSECTS THE FOREST FOR A RAY ORIGINATING AT PTA AND
C  TERMINATING AT PTB: SUMCL IS THAT DISTANCE
         IMPLICIT REAL*8 (A-H,O-Z)
         COMMON /CLAT/ XNEP,RATIO
         DIMENSION PTA(3),PTB(3),PTC(3),PTD(3)
C  PTC AND PTD ARE TWO VECTORS REPRESENTING POINTS ALONG THE LOWER
C  FRESNEL ELLIPSE OF THE RAY PTA PTB.
         PTC(1)=0.
         PTD(1)=0.
         PTC(2)=PTA(2)
         PTC(3)=PTA(3)
C  SLOPE AND CEPT ARE THE SLOPE AND INTERCEPT OF THE RAY
         SLOPE=(PTB(3)-PTA(3))/(PTB(2)-PTA(2))
         CEPT=PTA(3)-SLOPE*PTA(2)
C  THE DISTANCE ALONG THE RAY IS INCREMENTED BY 100'
10       PTD(2)=PTC(2)+100.
```

Figure C-4. (Continued).

```
C   THE PATH LENGTH IS LIMITED TO 4000'
      IF(PTD(2).GT.PTB(2).OR.PTD(2).GT.4000.) GO TO 30
C   FRES DETERMINES THE FRESNEL ELLIPSE MINOR AXIS FOR A POINT
C   ON THE RAY, PTC.
      CALL FRES(PTA,PTB,PTD,R)
C   THE VECTOR PTD IS UPDATED
      PTD(3)=SLOPE*PTD(2)+CEPT-R*RATIO
C   TOTAL IS CALLED TO DETERMINE THE INCREMENTAL DISTANCE
C   THAT THE FRESNEL ELLIPSE INTERSECTS THE TREES.
      CALL TOTAL(PTC,PTD,SUMCL)
      PTC(2)=PTD(2)
      PTC(3)=PTD(3)
      GO TO 10
30    RETURN
      END
      SUBROUTINE CLATT(SUMCL,CTREE)
C   CLATT MULTIPLIES CTREE BY AN ATTENUATION FACTOR PROPORTIONAL
C   TO THE DISTANCE THAT THE RAY FRESNEL ELLIPSE INTERSECTS THE
C   TREES.  THAT ATTENUATION FACTOR IS EXP(XNEPER*SUMCL).
      IMPLICIT REAL*8 (A,B,D-H,O-Z)
      IMPLICIT COMPLEX*16 (C)
      COMMON /CLAT/ XNEP,RATIO
      XTOT=SUMCL*XNEP
      CTOT=DCMPLX(XTOT,0.D0)
      COEF=CDEXP(CTOT)
      CTREE=CTREE*COEF
      RETURN
      END
      SUBROUTINE TOTAL(PTA,PTB,SUM)
C   TOTAL DETERMINES THE DISTANCE THAT THE RAY PTA,PTB IS WITHIN
C   THE TREES.
      IMPLICIT REAL*8 (A-H,P-Z)
      DIMENSION PTB(3),PTA(3),PTC(3)
      COMMON /KTREE/ THT,EF,RHOF,YONEW(30),ZONEW(30),TYPE(30),NEW
      COMMON /KTRANS/ DRV(50,3),NSKIP
      COMMON /KCDUM/ DUM(3),KM
      IBOTH=0
C   NEW IS THE NUMBER OF PLATES ON THE PROFILE WITH TREE DATA
      NEW1=NEW-1
C   DETERMINE WHICH PLATES THE SOURCE AND RECEIVER ARE ON
      DO 10 I=1,NEW1
      IF(PTA(2).GE.YONEW(I)) LA=I
      IF(PTB(2).GT.YONEW(I)) LB=I
10    CONTINUE
C   INCREMENT Z COMPONENTS TO INSURE THAT THEY ARE NOT ON
C   THE PROFILE ITSELF.
15    PTB(3)=PTB(3)+.01
      PTA(3)=PTA(3)+.01
C   INOUT DETERMINES IF POINT IS INSIDE OR OUTSIDE OF
```

Figure C-4. (Continued).

```
C   TREE BOUNDARY.
        CALL INOUT(PTA,LA,IN)
        CALL INOUT(PTB,LB,INB)
        IF(INB.LT.1.AND.IN.LT.1) IBOTH=1
C   KCLOGI DETERMINES IF RAY IS BLOCKED BY TREES; IF SO,
C   BLOCKAGE POINT IS GIVEN IN DUM.
16      CALL KCLOGI(PTA,PTB,DRV,LA,LB,LCHECK)
C   IF BOTH POINTS ARE OUT OF THE TREES, AND THERE IS NO
C   BLOCKAGE, RETURN TO MAIN.
        IF(LCHECK.EQ.-1.AND.IBOTH.EQ.0) RETURN
        IF(IBOTH.EQ.1) GO TO 17
        IF(IN.LT.1) GO TO 20
C   IF SOURCE IS ABOVE TREES, SET PTA TO BLOCKAGE POINT
        PTA(1)=DUM(1)
        PTA(2)=.01+DUM(2)
        PTA(3)=.01+DUM(3)
        IF(PTB(3).LT.PTA(3)) PTA(3)=PTA(3)-.02
        LA=KM
        DIFF=PTA(2)-PTB(2)
        IF(DABS(DIFF).LT.1.) RETURN
C   AGAIN CHECK FOR BLOCKAGE
        CALL KCLOGI(PTA,PTB,DRV,KM,LB,LCHECK)
        IF(LCHECK.EQ.1) GO TO 20
C   COMPUTE THE DISTANCE BETWEEN PTA AND PTB
17      DELX2=(PTA(1)-PTB(1))**2
        DELY2=(PTA(2)-PTB(2))**2
        DELZ2=(PTA(3)-PTB(3))**2
        SUM=SUM+DSQRT(DELX2+DELY2+DELZ2)
        RETURN
C   COMPUTE DISTANCE BETWEEN PTA AND BLOCKAGE POINT
20      DELX2=(PTA(1)-DUM(1))**2
        DELY2=(PTA(2)-DUM(2))**2
        DELZ2=(PTA(3)-DUM(3))**2
        SUM=SUM+DSQRT(DELX2+DELY2+DELZ2)
        PTA(1)=DUM(1)
        PTA(2)=.01+DUM(2)
        PTA(3)=.01+DUM(3)
        IF(PTB(3).LT.PTA(3)) PTA(3)=PTA(3)-.02
        LA=KM
        GO TO 16
30      RETURN
        END
        COMPLEX FUNCTION CKTR(SUM)
C   CKTR DETERMINES THE ATTENUATION AND PHASE SHIFT RESULTING FROM
C   TRAVELING A DISTANCE SUM THROUGH A LOSSY FOREST.  THE COMPLEX
C   PROPAGATION CONSTANT, CALBT, IS TRANSFERRED IN COMMON BLOCK
C   /CGAMMA/
        IMPLICIT COMPLEX*16 (C)
        IMPLICIT REAL*8 (A,B,D-H,O-Z)
```

Figure C-4. (Continued).

```fortran
      REAL*8 K
      COMMON /ANTNNA/ XP(40),YP(40),ZP(40),K,FREQ,N
      COMMON /KTREE/ THT,EF,RHOF,YONEW(30),ZONEW(30),TYPE(30),NEW
      COMMON /CGAMMA/ CALBTO,CALBT
      SUMM=SUM*.3048D0
      BETAO=DIMAG(CALBTO)
      PHAO=SUMM*BETAO
      BETA=DIMAG(CALBT)
      ALPHA=DREAL(CALBT)
      XNEPER=-SUMM*ALPHA
      PHA=SUMM*BETA
      DELPHA=PHAO-PHA
      CEX=DCMPLX(XNEPER,DELPHA)
      CKTR=CDEXP(CEX)
      RETURN
      END
      SUBROUTINE INOUT(PTX,LX,ITEST)
      IMPLICIT REAL*8(A-H,O-Z)
C  ITEST=1 PTX ABOVE TREE LEVEL;=0 AT TREE LEVEL;=-1 BELOW TREE LEVEL
      COMMON /KTREE/ THT,EF,RHOF,YONEW(30),ZONEW(30),TYPE(30),NEW
      DIMENSION PTX(3)
      YDIFF=PTX(2)-YONEW(LX)
      DELTY=YONEW(LX+1)-YONEW(LX)
      DELTZ=ZONEW(LX+1)-ZONEW(LX)
      IF(DELTY.EQ.0.) Z=ZONEW(LX+1)
      IF(DELTY.EQ.0.) GO TO 10
      Z=ZONEW(LX)+(DELTZ/DELTY)*YDIFF
10    ITEST=0
      IF(PTX(3).GT.Z) ITEST=1
      IF(PTX(3).LT.Z) ITEST=-1
      RETURN
      END
      SUBROUTINE FRES(PTA,PTB,PTC,R)
C  FRES DETERMINES THE MINOR AXIS OF THE FRESNEL ELLIPSE AT A POINT
C  PTC ON A RAY PTA-PTB. R IS THE MINOR AXIS.
      IMPLICIT REAL*8 (A-H,K,O-Z)
      COMMON /ANTNNA/ XP(40),YP(40),ZP(40),K,FREQ,N
      DIMENSION PTA(3),PTB(3),PTC(3)
      D=DSQRT((PTA(2)-PTB(2))**2+(PTA(3)-PTB(3))**2)
      D1=PTC(2)-PTA(2)
      D2=PTB(2)-PTC(2)
      SPEED=9.84251987D8
      XLAMDA=SPEED/FREQ
      R=DSQRT(XLAMDA*(D1*D2)/D)
      RETURN
      END
```

Figure C-4. (Continued).

D.   Input Data Requirements for GTD/Forest Model Operation.   The
GTD/Forest model requires certain information about an RCAG site in
order to predict received signal strength for a specified observation
point.   This appendix details data input requirements necessary for
model operation.   To illustrate the modeling procedure, input parame-
ters for an actual site are shown here as they would be input to the
model.   The example site discussed here is the South Raleigh RCAG
site, which is located south of Raleigh-Durham, North Carolina.

The first parameters that need to be specified are the non-terrain
parameters, which are: transmitting antenna height (feet MSL), effec-
tive radiated power (Watts), mean tree height (feet AGL), relative
permitivity and conductivity (mhos/meter) of the forested medium, the
Fresnel Ellipse correction factor, and the fraction of the Fresnel
Ellipse to be considered in applying the correction factor.   These
parameters are read by the program or the first card or card image
using an F8.0 FORMAT.

Figure D-1 shows these values for the South Raleigh site.   The
antenna height is 44' above the ground and thus 409' MSL because
ground level at the site is 365' MSL.   The next parameter is effective
radiated power, which is 10 Watts.   Tree height in the vicinity of
the site is quite variable, however a reasonable estimate is 30'.   A
median value of relative permitivity (1.05) is generally used for
modeling.   Conductivity is scaled down by a factor of 10^{-7} by the
program; thus the value of 300 seen in Figure D-1 represents a conduc-
tivity of 3×10^{-5} mhos/meter.   It should be noted here that input
values of conductivity and permitivity will not affect modeling
results unless propagation is through the forested medium.   The
-0.0008 in Figure D-1 is the empirically-derived Fresnel-Ellipse
correction factor, and 0.5 is the fraction of the Fresnel Ellipse that
must intersect the trees before any correction term is applied; the
numerical values shown for these parameters in this example have pro-
vided good modeling results for the sites considered in this study.
Thus, the numerical values given above for the last two parameters
discussed should be used for site modeling.

Subsequent inputs to the GTD/Forest model specify terrain con-
tours.   To provide insight into what contours are of interest, con-
sider the topographical map of the South Raleigh RCAG site and
vicinity shown in Figure D-2.   As seen in Figure D-2, radials from the
site have been drawn in 5°increments referenced with respect to True
North.   2-dimensional profiles along each of these radials are the
required inputs to the program.   These profiles are specified by coor-
dinates of points representing horizontal distance from the antenna
and elevation.   Thus, as described in Section IIE, a piecewise-linear
approximation to the terrain is assumed for modeling.   Figure D-3 pre-
sents a plot of a terrain contour for the 0° radial at the South
Raleigh site; the dotted lines on this contour represent trees, which
are discussed later in this appendix.   The terrain profile of Figure
D-3 was obtained using the topographical map of Figure D-2.

```
   409.0  10.0    3.0      1.05      300.   -.0008     .5
  13.0    0.
      0.0       365.0 C
    283.0       365.0 T
    750.0       340.0 T
   1062.0       360.0 C
   1100.0       370.0 C
   1400.0       370.0 C
   1723.0       360.0 T
   1800.0       340.0 T
   2150.0       340.0 T
   3250.0       390.0 C
   3400.0       400.0 C
   3700.0       400.0 C
   4000.0       380.0 C
  11.0   5.
      0.0       365.0 C
    283.0       365.0 T
    800.0       340.0 T
   1133.0       370.0 C
   1375.0       380.0 C
   1676.0       360.0 T
   2150.0       340.0 T
   3200.0       390.0 C
   3438.0       400.0 C
   3625.0       400.0 C
   4000.0       370.0 C
  13.0  10.
      0.0       365.0 C
    289.0       365.0 T
    688.0       350.0 T
    875.0       350.0 T
   1085.0       380.0 C
   1525.0       380.0 C
   1625.0       370.0 T
   1812.0       350.0 T
   2281.0       350.0 T
   2400.0       360.0 C
   3375.0       400.0 C
   3750.0       400.0 C
   4000.0       385.0 C
```

Figure D-1.   Sample Data Input to GTD/Forest Computer Model.

SCALE 1:24 000

CONTOUR INTERVAL 10 FEET
NATIONAL GEODETIC VERTICAL DATUM OF 1929

THIS MAP COMPLIES WITH NATIONAL MAP ACCURACY STANDARDS
FOR SALE BY U. S. GEOLOGICAL SURVEY, RESTON, VIRGINIA 22092
A FOLDER DESCRIBING TOPOGRAPHIC MAPS AND SYMBOLS IS AVAILABLE ON REQUEST
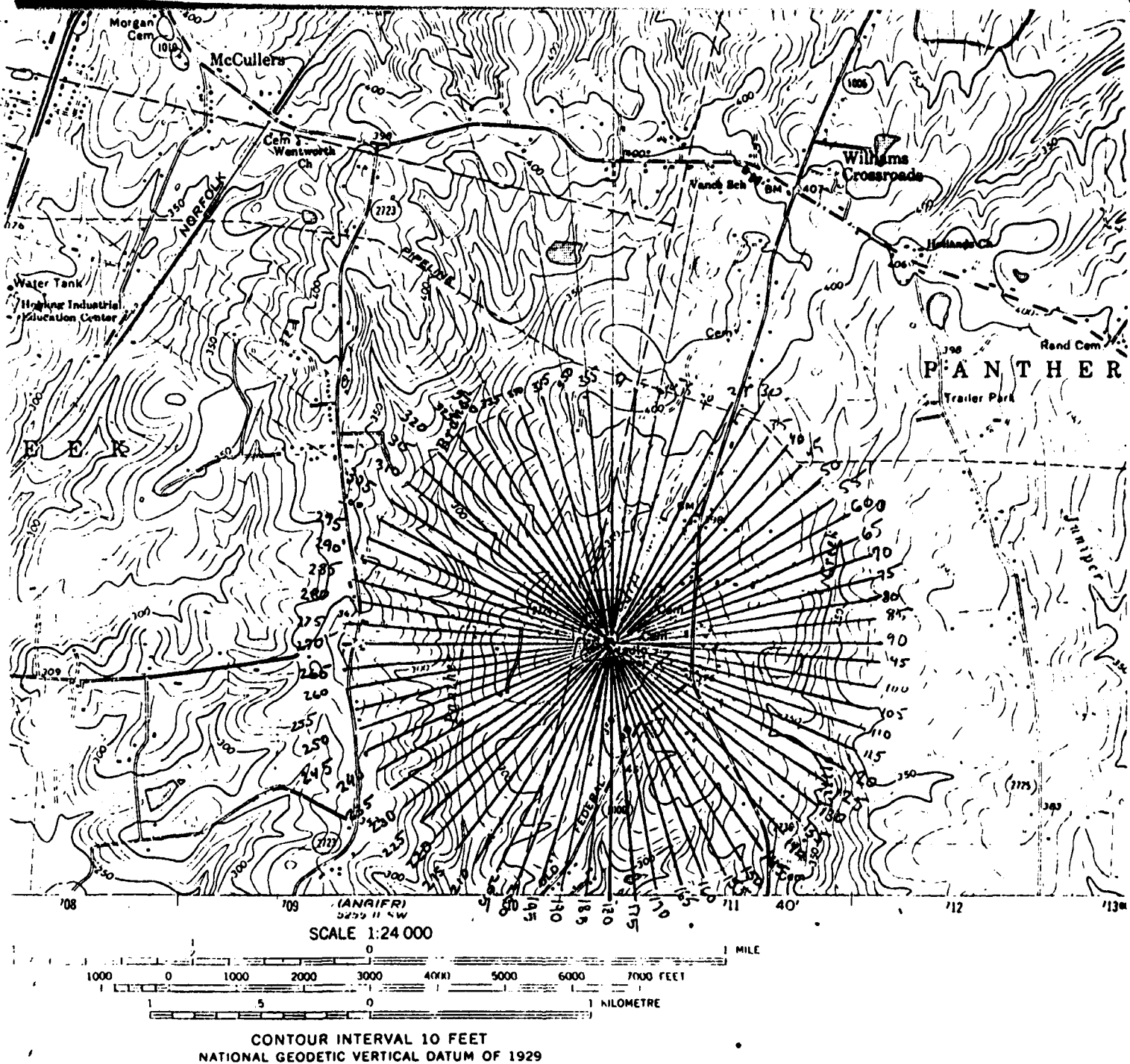
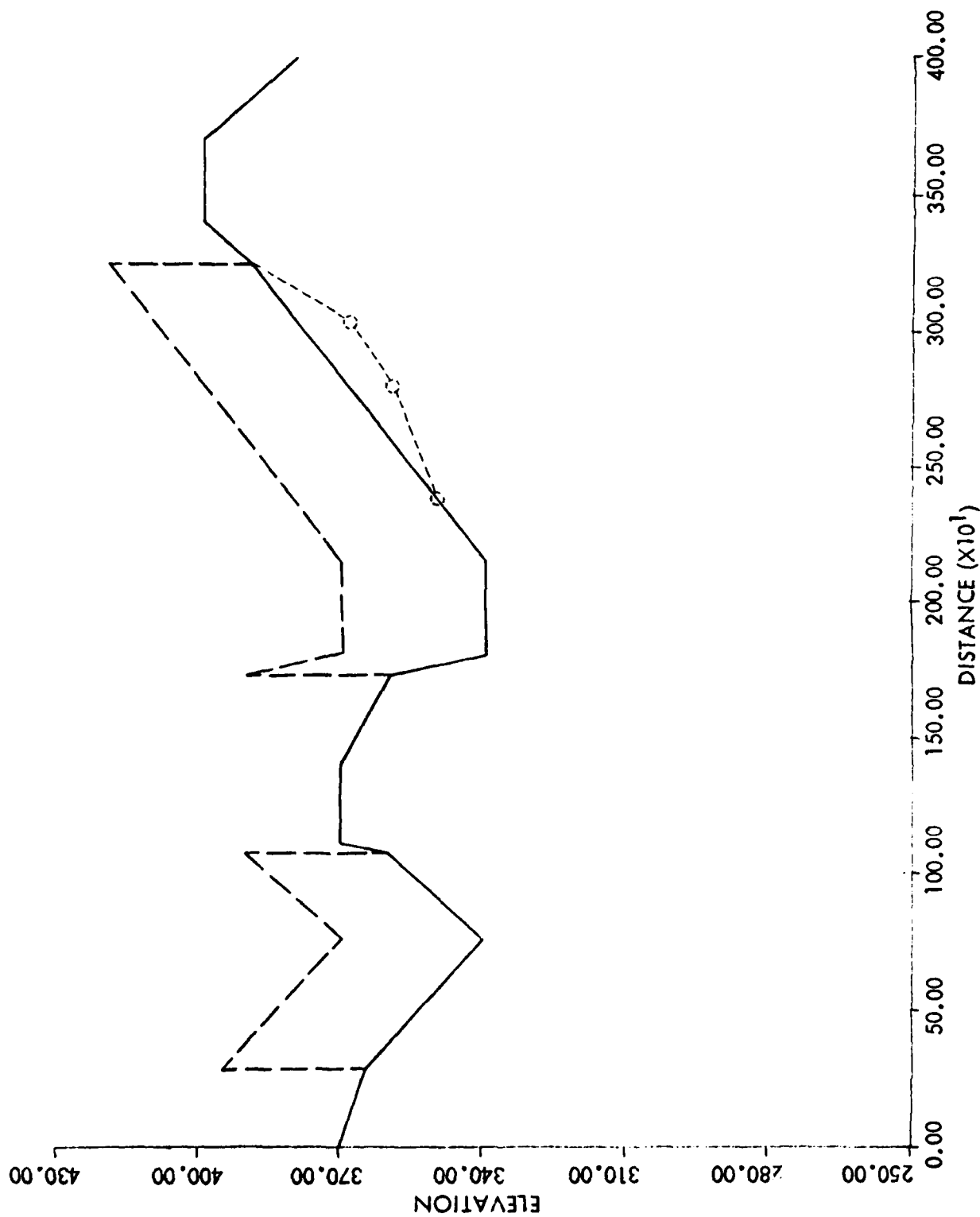Figure D-2.   Example of Data Reduction from Topographical Map.

Figure D-3. Plot of Terrain and Forest Data Input to the GTD/Forest Model. Piecewise-linear terrain indicated by solid line, and forest boundaries shown by dashed line.

The manner in which contour data is reduced is crucial to the performance of the GTD/Forest model. Clearly, a more accurate representation of the terrain profile will result as the number of sample points along the contour are increased. However, as the number of diffractive edges increases, errors associated with the diffraction coefficient tend to accumulate, resulting in a less accurate prediction. Thus, in site modeling, the terrain profile should be constructed using a minimal number of points to represent the general terrain characteristics.

There are no established guidelines for optimal construction of terrain profiles due to the extremely complex relationship between those profiles and received signal strength. Such guidelines can be offered only after an extensive perturbational study has been performed. However, some basic techniques are suggested based upon preliminary work with the GTD/Forest model. To illustrate how these techniques are applied in the construction of a terrain profile, again consider the terrain profile of Figure D-3. The terrain profile shown only extends to 4000' from the transmitting antenna. A profile of this length is generally adequate unless the terrain rises at some point beyond 4000' such that the Fresnel Ellipse between the transmitter and receiver intersects that terrain. If this does happen, the profile must extend at least to the furthest point that intersection occurrs. Very low resolution is necessary in the profile beyond 4000' for reasons given in Section IIIB; a general representation of the terrain slope beyond 4000' should be sufficient for accurate modeling results.

The number of edges defined along the contour, which is equal to the number of coordinates defining the contour, should not exceed 20. If more than 20 points are used, it is suggested that the contour be plotted out to determine what points can be removed without significantly altering the profile. For example, referring to Figure D-3, three terrain profile points are circled and connected by dotted lines in the distance interval between 2200' and 3000'; these points represent the actual terrain in that interval. These circled points are not used for creating the input data file, since their omission will not significantly alter the reflected or diffracted rays computed by the program. Generally, high and low points in the actual profile should appear on the input data profile, and the slope between high and low points should, on the average, be accurate. The terrain profile of Figure D-3 is reduced to tabular form as seen in Figure D-1 for input to the GTD/Forest model. Referring to Figure D-1, the second card, or card image, contains the numbers 13 and 0. These variables, read with an F6.0 FORMAT, indicate that there are 13 data points to be read, and that the profile is for 0° azimuth. The next 13 pairs of numbers, read with an F10.2 FORMAT, represent the coordinates of points along the terrain profile. The first variable represents the distance from the antenna, and the second represents terrain elevation.

The location of forested areas as indicated on topographical maps are not considered sufficiently accurate for signal strength modeling.

Consequently, high-resolution aerial maps are used to determine the boundaries of forested areas. These maps are inexpensive and readily available [49]. Radials are drawn on the aerial map every 5° in azimuth as they are drawn on the topographical map of Figure D-2. Thus, the distance to a forest boundary along any given radial can be accurately determined. A forest boundary is specified on the input data file by coding each terrain profile point with a T or C indicating that the terrain has trees on it, or it is clear of trees. Referring to the input data file of Figure D-1, T's and C's are seen to the immediate right of the edge coordinates; these letters are read by an A1 FORMAT. From Figure D-1, it is seen that the first forested area starts at 283' from the antenna mast along the 0 radial and ends at 1062'; similarly, the second forested area starts at 1723' and ends at 3250'. The terrain profile plot of Figure D-3 shows how these forested areas are seen by the computer model.

A completed data file for use by the GTD/Forest model will contain the type of data specified above and shown in Figure D-1. If signal strength data for an entire orbit are desired as outputs, terrain profiles from 0° to 355° must be specified in the input file. The model output is signal strength in decibels as a function of azimuth angle.